Minnesota Department of Transportation

RESEARCH SERVICES

Office of Policy Analysis, Research & Innovation

Wakota Bridge Thermal Monitoring Program Part II: Data Analysis and Model Comparison

Arturo E. Schultz, Principal Investigator
Department of Civil Engineering
University of Minnesota

May 2013

Research Project
Final Report 2013-12

Your Destination...Our Priority

To request this document in an alternative format, please contact the Affirmative Action Office at 651-366-4723 or 1-800-657-3774 (Greater Minnesota); 711 or 1-800-627-3529 (Minnesota Relay). You may also send an e-mail to ADArequest.dot@state.mn.us.

(Please request at least one week in advance).

Technical Report Documentation Page

1. Report No.	2.	3. Recipients Accession No.	
MN/RC 2013-12			
4. Title and Subtitle Wakota Bridge Thermal Monitoring Program Part II: Data Analysis and Model Comparison		5. Report Date May 2013 6.	
7. Author(s) Krista M. Morris and Arturo E. Schultz		8. Performing Organization Report No.	
9. Performing Organization Name and Address Department of Civil Engineering University of Minnesota 500 Pillsbury Drive SE Minneapolis, MN 55455		10. Project/Task/Work Unit No. CTS Project #2010011 11. Contract (C) or Grant (G) No. (C) 89261 (WO) 145	
12. Sponsoring Organization Name and Address Minnesota Department of Transportation Research Services 395 John Ireland Boulevard, MS 330 St. Paul, MN 55155		13. Type of Report and Period Covered Final Report 14. Sponsoring Agency Code	
15. Supplementary Notes http://www.lrrb.org/pdf/201312.pdf			

16. Abstract (Limit: 250 words)

In this work, a common refined design method is evaluated with respect to a recently constructed bridge. Two finite element models of the Wakota Bridge in South St. Paul, Minnesota were produced using a design level program (SAP2000). These models were analyzed and their results compared to the data collected from the bridge.

The second half of this study concerned the comparison of the collected field data with the values produced by evaluating the design-level finite element models previously created in Phase I of the project, and calibrating these models to provide an accurate prediction of the future behavior of the bridge. This was done by calculating changes in axial force and moment from strain data collected from the Wakota Bridge and changing various parameters within the design level model (DLM) in order to calibrate the models to the field data. The model using the refined design method was shown to correlate to the superstructure field data to within 2 percent, while between 13 percent and 35 percent correlation was seen between the model deploying the gross section method and the field data.

The pier behavior predicted by the two models showed much less correlation to the field data. After calibration, it was possible to predict the general trend of the pier behavior, but the values of changes in moment did not correspond to the field data. This was especially true in Pier 4. Further consideration of the model parameters is necessary to fully calibrate the models.

The two temperature application methods (Procedure A and B in the AASHTO LRFD) were also compared. The internal concrete temperature ranges measured in the field were much closer to the range specified in Procedure A.

17. Document Analysis/Descriptors	18. Availability Statement		
Temperature, Thermal stresses, Concrete, Bridge piers, Finite element method	No restrictions. Document available from: National Technical Information Services, Alexandria, Virginia 22312		
19. Security Class (this report) Unclassified	20. Security Class (this page) Unclassified	21. No. of Pages 167	22. Price

Wakota Bridge Thermal Monitoring Program
Part II: Data Analysis and Model Comparison

Final Report

Prepared by:

Krista M. Morris
Arturo E. Schultz

Department of Civil Engineering
University of Minnesota

May 2013

Published by:

Minnesota Department of Transportation
Research Services
395 John Ireland Boulevard, MS 330
St. Paul, Minnesota 55155

Acknowledgments

The authors would like to thank the Minneosta Department of Transportation for funding this project. The authors would also like to thank the Technical Advisory Panel (TAP) members for their help and guidance during the development of this report: Dave Dahlberg, Arielle Ehrlich, Shirlee Sherkow, Paul Stenberg, Jihshya Lin, and Dustin Thomas. Finally, the authors would like to thank Paul Bergson, Rachel Gaulke, Ben Dymond, Andrew Gastineau, and others in the Department of Civil Engineering at the University of Minnesota for their assistance and advice.

Table of Contents

List of Figures

List of Tables

List of Abbreviations

AASHTO	American Association of State and Highway Transportation Officials
ACI	American Concrete Institute
NOAA	National Oceanic and Atmospheric Association
RUBPier2	Rusticated face of the Up-station blade, at the Bottom instrumented section of Pier 2.
SUBPier2	Smooth face of the Up-station blade, at the Bottom instrumented section of Pier 2.
SDBPier2	Smooth face of the Down-station blade, at the Bottom instrumented section of Pier 2.
RDBPier2	Rusticated face of the Down-station blade, at the Bottom instrumented section of Pier 2.
RUBPier4	Rusticated face of the Up-station blade, at the Bottom instrumented section of Pier 4.
SUBPier4	Smooth face of the Up-station blade, at the Bottom instrumented section of Pier 4.
SDBPier4	Smooth face of the Down-station blade, at the Bottom instrumented section of Pier 4.
RDBPier4	Rusticated face of the Down-station blade, at the Bottom instrumented section of Pier 4.
RUTPier2	Rusticated face of the Up-station blade, at the Top instrumented section of Pier 2.
SUTPier2	Smooth face of the Up-station blade, at the Top instrumented section of Pier 2.
SDTPier2	Smooth face of the Down-station blade, at the Top instrumented section of Pier 2.
RDTPier2	Rusticated face of the Down-station blade, at the Top instrumented section of Pier 2.
RUTPier4	Rusticated face of the Up-station blade, at the Top instrumented section of Pier 4.
SUTPier4	Smooth face of the Up-station blade, at the Top instrumented section of Pier 4.
SDTPier4	Smooth face of the Down-station blade, at the Top instrumented section of Pier 4.
RDTPier4	Rusticated face of the Down-station blade, at the Top instrumented section of Pier 4.
TSpan3	Top flange of Span 3 cross-section.
BSpan3	Bottom flange of Span 3 cross-section.
LSpan3	Left web of Span 3 cross-section.
CSpan3	Center web of Span 3 cross-section.
RSpan3	Right web of Span 3 cross-section.
TSpan4	Top flange of Span 4 cross-section.

BSpan4	Bottom flange of Span 4 cross-section.
LSpan4	Left web of Span 4 cross-section.
CSpan4	Center web of Span 4 cross-section.
RSpan4	Right web of Span 4 cross-section.
SAP2000	Structural analysis program used often in design.
DLM_Gross	Design-level model created in SAP2000 using the gross-section method for ` calculating the stiffness of the piers after cracking.
DLM_Ref	Design-level model created in SAP2000 using the Common Refined Design Method for calculating the stiffness of the piers after cracking.
CRD	Common Refined Design
CTE	Coefficient of Thermal Expansion

Executive Summary

A two-part investigation into the behavior of bridges with fixed connections between pier substructure and the superstructure was conducted to better understand their behavior. The two main areas of interest in the study were the method of approximating the stiffness of the cracked pier sections and the effect of thermal loads on the behavior of the bridge. The Wakota Bridge is a five-span, post-tensioned, segmental box-girder bridge that employs fixed-flexible twin-blade piers in its substructure. The bridge was instrumented with a total of 84 vibrating wire strain gauges, with built-in thermistors, distributed uniformly across cross-sections both in superstructure segments of Spans 3 and 4 of the bridge as well as at two different elevations in the pier blades of Piers 2 and 4, where Span 4 and Pier 4 are located upstation from Span 3 and Pier 2. Two linear string potentiometers were also installed, one at each abutment, to record information about the total change in length of the superstructure with changing temperature.

There are two different methods allowed by the American Association of State Highway and Transportation Officials *LRFD Bridge Design Specifications* Fourth Edition (AASHTO LRFD) [1] for approximating cracked section stiffness in design. The first procedure, known as the gross section method, uses the full stiffness of the section during analysis and applies a factor of 0.5 to the thermal loads for lateral analysis of the section. The second procedure, the refined analysis method, requires a moment-curvature analysis of the section under consideration to estimate the effect of cracking on section stiffness and applies a factor of 1.0 to the thermal loads. The refined analysis method is a more complicated procedure and thus is more time consuming, which is undesirable in some cases. However, this procedure typically produces more accurate predictions of the stiffness of the section under consideration than does the much simpler gross section method.

A comparison of the two procedures allowed by the AASHTO LRFD for determination of thermal forces was also conducted. Procedure A uses an 80 °F temperature range, while Procedure B applies a 150 °F temperature range as interpreted by the Minnesota Department of Transportation (MnDOT) from contour maps developed by Roeder [2], showing the average maximum and minimum daily temperatures measured throughout the United States. The MnDOT LRFD Bridge Design Manual (BDM) uses a base temperature of 45 °F and applies a rise of 35 °F and fall of 45 °F for Procedure A, and a rise of 75 °F and fall of 75 °F for Procedure B.

This report describes the analysis of data collected from the Wakota Bridge, as well as comparison to the finite element models created in Phase I of the project. Initial analysis of the collected strain data showed that the superstructure underwent an increase in compressive force with increasing temperature across the cross-sections in both Span 3 and 4, and that the two instrumented piers underwent double-curvature bending. Changes in axial force and moment calculated for both the superstructure sections and the pier sections confirmed these initial conclusions. Initial analysis also showed that while the range of the ambient air temperature surrounding the bridge reached 119 °F, a 20 % lower value than the Procedure B temperature range, the internal concrete temperature ranges measured by the thermistors recorded an average temperature change of 83.8 °F, only a 5 % increase over the 80 °F temperature range specified in Procedure A.

Comparison of the field data to changes in axial force and moment as predicted by finite element models contrasted the two methods of approximating pier stiffness allowed by AASHTO LRFD. The first model approximated pier stiffness using a refined analysis method, an iterative process that calculated the actual cracked pier stiffness, while the second used the gross section method, which assumed the full stiffness of the gross sectionof the pier blade with an applied load factor of 0.5 to account for any loss of stiffness due to cracking. Both finite element models were able to predict the behavior of the superstructure sections with differing degrees of accuracy when compared to the field data: The use of the refined design method in combination with the temperature range measured from the field resulted in predicted superstructure behavior that matched that seen in the field, producing changes in moment across the cross-sections that were between 1-2 % different from those measured in the field. The model using the gross section method was not as accurate in its prediction of superstructure behavior; differences between changes in the measured and predicted moment were between 13% and 35% for this model. The gross section method would be best used in preliminary design only, followed by use of the refined design method for final design of the structure. Given that general principles of structural mechanics were used to model the bridge in this study, these procedures should also be adequate to address bridges with other pier types.

The two finite element models were less accurate in their predictions of pier behavior with respect to changes in temperature. While variation of a number of model parameters was sufficient to calibrate the behavior of Pier 2 to the measured field data, the parameters for Pier 4 were much more difficult to fully calibrate.

Two potential sources of error in the finite element predictions of the pier moments were investigated: a) the rotational support at the base of the piers, and b) the stiffness of the piers. This limited parametric study indicated that pier moments were sensitive to the magnitude and distribution of pier stiffness, and that neither of the refined analysis method or the gross section method fully represented the stiffness properties of Piers 2 and 4 in the Wakota Bridge. Further study of the most appropriate analysis procedures for this type of pier is recommended.

It was determined that the use of the refined design method to predict cracked pier behavior provided accurate predictions of the median behavior of the bridge with temperature. It is recommended that this method be used for the final design of non-typical bridges. The gross section method should be used only as a preliminary design tool, as it underpredicted the maximum changes in axial force and moment in all instrumented sections considered.

The design temperature range of 80 °F as specified by Procedure A in the AASHTO LRFD Article 3.12.2.1 was much closer to the 83.8 °F average internal concrete temperature range recorded at the bridge over a one-year period of time. However, although this range reflected the actual longitudinal behavior of the bridge and could be used to predict the actual expected longitudinal behavior of the bridge with respect to temperature after construction, the more conservative Proecdure B temperature range of 150 °F should be used to represent extreme conditions in the design of non-typical bridges similar to the Wakota Bridge. Note that the limited amount of data collected, the unique design of the bridge considered, and the consideration of only longitudinal effects limit the scope of the recommendations offered.

Chapter 1. Introduction

1.1 Overview

This document comprises the second part of a monitoring program aimed at investigating the effects of temperature variation on the axial forces and moments in bridges with fixed connections between sub- and super-structure. This report describes the collection and analysis of data from instrumentation in place on the MnDOT Bridge 82855 (Wakota Bridge) carrying the eastbound lanes of Interstate 494 across the Mississippi River, the Union Pacific Railroad (mile point 347.56), and Verderosa Avenue in South St. Paul, Minnesota, as well as the comparison of the collected data to behavior predicted by previously created finite element models.

An investigation into the behavior of bridges with fixed connections between pier substructure and the superstructure was conducted to better understand their behavior. The two main areas of interest in the study were the method of approximating the stiffness of the cracked pier sections and the effect of thermal loads on the behavior of the bridge.

There are two different methods allowed by AASHTO LRFD for approximating cracked section stiffness in design. The first procedure, called the gross section method, uses the full stiffness of the section during analysis and applies a load reduction factor of 0.5 to the thermal loads for lateral analysis of the section. The second procedure, the refined analysis method, requires iterative moment-curvature analysis of the section under consideration in order to produce the correct section stiffness and applies a factor of 1.0 to the thermal loads. The refined analysis method is a more complicated procedure and thus is more time consuming to the engineer, which is undesirable in some cases. However, this procedure produces more accurate predictions of the stiffness of the section under consideration than does the much quicker gross section method.

The temperature range experienced in Minnesota throughout the year is very large; average daily temperatures are high in the summer and very low in the winter, resulting in large thermal stresses on the bridge structures in the state. It has been shown that these stresses can be higher even than those due to applied dead and live loads [3]. A comparison of the two procedures allowed by AASHTO LRFD Article 3.12.2 was also conducted. Procedure A temperature range is 80 °F in Minnesota. Using a base temperature of 45 °F per MnDOT BDM results in a rise of 35 °F and a fall of 45 °F. Procedure B uses a range of 150 °F as interpreted by the MnDOT BDM from contour maps developed by Roeder [2] in 2002 showing the average maximum and minimum daily temperatures measured throughout the United States. Using a base temperature of 45 °F per the MnDOT BDM results in a rise of 75 °F and a fall of 75 °F.

The Wakota Bridge was chosen for the investigation into the effects of thermal loading on concrete bridges. It was chosen because it employs the use of fixed-flexible twin-blade piers, and because its recent construction allowed for the placement of data collection instruments within the structure of the bridge. In addition, due to the high temperature range experienced in Minnesota, correspondingly large induced thermal loads are expected.

1.2 Background

In the first part of this study, finite element models of the Wakota Bridge were created and evaluated for effectiveness in determining the behavior of the bridge under various conditions. Many different aspects were considered in the development of these models, including the two main design aspects that are of interest in this study: Cracked section stiffness and thermal loading. Models were created in two different analysis programs: ABAQUS is a research-level program which produces very powerful models, while SAP2000 is a design-level program used by many design engineers, due to its user-friendly platform. The design-level models (DLM) created in SAP2000 were compared to the more comprehensive research-level models (RLM) created using ABAQUS to determine initial effectiveness in modeling the bridge behavior. These DLM were created for comparison in the current part of the study to data collected from the bridge itself. The ultimate goal was to calibrate these models to the collected data to offer a prediction of the bridge's behavior throughout its life.

The finite element models in the previous study were created using the two different stiffness approximations allowed by AASHTO LRFD. A model was created employing the gross section method, in which each pier blade was assigned a single stiffness that was equal to one-half of the actual stiffness of that blade. Models were also created that used the refined analysis method, using 2, 4, and 6 stiffness updates along the heights of the pier blades and the corresponding calculated stiffness of those sections. It was determined that the gross section method produced reasonable values for axial force and moment when compared with the RLM. The refined section method using 4 and 6 stiffness updates along the pier blade heights produced shear and moment results that most closely matched those from the RLM; the axial forces produced showed some degree of inaccuracy that was lessened at very high axial loads such as those seen by the actual piers of the Wakota Bridge due to the self-weight of the bridge superstructure.

The first part of the study also looked at the two different methods for temperature design allowed by AASHTO LRFD by analyzing the finite element models under different applied theoretical temperature loads. This was mainly a qualitative investigation of the temperature ranges, since no actual temperature data had been collected from the bridge. Maximum and minimum design temperatures were applied to each DLM and RLM. It was shown that Procedure B, which had a much higher range of temperatures for design, produced correspondingly higher changes in axial force and moment in the bridge structure.

1.3 Scope of Work

The second part of this study concerns the collection and processing of the field data, and the comparison of the field collected data with the values produced by evaluating the DLM finite element models previously created, and calibrating these models to provide predictions of the future behavior of the bridge. This was done by calculating changes in axial force and moment from strain data collected from the Wakota Bridge and changing various parameters in the DLM in order to calibrate the models to the field data.

In order to provide a background for the study, a brief literature review is provided in Chapter 2 of this report, which includes a summary of the work done in Part 1 of this investigation. Chapter 3 of this report describes the data collection process, as well as the preliminary processing of this

data that was performed in order to produce strain and temperature data from the instruments located within the bridge structure. This chapter also describes preliminary analysis of the data collected from the linear string potentiometers located at the bridge abutments. Chapter 4 describes in detail the secondary processing of the strain data, as well as the process of calculating stress distributions across the instrumented cross-sections. Chapter 5 provides a detailed procedure for the calculation of changes in axial force and moment from the data. Chapter 6 presents a comparison of the two different temperature design procedures allowed by AASHTO LRFD, and compares these procedures to the temperature ranges actually experienced by the bridge structure over the yearlong data collection period. Chapter 6 also provides comparison of the actual bridge behavior to that predicted by two different DLM created in the first half of this study, and explains any changes made to these models for calibration purposes. In this section are outlined the parameters of each of the DLM used for comparison, including details on the stiffness approximations. Finally, Chapter 7 presents conclusions and recommendations on the various design procedures for temperature and stiffness approximations investigated in this project.

Chapter 2. Literature Review

Pertinent literature on the approximation of cracked section stiffness of bridge piers and the behavior of bridge structures with changing temperature is summarized here to provide context for the current investigation. A summary of Phase 1 of this project, in which the finite element models of the Wakota Bridge were created, is also provided for background.

2.1 Modeling Cracked Concrete Sections

Modeling the effect of cracking on pier stiffness in design is dependent on a number of factors. There are two methods most often used by designers for considering the ratio of cracked-to-uncracked concrete stiffness in bridge piers. The first uses the full stiffness of the cross-section with a load factor of 0.5 applied to the thermal load. The second is a refined method, and requires calculation of the stiffness of the cracked section using iterative moment-curvature analysis of the pier section. In Section 3.11.1 of the MnDOT BDM, it is stated that the designer of a non-typical bridge, a category under which the Wakota Bridge falls due to the fixed-flexible twin-blade pier substructure and box girder superstructure, must consider the reduced pier stiffness along the height of the pier using a refined method. AASHTO LRFD requires a three-dimensional (3D) finite element model of some non-typical bridges in order to determine the movement of, thermal forces in, and interaction between piers to determine the cracked section stiffness. This analysis may result in a range of stiffness values rather than a single value, with the gross section stiffness as the upper bound and the fully cracked section stiffness as the lower bound. Ambient temperature at the time of construction must also be considered when the piers are fixed to the superstructure, as in the Wakota Bridge [4].

AASHTO LRFD does not specify a method for using this design procedure, and the large number of variables that must be considered can result in a complicated analysis. The following is a summary of a common refined design method, for a more detailed description see Chapter 3.2 of the Phase I report.

2.1.1 Common Refined Design Method

The common refined design (CRD) method calculates the actual stiffness of the cracked pier sections. This method uses both finite element modeling of the structure under consideration and sectional analysis of individual pier sections. The loads induced by temperature are considered after first determining the effects of other pier loading variables such as the initial jacking force applied to the piers during the closure pours and lateral deflections due to long-term sustained forces such as creep and shrinkage. The procedure used in this study discretized each pier into a number of segments for which the stiffness of the section is to be varied. Each segment is assigned a stiffness that is an assumed percentage of the gross section stiffness; AASHTO LRFD Article 5.7.4.3 recommends an initial stiffness of $EI_{Gross}/2.5$ for segments with maximum moment in piers with double curvature (i.e. the segments connected to the superstructure and pier footing) while segments at mid-height can be assumed to have the full stiffness, EI_{Gross} [5]. Linear analysis of the finite element model is completed to evaluate the deflection of the structure at a single moment in time. Sectional analysis is performed to analyze the sectional response of the pier cross-section and compare the results to those originally assumed in the

finite element model. The stiffness coefficients for the pier segments in the finite element model are updated to match the sectional response results (i.e., from moment-curvature analysis), and the linear analysis is repeated. This process is repeated until the pier stiffness and deflections as evaluated by the linear analysis correspond to those from the sectional response.

2.1.2 Gross Section Method

The gross section method of approximating the stiffness of cracked sections is a much simpler method than the refined analysis method. In this method, the thermal loads on the structure are modified by a load factor of 0.5 to account for any loss of stiffness due to cracking. This method also has a number of shortcomings in its simplicity. By applying the single factor to the thermal loads, it assumes that all members, including the superstructure, are cracked and have reduced stiffness. This would not necessarily be true, especially in bridges with prestressed or post-tensioned superstructures. Secondly, this method treats all piers exactly the same, which again may or may not be true. In a bridge where one or more of the piers is taller than another, the shorter pier is likely to experience larger shear forces and moments, and therefore undergo more cracking than its taller counterparts. The fixity between the pier bases and footings, and between piers and the superstructure, may also be different as is the case in the Wakota Bridge; these differences will also cause a different distribution of shear and moment for different piers.

Although this method would not be used to approximate pier section stiffness in the design of the Wakota Bridge, in order to compare the two methods, a finite element model was developed using this design procedure as well as the refined analysis method.

2.2 Design for Thermal Effects

Much research has been dedicated to investigation of the effects of thermal loading on bridge superstructures. However, not nearly as much research effort has been invested to understand the effects that these loads can have on the substructure of a bridge. Nonetheless, the literature regarding the superstructure behavior is also important to this study given that the piers are fixed to the superstructure of the Wakota Bridge, causing any movement of the superstructure to affect the behavior of the piers.

In a study conducted by Moorty in 1992, it was shown that AASHTO LRFD requirements for superstructure movement induced by thermal changes might be exceeded in certain areas of the U.S. It was determined that the simple method of predicting these movements that is provided in the AASHTO LRFD was adequate for orthogonal bridges, but needed to be modified for more complicated bridges such as highly skewed bridges or curved bridges. The Wakota Bridge, which would be included in this category of “complicated bridges”, could exceed these restrictions. Increasing the bearing stiffness through integral construction could result in larger internal forces, and these forces may be underestimated with the simpler design method [5]. Although the authors were mainly referring to bridges with integral abutments, the fixed connections between the piers and the superstructure and the corresponding monolithic nature of the bridge overall could also be interpreted as integral construction given that they reduce the number of movable joints in the bridge structure.

The most important research into thermally induced bridge superstructure movement and requirements for thermal loading was conducted by Roeder [2], and it involved a thorough investigation of temperature data across the country and corresponding concrete bridge behavior. This study offered suggestions for design temperature ranges that were very different from those required by AASHTO LRFD, and in many cases they were much larger [2]. This research has since been included in the AASHTO LRFD design requirements for temperature effects, and has helped to alleviate some of the problems discovered by Moorty [5] regarding the large movement of bridge superstructures caused by thermal changes after construction.

AASHTO LRFD outlines their design guidelines in two documents: "Thermal Effects in Concrete Bridge Superstructures" [6] and AASHTO LRFD [1]. MnDOT has produced the MnDOT BDM [4] in order to further explain or in some cases modify requirements set forth by AASHTO LRFD. Bridges must be designed to withstand the stresses and movements induced by a uniform temperature change as well as those caused by a thermal gradient, mainly due to solar radiation on the bridge deck. Described below is a brief overview of the design requirements from both AASHTO LRFD and the MnDOT BDM.

2.2.1 Uniform Temperature

The effect of uniform thermal loading was the main consideration of this investigation. There are two different design procedures specified in the AASHTO LRFD in Article 3.12.2 for consideration of thermal stresses, and they are labeled Procedure A and Procedure B [2].

Procedure A is the older and more commonly used procedure, and it is generally assumed to generate smaller thermal loads than Procedure B for the state of Minnesota. Procedure A uses the temperature range shown in Table 2.1 below, where a moderate climate is defined as a climate with fewer than 14 days with an average temperature of less than 32 °F. The temperature range shown in Table 2.1 is used to predict bridge superstructure movement due to temperature expansion, and these movements generate the thermally induced stresses if the bridge structure is restrained from such movement.

Table 2.1: Procedure A temperature ranges [1].

Climate	Steel or Aluminum	Concrete	Wood
Moderate	0-120 °F	10-80 °F	10-75 °F
Cold	-30-120 °F	0-80 °F	0-75 °F

Procedure B is a relatively new procedure and is a result of research done by Roeder [2]. The temperature range in this procedure is determined from temperature contour maps of the United States, one of which shows the maximum design temperature while the other shows the minimum design temperature. The design temperature range is taken as the difference between the maximum and minimum temperatures at the desired location in the United States. The maps for concrete bridges are shown in Figures 2.1 and 2.2.

The first map gives minimum temperature contours and the second shows the maximum temperature contours. The two maps are used together; temperature ranges are determined by

finding the difference between the maximum and minimum contours for a given location. MnDOT allows the use of Procedure A when designing "typical" bridges, and Procedure B for "non-typical" bridges. The definition of these two types of bridges is provided in Section 2.2.2.

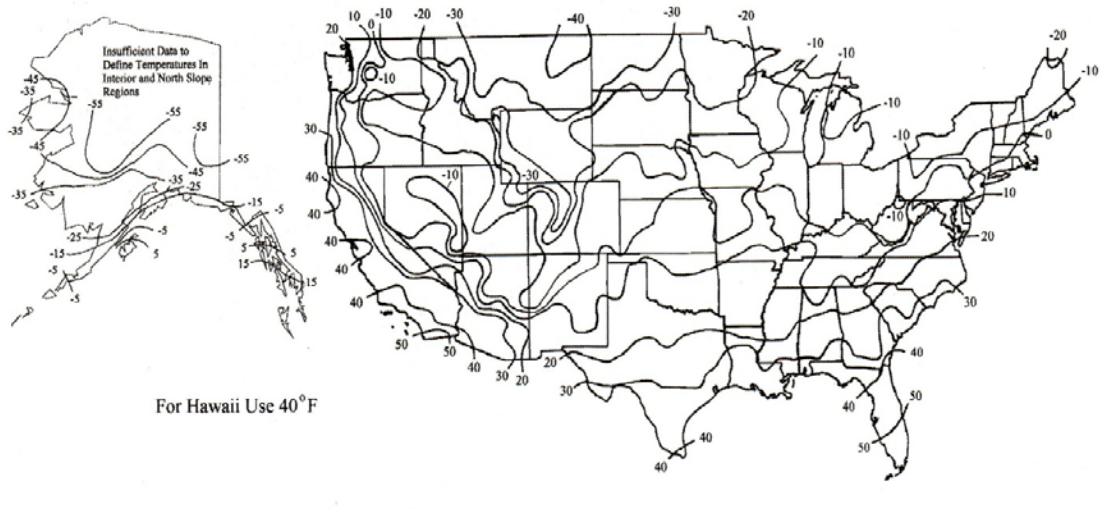

Figure 2.1: Minimum design temperatures (°F) for concrete girder bridges with concrete decks [2].

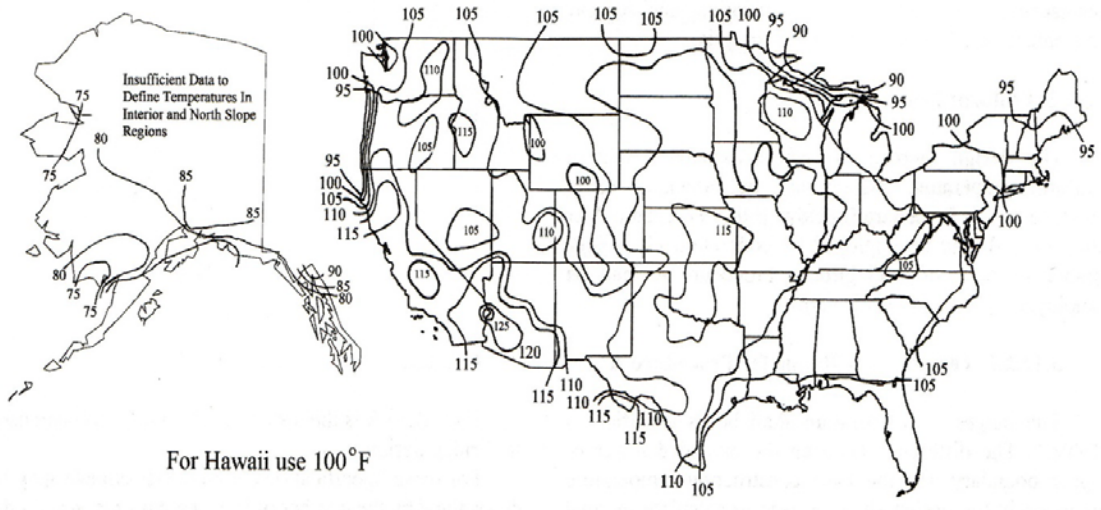

Figure 2.2: Maximum design temperatures (°F) for concrete girder bridges with concrete decks [2].

The thermal movements to be considered in design for both methods are based on the well-known linear expression for temperature expansion,

$$\Delta_T = \alpha L(\Delta T) \quad (1)$$

where Δ_T is the thermal design movement, α is the coefficient of thermal expansion (CTE), and ΔT is the temperature change.

2.2.2 Minnesota Requirements

Although either method is acceptable according to AASHTO LRFD, MnDOT BDM Article 3.11.1 requires that Procedure B be used for non-typical bridges, whereas Procedure A can be used for the internal pier frame forces in typical bridges [4]. This study investigates the appropriateness of using Procedure B versus Procedure A in design.

A typical bridge is defined as one that falls under the following categories: Routine single or multiple span prestressed concrete beam, steel beam, and concrete slab bridges, bridges with two or fewer fixed piers, and bridges with piers that are less than 20 ft. tall [4]. Procedure A allows for a temperature range of 80 °F in Minnesota. Designers are recommended by the MnDOT BDM to use a 45 °F base temperature, which results in a 45 °F fall and a 35 °F temperature rise [4]. Also, for flexible pier considerations, a strength limit state load factor of 0.5 can be applied to the thermal loads to account for the reduction of stiffness in the piers due to cracking in the concrete while using gross section properties. For longitudinal effects, MnDOT requires Procedure B to be used. The MnDOT BDM interprets the maps in Procedure B to imply a temperature range of 150 °F. A strength limit state load factor of 0.5 can still be used with gross section properties in lieu of a refined method for typical bridges.

A number of factors must be considered in analyzing non-typical bridges in addition to the design for temperature gradient and uniform temperature load. An abbreviated list of these factors is provided here.

- Pier Stiffness – Use a refined method to determine the appropriate percentage of gross stiffness along the height of the pier.
- Bearing fixity and flexibility – Account for the stiffness of expansion bearings in determination of the overall bridge movements.
- Construction method, staging, temperature range at erection, and their effects on the connectivity of the structural system.
- Foundation stiffness – Elastic shortening of the piles provides a significant relaxation to forces applied to the substructure, and horizontal displacements of piling will provide moment reduction.
- Use a 150 °F range and a thermal movement load factor of 1.2 for joint and bearing sizing at Service Limit State conditions, as specified by the MnDOT BDM[4]. Use this movement to determine horizontal force requirements for guided bearings.
- Use a 150 °F range and a thermal movement load factor of 1.0 for longitudinal force effects. An 80 °F range, with a base construction temperature of 45 °F may be used for transverse effects within individual pier frames.

Since it was desired to compare the uses of the two procedures, the temperature ranges and design considerations for both Procedures A and B were used in the finite element models that were compared to the actual bridge data.

2.3 Summary of Phase 1

A summary of the proceedings and conclusions made in the Phase I report is provided here [7].

2.3.1 Research Level Model

The rigorous research level models (RLM) were created in order to provide a comparison and preliminary method of calibration for the design level models (DLM) that were to be compared to collected data. The geometries of the models were created in a common CAD program and imported to ABAQUS, an analysis program that was chosen for its user-friendly interface, variety of meshing options, and also the ability to perform nonlinear analyses for the cracking of concrete.

The structure of the Wakota Bridge has many varying geometric parameters, including the overall width, depth, and web and slab thicknesses of the superstructure. It also employs both pile-driven footings and one spread footing poured on rock, fixed flexible piers, post-tensioning, and 5 superstructure spans. Some features of the Wakota Bridge were eliminated from the modeling process because they were considered inconsequential to the analysis and to allow for a more efficient finite element model analysis. A brief description and explanation for all eliminations is provided here.

- *Profile Elevation:* The profile elevation was excluded in the 3D model. Thermal stresses act mainly in the longitudinal direction of the superstructure, and would not be significantly affected by the slope along the profile. This resulted in a simpler deck elevation, and thus an easier application of the thermal gradient loading since the gradient is dependent on the deck elevation.
- *Pier Flanges:* It was assumed that the architectural flanges on the pier walls perpendicular to the longitudinal direction of the bridge would play a negligible role in overall pier behavior. These flanges were omitted from the model.
- *Traffic railing:* The concrete base was included in the analysis model, but the attached steel railing was ignored because it was assumed to provide no stiffness contribution to the structure when compared with the stiffness of the concrete superstructure.
- *Abutments:* The abutments are attached to the superstructure with expansion joints and therefore do not affect the behavior of the main bridge structure. Because of this, they do not affect the superstructure behavior. They were replaced with idealized support conditions at the ends of the superstructure. It was assumed that the superstructure was so axially stiff that the piers would offer negligible restraint to its longitudinal movement: No restraints were placed on abutment supports.
- *Diaphragm Openings:* The openings in the diaphragms on the interior of the superstructure were ignored. These elements were assumed to have no impact on the behavior of the structure because of their small dimension relative to superstructure dimensions.

Stiffness of and friction at the abutment bearings were not considered; the axial stiffness of the superstructure was assumed to be large enough that these would not significantly restrain the longitudinal movement of the superstructure at the abutments.

Other considerations that went into the modeling of the Wakota Bridge included meshing of the finite elements, tie constraints between elements, boundary conditions, and loading options. Concrete compressive behavior was modeled using a popular nonlinear model for the uniaxial stress-strain of concrete that is available in Response-2000 [8], a common sectional analysis program.

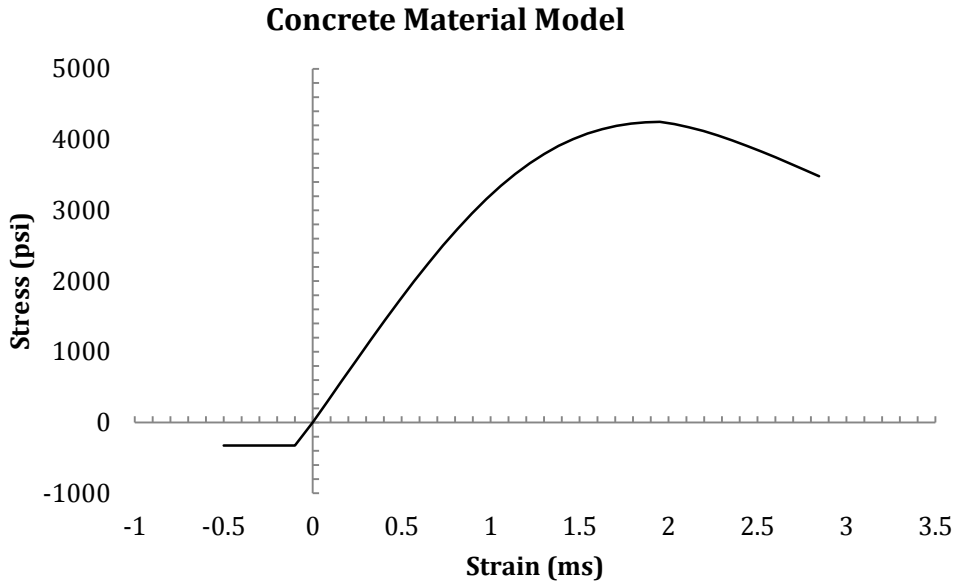

Figure 2.3: Concrete compressive model for RLM.

This concrete material model represents both the nonlinearity of concrete in compression, as well as its very limited strength in tension. After cracking, the concrete was considered to be plastic; stress would have been redistributed to the reinforcement and the adjacent concrete.

Because this research-level model was created expressly for comparison to the design-level model, only a brief summary of the model details was provided here. See Phase 1 for a full description of the model considerations.

2.3.2 Design Level Model

Of more importance in this second phase of the study are the design-level models (DLM) developed in Phase 1, since the forces resulting from analysis of these models were compared to the collected field data. The DLM were analyzed in SAP2000, which is a commercial structural analysis software that is popular because of its user-friendly interface and wide range of analysis options [9]. A number of parameters were considered in the creation of these models, including, the prestressing tendons, time-dependent effects, analysis of the staged construction of the bridge, footing constraints and pile analysis, the number of stiffness updates along the pier blade heights used in the CRD method, and the temperature ranges applied to the models for comparison to the RLM. These parameters, and a number of conclusions regarding the creation of these models, are described here.

2.3.2.1 Staged Construction

SAP2000 is able to analyze a bridge structure over time, including any effects caused during the actual construction of the bridge. The actual timeline of construction for the bridge was used and the sequence of construction was incorporated into the staged construction model, which was used for comparison to the field data. In analyzing the staged construction model, the prestressing tendons were placed first, then the time dependent effects were included using the staged-construction option in SAP2000.

Some simplifications were made in the consideration of the prestressing tendons in the DLM. Only longitudinal bars were considered, tendon paths were idealized as straight paths through the bridge superstructure, and the tendon paths were simplified into a single idealized tendon path through the center of the girder, even though in reality ducts ran along paths at the top of each girder web. Each tendon was modeled as an individual element at the appropriate vertical position along the height of the superstructure. The loads applied to the tendons consisted of the forces recorded in the as-built stressing tables, and the tendons were stressed from the specified end using specified frictional loss properties. The timeline for stressing the tendons in the model was the same as was used in the field; all prestressing strands were stressed the day after the concrete section was constructed.

Time-dependent effects from both the construction period and from loading were modeled in the DLM using the CEB-FIP model [9], which is the model supported by SAP2000. Creep and shrinkage curves were generated in SAP2000 based on the size of the section considered, a shrinkage coefficient corresponding to the type of concrete used, the relative humidity, and the age of the concrete at the beginning of shrinkage. The size of the superstructure sections was taken to be a constant for simplicity, although these sections had varying dimensions. Shrinkage, creep, and relaxation of the prestressing tendons were also computed in SAP2000 based on the CEB-FIP code for grade 270 prestressing steel.

Other specific considerations in the construction process included the falsework used for Spans 1, 2, and 5, the jacking sequence prior to closure pours, and the friction at the expansion joints. Each span was jacked apart longitudinally prior to pouring the closure pour, and this was included in the jacking sequences. This initial jacking induced a slight outward bowing of both Pier 2 and Pier 4, which would account for a small amount of the creep and shrinkage effects in the superstructure.

2.3.2.2 Footing Constraints and Pile Analysis

Appropriate modeling of the pier footings was important in the modeling of the bridge. The rotation and translation at the pier footings would relieve some of the forces induced in the piers by the expansion and contraction of the superstructure. The footings for Piers 1-3 are pile footings, while Pier 4 has a spread footing on rock.

Consideration of the footing at Pier 1 was of less importance than the other three pier footings, because at this pier the expansion joints in place at the connection between the pier blades and the superstructure would relieve much of the lateral forces on the pier blades. The footing at this

pier would not translate or rotate significantly because of these small lateral loads, so in the DLM the restraints at this footing were modeled as fixed.

Piers 2 and 3 also used pile footings, but the pier blades in these piers were fixed to the superstructure, resulting in lateral forces due to superstructure movement and corresponding rotation and translation of the footing. The translation and in-plane moment restraints were modeled as springs with stiffness determined using a simplified beam theory, using the results of a full bridge analysis assuming fixed-connection footings.

2.3.2.3 Pier Stiffness Updates and Temperature Ranges

The number of stiffness updates along the pier blade heights was a main consideration in Phase 1 of the project. Note that in this context, the term "update" refers to a change in the stiffness of the pier blade along its height, rather than a change in time. The DLM using the CRD method were analyzed using 2, 4, and 6 stiffness updates along the pier blade heights and it was determined that 4 and 6 stiffness updates produced models that were reasonably accurate when compared to the more rigorous RLM.

A variety of temperature ranges were also applied to the models for the purpose of determining accuracy relative to the RLM. For comparison to the RLM, temperature ranges of 40°, 70°, and 100 °F were applied, a range of 85 °F was applied to compare the methods of fixity for the pier bases, and finally the 80 °F and 150 °F ranges from Procedures A and B respectively were applied to compare the induced axial force and moment changes due to these design temperature ranges.

Concluding comments regarding the modeling of the Wakota Bridge reached in Phase 1 are summarized here because they are relevant to the present study

Several conclusions regarding thermal design and the refined design method were drawn as a result of the finite element simulations that were constructed and evaluated. The first was that both the refined design method and the gross section method produced similar results for the analysis of the critical piers in the Wakota Bridge. It was seen that the connection between the pier wall bases and the icebreaker became less important under increasing axial and lateral loading of the piers in both the refined design method and the gross section method. Approximate effective lengths for both translational and rotational springs at the pier bases were found for each case. For the translational springs, an effective length of L to $1.5L$, where L is the length of the pile, was found to approximate the translational stiffness, while an effective length between $L/3$ and L approximated the rotational stiffness. These approximations were important in the calibrating of the DLM for comparison to the collected data.

It was determined that the use of four and six update sections along the height of the piers would be sufficient to predict the cracked section stiffness, when compared to the RLM. The refined method predicted shear forces and moment most accurately when compared with the RLM; a degree of inaccuracy in prediction of axial forces was noted when small axial loads were applied. This inaccuracy was significantly reduced as axial load on the piers increased, as would be the case with the Wakota Bridge piers due to the self-weight of the superstructure. The accuracy of

the refined cracked section also increased significantly under increasing lateral loading of the piers.

The final conclusion made was in regards to the temperature design procedures. It was seen that Procedure B produced very different force and moment requirements at the bases of the pier walls than did Procedure A. This was expected, given the very large difference in design temperature ranges used by the two procedures.

Chapter 3. Data Collection

3.1 Overview

Data was collected and stored for a one-year period, beginning January 10, 2011 at 2:00pm and ending on January 10, 2012 at 2:15pm. The Campbell Scientific CR1000 dataloggers recorded strain and temperature data from a total of 84 Geokon Model-4200 vibrating wire strain gauges installed within the bridge super- and sub-structure as well as displacement measurements from two Unimeasure HX-P420 linear potentiometers, one located at each abutment of the bridge. Data was transferred from the dataloggers by a wireless connection to a computer in the University of Minnesota Civil Engineering department, in which all data has been stored. This data is stored in multiple locations, to prevent its loss in the case of a computer malfunction. As of this time, the data acquisition system is still operational.

The vibrating wire strain gauges were installed in two cross-sections of the span superstructure and four cross-sections of the pier sub-structure of the bridge in an earlier phase of this project and while the bridge was under construction. The instrumented superstructure cross-sections were segments P2-4U in Span 3, and P4-6D in Span 4. The two piers instrumented were Pier 2 and Pier 4. One linear potentiometer was installed at each abutment. The locations of these instrumented cross-sections are described in Figures 3.1-3.3 and gauge distributions across each cross-section are shown in Figures 3.4 and 3.5.

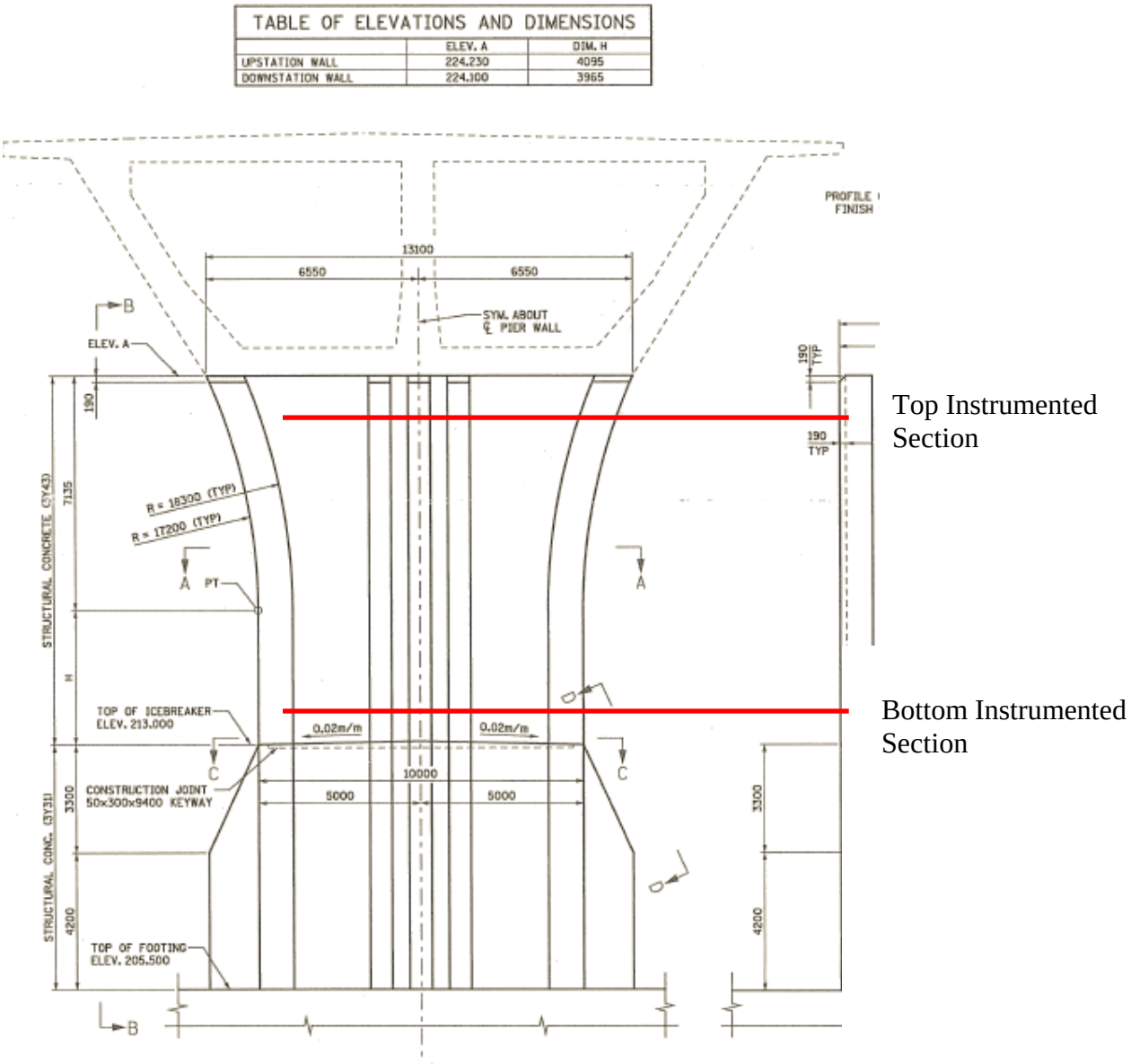

Figure 3.1: Instrumented levels of MnDOT Bridge 82855 Piers 2 and 4 [10].

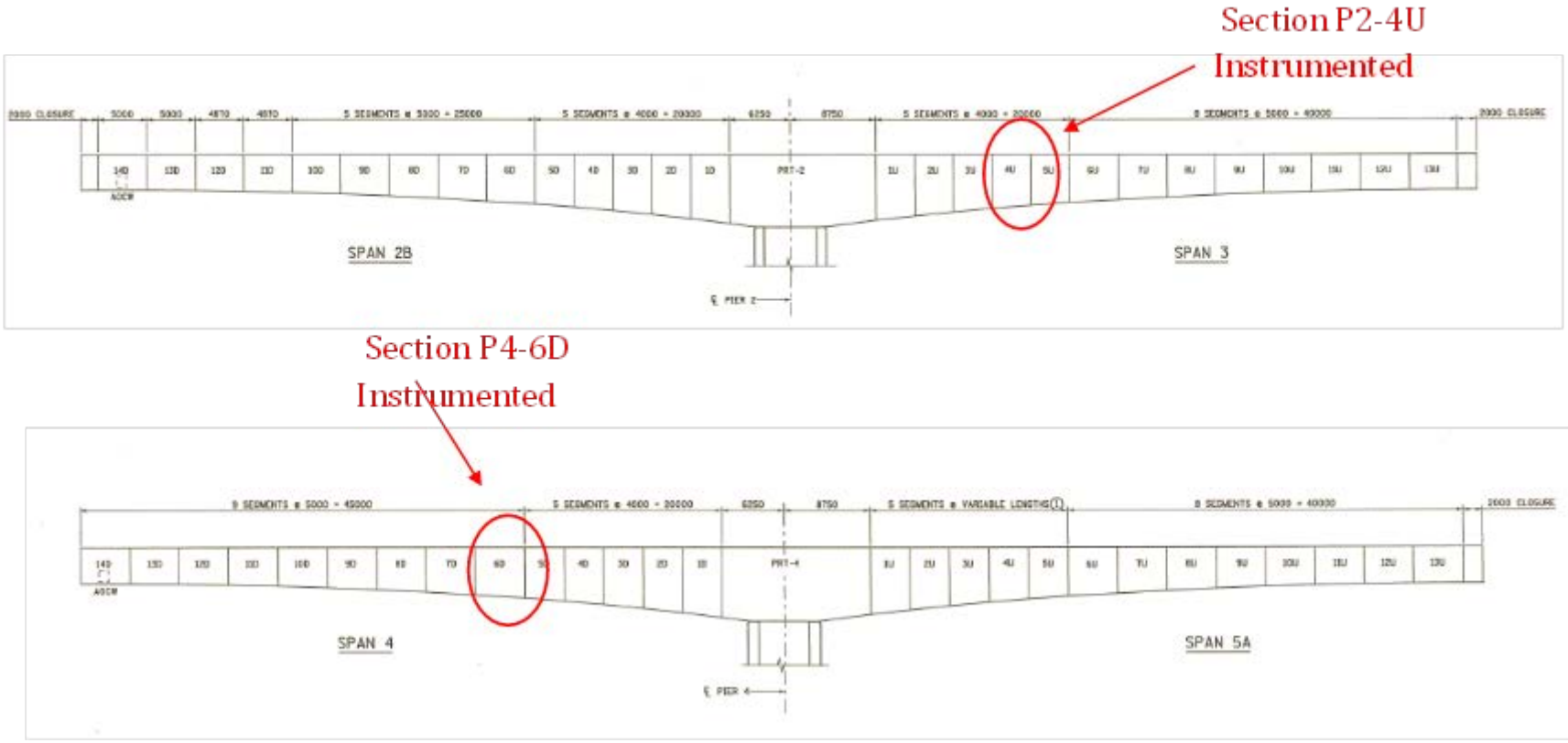

Figure 3.2: Elevation of MnDOT Bridge 82855 with instrumented Pier s 2 and 4 [10].

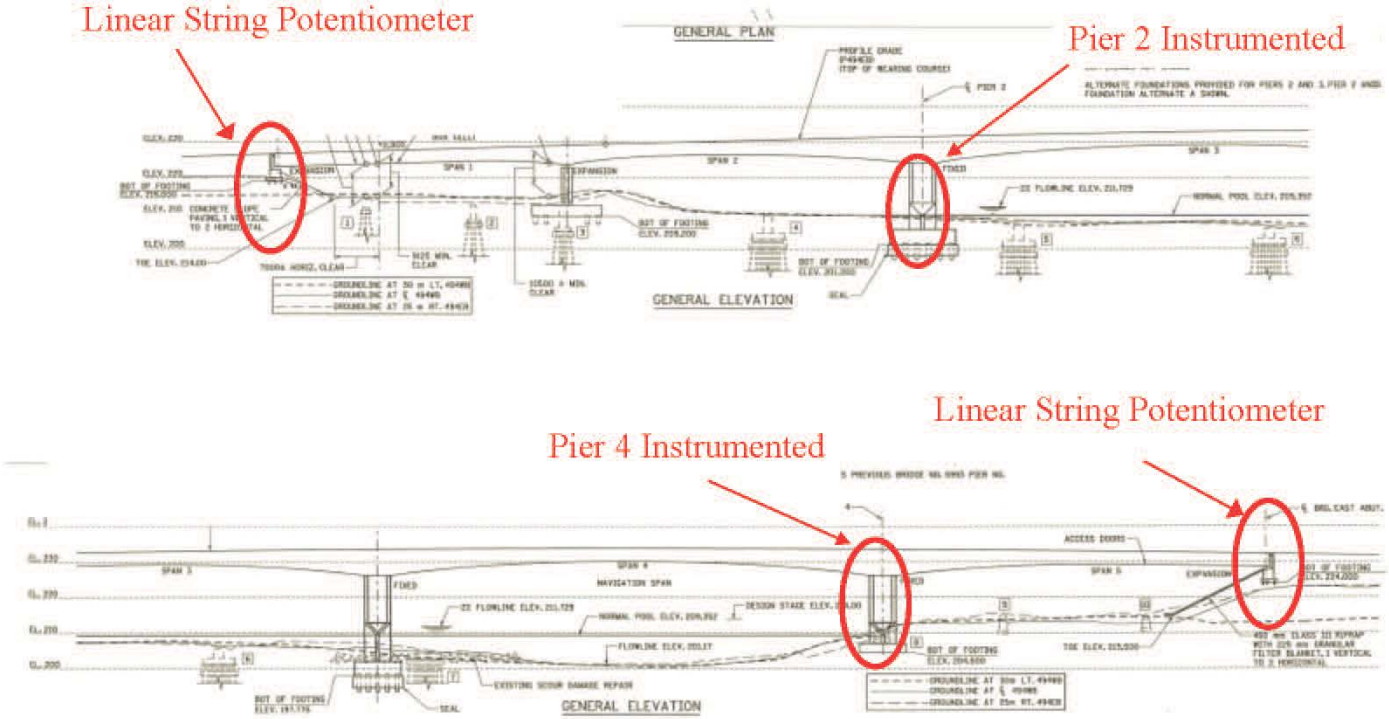

Figure 3.3: Elevation of MnDOT Bridge 82855 with instrumented Spans 3 and 4 [10].

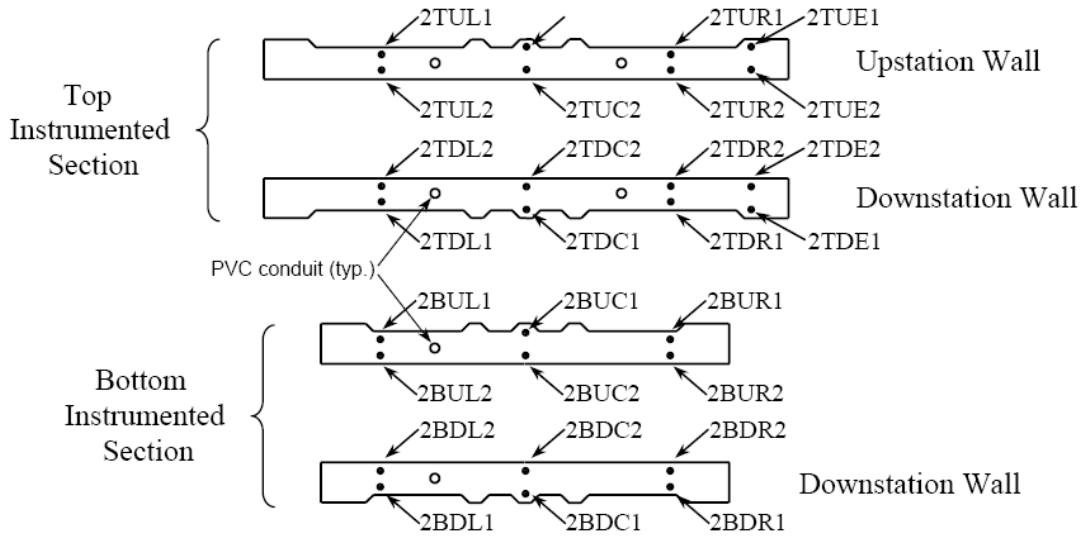

(*a*)

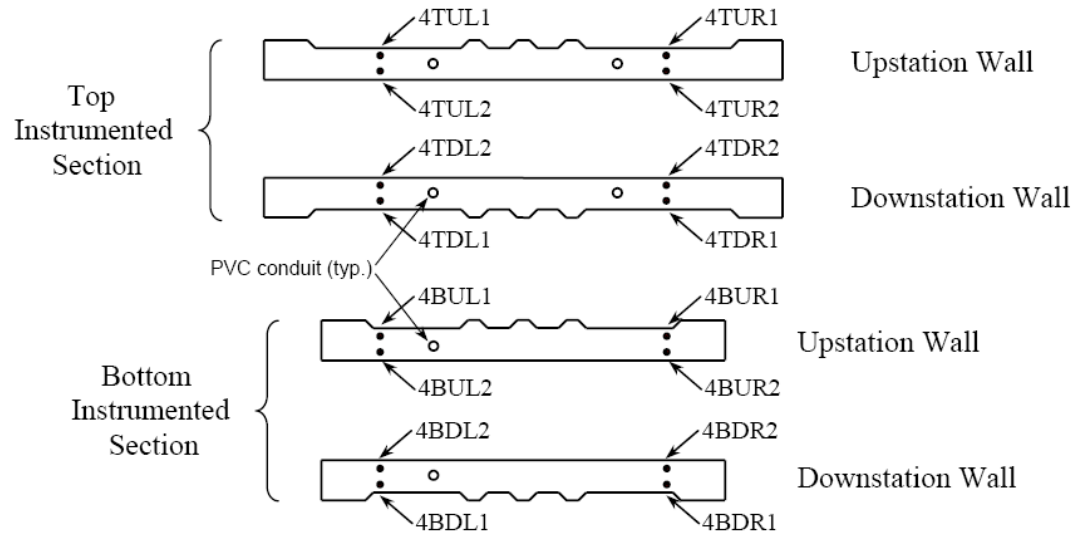

(*b*)

Figure 3.4: Gauge designation and location in *a*) Pier 2 and *b*) Pier 4.

In the diagrams shown in Figure 3.4, the gauges with "T" designations are located at the top instrumented section of the pier, while those with the "B" designations are located at the bottom instrumented sections. The designations "U" and "D" refer to whether the gauge is located in the up-station pier blade or the downstation blade, while the "1" refers to a gauge along the rusticated face of the blade, and "2" refers to a gauge along the smooth face of the blade.

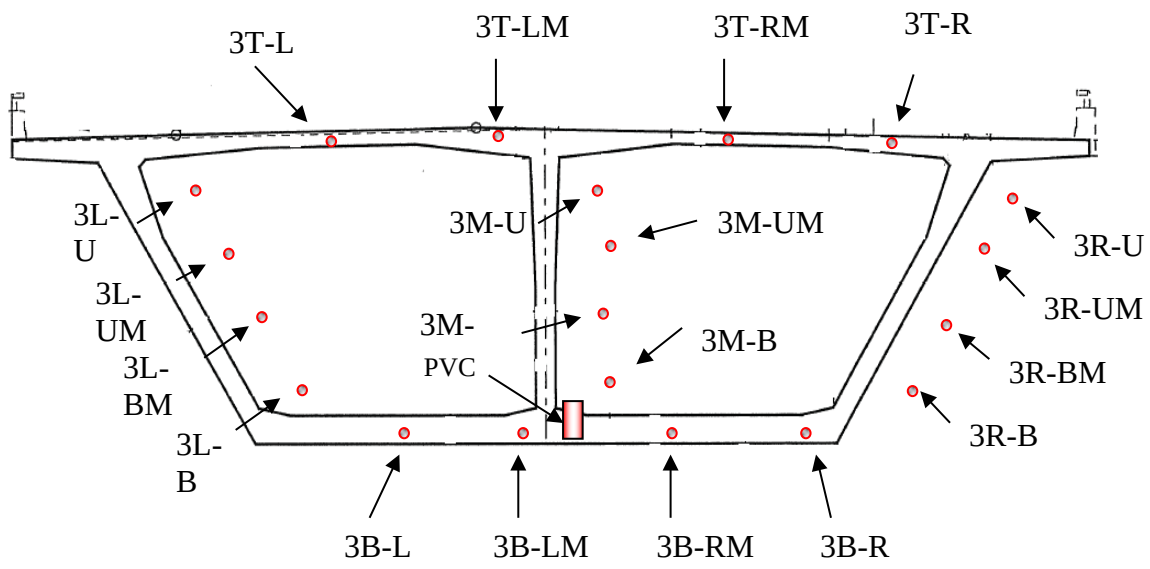

Figure 3.5: Gauge locations and designations in Span 3.

Note that the instrumented cross-section in Span 4 has the same gauge layout as that of Span 3.

Each strain gauge is connected to one of four Campbell Scientific AVW200 multiplexers, which are in turn connected to one of two CR1000 dataloggers located at either Pier 2 or Pier 4 inside the bridge superstructure. These dataloggers are connected to the modem enclosure on the abutment of the bridge, and the data is transferred from that modem to the computer at the University of Minnesota via a wireless signal.

The data acquisition system was also controlled remotely using the wireless modem. The software used to control the data acquisition system, Loggernet, is provided by Campbell Scientific for use with its data acquisition systems. With Loggernet, programs are written specifying the data to be collected, the programs can be transferred to the dataloggers, and the data collected and analyzed using a single software package [11].

The program for collecting data was written in the programming language CRBasic; this language controls the function of the CR1000 dataloggers used in the data acquisition system [12]. This program controlled all aspects of dataloggers that dealt with data collection, and was sent to the two dataloggers installed in the bridge superstructure via the wireless modem. Figure 3.6 shows one of the two datalogger enclosures located within the superstructure of the bridge; each enclosure contained two AVW200 multiplexers into which the strain gauges were plugged, one CR1000 datalogger that stored the strain data, one multidrop to allow for data transfer from the datalogger to the modem enclosure located on the abutment of the bridge, and one power source that supplied the electricity to the equipment. Figure 3.7 shows the modem enclosure and wireless antenna at the abutment of the bridge, and Figure 3.8 describes the contents of the modem enclosure.

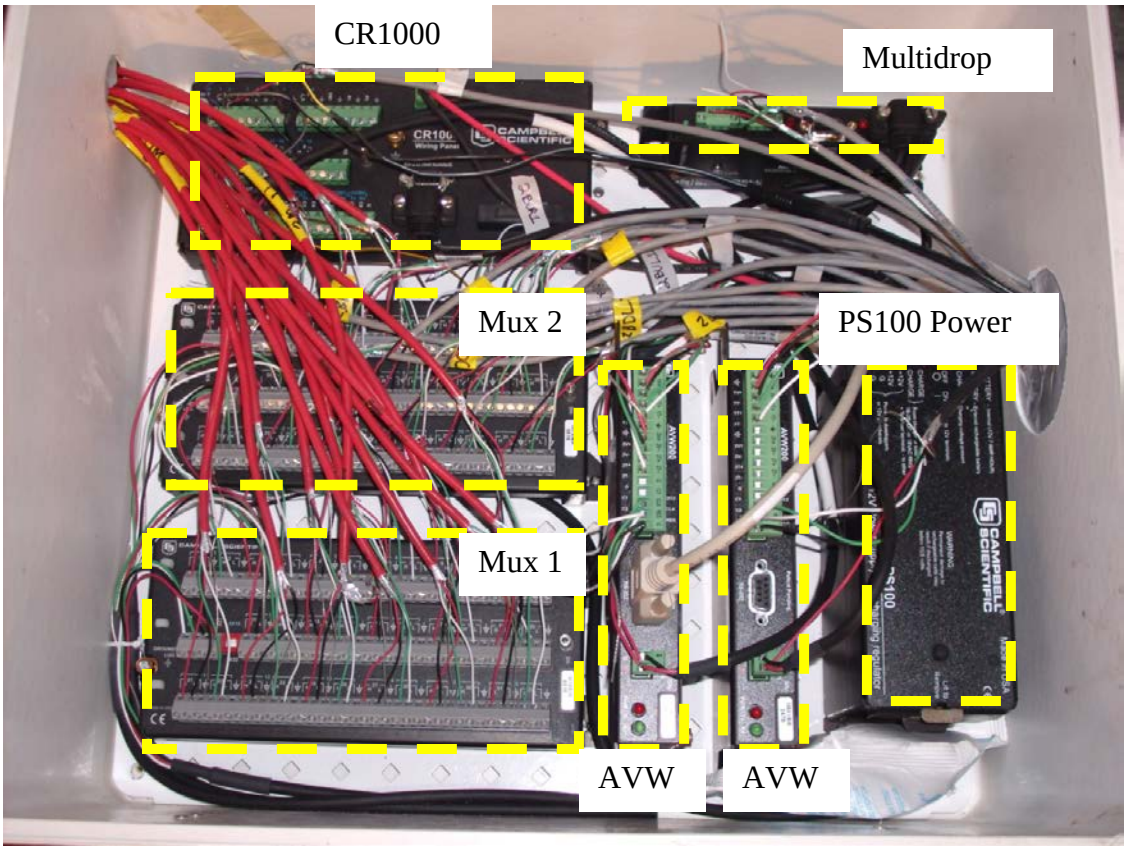

Figure 3.6: Datalogger enclosure at Pier 2 inside the superstructure.

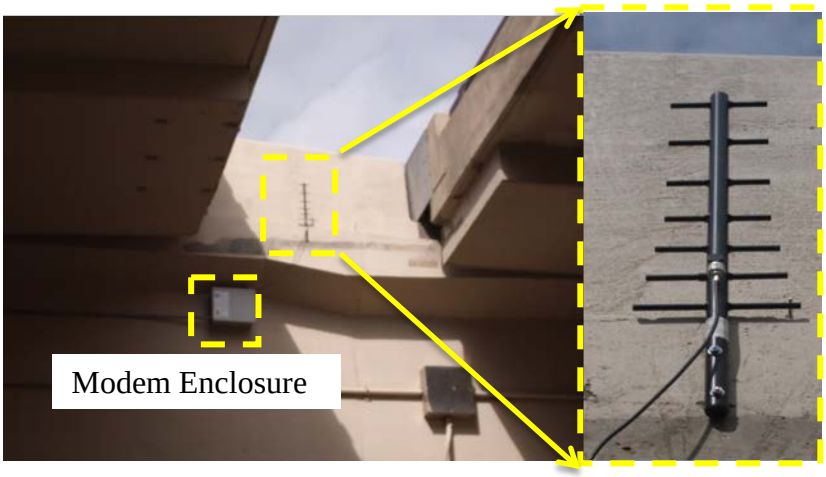

Figure 3.7: Wireless modem enclosure and RavenXT wireless antenna installed at abutment face.

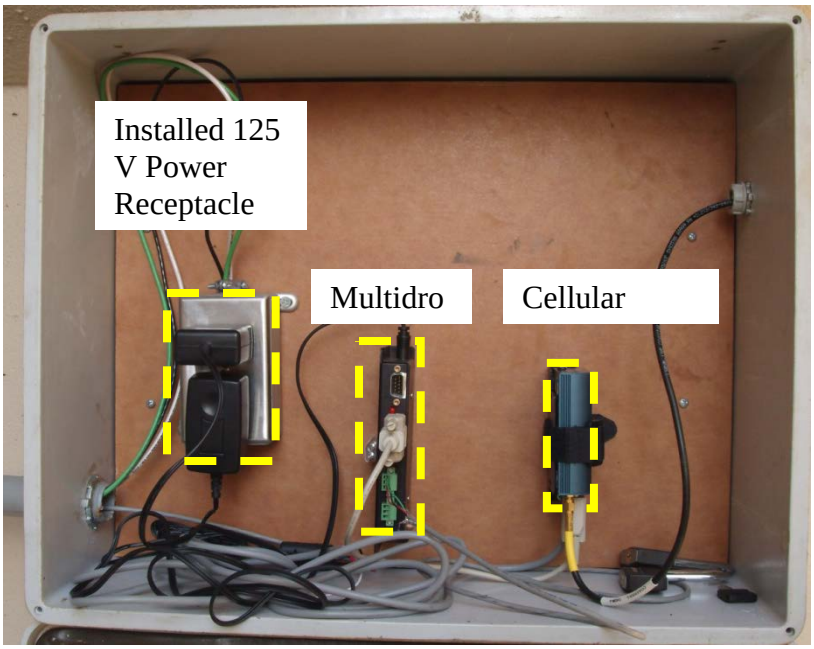

Figure 3.8: Modem enclosure installed at bridge abutment.

For a full description of the data acquisition system and the system set-up, see Chapter 2 of Phase 1 of the study [7].

3.2 Data Collection Issues

Data collection began on January 10, 2011, which was approximately one year after the intended start date. This late start was due to a number of problems that arose with both access to the bridge and collection of data during bridge construction, as well as with technical malfunctions after the bridge was fully constructed and opened to traffic.

3.2.1 Lack of Accessibility

The first major hurdle that had to be overcome in the study was the lack of accessibility to the bridge during construction. This was a problem because it prevented the measuring of initial strain values from the bridge immediately at the completion of construction: The strain gauges were installed but there was no way to access the gauges in order to collect any data from them, nor were they connected to a data acquisition system so that data could be stored for later use. Therefore, the decision to investigate *changes* in axial force and moment rather than absolute values became a necessity, given the complex nature of the construction of this type of bridge and the lack of accessibility to the gauges. Only changes in axial force and moment were used to evaluate the thermal analysis procedure.

3.2.2 Technical Malfunctions

Another problem during data collection was the recurring technical difficulties with the connection to the wireless modem. The power sources for the entire data acquisition system, including the wireless modem and antenna, were the electrical circuits that also powered the lighting systems for the interior of the superstructure box sections. The datalogger and multiplexer system for Pier 2 were powered by a different circuit than those at Pier 4. On a

number of occasions, the circuit breaker for one or the other of the two circuits would trip. In these instances, the strain gauges would continue to run on the battery power in the dataloggers, and data was collected and stored by the dataloggers. The data was retrieved at a later time by plugging a laptop computer directly in to the dataloggers at each pier. The linear string potentiometers did not run on this battery power, and for each period of power outage for the circuit the data from these instruments was lost.

The power interruptions were a costly issue in both time and project funds. The circuit breakers for the lighting circuits were located within the superstructure and access to the interior of the box required (a) use of a 30-ft. scissor lift and (b) supervision by a MnDOT maintenance employee or bridge inspector. As such, a number of different measures were taken to prevent the circuits from tripping. Inside the superstructure, the CR1000 enclosures were lifted off of the concrete bottom of the box girder and placed on Styrofoam to prevent any moisture seeping from the concrete into the box. Electrical tape was placed around all unused outlets on any surge protectors, again to prevent moisture from causing power surges and tripping the circuit breaker. A ground fault circuit interrupter (GFCI) was installed in the modem enclosure, and the modem and antenna and multiplexer were connected to this interrupter to ensure that the modem and antenna would not cause the circuit to trip. After the measures described here were taken, the number of circuit interruptions greatly decreased.

3.2.3 Damaged Gauges

Some of the vibrating wire strain gauges were damaged during installation or when the concrete was poured and consolidated. These gauges, recorded inaccurate data or did not record data at all. Table 3.1 lists the designations of the damaged gauges, as well as the signal that was not recorded, or recorded inaccurately.

Table 3.1: Damaged gauge designations.

Damaged Gauge Designation	Inaccurate Reading
3R-U	Strain
2BUC1	Strain
2BUC2	Strain
2BDC1	Temperature
2BDR2	Temperature
4BDL1	Temperature
4BDL2	Temperature

The data collected from strain gauges recording inconsistent strain readings have been excluded from analysis. The gauges that recorded strain values consistent with the gauges surrounding them, but inconsistent temperature readings, were used in analysis. The temperatures assigned to these gauges were the average of the temperature readings of the adjacent gauges.

3.3 Collection Time Interval

The multiplexers to which the strain gauges were connected required a minimum two-second time interval per gauge between recordings. Since the maximum number of gauges connected to a single multiplexer was 32, the minimum time between recordings was 64 seconds (1:04 minutes). A time interval of fifteen minutes was used for the entire data collection period, with

the exception of a one-week period between April 1, 2011 and April 8, 2011; during this period measurements were collected on two-minute intervals. The fifteen-minute collection interval was short enough to record a continuous strain distribution over time without being so short as to cause an excess of data, which would have been more costly both in terms of electrical power usage as well as data transmission via the wireless modem and permanent storage in electronic media. The gauges used were not designed to measure dynamic loads, and it was not believed that any further information would be gained from decreasing the time between readings to this minimum value (i.e., 64 seconds).

The use of the shortened collection time interval between April 1 and April 8 was to ensure that the strains being measured were due to changing temperature, and not due to variations in traffic loading throughout the week. The traffic loads during the rush-hour periods for the week are different from those at off-hours on the weekends, and could possibly have had an effect on the strain readings. The instrumented bridge carries eastbound traffic, so the heaviest rush-hour traffic load would be in the evenings as drivers are leaving the Minneapolis and St. Paul downtown areas towards the suburbs.

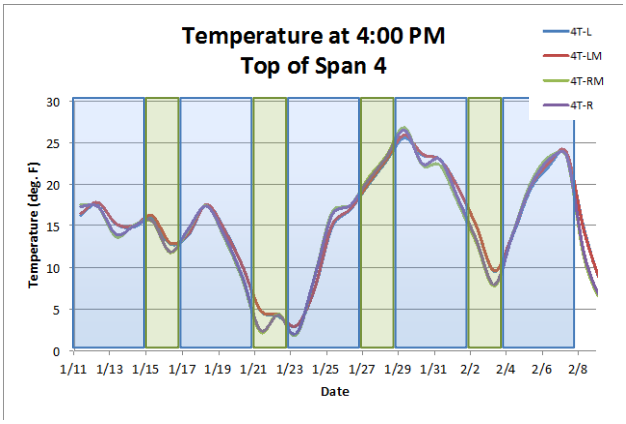

(a)

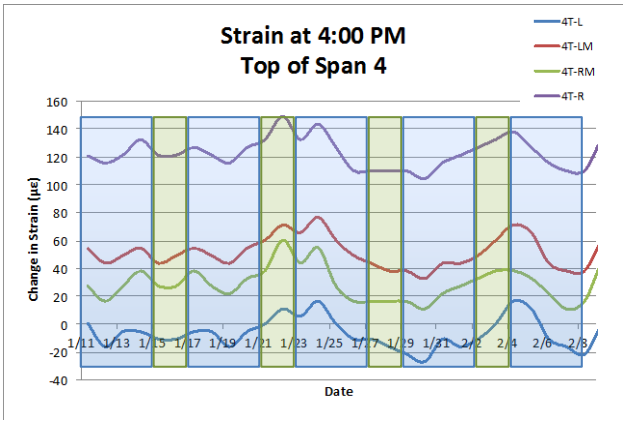

(*b*)

Figure 3.9: Temperatures and strains vs. time for top flange gauges in Span 4, during rush hour at 4:00pm.

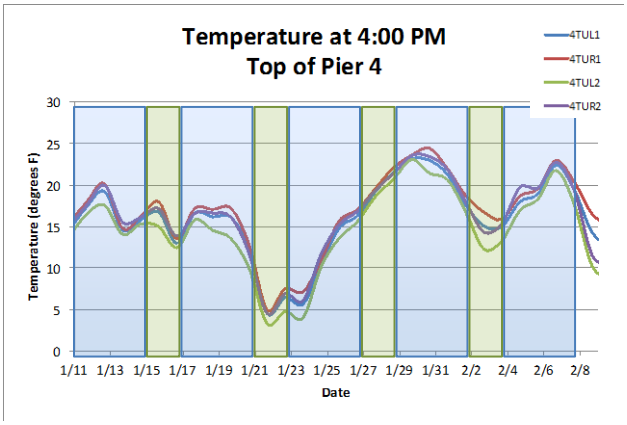

(*a*)

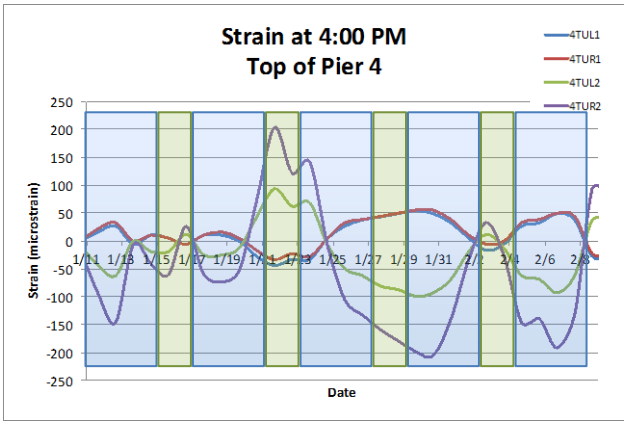

(*b*)

Figure 3.10: Temperatures and strains vs. time for gauges in the top of the up-station blade of Pier 4, during rush hour at 4:00pm.

From the plots shown in Figures 3.9 and 3.10, it can be seen that the strain histories follow the temperature histories. The blue areas correspond with work days (i.e., Monday through Friday), while the green areas correspond to weekend days (i.e., Saturday and Sunday). There is no noticeable difference between the strain histories during the week and during the weekend; in each case the strain histories closely follow the trends of the temperature histories, verifying that the strains being measured by the strain gauges were in fact due to changes in temperature rather than changes in loading due to different traffic conditions. The strain histories have the same qualitative characteristics as the temperature histories: Strain histories for gauges 4TUL1 and 4TUR1 both have the same sign as the temperature histories, while gauges 4TUL2 and 4TUR2 have opposite signs. This is due to bending in the section, and was not unexpected.

After this verification, the time interval between data measurements was increased back to its original length of 15 minutes. This time interval was used for the remainder of the data collection process.

3.4 Preliminary Strain Data Processing

The raw strain data was collected in the form of frequency readings, measured in Hertz, and temperature readings, measured in degrees Celsius. The preliminary analysis performed on the raw data consisted of translating the collected frequency values to strains and modifying these strain values based on the varying coefficients of thermal expansion of the steel vibrating wire gauge cases and the concrete in which the gauges were embedded.

Frequency measurements were translated into strains based on a set of constants and equations supplied by the manufacturer of the strain gauges and measured as strain [13]. The equation provided is as follows:

$$\varepsilon \times 10^6 = \frac{3.304 * f^2}{1000} \tag{2}$$

where ε is the strain and f is the frequency (in Hz) measured by the strain gauge. This equation is based on the physical relationship between strain and changes in the frequency of the tensioned wire inside of these devices. The equation includes constants that represent the characteristics of the specific model of vibrating wire gauge used in this project. The strains are multiplied by 10^6 given the small magnitudes of strain changes in structures under typical service loads, and strain computed in this manner are said to be in microstrain (με). One με has a strain magnitude of 10^{-6}.

The strain readings reported here were modified based on temperature to account for the different coefficients of thermal expansion of the steel housing of the gauges and the concrete surrounding it. This difference causes the steel case and the concrete to expand and contract at different rates with changing temperature. This effect was accounted for by applying the following temperature correction to the strains recorded [13]:

$$\varepsilon_i \times 10^6 = \varepsilon_{i-1} \times 10^6 + (C_s - C_c)(T_i - T_{i-1}) \tag{3}$$

where $\varepsilon_i \times 10^6$ and $\varepsilon_{i-1} \times 10^6$ are the current and previous strain readings, C_s = 6.7 / °F (12.2 /° C) [13] and C_c =6.0 / °F (10.0 /° C) [14] are the coefficients of thermal expansion for steel and concrete respectively, and T_i and T_{i-1} are temperature values for the current and previous data readings.

It is important to note that the data presented here is not referenced to any initial strain readings. The strain gauges were pre-strained by the manufacturer to a nominal specified value of $\varepsilon_{initial} \times 10^6 = 2500$ at zero-stress condition. However, because of the sensitivity of the gauges, this initial pre-strained value may differ by as much as ±100-200 με from the specified values for any given gauge. The strain values reported here are the total strain values as measured from the strain gauges, modified only with the correction for the differing coefficients of thermal expansion given in Equation 9.

Due to the large amount of data collected, plots representative of the entire data record are shown below, while the other plots are included in Appendix A of this report. Strain plots discussed in Chapter 2 include strain distributions across the down-station halves of the down-station blades of the top and bottom instrumented sections of Pier 2, both halves of the up-station blade of the bottom instrumented section of Pier 4, and the bottom flange of the instrumented section in Span 4. Plots of the total displacement versus time and temperature measured by the linear string potentiometers at both abutments are also discussed. In all plots presented in this chapter, a decrease in overall strain corresponds to increased compression, while an overall increase in strain corresponds to increased tension.

3.4.1 Strain and Temperature Along Blade Width

Data presented here was collected from gauges along the smooth face of the down-station blade of the top instrumented section of Pier 2 (SDTPier2).

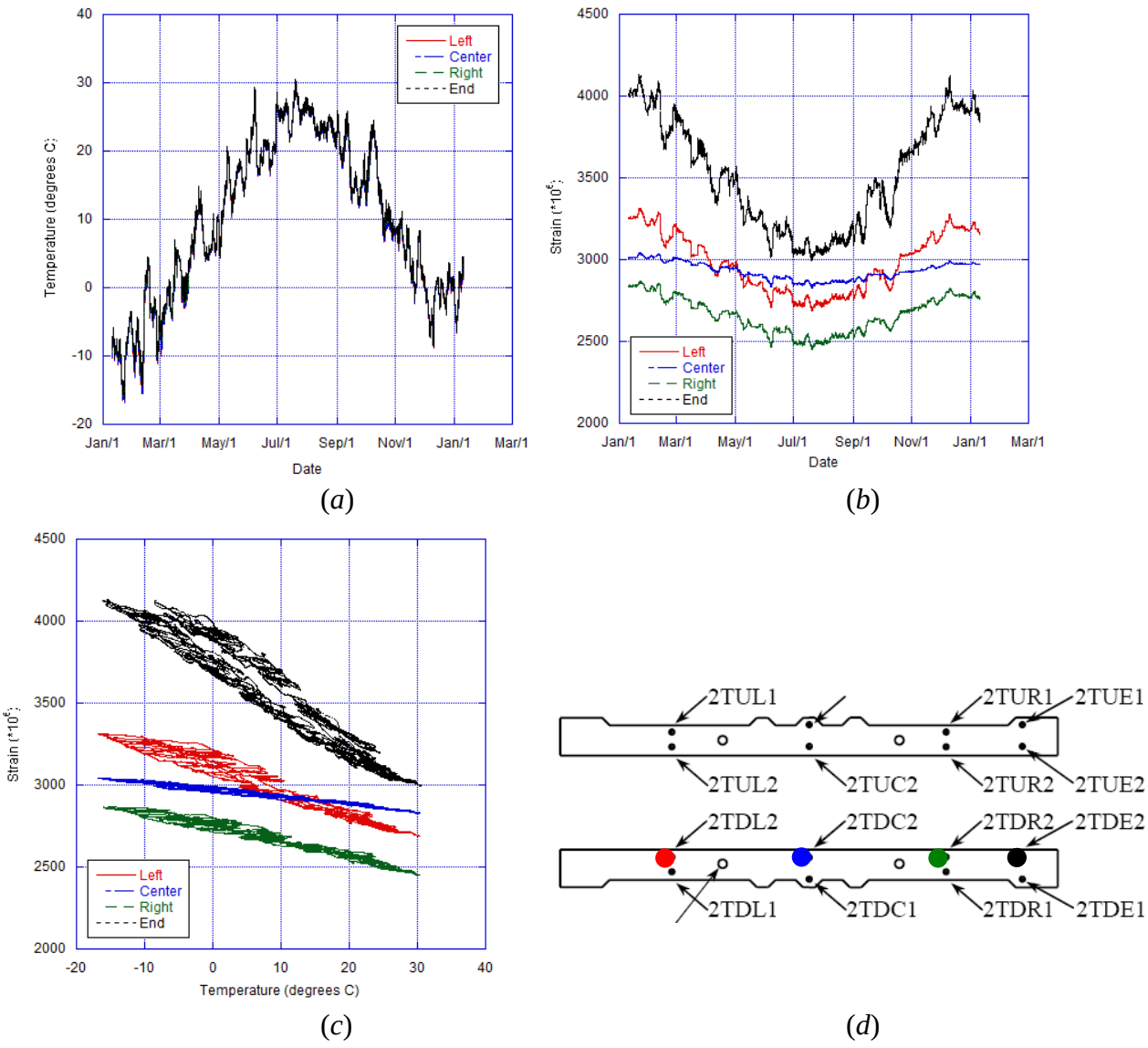

Figure 3.11: SDTPier2, a) Temperature versus time; b) Strain (*10^6) versus time; c) Strain (*10^6) versus temperature; d) Gauge designations and locations by color.

The pier cross-section shown in Figure 3-12*d* is viewed looking downward from the top of the pier. This same perspective is used in all pier cross-sections shown in this report. The temperatures did not vary much across the cross-section, shown by the overlapping of the data lines in Figure 3.11*a*. This same uniformity of cross-sectional temperatures was seen in every instrumented section. Figure 3.11*b* shows that gauge 2TDE2, located at the far right end of the pier blade, showed the largest overall change in strain over time, while gauge 2TDC2, located in the center of the pier blade, shows the least. Gauges 2TDR2 and 2TDL2, placed symmetrically about the center of the pier blade, show similar overall changes in strain throughout the year. Figure 3.11*c* shows the strains clearly decreasing with increasing temperature. Note that these and all other strain values reported are not referenced to initial strain values.

Figure 3.11*b* also shows that the strain values recorded in January of 2011 were slightly higher overall than those seen at the end of the data collection period in January of 2012. This same

trend was seen in all instrumented cross-sections, and was perhaps due to the warmer temperatures of the current winter season; January and February of 2011 saw significantly colder temperatures than were recorded in December 2011 and January 2012, and corresponded with higher strain readings at all gage locations. Further data collection would be necessary to see if the strain values would return to the values seen at the beginning of the collection period if the temperatures were to drop to similar levels.

3.4.2 Strain and Temperature Data Along Blade Height

Data presented here was collected from gauges along the rusticated face of the down-station blade of the bottom instrumented section of Pier 2 (RDBPier2).

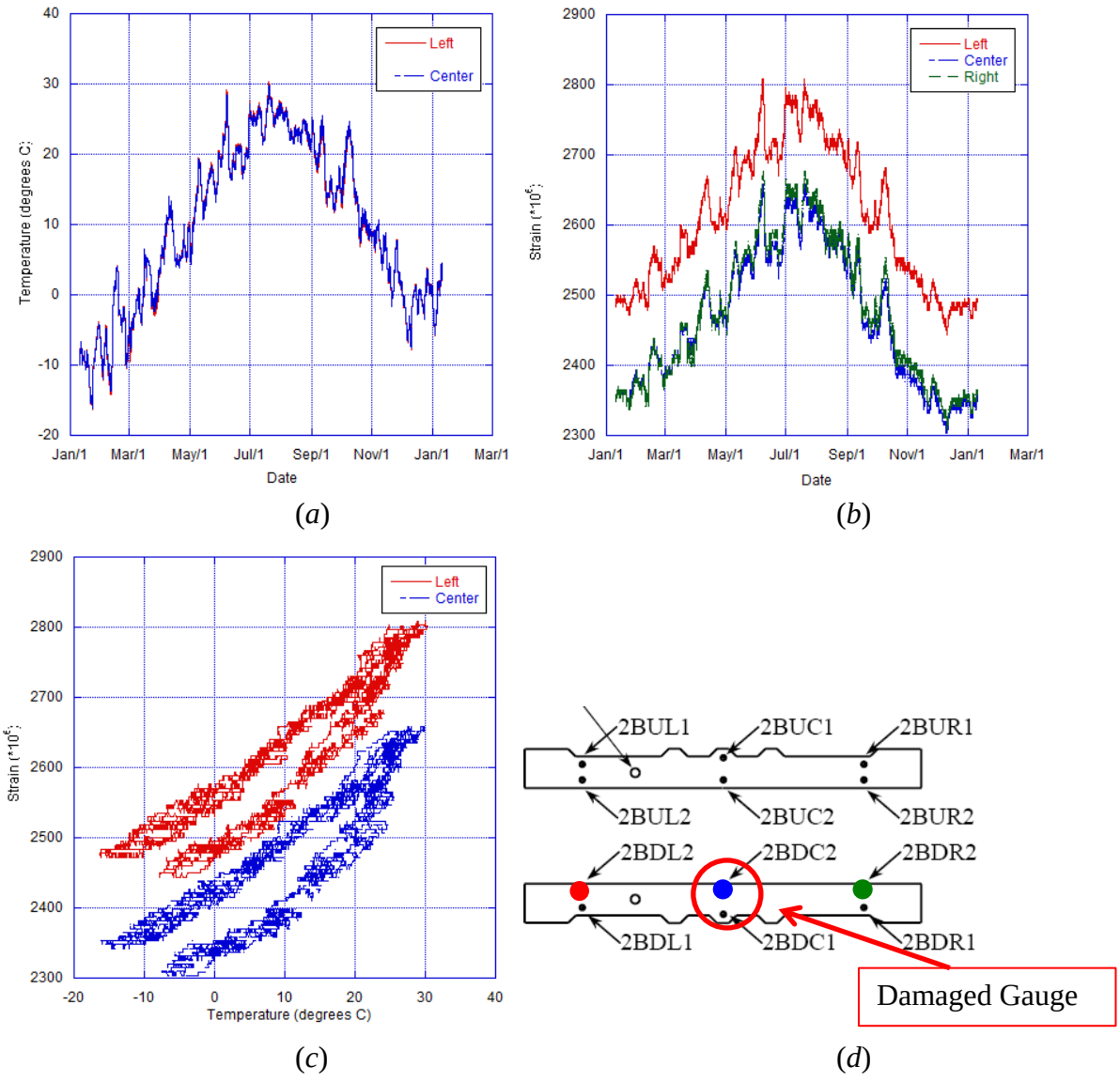

Figure 3.12: SDBPier2, a) Temperature versus time; b) Strain (*10^6) versus time; c) Strain (*10^6) versus temperature; d) Instrument locations by color. Note that gauge 2BDC2 has a damaged thermistor and recorded inaccurate temperature readings which were excluded from these plots.

The gauges in the bottom instrumented section of Pier 2 (Figure 3.12) are located directly below those in the top instrumented section (Figure 3.12), whose behavior was described previously. The slopes of the strains plotted versus temperatures for the bottom section in Figure 3.12*c* are clearly positive, whereas those of the top-instrumented section are negative (Figure 3.12*c*). This same reversal in the direction of the slopes of the strain versus temperature plots is seen for every pair of top and bottom instrumented sections in both piers, suggesting that the pier blades may be in reverse-curvature bending.

Some hysteresis is seen in the strain versus temperature plots in Figure 3.12; a possible explanation for this behavior is the dissipation of force at the expansion bearings due to friction at these locations. While the expansion bearings at the abutments and at Pier 1 serve to minimize the force transferred at these locations, some amount of friction would still be present. As the bridge expands and contracts with temperature, some force would be dissipated as friction at these bearings, possibly resulting in lower axial strains, stresses, and forces applied at Piers 2 and 4. This phenomenon is discussed further in Section 6.2.

3.4.3 Strain and Temperature Data Along Blade Depth

Data presented here was collected from gauges across the up-station blade of the bottom instrumented section of Pier 2 (RUBPier2 and SUBPier2).

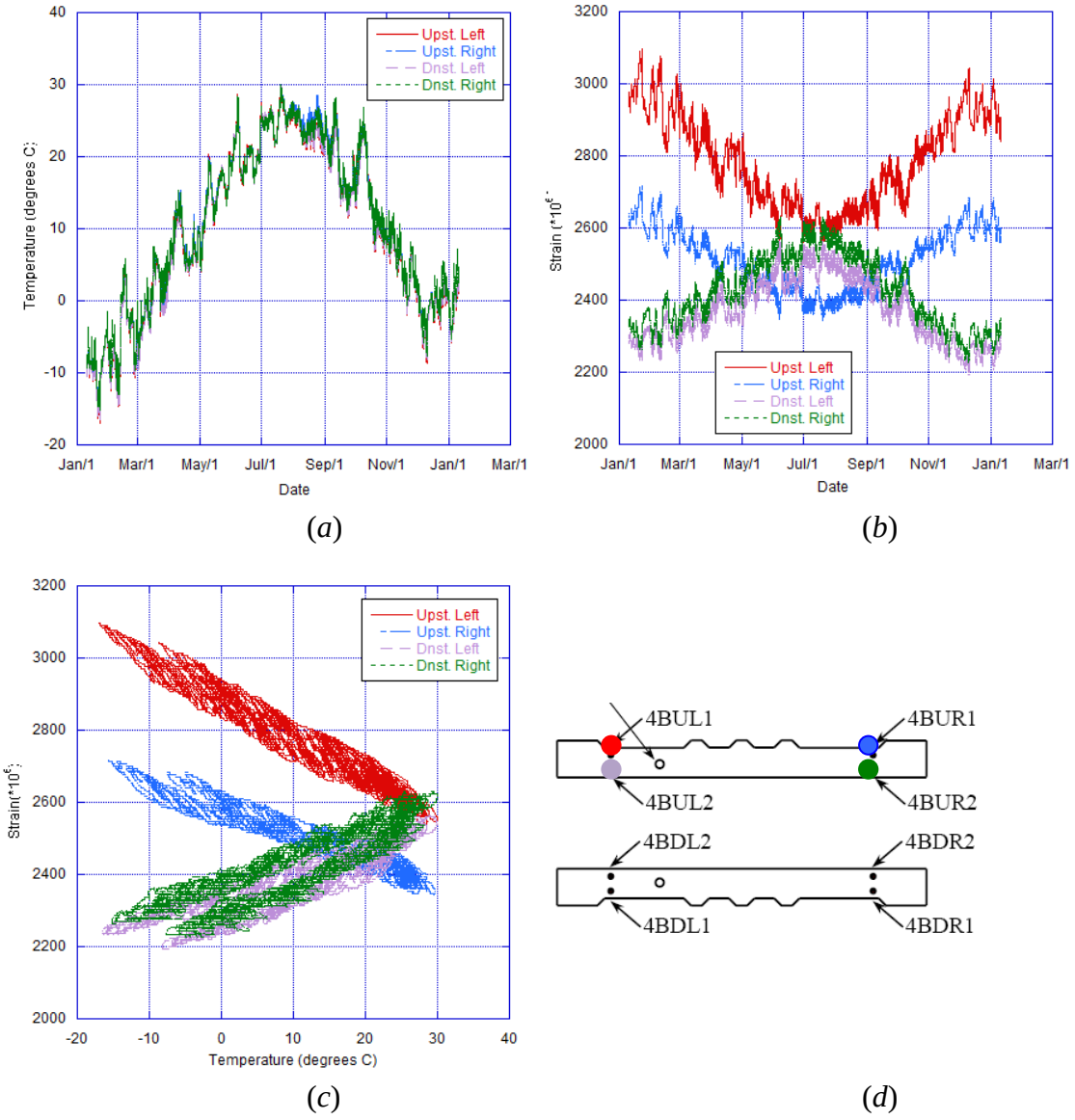

(*a*) (*b*)

(*c*) (*d*)

Figure 3.13: RUBPier4 and SUBPier4, a) Temperature versus time; b) Strain (*10^6) versus time; c) Strain (*10^6) versus temperature; d) Instrument locations by color.

Figures 3.13(*a*-*c*) show the strains and temperatures over time across both the rusticated and smooth faces of the up-station blade of the bottom instrumented section of Pier 4. The two faces of the blade showed opposing behavior; when the strain was decreasing over time along the smooth face of the blade, it was increasing along the rusticated face. This same behavior was seen in all pier blade sections, suggesting that the pier blades were acting as elements in bending and not purely as flanges of a larger section comprising the entire pier. The two gauges on the smooth face had approximately the same positive slope to the strain versus temperature plot, and the two gauges along the rusticated face had approximately the same negative slope.

The behavior seen in Figures 3.13(*a*-*c*) was the same in the case of the down-station pier blade, which is shown in Figures A13(*a*-*c*) in Appendix A: The up-station faces of each blade showed the same strain versus temperature relationship, in this case both decreasing with increasing

temperature, while the down-station faces of the blades showed the same behavior, which was the reverse of the behavior seen on the up-station faces. This suggests that significant axial load changes across the total pier cross-section may also be occurring with changing temperature.

3.4.4 Strain and Temperature Data Across Span Sections

Data presented here were collected from gauges across the bottom flange of Span 4 (BSpan4).

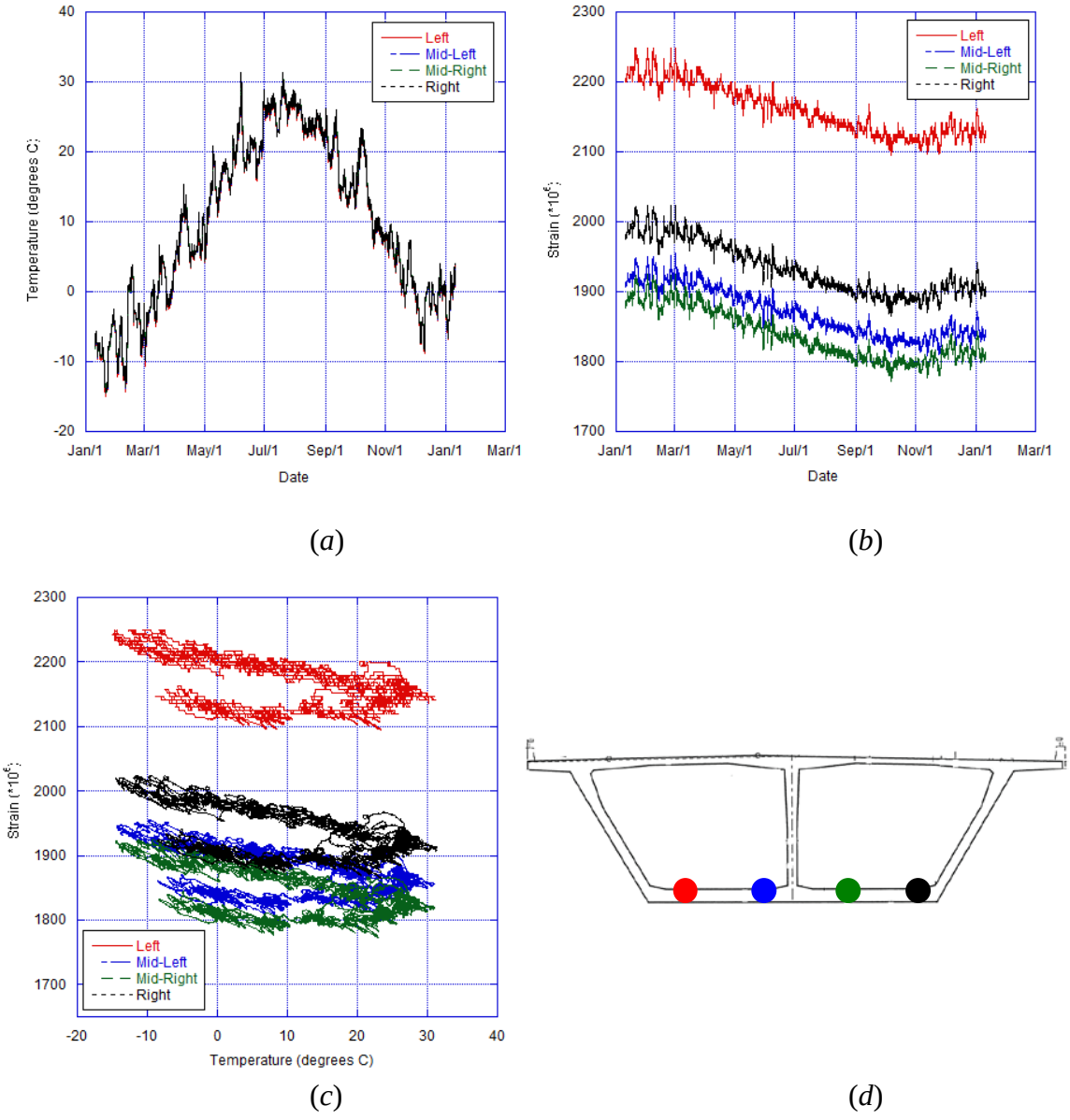

Figure 3.14: BSpan4, a) Temperature versus time; b) Strain (*10^6) versus time; c) Strain (*10^6) versus temperature; d) Instrument locations by color.

Figure 3.14*c* shows the strain decreasing with increasing temperature in the bottom flange of Span 4, and the same inverse relationship between strain and temperature was seen in all instrumented sections in both Span 3 and Span 4 (See Appendix A). This behavior was expected

because as the temperature increased, the bridge superstructure expanded. The fixity of the piers may provide this restraint, resulting in compressive strains developing along the length of the bridge and correspondingly lower strain recordings. As was seen in the top-section of Pier 2, the strains in the bottom flange of Span 4 did not return to the same maximum values that were seen in January of 2011, which again was most likely due to the relatively warm winter season of December 2011-January 2012. As discussed in Section 3.4.1, friction at the bearings and the resulting dissipation of longitudinal forces may have been a cause of this hysteresis.

3.5 Linear String Potentiometer Data

Displacement readings were collected from the string potentiometers over one full year, starting on January 10, 2011 and ending on January 10, 2012. The raw data were collected in the form of displacements, measured in inches. The data were collected at the time intervals described in Section 3.3.

Since each string potentiometer measured the displacement of the superstructure at only one location, i.e. at each abutment, the total expansion or contraction of the superstructure is the combination of the two displacements. Plots of displacement at each abutment with respect to time are shown in Figures 3.15(*a*-*b*).

It is apparent that the displacement of the face of the end of the bridge superstructure away from the face of the abutment decreases with increasing temperature, and increases with decreasing temperature. This shows that the bridge is expanding with increasing temperature and contracting with decreasing temperature, which agrees with the behavior of the strains measured in the instrumented sections in Span 3 and Span 4.

There are three linear sections highlighted in green in Figure 3.15*a*, which represent times at which, due to technical malfunctions, power to this string potentiometer was lost, resulting in no data being collected. The general trend of the data suggests that there would have been daily fluctuations similar to those seen in the rest of the history, as well as in the data from the string potentiometer at the other abutment. The technical difficulties present in the collection of data from the first string potentiometer did not occur with the second, and so there are no gaps in the data from the latter sensor.

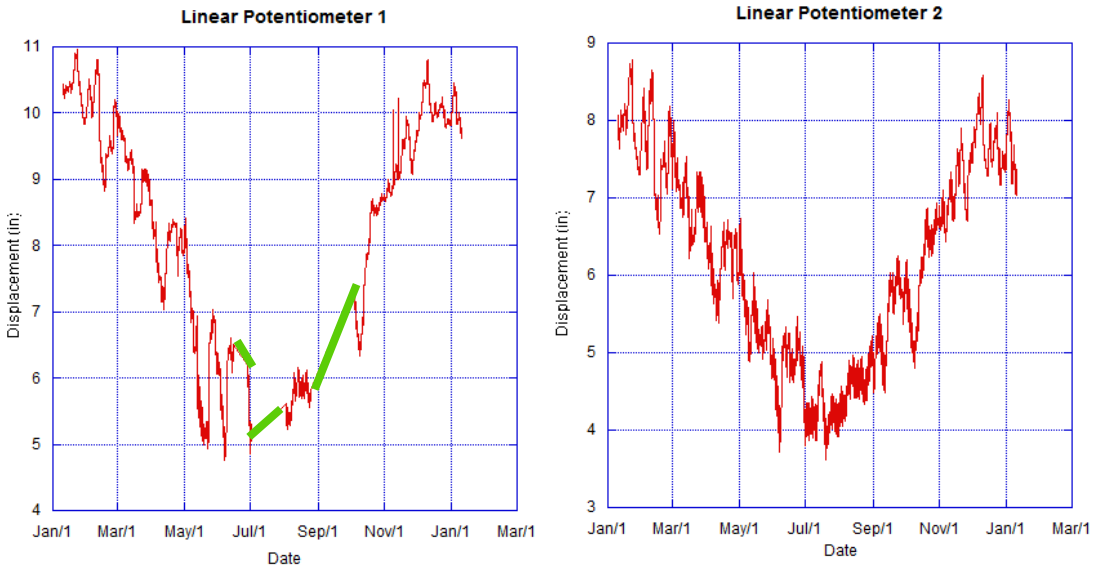

(*a*) (*b*)

Figure 3.15: Measured superstructure displacement versus time at the *a*) West abutment; *b*) East abutment.

Chapter 4. Data Analysis

4.1 Overview

This section describes the method of calculation of the distributions of stress changes in the instrumented cross sections from the processed strain data, and provides discussion of the behavior of these sections. The stresses, like the strains, are actually changes occurring at the instrumented locations from the time that data collection began. Several issues had to be addressed with respect to the accuracy of the strain data collected before any stress distributions could be defined. These issues concerned the corrections to the data to account for effects caused by the construction of the gauges themselves and the collection of initial values for reference. Any modifications to the strain data not presented in the preliminary analysis discussed in Chapter 3 were completed before changes in stress were calculated, and are presented in this chapter.

4.2 Secondary Data Analysis

4.2.1 Batch Gauge Factors

The vibrating wire strain gauges used in this project did not directly output a strain reading. The gauges recorded frequencies of vibration of wires housed within steel cases (Figure 4.1) that were used to calculate the measured strains using an equation provided by the manufacturer that represents the relation between frequency and strain. Each strain measurement had to be corrected based on temperature as well as the different coefficients of thermal expansion for steel and concrete so that the strain being recorded was that of the concrete surrounding the gauge rather than that of its steel case. Both of these corrections were discussed in Chapter 3. In addition to these corrections, the clamping of the ends of the steel wire within the gauge effectively shortened the length of that wire, requiring the application of a batch gauge factor to account for the slightly overestimated frequencies that would be produced. The batch gauge factor provided by the manufacturer was a multiplicative factor equal to 0.98 that was applied to the strain value after conversion from a frequency and temperature modification [13].

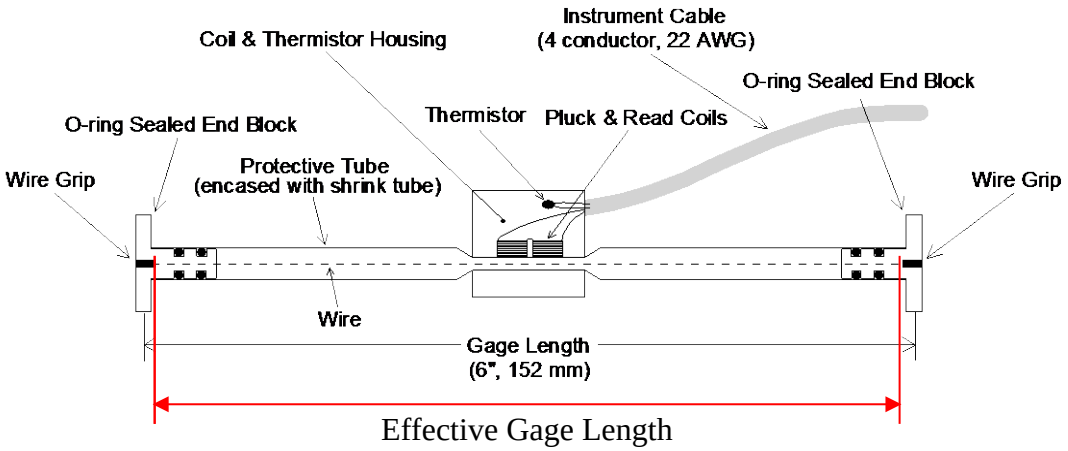

Figure 4.1: Schematic of clamping of the steel vibrating wire within the gauge [13].

Figure 4.1 shows a simplified schematic of the steel wire within the gauge. The effective length of the steel wire is shortened by the clamps holding the wire in place within the gauge case. The batch gauge factor was applied to the strains measured by the strain gauges.

4.2.2 Initial Reference Values

The second issue addressed was the lack of initial strain readings for each gauge. The manufacturer of the vibrating wire strain gauges installed within the bridge does not set the gauges to read a zero-value at zero-strain, but rather pre-tensions the gauges to read a strain of approximately 2500×10^{-6} at zero-strain [13] . However, due to the high sensitivity of the gauges, the actual initial value may range anywhere from strains of $100\text{-}200\times10^{-6}$ higher or lower than that expected value.

Recordings were taken from the gauges after installation, but before the pouring of the pier and superstructure concrete, for several reasons. Attaching the gauges altered the tensions in the gauge wires, and for analysis purposes, it was necessary to record the value of strain before creep, shrinkage, and post-tensioning introduced real strain in the concrete. The contractors' insistence not to allow the University of Minnesota researchers access to the bridge to install the dataloggers and record data until that time when the bridge had been completed and turned over to MnDOT became an issue, because access to the gauges during this time was nearly impossible. Nonetheless, the U of M researchers were able to collect three sets of data using a simple readout box (as opposed to the dataloggers) between the time of completion of bridge construction and the official beginning of the one-year data collection period. However, the reliability of these datasets is low because they were made using a simple readout box and because they were made under duress as the researchers were rushing to collect the data while the contractor was pressuring them to vacate the bridge. There was not enough time to ensure that the leadwires for each sensor had been connected properly, or to repeat the readings several times to ensure repeatability. Moreover, these readings were taken well after the concrete had been poured, thus the gauges were not totally free of stress, and thus do not represent a true zero (i.e., a stress-free state).

For these reasons, it was decided to consider only the changes in strain and the associated changes in stresses, axial forces and moments, thus rendering the initial strain readings unnecessary. The "initial" strain reading for each gauge was taken as the first strain recorded by that gauge using the datalogger system; the initial strain recordings were taken on January 10, 2011 at 2:00pm. The initial values were different for each gauge, and each was subtracted from all subsequent strain recordings for that gauge. A table of the measured initial values for all gauges is provided below.

Table 4.1: Initial strain readings for each vibrating wire strain gauge.

Gauge	PIER 2 Initial Strain $\times 10^6$	Gauge	PIER 4 Initial Strain $\times 10^6$	Gauge	SPAN 3 Initial Strain $\times 10^6$	Gauge	SPAN 4 Initial Strain $\times 10^6$
2TUL1	2802.6	4TUL1	2259.7	T-L	22421.0	T-L	2331.3
2TUC1	2495.1	2TUR1	2331.3	T-LM	2265.1	T-LM	2387.1
2TUR1	2712.0	4TUL2	2938.0	T-RM	2336.9	T-RM	2364.7
2TUE1	2748.1	4TUR2	3403.8	T-R	2281.6	T-R	2460.7
2TUL2	2381.5	2TDL1	3025.9	B-L	2037.0	B-L	2205.4
2TUC2	3444.2	4TDR1	2919.4	B-LM	1885.4	B-LM	1911.9
2TUR2	2348.0	4TDL2	2754.1	B-RM	2005.5	B-RM	1885.4
2TUE2	2611.2	4TDR2	2718.0	B-R	2265.2	B-R	1981.4
2TDL1	2421.0	4BUL1	2975.6	L-U	2342.4	L-U	2438.0
2TDC1	3038.6	4BUR1	2640.7	L-UM	1964.0	L-UM	2210.8
2TDR1	2472.1	4BUL2	2281.6	L-BM	1687.2	L-BM	2098.2
2TDE2	2857.6	4BUR2	2325.8	L-B	2265.2	L-B	2183.8
2TDL2	3257.9	4BDL1	2748.0	C-U	2029.8	C-U	2455.0
2TDC2	3013.3	4BDR1	2907.0	C-UM	2098.2	C-UM	2254.2
2TDR2	2839.2	4BDL2	2851.5	C-BM	1803.4	C-BM	2205.4
2TDE2	4005.1	4BDR2	2359.1	C-B	2364.7	C-B	2075.6
2BUL1	2237.9			R-U	2232.5	R-U	2375.9
2BUC1	87494.3			R-UM	2119.8	R-UM	2151.7
2BUR1	2426.6			R-BM	2011.2	R-BM	2221.6
2BUL2	2802.6			R-B	1965.6	R-B	1831.8
2BUC2	963.8						
2BUR2	2512.3						
2BDL1	3179.6						
2BDC1	3251.3						
2BDR1	2981.9						
2BDL2	2489.3						
2BDC2	2353.6						
2BDR2	2353.6						

Italicized values were recorded by malfunctioning vibrating wire strain gauges and were discarded from analysis; Underlined values corresponded to gauges with malfunctioning thermistors, resulting in inaccurate temperature readings. The strain values from these gauges were used in analysis, but were compared with average temperature values from surrounding gauges.

4.2.3 Age of Bridge Elements

Certain of the sections at which data were collected were older than other parts of the bridge, resulting in possible differences in the influence of time-dependent effects on the strains recorded and resulting calculated axial forces and moments. A total of six cross-sections in the

bridge were instrumented for this project. The approximate age of each of these sections at the beginning of the data collection period is provided in Table 4.2.

Table 4.2: Approximate age of instrumented cross-sections at beginning of data collection period.

Bridge Cross-section	Approximate Age at Initial Data Collection	
Pier 2 Top Elevation	23 months	690 days
Pier 2 Bottom Elevation	23 months	690 days
Pier 4 Top Elevation	25 months	750 days
Pier 4 bottom Elevation	25 months	750 days
Span 3, Section P2-4U	17 months	510 days
Span 4, Section P4-6D	19 months	570 days

The age of the sections considered would have an effect on the amount of strain in the structure due to concrete creep and shrinkage, both of which are discussed in Section 4.3.2.1.

4.3 Calculation of Stresses

A great deal of information about the calculation of stresses from strains in concrete was found in the American Concrete Institute (ACI) code [15] as well in reports published by various ACI committees. The most pertinent reports for this project were the ACI 318-08 Building Code and Commentary [15] and the ACI Committee Report 209R-92 [16]. The MnDOT Standard Specifications for Construction [17] was also referenced for information on the specific concrete mixes used in the bridge. Concrete compressive strengths were taken as specified on the actual bridge plans.

Different types of concrete, with different specified 28-day compressive strengths, were used for the superstructure and for the pier blades; an elastic modulus was calculated for each type of concrete. It was assumed that the relationship between strain and stress was elastic, so that a single modulus, for each type of concrete, was sufficient to define stress from strain at all stress levels considered in the calculation of axial force and moment changes from the field data.

Note that the elastic moduli of the concretes were varied in the finite element models in order to represent the reduced stiffness of the sections due to cracking; this variation is explained fully in the Chapter 6 discussion of the comparison of the field data to results predicted by the finite element models.

4.3.1 Concrete Material Properties

Assuming that the relationship between stress and strain in the concrete remains elastic (i.e., total stresses in the concrete are assumed to be less than $0.45f'_c$, the stress distribution across the instrumented cross-sections of the bridge can be calculated very easily using the modulus of elasticity of the concrete for each section. These moduli were calculated using the minimum concrete compressive strengths specified for each type of concrete in the bridge plans: For the pier blades, the concrete used was MnDOT mix 3Y43, with a specified 28-day concrete strength

of 4000 psi (28 MPa), while for the box-girder the concrete mix 3U36 was used, with a specified strength of 6000 psi (42 MPa) [17]. Note that the bridge plans are written using metric units, and that the conversion from MPa to psi is a soft conversion and is not exact. The elastic modulus of the pier concrete was calculated using the relationship as specified in the ACI 318-08 Code for calculation in US units,

$$E_c = 57000\sqrt{f_c'} \text{ (psi)}, \tag{4}$$

with f'_c measured in pounds per square inch, or psi [15]. The elastic modulus of the higher strength concrete used in the span sections was calculated using a modified relationship, recommended by the ACI 363 Committee Report for use with concrete with compressive strength higher than 6000 psi [18],

$$E_c = 50000\sqrt{f_c'} \text{ (psi)}. \tag{5}$$

It has been determined that Equation 5 provides a more accurate a prediction of the elastic modulus of concrete with compressive strengths above 6000 psi; Equation 4 results in an overestimated value. The overestimation would have resulted in an associated overestimation of the actual axial forces and moments present within the bridge structure, and inaccurate analysis of those values. All stress calculations were made using these elastic moduli. Table 4.3 provides certain material properties of the two types of concrete under consideration, as specified in MnDOT 2401-2480 concrete mix design specifications [17].

Table 4.3: Concrete mix material properties as specified by MnDOT.

	Piers, Mix 3Y43	Spans, Mix 3U36
Concrete type	Type III	Type III
Slump	3 in.	4 in.
Aggregate size	CA35-50	CA50-70
Air entrainment	6.5%	6.5%

Type III concrete has an approved air-entraining admixture, to produce a specified air content of 6.5%. The aggregate used in both the superstructure and the piers was glacial gravel. The designation CA35-50 refers to aggregate of size 1.0-1.5 inches, and CA50-70 refers to aggregate of size 0.5-1.0 inches [17].

Concrete types, mix designations, aggregate size designations are described in the MnDOT Standard Specifications for Construction [17]. These properties were necessary in the calculation of creep and shrinkage effects on the stress changes over time, as will be discussed in the Section 4.3.2.1.

4.3.2 Calculation of Changes in Stress

Assuming a linear relationship between stress and strain for the concrete in both the box-girder sections and the pier blades, the stress in each section from time t_i to time t_j can be calculated as

$$\Delta\sigma_{ij} = E_c\left(\Delta\varepsilon_{ij}'\right) \times 10^{-6} \text{ (psi)}, \tag{6}$$

where $\Delta\varepsilon'_{ij} = \varepsilon_i{}' - \varepsilon_j{}'$ is the change in total strain recorded by the gauge at that location over a single time increment $\Delta t_{ij} = t_i - t$. The multiplication factor of 10^{-6} was needed due to the fact that the measured strain values were recorded expressed in micro-strain, $\varepsilon_i \times 10^{-6}$. Recall that the time interval between strain measurements was 15 minutes throughout most of the data collection period, the only exception being a single week in the beginning of April during which the data collection time interval was decreased to 2 minutes.

Strain readings were compared at a specific temperature both at the beginning of the data collection period to those at the end of the collection period. Strains measured at a 1.8 ºF temperature range between 37.4 °F and 39.2 ºF (a 1 ºC range between 3 ºC and 4 ºC) in both the winters of 2011 and 2012 were compared, the differences between which were assumed to be the values of the strain due to some combination of creep, shrinkage, temperature, and in the case of the spans, restraint. Table 4.4 provides the average percentage of change in strains measured at these temperatures for each cross-section.

Table 4.4: Average change in strain values measured between 37.4 and 39.2 °F.

Bridge Cross-section	Average Change in Strain
Pier 2 Top Elevation	5%
Pier 2 Bottom Elevation	9.5%
Pier 4 Top Elevation	5.7%
Pier 4 bottom Elevation	9.3%
Span 3, Section P2-4U	16.8%
Span 4, section P4-6D	19.5%

The total percentage change in strain between start and end values at the given temperatures were large enough, particularly for the superstructure spans, to warrant further consideration of their possible causes. Further investigation into the creep and shrinkage strain changes was done to determine the magnitude of these effects, and is described in the following section.

4.3.3 Creep and Shrinkage

Concrete creep and shrinkage will cause changes in strains and stresses present in a concrete structure over time. These values are both dependent on time; the values of these strains increase with the age of the structure. Because the data collection period did not begin until approximately 1.5 years after the bridge had been fully constructed and opened to traffic, it is believed that the majority of the creep and shrinkage deformations would already have occurred by the time that strain measurements began. ACI Committee 209 reports that approximately 78% of the total strain due to combined creep and shrinkage expected of a given concrete structure occurs within the first year of its lifespan, after which the magnitude of the strains produced by these effects significantly decrease [16]. The structures under consideration had been in place longer than this one-year period, and so would undergo a further reduced amount of creep and shrinkage over the year-long data collection period. An approximation for the contribution of these two values to the total stress calculated at each strain gauge location was approximated using the recommendations provided in ACI-209R-92 and is described below.

The effect of shrinkage was taken into account by subtracting the predicted strain due to shrinkage from the actual total strain measured by the strain gauge. This shrinkage strain was approximated using a number of factors determined by the material properties of the concrete used in construction. The approximate strain caused by shrinkage, as proposed by ACI Committee 209, is given in Equation 13,

$$\varepsilon_{sh} = \varepsilon_{shu} s_t s_h s_{th} s_s s_f s_e s_c \tag{7}$$

where ε_{shu} is the ultimate shrinkage strain for concrete, with an approximate value being provided by ACI 209R-92, $s_t = \frac{t}{t+35}$, with t being the age of the member in days, $s_h = 1.4 - 0.0H$, with H being the relative humidity of the air surrounding the structure, and the values of s_{th}, $s_{s,}$ s_s, s_s, and s_c are coefficients corresponding to the thickness of the member, the amount of concrete slump, the amount of fine aggregate in the concrete mix, the effect of air entrainment in the concrete, and the density of the concrete mix, respectively. The values for these coefficients were taken as recommended by ACI 209R-92 and are listed in Table 4.5.

Table 4.5: Values used in calculation of shrinkage coefficient.

	Location			
Coefficient	Pier 2	Pier 4	Span 3	Span 4
s_t	0.952	0.955	0.936	0.942
s_h	0.68	0.68	0.68	0.68
s_{th}	0.20	0.20	0.20	0.20
s_s	1.09	1.09	1.05	1.05
s_f	1.00	1.00	1.00	1.00
s_e	1.01	1.01	1.01	1.01
s_c	1.056	1.056	0.965	0.965

The ACI 209R-92 report recommends assessing the effect of concrete creep by using an effective modulus of elasticity that is calculated based on the concrete material properties, similar to the method used to approximate the shrinkage strain present in the member under consideration. Equation 14 was used to calculate this creep coefficient.

$$c_t = c_u k_t k_a k_h k_{th} k_s k_e k_f, \tag{8}$$

where c_u is the ultimate creep coefficient, taken as 2.35 by recommendation of ACI 209R-92, $k_t = \frac{t^{0.6}}{t^{0.6}+10}$, with t being the age of the structure in days, $k_a = 1.25 t_i^{-0.118}$, with t_i being the member age at loading measured in days, $k_h = 1.27 - 0.0067H$, with H being the relative humidity of the air around the structure, and the values of k_{th}, k_s, k_e, and k_f are coefficients corresponding to the thickness of the member, the amount of concrete slump, the effect of air entrainment in the concrete, and the amount of fine aggregate in the concrete mix, respectively. As with the approximation of the shrinkage strain, the values for these coefficients were taken as recommended by ACI 209R-92 and are listed in Table 4.6.

Table 4.6: Values used for calculation of creep coefficient.

	Location			
Coefficient	Pier 2	Pier 4	Span 3	Span 4
k_t	0.83	0.84	0.82	0.81
k_a	1.00	1.00	1.00	1.00
k_h	0.788	0.788	0.788	0.788
k_{th}	0.67	0.67	0.67	0.67
k_s	1.02	1.02	1.09	1.09
k_e	1.09	1.09	1.09	1.09
k_f	1.00	1.00	1.00	1.00

Both the creep coefficients, c_t, and the predicted shrinkage strains, ε_{sh}, are provided in Table 4.7 for both the piers and the spans instrumented. These values were calculated at the beginning of the data collection period; the approximate age of each pier and superstructure section are listed in Table 4.2 in both numbers of months and days.

Table 4.7: Coefficients for calculation of creep coefficient and shrinkage strain at the beginning of data collection.

	Creep Coefficient, c_t	Shrinkage Strain, $\boldsymbol{\varepsilon_{sh}}$
Span 3	1.109	0.000114
Span 4	1.123	0.000115
Pier 2	1.225	0.000102
Pier 4	1.235	0.000102

The ultimate creep coefficient (c_u) is the long-term value after creep deformation stops increasing with time, while the percentage of change in the creep coefficient compares the coefficient as calculated at the beginning of the data collection period to that at the end (Δc_t). The ultimate shrinkage strain (ε_{shu}) and change in shrinkage strain ($\Delta\varepsilon_{sh}$) are given in Table 4.8 along with the corresponding creep values.

Table 4.8: Ultimate creep and shrinkage strains over the data collection period.

	Ultimate Creep Coefficient	% Change in Creep $\left(\Delta c_t / c_u\right) \times 100\%$	Ultimate Shrinkage Strain	% Change in Shrinkage Strain $\left(\Delta \varepsilon_{sh} / \varepsilon_{shu}\right) \times 100\%$
Span 3	1.171	5.6	0.000117	2.6
Span 4	1.175	4.6	0.0001175	2.2
Pier 2	1.269	3.6	0.000104	2.0
Pier 4	1.275	3.2	0.000104	2.0

In Table 4.8, $\Delta c_t = c_{t\_f} - c_{t\_0}$, and $\Delta \varepsilon_{sh} = \varepsilon_{sh\_f} - \varepsilon_{sh\_0}$, where c_{t_0} and c_{t_f} are the concrete creep coefficients at the beginning and the end of the data collection, respectively, and ε_{sh_0} and ε_{sh_f} are the shrinkage strains, also at the beginning and the end of the data collection.

4.3.3.1 Thermal Expansion

The changes in strain due to the expansion and contraction of the concrete with changing temperature were also investigated. Because these factors depended on temperature alone, rather than time, their effects could not be considered negligible as in the case of creep and shrinkage. The ACI 209-92 report also includes recommendations for calculating the coefficient of thermal expansion of concrete based on mix design, and these recommendations were used to find the coefficients for both types of concretes considered [16]. The equation used to fined the coefficient of thermal expansion is

$$\alpha = e_{mc} + 1.72 + 0.72 \cdot e_a \tag{9}$$

Where e_{mc} is the degree of saturation of the concrete, and e_a is the coefficient of thermal expansion of the concrete. The aggregate used in the pier concrete was a glacial gravel, but the degree of saturation of the concrete was unknown. Research performed by Naik et. al. at the University of Montana [14] showed that the coefficient of thermal expansion for the concrete using glacial gravel as aggregate had a coefficient of thermal expansion of between 5.8 /°F and 6.0/°F. The value of 6.0/°F was used for both superstructure and pier concrete.

Strain due to thermal expansion was calculated as follows:

$$\varepsilon_{\Delta T} = \alpha(T_i - T_o) \cdot \gamma \tag{10}$$

$$\delta_{\Delta T} = \alpha(T_i - T_o) \cdot \gamma \cdot L \tag{11}$$

$$\gamma = \frac{\delta_{restrained}}{\delta_{unrestrained}} \tag{12}$$

where α is the coefficient of thermal expansion of the concrete, T_i is the temperature of the concrete at time = i, T_o is the temperature of the concrete at time = 0, and γ is the ratio of the retrained thermal deflection to the fully unrestrained thermal deflection and accounts for any restraint opposing the thermal expansion.

The displacements recorded at the abutments were nearly equal to the fully unrestrained deflection movements that were calculated in Section 3.5, and so the full effect of thermal expansion was taken into account in the stress calculations in the superstructure sections (i.e. $\gamma = 1.0$). However, the piers were assumed to have some restraint to their vertical expansion with temperature due to the self-weight of the superstructure. Approximate γ-factors were calculated using the vertical deflections of the tops of the pier blades as calculated in the finite element models in order to have some idea of the restraint on the pier blade movement. Table 4.9 lists the predicted changes in axial length of the piers due to thermal expansion from the measured average 83.8 °F internal concrete temperature range, vertical deflections as calculated in the finite element models for the piers, and associated γ-factors.

Table 4.9: Approximate γ-factors for determining change in strain due to thermal expansion of pier blades.

Model	Pier Blade	$\delta_{unrestrained}$ [inches]	$\delta_{assumed}$ [inches]	γ_{blade}	γ_{pier}
Refined	Pier 2 Upstation	0.37	0.279	0.697	0.900
	Pier 2 Downstation	0.37	0.441	1.102	
	Pier 4 Upstation	0.40	0.445	1.112	0.919
	Pier 4 Downstation	0.40	0.290	0.726	
Gross	Pier 2 Upstation	0.37	0.254	0.635	0.883
	Pier 2 Downstation	0.37	0.452	1.131	
	Pier 4 Upstation	0.40	0.463	1.156	0.898
	Pier 4 Downstation	0.40	0.255	0.639	

Both models were considered, and because the values calculated for the γ-factors were very similar for each pier cross-section, an assumed $\gamma = 0.9$ was used for all pier cross-sections.

Stress histories for the same gauge locations described previously in Section 3.4 are shown in Figure 4.2, for stresses calculated taking into account the effects of thermal expansion.

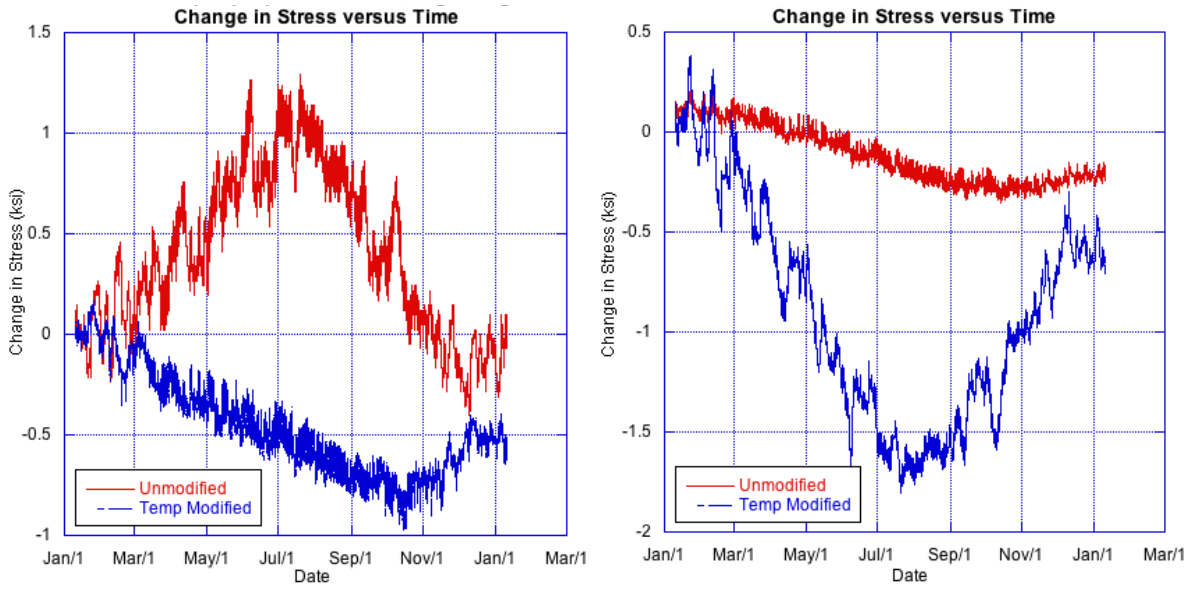

(*a*) (*b*)

Figure 4.2: Effect of thermal expansion strain on calculation of stress for (*a*) Gauge in Pier 2, and (*b*) Gauge 3B-LM in bottom flange of Span 3.

The effects of changes due to thermal expansion were much more significant than those due to creep or shrinkage. The addition of the strains from thermal expansion caused the positive changes in strain and stress in the piers to decrease and become negative, and the negative changes in stress and strain in both the piers and spans to become more negative.

4.4 Changes in Stress Across Cross-sections

A summary of the changes in stress as calculated from strain data and including all modifications discussed in Section 4.3.2 is provided in Figures 4.3-4. Stress changes were plotted with respect to time and temperature for all gauges, though not all plots are shown in this chapter. Any plots not shown are included in Appendix B.

4.4.1 Changes in Stress in Span Sections

Two locations were chosen to represent the calculated changes in stress for the span sections: The left web of Span 3 and the top flange of Span 4. These locations were typical of all other locations in the instrumented span sections.

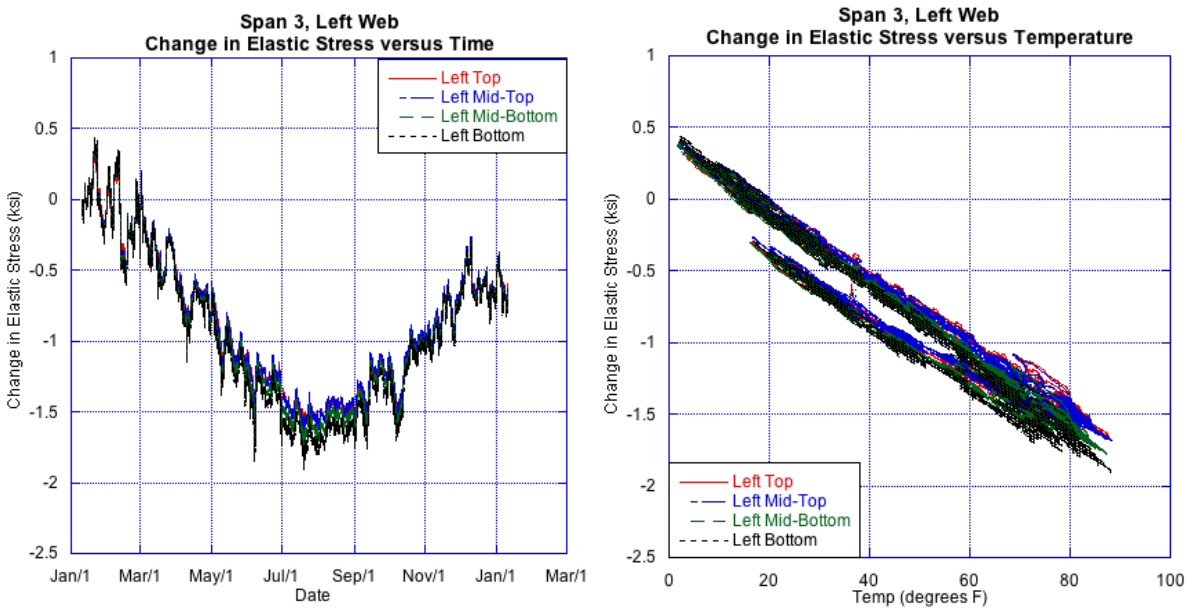

(*a*) (*b*)

Figure 4.3: Changes in stress for left web of Span 3 (LSpan3) versus *a*) Time and *b*) Temperature.

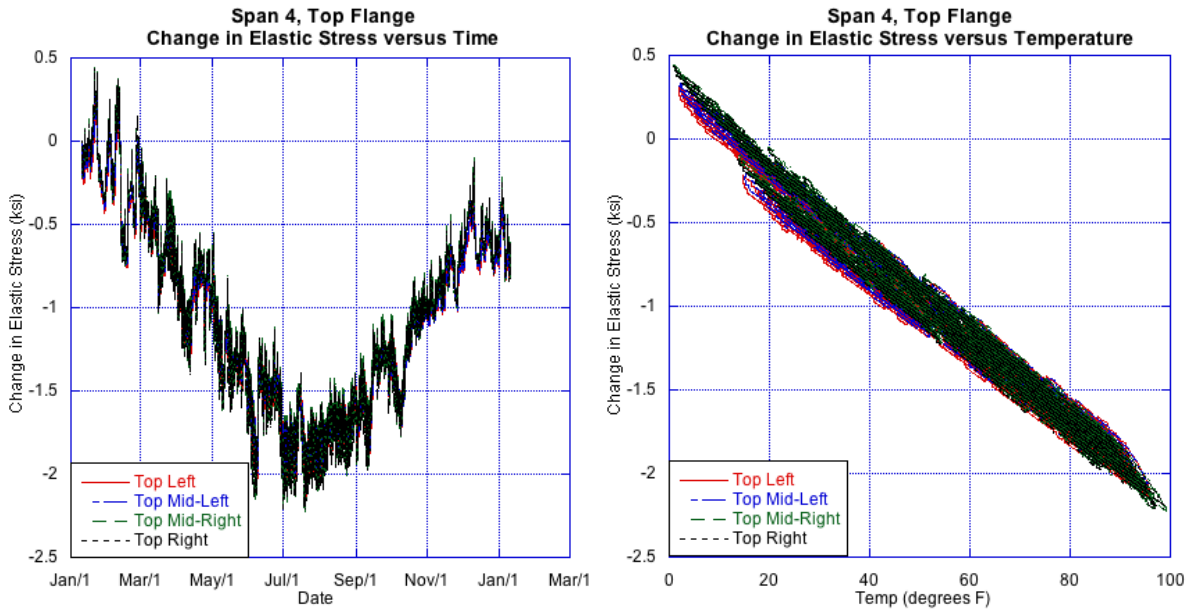

(*a*) (*b*)

Figure 4.4: Changes in stress for top flange of Span 4 (TSpan4) versus *a*) Time and *b*) Temperature.

As can be seen, the changes in stress for both locations have an inverse relationship with the temperature measured, implying that the box-girder sections are under increasing compression as the temperature increases. This behavior was expected; the concrete of the superstructure would

want to expand with increasing temperature, but the abutments would prevent some of this expansion introducing compressive stresses within the superstructure concrete.

The changes in stress follow a similar trend as the changes in strain, which was also expected given the assumed linear relationship between the two. However, the addition of the effects of thermal expansion did change the general trends of these changes over time.

4.4.2 Changes in Stress in Pier Sections

As with the span sections, two locations were chosen to represent the calculated changes in stress for the pier sections. In this case the two sections were the top and bottom elevations of the up-station blade of Pier 2. Comparison of these two locations offered insight into the behavior of the pier blades throughout the data collection period, and with respect to changes in temperature.

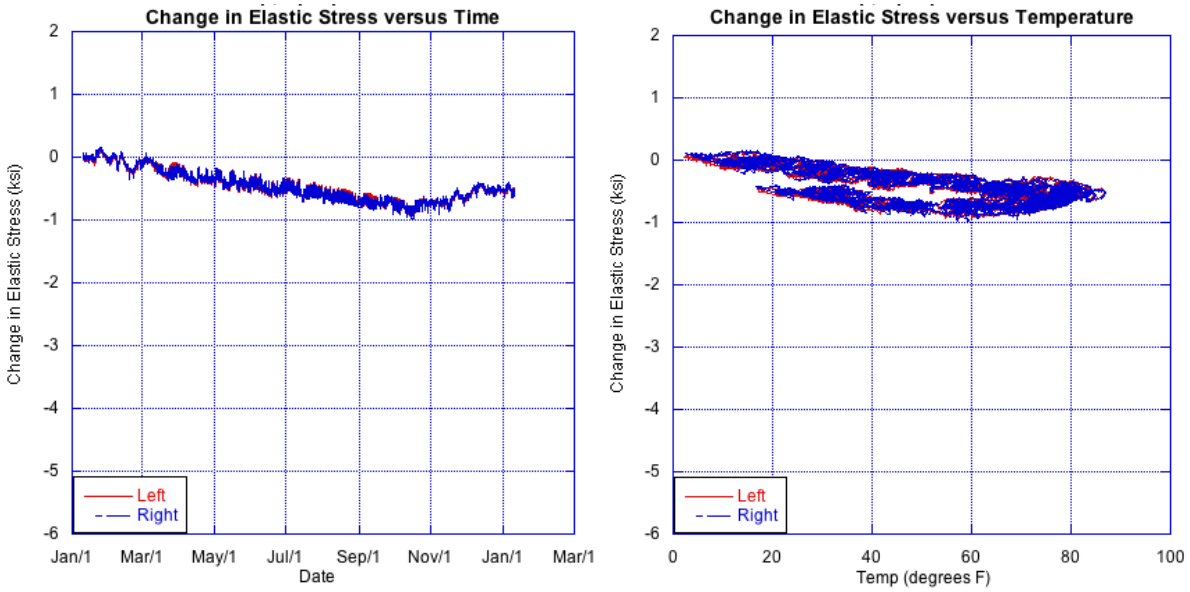

(*a*) (*b*)

Figure 4.5: Changes in stress in RUTPier4 versus *a*) Time and *b*) Temperature.

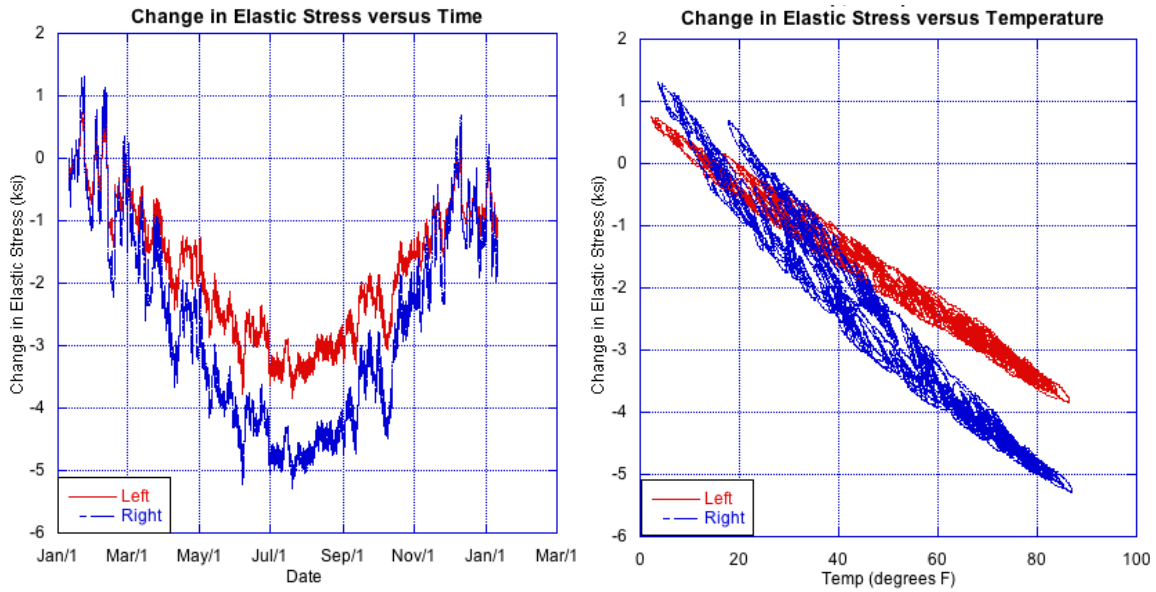

(*a*) (*b*)

Figure 4.6: Changes in stress in SUTPier4 versus *a*) Time and *b*) Temperature.

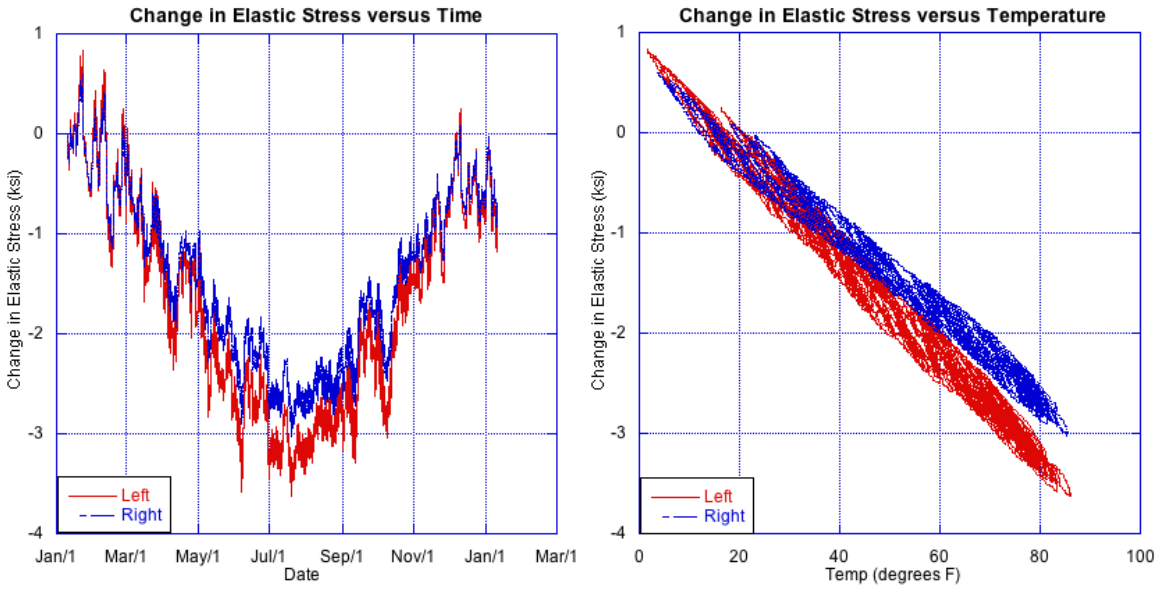

(*a*) (*b*)

Figure 4.7: Changes in stress in RUBPier4 versus *a*) Time and *b*) Temperature.

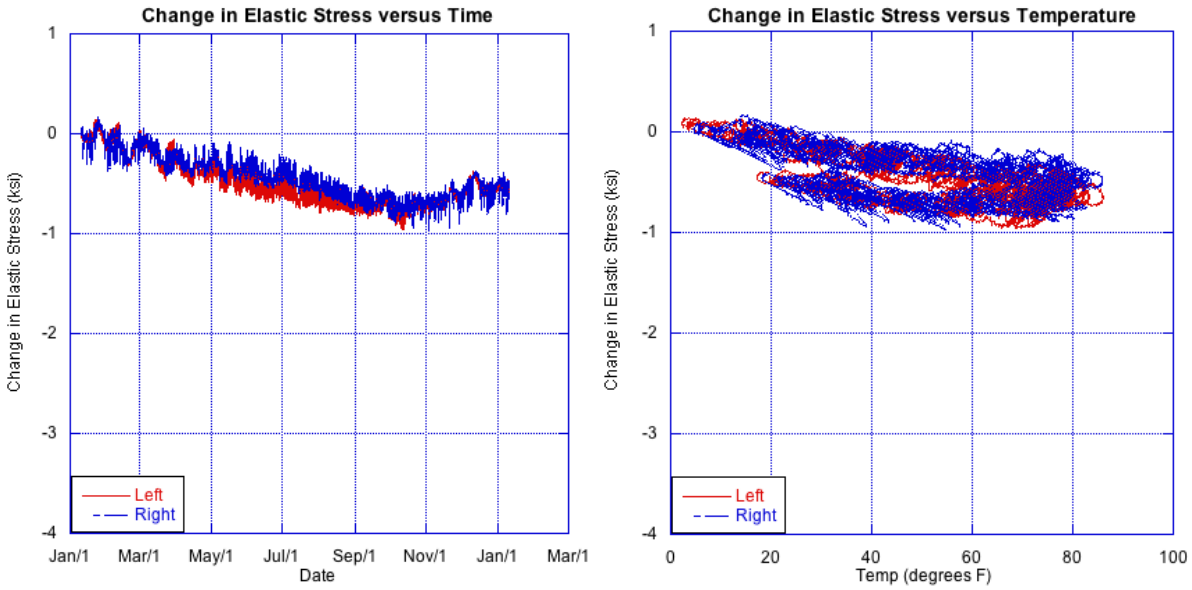

(*c*) (*d*)

Figure 4.8: Changes in stress in SUBPier4 versus *a*) Time and *b*) Temperature.

Again, the changes in stress shown in Figures 4.5-8 follow the same pattern as seen in the changes in strain for the pier cross-sections. Where the strain change had been positive, the addition of the thermal expansion strain when calculating stress changes resulted in stresses that were negative, while in those gauges where the strain change had been negative, the corresponding stress change was more negative.

The pier cross-sections showed a much more distinctive distribution of stress changes across their depths, and some investigation into the changes in stress at each cross-section offers hints at the behavior of the piers with respect to changing temperature. The first observation made is that the stress changes along either face of the blade are different: At the top of the pier, the rusticated face shows much lower magnitudes of stress changes than does the smooth face, while in the bottom section of the blade the opposite is true. This implies that the blade is undergoing some double curvature bending, inducing higher stresses on opposite sides of the blades at the two different heights. Figure 4.9 offers a schematic diagram of the possible double-curvature bending of a single pier, while Figure 4.10 shows the reversed behavior of Pier 2 and Pier 4.

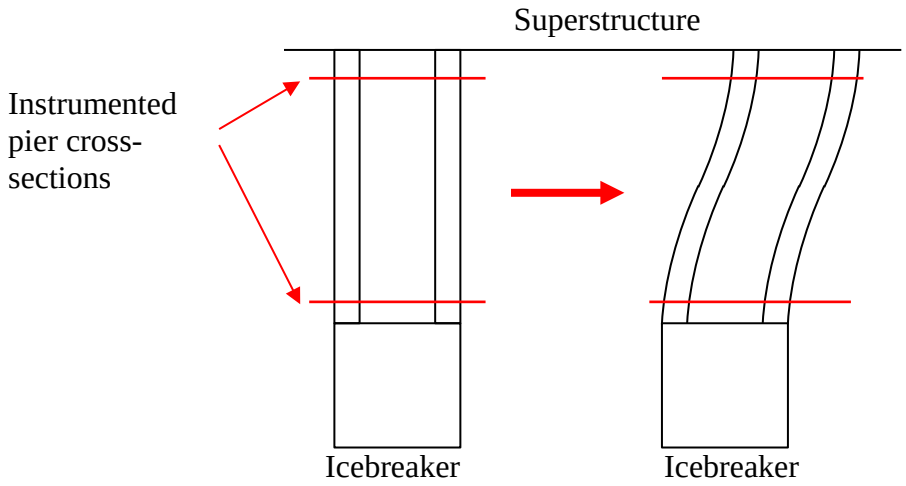

Figure 4.9: Double-curvature bending of pier blades due to thermally induced stresses.

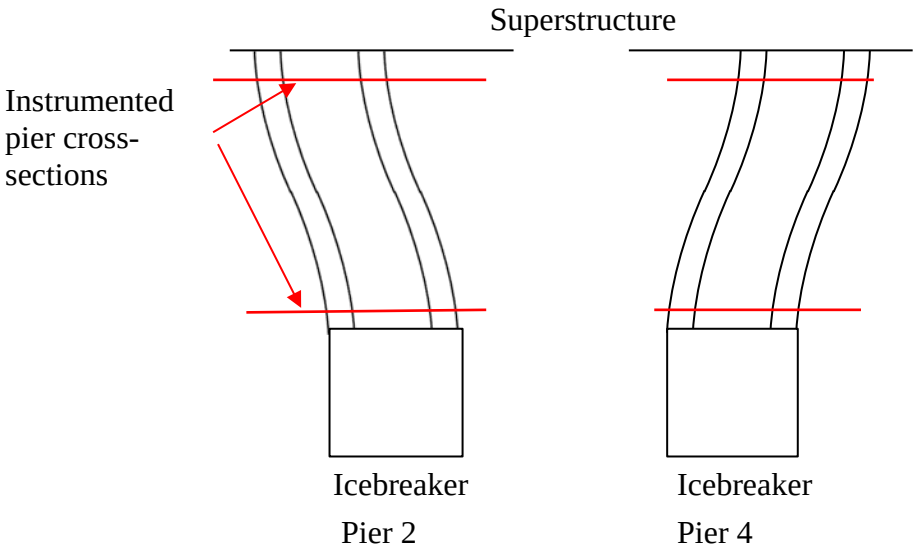

Figure 4.10: Opposing behavior of Pier 2 and Pier 4 due to the same change in temperature.

This possibility was first postulated in Chapter 3 discussion of the measured strains, and is reaffirmed by interpreting the stress changes.

4.5 Distribution of Changes in Stress

The investigation the changes in stress across the pier cross-sections resulted in a more in-depth review of the stresses across both the span cross-sections and the pier cross-sections. These stress

distributions were eventually used in the calculation of the changes in axial force and moment. The stress distributions were calculated differently for the span sections than they were for the pier sections, due to the different geometries of the two kinds of cross-sections.

4.5.1.1 Stress Distributions across Span Sections

The stress distributions across the span cross-sections were assumed to be linear and segmental. Because there is only a single row of gauges along any flange or web section, it was decided that a linear distribution along the "length" of each flange or web would be useful in calculating the axial force and moment changes. A MATLAB program was written to calculate the stress distributions, based on the geometry and strain data of each cross-section. The program subdivided each cross-section into a number of sections corresponding with the number of functioning strain gauges within that section. The slope of the linear stress distribution was calculated between adjacent gauges as

$$s = \frac{\sigma_i - \sigma_{i-1}}{r_i - r_{i-1}}, \tag{13}$$

where r_i and σ_i are the distance along the section of the cross-section and the stress at a given gauge location, respectively.

The stress distributions were created along both the width and the height of the sections. Individual distributions were created for each of the flanges and webs of the box cross-sections, resulting in a total of five changes in stress distributions for each instrumented span section. As with the pier blades, the horizontal stress distributions along the flanges ran from left to right, while the distributions along the web sections ran from top to bottom. These directions are summarized in Figure 4.11*a*, while a typical stress distribution across a span section is showed in Figure 4.11*b*.

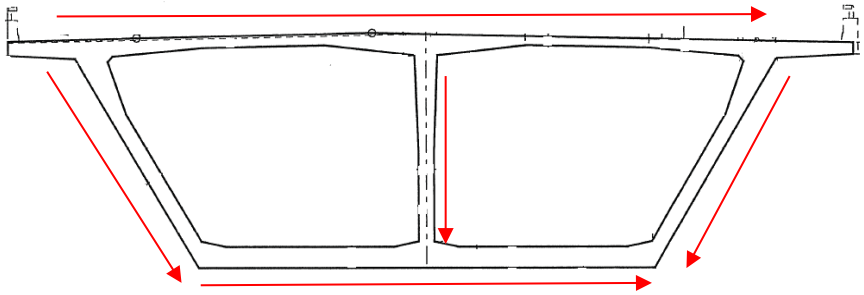

(*a*)

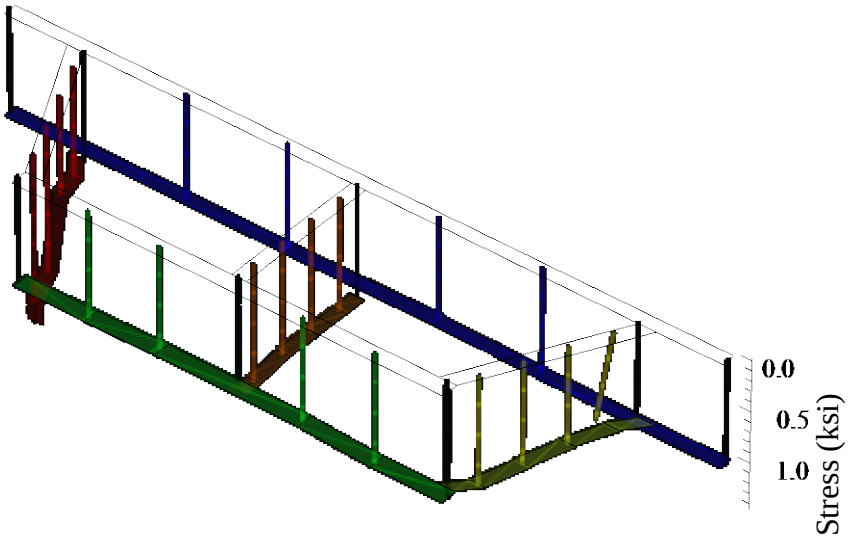

(*b*)

Figure 4.11: *a*) Stress distribution directions along span cross-sections and *b*) Typical linear stress distribution across a span section.

This method of calculation was chosen to correspond with the way in which the strain gauge data was recorded; the directions of the distributions follow the order in which data was recorded from the strain gauges, simplifying the calculation both of the distributions themselves as well as the later calculations of the changes in axial force and moment.

As is shown in Figure 4.11*b*, the changes in stress across both of the span cross-sections were negative, implying an over all negative change in stress across each section.

4.5.1.2 Stress Distributions across Pier Sections

Stress distributions were calculated for each pier blade, with each distribution corresponding to a pair of gauges across the depth of each blade. The distributions were assumed to be linear between gauges. Figure 4.12 shows a typical distribution across a pier cross-section, in this case the distribution is shown in three dimensions.

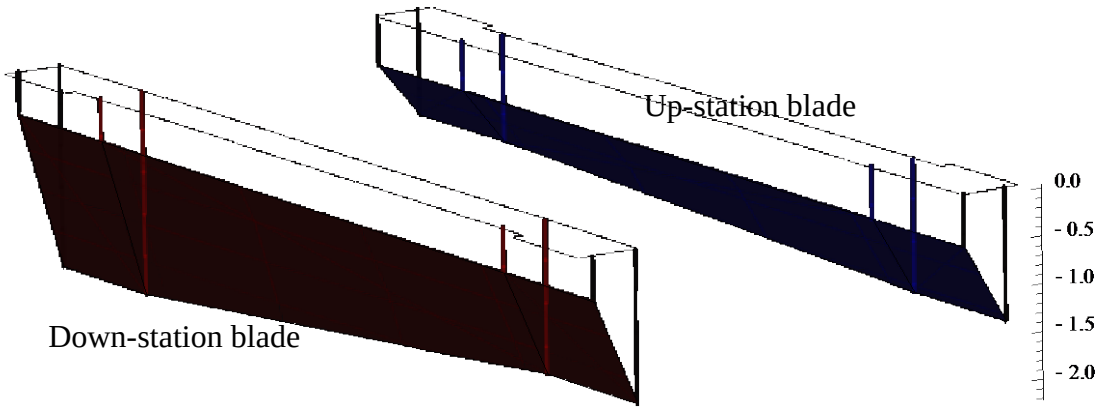

Figure 4.12: Typical linear stress distribution across a pier section.

The blue area corresponds with the stress distribution of the up-station blade, while the pink area corresponds with the down-station blade. The bold pink and blue lines correspond with actual stress values as calculated from the strain data collected from gauges at those locations. The stresses were negative, showing that this section had increased in compression since the beginning of the data collection; this was the case in each of the instrumented pier cross sections to varying degrees.

More detail into the distributions of changes in stress across the pier cross-sections is offered in the plots below. The diagrams shown in Figures 4.13(*a*-*d*) are two-dimensional (2D) plots of the stress changes along the depths of the pier blades. The "U" designation corresponds with the up-station face of each pier blade, while a "D" corresponds with the down-station blades. Plots are shown at each gauge location starting with 4TDL1, 4TDL2, and 4TUL2, 4TUL1.

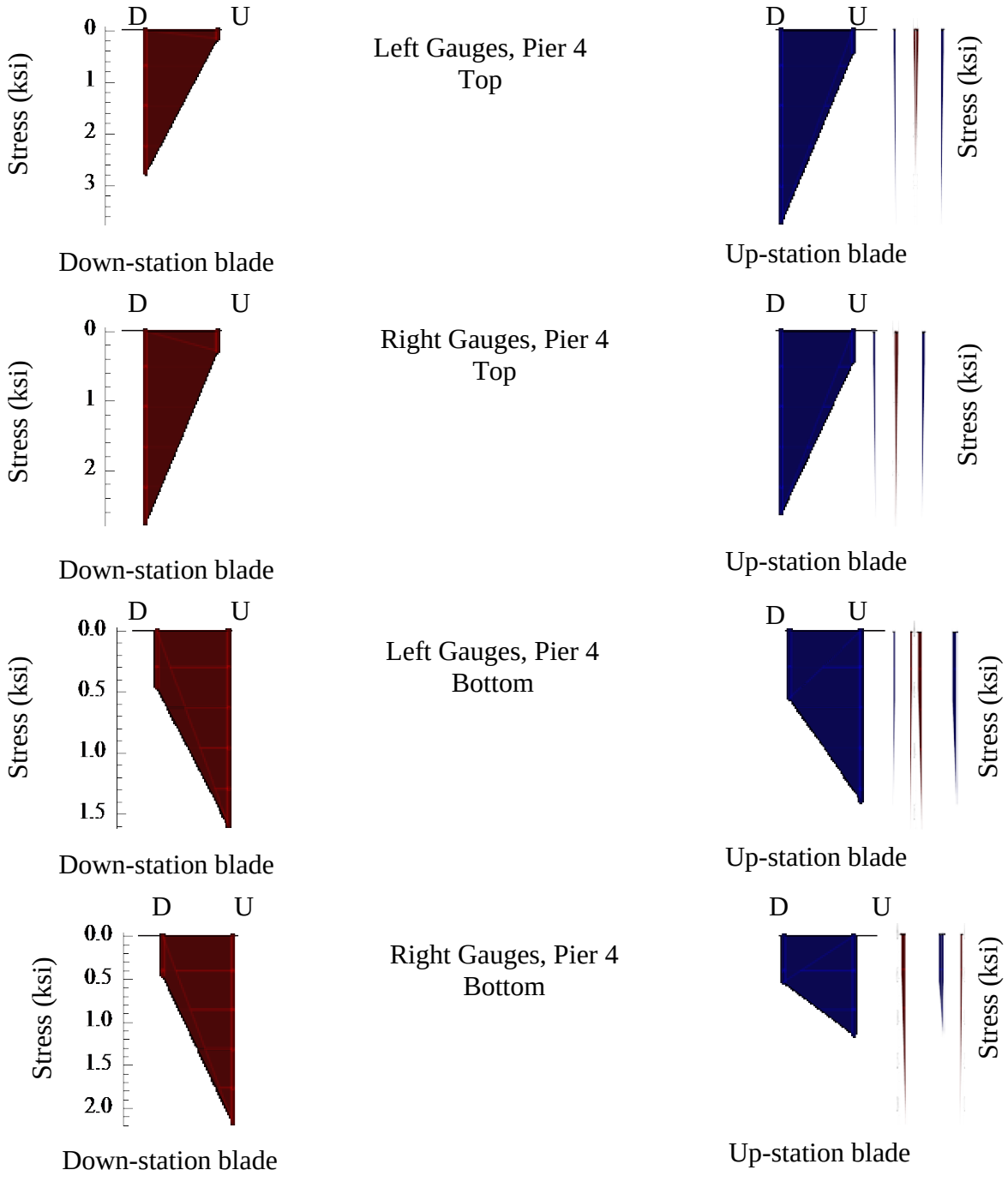

Figure 4.13: 2D plots of stress versus pier cross-section depth along the width of the bottom of Pier 4 for *a*) Left gauges; Right gauges.

These 2D plots correspond with the 3D stress distribution shown in Figure 4.12. Both blades have higher compressive stress changes along their down-station faces and lower changes along the up-station faces. As was discussed in Section 4.4.2, this reversal of stress distribution implies double curvature bending of the pier blades.

Chapter 5. Calculation of Changes in Axial Forces and Moments

To calculate the changes in axial force and moment across each instrumented section, a number of considerations were addressed in order to accurately analyze the collected data. In general, the change in axial force can be calculated as the integral of the stress over the area of the cross-section. Given a linear distribution, the area under the distribution is triangular, and the integral can be evaluated as a sum of a series of force increments,

$$\Delta F = \sum \Delta F_i = \sum \left[\left(\Delta \sigma_{ij} \cdot r_i \right) \cdot b_i \right], \tag{14}$$

where ΔF_i is the change in axial force for one segment of the cross-section between two gauge locations, $\Delta \sigma_{ij}$ is the change in stress at location i over time interval j, r_i is the length of the segment associated with gauge i, and b_i is the width of the segment. In evaluating Equation (14), the segment is assumed to be rectangular in shape. However, complex geometry complicated this straightforward calculation.

The first issue was that the changes in stress being computed required differences between two small quantities with similar magnitudes. The measurement error inherent in data collection represented a significant percentage of the differences that were calculated. However, due to the relatively large number of gauges that were installed, which was more than the minimum number needed to simply compute the internal forces in the instrumented sections, it was possible to compute average stress change values across each section, reducing the effect the measurement error would have on the analysis. The second issue was that the complicated cross-section geometry of the span sections made creating a program to calculate changes in axial force and moment difficult. This was overcome by subdividing the cross section into a series of rectangular segments. In all calculations, the resultant forces were computed such that they were in equilibrium with the stress fields that generated them.

5.1 Span Sections: Changes in Axial Force and Moment

Changes in axial force were calculated for each gauge individually for each flange or web segment, and also across each span cross-section as a whole. In order to facilitate the calculation of axial force changes at each gauge, the cross-section was split into segments that were approximately rectangular (with length r_i and width b_i) that had the gauge locations at their centers. All sections were assumed to be rectangular.

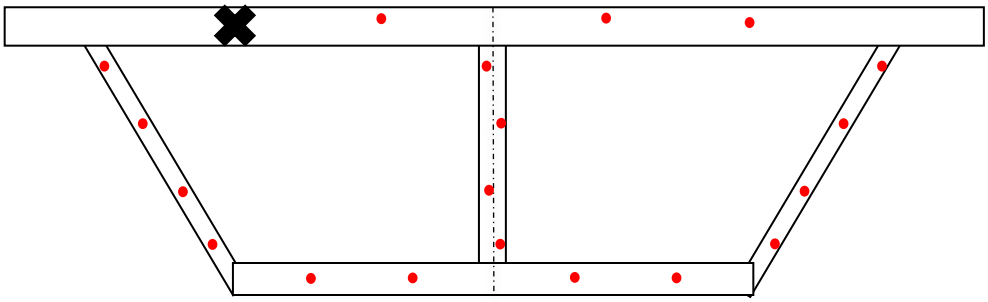

*(*a) Gauge locations.

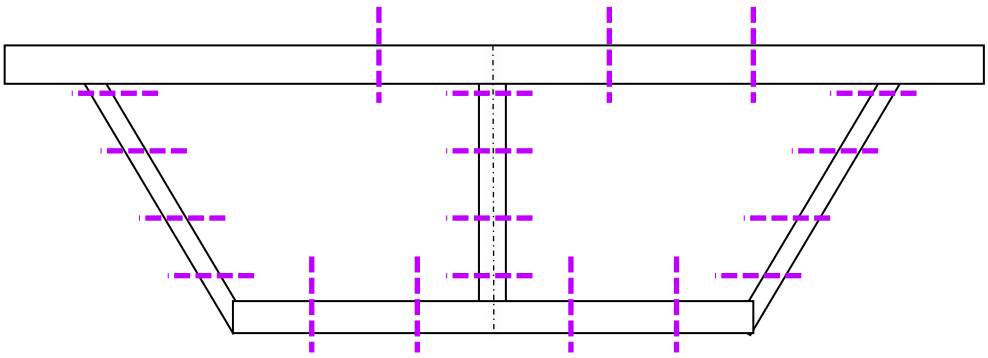

(*b*) Initial section cuts, at gauge locations.

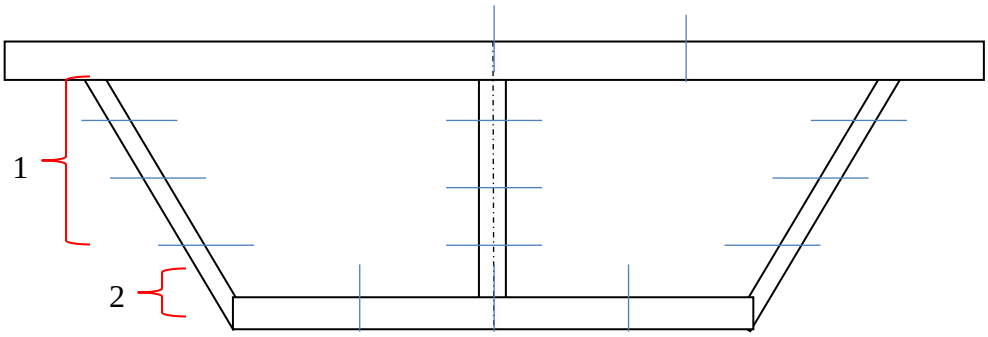

(*c*) Final section cuts, between gauges, to allow for calculation of values at gauge locations.

Figure 5.1: Section cuts for Span 3 (Note the damaged gauge in the top flange, marked with the black 'x').

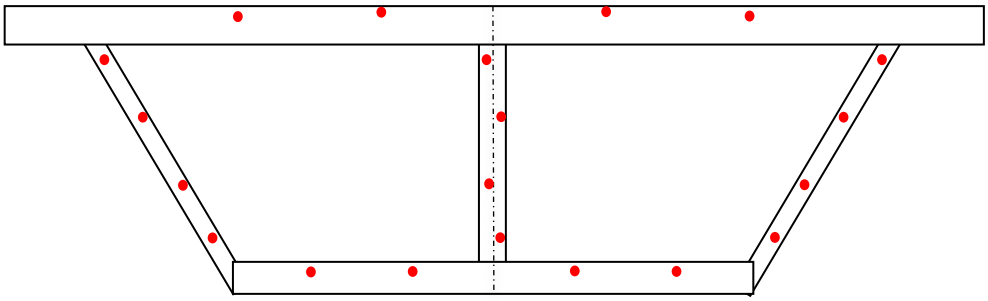

(*a*) Gauge locations.

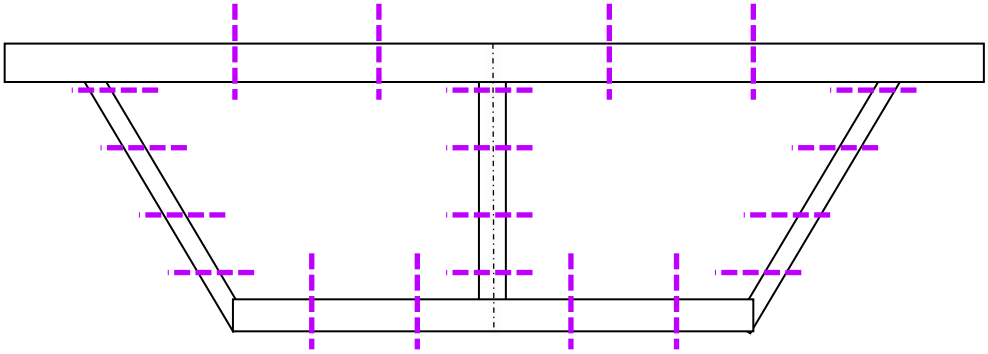

(*b*) Initial section cuts, at gauge locations.

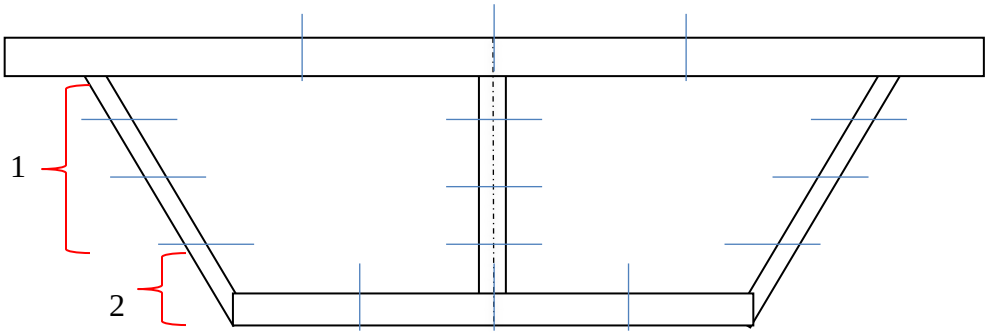

(*c*) Final section cuts, between gauges, to allow for calculation of values at gauge locations.

Figure 5.2: Section cuts for Span 4.

Not all section cuts resulted in segments that were perfectly rectangular. Segments that were parallelograms, such as the segments labeled with a “1” in Figures 5.1 and 5.2, were treated in the same manner as rectangles. The area and centroid of a parallelogram is calculated in the same way as those of a rectangle. Any segments that were trapezoidal were modeled as rectangles: the total area of the trapezoid was calculated and used in combination with the width of the web to calculate an effective length and centroid of a rectangle with the same area.

The initial section cuts were made at the gauge locations to allow for calculation of the stress distributions across the flanges and webs. The final section cuts divided the cross-sections into areas corresponding with individual gauges, and were used to calculate axial forces and moments for each individual gauge.

It was possible to use the simplified calculation of change in axial force described in Section 3.2.5 when analyzing the span sections. Table 5.1 summarizes the geometric data of the two span sections used to determine these changes.

Table 5.1: Span cross-sectional geometries.

	Section	Width, *b* (in)	Depth, *h* (in)	Area (in^2)	I (in^4)
Span 3	Top flange	1030.71	16.35	20,056.38	377,000,105
	Bottom flange	308.58	17.82		
	Left web	24.95	174.87		
	Center web	20.18	174.87		
	Right web	24.95	174.87		
Span 4	Top flange	1030.71	16.35	19,700.00	342,089,314
	Bottom flange	308.58	18.41		
	Left web	22.88	174.28		
	Center web	18.40	174.28		
	Right web	22.88	174.28		

A summary of the maximum and minimum axial forces and moments is given below for the two span sections. Note that a negative change in axial force was defined to be an increase in compression, and negative moment was defined as bending that produced compression in the bottom flange of the box-girder.

Table 5.2: Summary of maximum and minimum superstructure axial force and moment changes.

	Span 3		Span 4	
	Minimum	Maximum	Minimum	Maximum
ΔP_T	-56733.0	7380.0	-57789.6	7887.6
ΔM_T (k-	45769.1	-11721.5	26880.9	4247.9

The measured changes in axial force were approximately constant at both cross-sections, but the changes in moment were of much greater magnitude in the Span 3 section than in the Span 4 section.

5.1.1 Verification of Span Analysis

In order to verify that the MATLAB program was correctly calculating the changes in axial force and moment from the collected strain data, a simple hand calculation of these same values was performed using basic mechanics for comparison. The bending stress was calculated across each cross-section and was used to calculate the approximate change in force across the section as well as the approximate change in bending moment.

Given the large amount of data collected, only four data points were selected for comparison representing four distinct times during the year-long data collection period. These data points ranged across the entire period, and also corresponded with a wide range of temperatures. A summary of the approximations used to verify the MATLAB calculations is provided here.

For the span verification, the cross-sections were subdivided into web and flange sections, and the stiffness and area were approximated for each. The area moment of inertia was calculated using the parallel axis theorem:

$$I_{parallel} = \frac{bh^3}{12} + Ar^2 \tag{15}$$

where *b* is the "width" of the web or flange section, *h* is the "depth" of the web or flange section, *A* is the area of the flange or web section, and *r* is the distance along the box height between the flange or web section centroid and the centroid of the entire span section. The bending stress was taken as a distribution across the height of the box girder. Table 5.3 summarizes the cross-section geometries of the span sections.

Table 5.3: Moments of Inertia for span sections.

Section	I (in^4)
Span 3	377,000,105
Span 4	342,089,314

For the approximations, change in axial force was calculated as a product of the axial stress, f_a, and the area corresponding to each gauge; moment was calculated as the product of the bending stress, f_b, and the section modulus of the cross-section.

$$f_b = \frac{(f_1 - f_2)}{2} \tag{16}$$

$$f_a = \frac{(f_1 + f_2)}{2} \tag{17}$$

$$F_{gauge} = f_a \cdot A_{gauge} \tag{18}$$

$$M_{gauge} = \frac{I}{y} \cdot f_b = S \cdot f_b \tag{19}$$

where *y* is the distance from the centroid of each line of strain gauges to the centroid of the span cross-section.

Stress distributions were defined across the heights of the webs, as well as at the top and bottom flanges, and so it was possible to create an approximate stress distribution across the height of the box. Rather than taking the values of f_1 and f_2 at specific locations on the cross-section, stress values at each height were averaged together to create the approximate stress distribution. The maximum of these averaged values was taken to be f_2 and the minimum was taken to be f_1. Stresses were averaged across each height of the instrumented box-girder cross-sections, denoted by the red lines below in Figure 5.3.

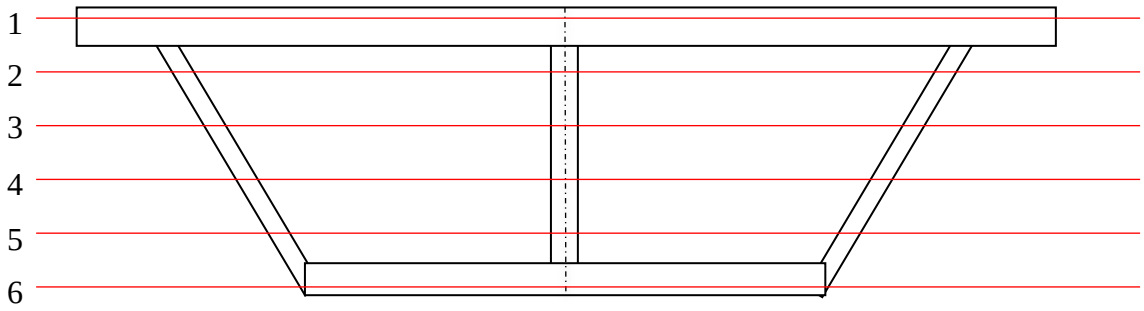

Figure 5.3: Stress distribution locations on span cross-sections

The stress change distributions for each span section were negative; these sections were under compression throughout data collection. As temperatures increased, the magnitude of the compressive stresses increased, (i.e. became increasingly negative), while for decreasing temperatures, the magnitude of compression decreased (i.e. became less negative).

The distributions across the span sections were relatively uniform, so rather than considering stress values at a physical location, the axial and bending stresses were approximated using the maximum and minimum stress values across the height of the box girder at various locations. These bending stresses were averaged, to give the final approximation used. These estimations provided useful comparisons to the MATLAB values. The approximated values were superimposed on the change in axial force or moment versus time history for each section.

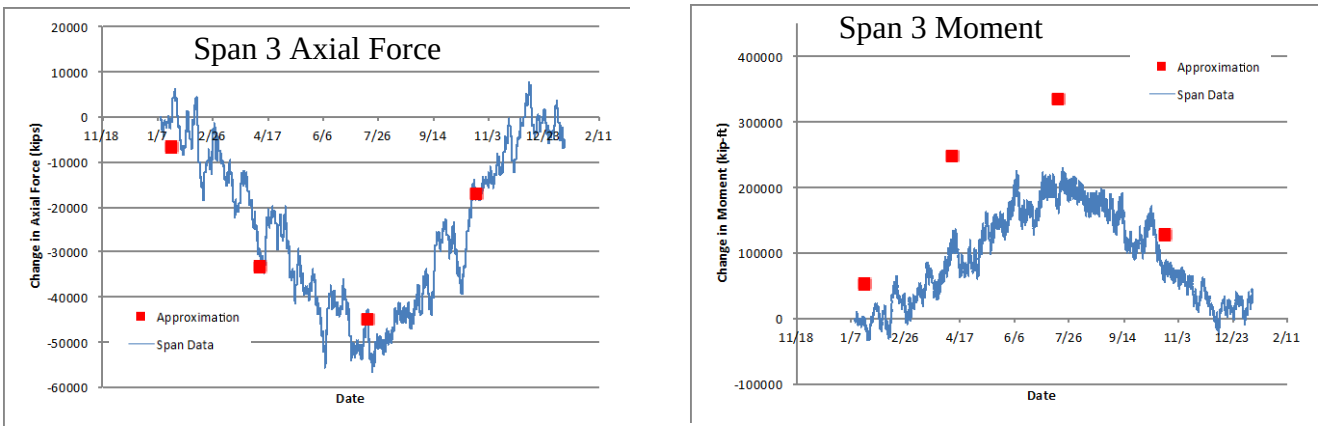

(*a*) (*b*)

Figure 5.4: Span 3 MATLAB value comparison to the hand calculations of a) change in axial force and b) moment.

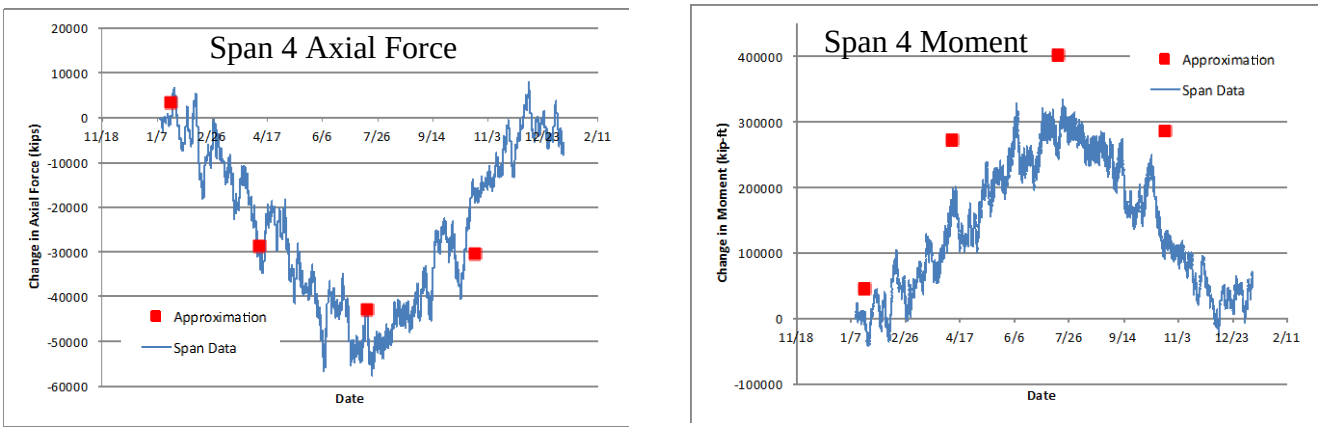

(*a*) (*b*)

Figure 5.5: Span 4 MATLAB value comparison to the hand calculations of a) change in axial force and b) moment.

The approximate trends with time followed the actual force and moment histories well. The moment changes were overestimated in both Spans 3 and 4, which could be due to the approximations of the cross-sectional areas and stiffnesses of the sections, but overall the results show that the MATLAB program accurately calculated the changes in force and moment from the strain data collected from the span sections.

5.2 Pier Sections: Changes in Axial Force and Moment

The pier blades are fixed at the top to the superstructure, and at the bottom to the icebreaker, but have no connection along the rest of their heights, resulting in pier sections that act neither as fully composite sections nor as two fully independent blades. The procedure used to calculate the internal forces in the piers first required calculation of an axial force and bending moment for each blade. Subsequently, an equivalent total axial load and total bending moment about the centroid of the pier section were obtained to replace the axial forces and bending moments in the two blades.

In the following calculations, strains in gauges at opposite faces of each blade were used to calculate curvatures. The following equations apply to the Pier 2 calculations; the method was modified slightly for the other pier sections because they had fewer gauges along the blade widths. Negative changes in axial force increased compression in the pier sections, while positive changes decreased compression. Negative moment was defined as bending that produced compression in the downstation pier blades, and positive bending produced compression in the upstation pier blades.

The change in axial force was calculated from changes in stress for each blade of the pier section, and the axial forces on each were summed to result in the total axial force on the entire pier section. In defining the blade axial forces, it was assumed that each gauge measured a strain that represented an influence area, and that the influence areas were equal for all gauges. The resulting axial forces were obtained using the following:

$$P_U = \frac{(\sum \sigma_{Ui})}{N} A_{blade} = \frac{A_{blade}}{8} (\sigma'_{U1} + \sigma_{U1} + \sigma_{U2} + \sigma'_{U2});\ \sigma'_{U2} = \sigma_{U2} \quad (20)$$

$$P_D = \frac{(\sum \sigma_{Di})}{N} A_{blade} = \frac{A_{blade}}{8} (\sigma'_{D1} + \sigma_{D1} + \sigma_{D2} + \sigma'_{D2});\ \sigma'_{D2} = \sigma_{D2} \quad (21)$$

$$P_T = P_U + P_D \quad (22)$$

where P_U is the change in axial force across the up-station blade, P_D is the change in force across the down-station blade, N is number of gauges across the cross-section of interest (note that in the case of Pier 2, which is described in Eq. 20-21, N = 8), the value of $\frac{A_{blade}}{N}$ is the influence area of a single gauge, and P_T is the total change in force across the pier cross-section. Table 5.4 defines the stresses. Note that because Pier 2 did not have a symmetric layout of strain gauges, "virtual" gauges were included to mirror the outlying gauges located at the far right ends of the blades. This virtual gauge, TUE2 and TDE2, had the same values as their "real" counterparts, TUE1 and TDE1.

Table 5.4: Definitions of stress designations for top section of Pier 2.

Up-station		Down-station	
Stress	Gauge(s)	Stress	Gauge(s)
σ'_{U1}	TUE1	σ'_{D1}	TDE1
σ_{U1}	TUL1, TUC1, TUR1	σ_{D1}	TDL1, TDC1, TDR1
σ_{U2}	TUL2, TUC2, TUR2	σ_{D2}	TDL2, TDC2, TDR2
σ'_{U2}	TUE2	σ'_{D2}	TDE2

Changes in moment were also calculated for each pier individually. This calculation included the contributions from the bending of the pier blades across their depths as well as from the axial forces acting on those blades. For each blade, the moment was calculated using an average curvature computed as the mean value of the curvatures resulting from the strain gradients defined for each pair of opposing gauges.

$$\bar{M}_U = \phi_U E_c I_n = \left(\frac{\varepsilon_{U1} - \varepsilon_{U2}}{d'_2}\right) E_c I_n = \left(\frac{\sigma_{U1} - \sigma_{U2}}{d'_2}\right) I_n \quad (23)$$

$$\bar{M}_D = \phi_D E_c I_n = \left(\frac{\varepsilon_{D1} - \varepsilon_{D2}}{d'_2}\right) E_c I_n = \left(\frac{\sigma_{D1} - \sigma_{D2}}{d'_2}\right) I_n \quad (24)$$

$$\bar{M}_P = \frac{1}{2}(P_U - P_D) d_s \quad (25)$$

$$\bar{M}_T = \bar{M}_U + \bar{M}_D + \bar{M}_P \quad (26)$$

The total moment, $\bar{M}_T$, includes the sum of the blade moments, plus the moments they produce about the centroid of the pier section.

As with the axial force calculation, variables subscripted with a "*U*" are located on the up-station blade, those subscripted with a "*D*" are located on the down-station blade. The value d_s is the distance between the centroids of the lines of gauges.

A summary of the maximum and minimum axial forces and moments is given below for the four pier sections: See Appendix C at the end of this report for a full description of the procedure for calculating internal forces.

Table 5.5: Summary of forces from measured field strains – Year 1.

Forces	Pier 2				Pier 4			
	Top Section		Bottom Section		Top Section		Bottom Section	
	min	max	min	Max	min	max	min	max
P_U (kips)	-22,064	5,824	-24,654	4,672	-38,123	8,535	-22,858	4,503
P_D (kips)	-30,607	4,921	-24,733	3,898	-31,044	8,223	-23,493	5,287
P_T (kips)	-52,310	10,745	-49,375	8,525	-69,102	16,637	-46,341	9,790
M_U (k-ft)	-15,944	1,342	-1,492	16,315	-5,759	24,029	-13,834	3,359
M_D(k-ft)	-13,985	1,335	-1,507	15,194	-5,520	22,192	-15,345	3,276
M_P(k-ft)	-18,407	115,302	-40,045	13,664	-79,269	10,121	-17,571	21,762
M_T(k-ft)	-17,443	89,773	-32,219	42,516	-38,142	12,509	-24,776	5,845

P_u- Axial force (kips) in up-station blade.
P_D- Axial force (kips) in down-station blade.
P_T- Total axial force (kips) acting on pier.
M_U- Bending moment (ft-kips) acting through the centroid of the up-station blade.
M_D- Bending moment (ft-kips) acting through the centroid of the down-station blade.
M_P- Bending moment (ft-kips) produced by blade axial forces about the centroid of the pier.
M_T- Total bending moment (ft-kips) acting on the pier.

Note that axial forces are negative in compression and positive in tension, and bending moments are negative if they produce relative compression on the down-station face/blade (and relative tension on the up-station blade/face), and positive if they produce relative compression on the up-station face (and relative tension on the down-station blade/face).

5.2.1 Verification of Pier Analysis

The geometries of the pier cross-sections were relatively simple, but the combination of composite and independent behavior of the sections made analysis more complicated than originally had been expected. The behavior of each blade was investigated individually. The area of each blade was approximated as the area of a rectangle, and the area moment of inertia, *I*, was approximated assuming the same. The area moment of inertia was calculated about the centerline of each pier blade cross-section. The depth of the blade was taken as an average value to account for the increased depth at the outer edges of the blades. See Figure 5.6 for further description.

$$A = b \cdot h \tag{27}$$

$$I_{rect} = \frac{bh^3}{12} \tag{28}$$

The value *h* was taken as an averaged depth of the blade section, *b* was taken as the width of the blade section at the instrumented elevation, and *y* is the distance from the centroid of the line of gauges under consideration to the centroid of the individual pier blade. Table 5.6 shows the values of *h*, *b*, *A*, and *I* calculated for each instrumented pier section. Note that the values shown below have been rounded. The depth was taken as an averaged value to include the contribution of the deeper end-sections of the blades. The area moment of inertia was taken about the centerline of the pier cross-section as a whole.

Table 5.6: Pier blade approximate cross-sectional geometries.

Section	Width, *b* (in)	Depth, *h* (in)	Area (in^2)	I (in^4)
Pier 2 Top Upst.	497.44	34.43	17,128.15	1,694,676
Pier 2 Top Dnst.	497.44	34.43	17,128.15	1,694,676
Pier 2 Bottom Upst.	393.70	34.95	13,760.62	1,341,245
Pier 2 Bottom Dnst.	393.70	34.95	13,760.62	1,341,245
Pier 4 Top Upst.	498.98	40.13	20,023.95	2,175,547
Pier 4 Top Dnst.	498.31	40.13	19,998.06	2,175,547
Pier 4 Bottom Upst.	393.70	40.85	16,085.62	1,716,543
Pier 4 Bottom Dnst.	393.70	40.85	16,085.62	1,716,543

The bending stress is defined as the change in stress across the blade cross-section. Figure 5.6 defines the locations of various important values taken from the data. Figure 5.7 shows a typical pier section stress distribution, with labeled f_1 and f_2.

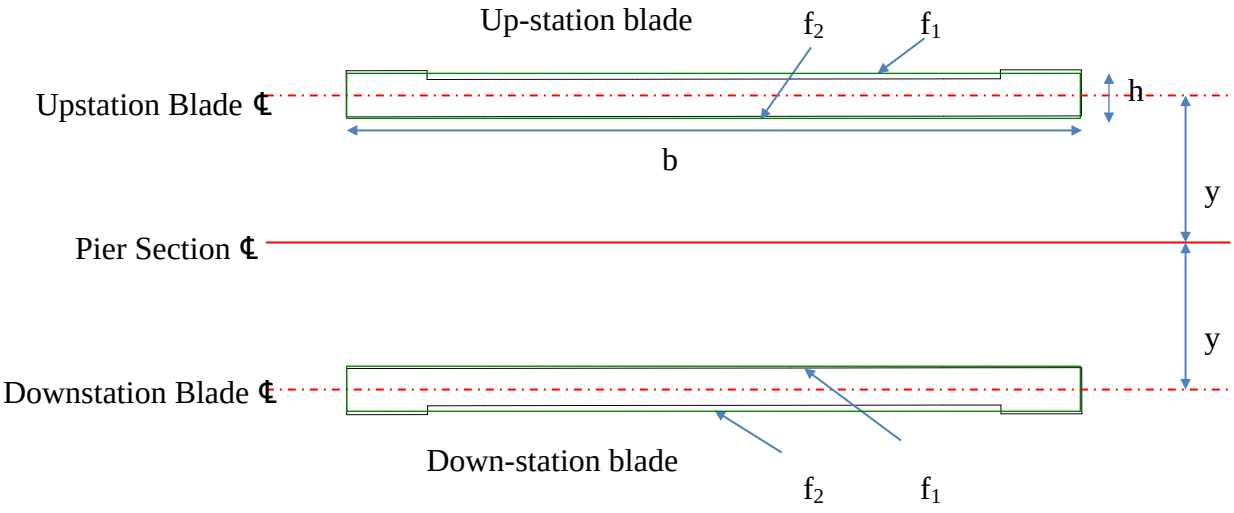

Figure 5.6: Typical pier cross-section, used for hand verification of MATLAB calculations. Green boxes denote the areas used for approximations.

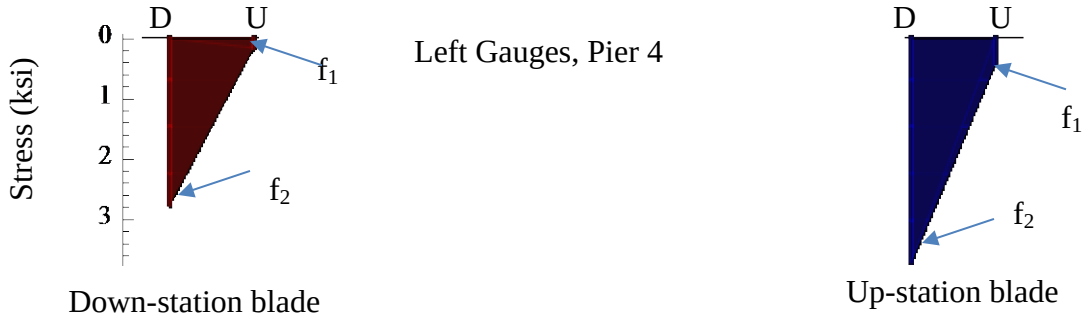

Figure 5.7: Stress distributions across pier blades, with labeled "f_1" and "f_2".

For the approximations, change in axial force was calculated as a product of the axial stress, f_a, and the area corresponding to each gauge; moment was calculated as the product of the bending stress, f_b, and the section modulus of the cross-section. The distance y from the centroid of each line of strain gauges to the centroid of the pier section was constant for each pier. For Pier 2 sections, y = 129 inches, and for Pier 4 sections, y = 126.6 inches. Figures 5.8-5.11 compare the 4 approximated data points with the actual force and moment histories as calculated using equilibrium for each instrumented pier section.

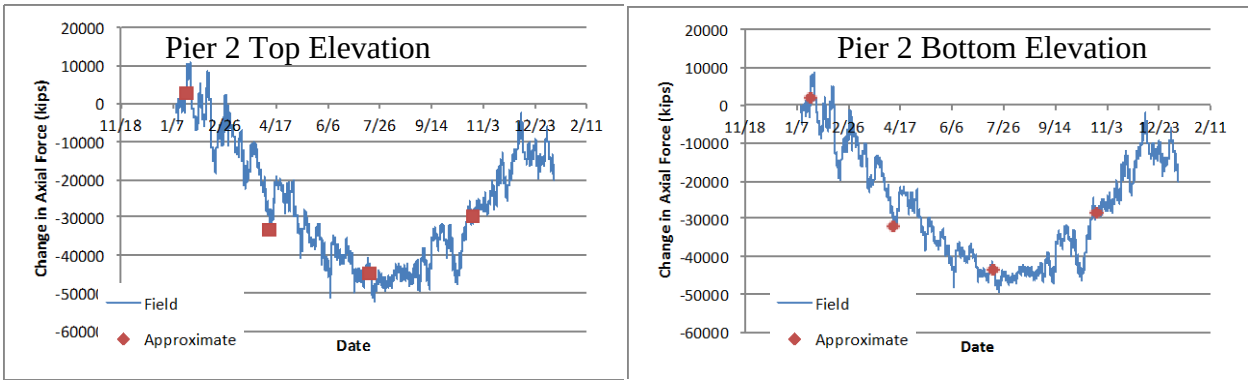

(*a*) (*b*)

Figure 5.8: Comparison of change in axial force in Pier 2 to approximate values versus time at a) Top instrument locations, b) Bottom instrument locations.

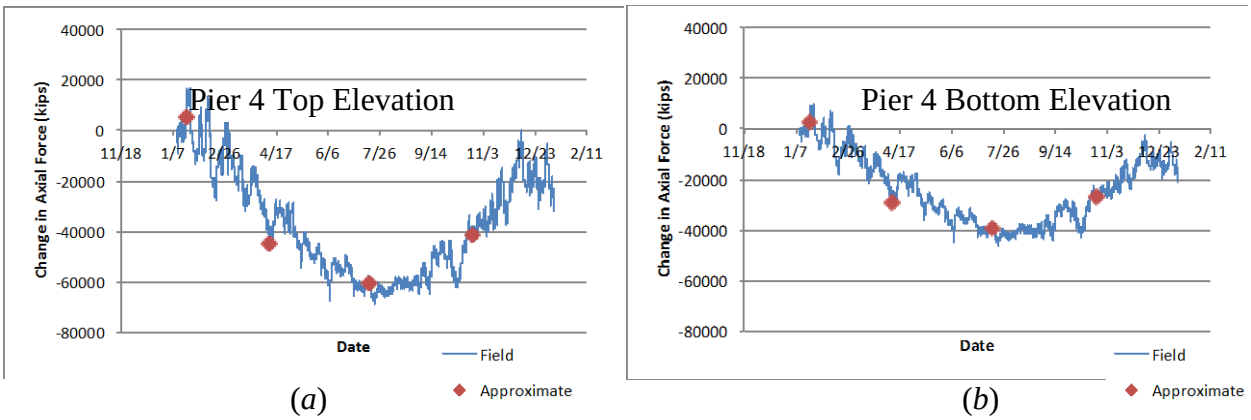

(*a*) (*b*)

Figure 5.9: Comparison of change in axial force in Pier 4 to approximate values versus time at a) Top instrument locations, b) Bottom instrument locations.

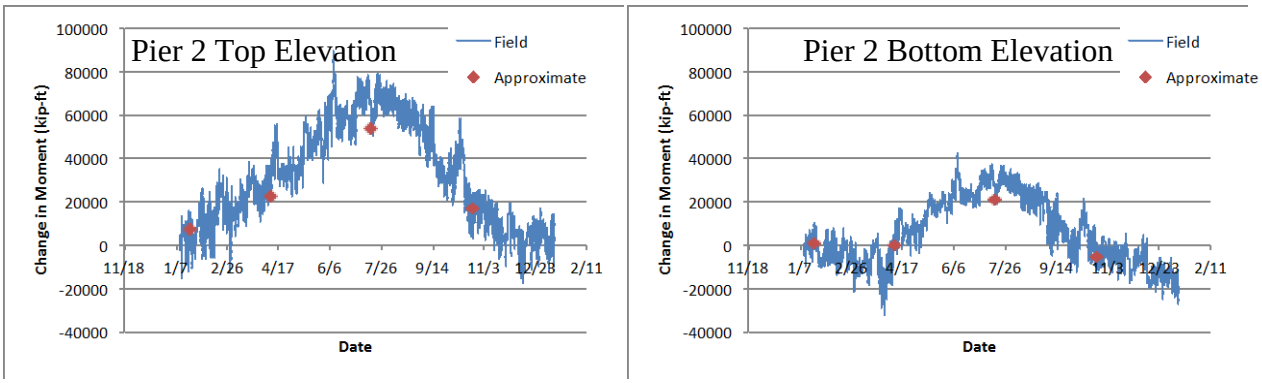

(*a*) (*b*)

Figure 5.10: Comparison of change in moment in Pier 2 to approximate values versus time at a) Top instrument locations, b) Bottom instrument locations.

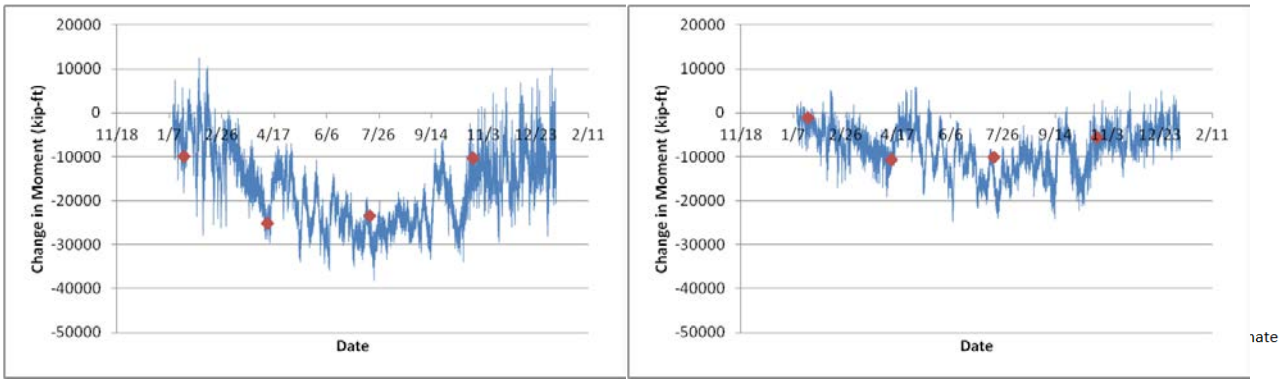

(*a*) (*b*)

Figure 5.11: Comparison of change in moment in Pier 4 to approximate values versus time at a) Top instrument locations, and b) Bottom instrument locations.

The moment values were calculated about the centroids of the pier cross-sections. As can be seen, the approximated values fell within a reasonable range of the values calculated using equilibrium; this verified the proper calculation of changes in axial force and moment in the pier

sections. This was especially true in the case of the axial force changes. This comparison with simplified calculations of axial force and moment confirmed that the detailed calculation correctly calculated both changes in axial force and changes in moment across the instrumented pier cross-sections.

Chapter 6. Comparison to Models

An analytical effort was expended in Phase I by Scheevel et. al. to develop finite element models of the Wakota Bridge in order to compare both the AASHTO LRFD temperature design Procedures A and B, as well as to investigate the accuracy of different methods of incorporating the reduction in stiffness of the piers due to cracking under service loads. As was reported in Phase I, it was concluded that the refined design method of calculating pier stiffness produced values that more accurately predicted those found using the research level model. In Phase II of the study, both the reduced stiffness method and the gross section method were used to analyze the effects of the applied temperature change recorded at the bridge. In the following sections, the changes in axial force and bending moment calculated from these models are compared to those calculated from the strain data measured in the field using the array of vibrating wire gauges.

In order to apply the temperature range recorded in the data collection, the average maximum and minimum recorded temperatures were applied to the entire bridge structure. It was not necessary to apply the recorded temperature history to the bridge model, as the focus of this study is the forces changes generated by the temperature extremes. Instead, a uniform temperature change was applied to the whole structure, as was done in Phase I in the comparison of the AASHTO LRFD temperature ranges. The average minimum temperature recorded on the bridge was 3.8 °F, and the maximum was 87.6 °F. The temperature of the first recorded data point was 14.9 °F, so this temperature was applied to the entire bridge structure. A uniform temperature increase of 72.7 °F was applied to reach the maximum temperature. Further analyses were performed using temperature changes of -11.1 °F, 20 °F, 40 °F, and 60 °F in order to investigate behavior at the minimum average temperature as well as at temperatures between the minimum and maximum values. A note is made here regarding the measured temperatures in the bridge: At any given temperature, the thermistors in the vibrating wire gauges that were embedded in two piers at two elevations each, and in two sections of the superstructure, the temperatures measured were approximately uniform. Thus, it was tacitly assumed in the analysis for temperature effects that the entire bridge had the same temperature at any given time.

The model used for comparison to the field data was the DLM3 model. This model used fixed connections at the ends of all of the pier blades. Unrestrained longitudinal movement was allowed at both abutments and at the base of Pier 1, the connections at the bases of Piers 2 and 3 were modeled using springs with stiffness approximated from analysis of the pile footings at these locations, and the base of Pier 4 was modeled as fixed to its footing. Most importantly, this model was developed to include the long-term effects of the staged construction process on the bridge structure. Both the piers and the superstructure were modeled using frame elements.

Two versions of DLM3 were used, one that approximated pier stiffness with the refined design method, and one that used the gross section method. The refined analysis model, hereafter called DLM_Ref accounted for reduction in pier stiffness due to cracking by using 4 stiffness updates along the pier blade height. Ratios for the approximate stiffness to the full stiffness were taken from the recommendations in Phase I of this project for use in a model employing 4 stiffness updates for use with either Procedure A and Procedure B. The following Table 6.1 lists the ratios recommended for each pier stiffness-updating segment for both design temperature ranges.

Table 6.1: Stiffness ratios for pier stiffness-updating segments as recommended by Scheevel et. al.

Pier Wall	Section	$EI_{Refined}/ EI_{Gross}$	E, Used in DLM_Ref (ksi)
2D	1	0.66	2379
	2	0.88	3172
	3	0.98	3532
	4	0.60	2162
2U	1	0.68	2451
	2	0.89	3208
	3	1.00	3604
	4	0.63	2271
4D	1	0.63	2271
	2	0.80	2883
	3	1.00	3604
	4	0.58	2090
4U	1	0.62	2234
	2	0.78	2811
	3	1.00	3604
	4	0.56	2018

The pier walls labeled 2D and 4D are the downstation blades, 2U and 4U are the upstation blades. Section 1 is located at the bottom of the pier blade heights, while section 4 is located at the top of the blades.

The stiffness ratios described above were recommended for use with the Procedure A design temperature range. This set of stiffness ratios was chosen because the Procedure A temperature range was closest to the internal concrete temperature range measured in the field: This is discussed fully in Section 6.1.

DLM_Gross, the model using the gross section analysis, used a constant stiffness of 0.5*EI* along the entire height of the pier blade. In order to accomplish this, the modulus of elasticity, *E*, of the pier blade sections was reduced to 0.5*E* in the material property input in SAP2000. This is not the method specified in the AASHTO LRFD, which instead applies the 0.5 factor to the thermal load. However, since the only load under consideration was the thermal load, the 0.5 factor could alternatively be applied to the modulus of elasticity. This was done because it was more efficient in the modeling process. This alternative application of the 0.5 factor effectively decreased the stiffness of the pier blade sections to one-half of their gross stiffness.

It is important to note that all data collected has been referenced to the initial value collected at the beginning of the monitoring period, which was January 10, 2012, meaning that all stresses were zeroed out initially. It was not possible to record initial readings when the gauges were first installed, nor when the concrete was poured, nor when the concrete hardened, nor when the superstructure was post-tensioned. Thus, there is no practical way to accurately measure the total internal stresses within the bridge structure when it is in place. SAP2000 models were analyzed

assuming zero initial strain, and using the change in concrete temperature as recorded by the thermistors in the bridge.

The finite element models of the Wakota Bridge that were developed in SAP2000 and reported in Phase I were originally analyzed at somewhat arbitrary temperature ranges in order to calibrate them with the RLM. To determine the appropriate number of stiffness-updating segments to use with the CRD method, the DLM were compared to the RLM at temperature ranges of 40° F, 70° F, and 100° F. In considering the use of rotational springs at the bases of the pier blades, a temperature range of 85° F was used. Finally, the two design temperature ranges of 80° F and 150° F were considered in the comparison of Procedures A and B. With the exception of the temperature ranges used to compare Procedures A and B, the ranges chosen for comparison between RLM and DLM were arbitrary. They were chosen simply to provide a wide range of values with which to calibrate the DLM to the RLM.

6.1 Temperature Consideration

In this chapter, the temperature range was obtained from the temperatures measured by the thermistors in the vibrating wire gauges. Tables 6.2-6.5 list the maximum and minimum temperatures recorded at each gauge, as well as the total temperature changes over the data collection period.

Table 6.2: Temperature ranges at Pier 2 gauge locations.

Gauge	Average Max. Temp. (°F)	Average Min. Temp. (°F)	Temperature Range (°F)
2TUL1	86.63	1.92	84.71
2TUC1	85.55	2.25	83.30
2TUR1	86.32	2.44	83.88
2TUE1	90.03	-1.19	91.22
2TUL2	86.99	1.44	85.55
2TUC2	87.24	1.90	85.34
2TUR2	87.53	3.06	84.47
2TUE2	91.81	-1.25	93.06
2TDL1	87.08	2.07	85.01
2TDC1	86.50	2.68	83.83
2TDR1	87.46	3.81	83.65
2TDE1	85.86	4.32	81.54
2TDL2	86.74	1.67	85.07
2TDC2	86.52	1.83	84.69
2TDR2	86.63	3.09	83.54
2TDE2	86.99	2.82	84.17
2BUL1	86.63	2.01	84.62
2BUR1	86.31	3.11	83.20
2BUL2	88.05	1.69	86.36
2BUR2	87.21	4.08	83.12
2BDL1	86.92	3.15	83.77
2BDC1	87.06	3.61	83.45
2BDR1	87.69	4.12	83.57
2BDL2	86.68	2.66	84.02
2BDC2	85.84	3.06	82.78
2BDR2	85.84	3.06	82.78

Table 6.3: Temperature ranges at Pier 4 gauge locations.

Gauge	Average Max. Temp. (°F)	Average Min. Temp. (°F)	Temperature Range (°F)
2TUL1	86.67	2.19	84.47
2TUR1	86.86	2.52	84.35
2TUL2	86.50	2.19	84.31
2TUR2	86.95	3.54	83.41
2TDL1	87.71	4.64	83.07
2TDR1	87.39	5.88	81.50
2TDL2	86.59	2.48	84.11
2TDR2	86.41	3.58	82.84
2BUL1	86.02	1.54	84.47
2BUR1	85.50	3.72	81.77
2BUL2	86.04	2.34	83.70
2BUR2	85.96	4.59	81.38
2BDL1	86.04	4.41	81.63
2BDR1	86.04	4.41	81.63
2BDL2	85.57	3.34	82.22
2BDR2	85.57	3.34	82.22

Table 6.4: Temperature ranges at Span 3 gauge locations.

Gauge	Average Max. Temp. (°F)	Average Min. Temp. (°F)	Temperature Range (°F)
3T-LM	103.57	-1.53	105.10
3T-RM	104.72	-2.29	107.01
3T-R	106.09	-2.45	108.54
3B-L	86.92	3.79	83.12
3B-LM	87.28	4.62	82.66
3B-RM	87.06	4.46	82.60
3B-R	87.66	4.62	83.03
3L-U	87.67	2.79	84.89
3L-UM	88.23	2.35	85.88
3L-BM	87.30	1.65	85.64
3L-B	88.05	1.99	86.06
3M-U	87.75	6.93	80.82
3M-UM	87.40	7.88	79.52
3M-BM	87.17	7.16	80.01
3M-B	86.68	6.67	80.01
3R-U	88.99	4.03	84.96
3R-UM	88.99	4.77	84.22
3R-BM	89.13	4.46	84.67
3R-B	89.10	5.09	84.01

Table 6.5: Temperature ranges at Span 4 gauge locations.

Gauge	Average Max. Temp. (°F)	Average Min. Temp. (°F)	Temperature Range (°F)
4T-L	95.94	1.00	94.94
4T-LM	95.59	2.00	93.59
4T-RM	99.23	0.79	98.44
4T-R	98.82	0.86	97.96
4B-L	87.98	5.00	82.98
4B-LM	87.67	6.00	81.67
4B-RM	87.67	5.99	81.68
4B-R	88.41	5.83	82.58
4L-U	87.96	5.31	82.66
4L-UM	88.18	5.38	82.80
4L-BM	88.43	5.31	83.12
4L-B	87.89	4.46	83.43
4M-U	88.61	7.43	81.18
4M-UM	88.07	8.80	79.27
4M-BM	86.79	7.77	79.02
4M-B	87.04	7.74	79.31
4R-U	88.79	6.30	82.49
4R-UM	88.70	7.03	81.67
4R-BM	88.79	7.93	80.86
4R-B	88.65	7.14	81.50

With the exception of the gauges located in the top flanges of Spans 3 and 4, the thermistors recorded temperature ranges over the data collection period that were uniform to within 6° F. The largest changes in temperature were correspondingly measured at the top flanges of the Span sections. These gauges would be surrounded by the least amount of concrete, and would receive direct sunlight during the day. The combination of little insulation by surrounding concrete and high incidence of solar rays caused the higher temperature ranges.

The recorded maximum and minimum temperatures were averaged across areas of the six different instrumented sections. The average ranges are summarized in Table 6.6.

Table 6.6: Average temperature ranges across instrumented cross-sections.

Section	Average Max. Temp. (°F)	Average Min. Temp. (°F)	Temperature Range (°F)
Span 3	89.7	4.0	85.7
Span 4	89.4	6.4	83.0
Top Pier 2	87.0	2.4	84.5
Bottom Pier 2	86.7	3.0	83.7
Top Pier 4	86.9	3.4	83.5
Bottom Pier 4	85.8	3.4	82.4
TOTAL AVERAGE	87.6	3.8	83.8

The temperature ranges in Table 6.6 were calculated as the differences between the maximum and minimum average temperatures calculated from the temperature values recorded at each gauge across the section in question. Note that these ranges were averaged across entire pier and

superstructure sections. As can be seen, the ranges did not vary significantly across the bridge structure; a maximum difference of 3.3 °F was seen between the highest average range, in Span 3, and the lowest average range, seen at the bottom of Pier 2. This corresponded to a maximum percentage difference of only 3.8%, which was considered small enough to allow for the use of a single average temperature range for the entire bridge structure.

AASHTO LRFD and the MnDOT BDM call for analysis based on uniform temperature change. Because analysis with respect to the *total change* in temperature was desired, rather than with respect to incremental changes over time, it was not necessary to apply the full temperature history to the finite element models. As highlighted in the bottom row of Table 6.6, the final average temperature range was 83.8 °F.

The ambient air temperature varied from the temperature of the concrete by a significant amount. The National Weather Service and the National Oceanic and Atmospheric Association provides archived information on the climate of St. Paul, which was used to determine maximum and minimum daily temperatures near the bridge [19] While this data was not taken directly from the bridge location, but rather was recorded in St. Paul at the St. Paul Downtown Airport-Holman Field, it was the closest location to the bridge that had recorded temperature information. The airport is located approximately 5 miles northwest of the bridge.

Two different air temperature ranges were calculated: The first included only the maximum daily temperatures, while the second included the minimum daily temperatures, creating an envelope of temperatures. Figure 6.1 compares the daily maximum and minimum air temperature with the recorded concrete temperatures.

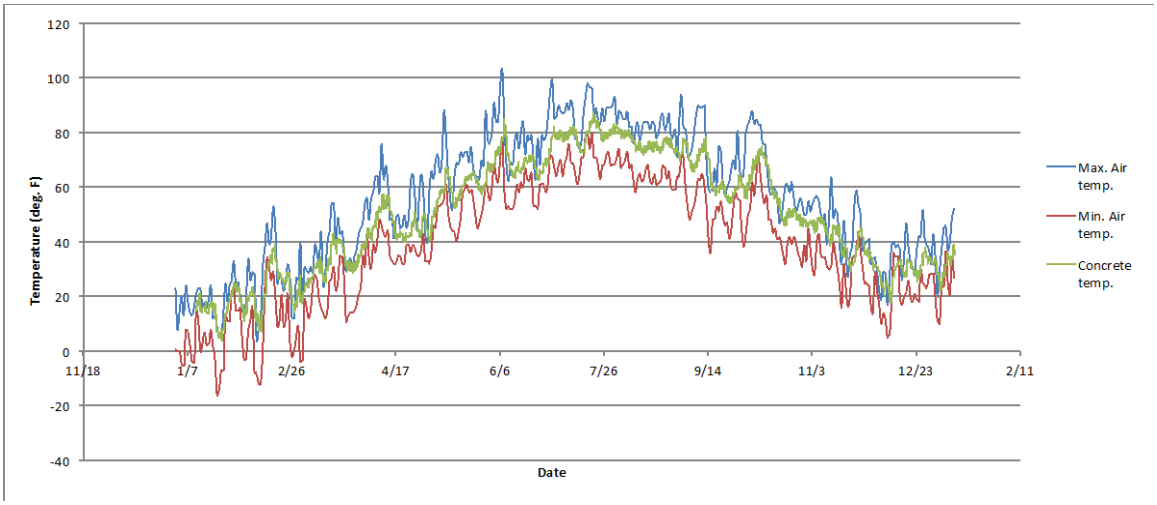

Figure 6.1: Average recorded concrete temperature range compared with daily maximum and minimum air temperature ranges.

The maximum daily air temperature seen during the data collection period was 103.0 °F, while the minimum temperature was -16 °F, resulting in an average temperature range of 119 °F, which was a much larger range than that seen within the concrete of the bridge. Because the gauges within the bridge were nearly all well insulated by concrete cover, analysis was conducted using the internal concrete temperature ranges rather than the ambient air temperature

ranges. For this reason, the stiffness ratios recommended by Scheevel et. al. for use with the Procedure A design temperature range were used in DLM_Ref.

6.2 Global Behavior

In order to compare the two design temperature ranges allowed by AASHTO LRFD, a simple calculation of the overall expected change in length of the bridge superstructure was performed using both temperature ranges. Two linear string potentiometers were installed at the bridge, one on each abutment face, to record expansion and contraction of the bridge superstructure. The west abutment potentiometer recorded a total length change between the face of the abutment and the bridge deck of 6.2 in., while the east abutment had a 5.2 in. distance change; the total length change over the data collection period was 11.4 in.

The coefficient of thermal expansion for the concrete in the bridge superstructure was taken to be 6×10^{-6} / °F. Multiplying this coefficient by the temperature range and the original length of the bridge results in the expected change in length of the bridge with respect to temperature. The total length of the Wakota Bridge superstructure is 1,889 ft, or 22,668 inches. Thus, the equation used to calculate change in length with respect to change in temperature in °F is

$$\Delta L = (6 \times 10^{-6}) \cdot \Delta T \cdot L_o = (6 \times 10^{-6}) \cdot \Delta T \cdot 22{,}668 \text{ (psi)}, \quad (29)$$

The AASHTO LRFD Procedure A temperature range of 80 °F would produce an overall longitudinal change in length of 10.9 inches, while the Procedure B range of 150 °F would produce a change in length of 20.4 inches. It is clear that Procedure A produced a much more reasonable predicted change in length when compared to the field measurement of 11.4 inches over the year-long data collection period than the Procedure B temperature range.

The internal average concrete temperature range of 83.8 °F resulted in a total calculated change of length of 11.4 inches, which was comparable to the change in length seen in the data collected from the linear string potentiometers at the abutments of the bridge. The average air temperature range of 119.0 °F resulted in a total calculated change of length of 16.2 inches. This simple calculation reaffirms that the correct temperature range with which to compare the models is the internal concrete temperature range, rather than the air temperature range over the data collection period. The accuracy of the theoretically calculated value when compared to the field data collected also shows that the value of thermal expansion coefficient that was calculated in a previous task is also an appropriate approximation to be using. This comparison also verifies the assumption used in the finite element models of fully unrestrained longitudinal movement at the abutments.

Figures 6.2*a* and *b* show the predicted displacements at each abutment over time superimposed on the displacement history as measured in the field.

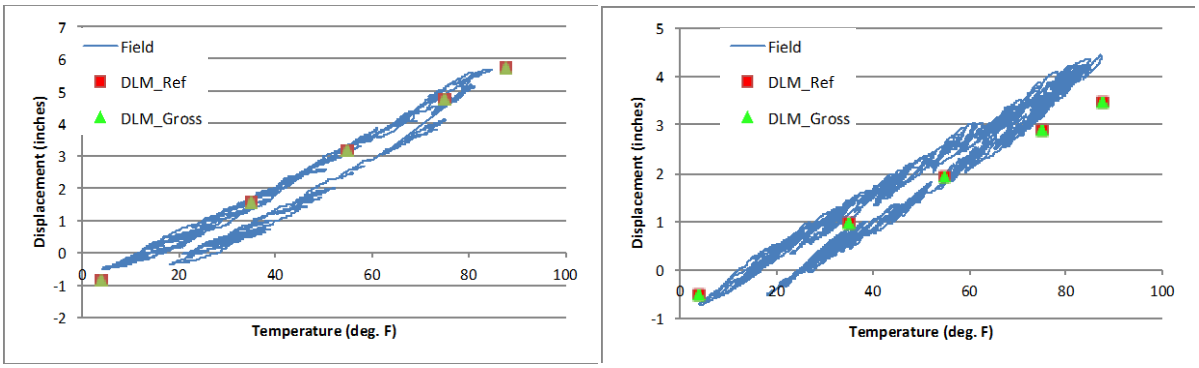

(*a*) (*b*)

Figure 6.2: Measured change in superstructure length over time compared to predicted changes in superstructure length for *a*) West abutment and *b*) East abutment.

As can be seen, both DLM_Ref and DLM_Gross very accurately predict the magnitude of the displacement at the west abutment of the bridge. The predicted displacement of the east abutment was underestimated by both DLM_Ref and DLM_Gross. Table 6.7 provides a summary of the finite element predicted displacements compared with the displacements measured in the field.

Table 6.7: Comparison of predicted abutment displacements to measured displacements.

	Measured Displacement (inches)	DLM_Ref (inches)	% Difference from Field Values	DLM_Gross (inches)	% Difference from Field Values
West Abutment	6.21	6.58	6.08	6.57	5.95
East Abutment	5.17	3.46	-32.94	3.46	-33.03

Both DLM_Ref and DLM_Gross predicted very similar displacements at the abutments. The total change in superstructure length predicted by DLM_Ref was 10.04 inches, while DLM_Gross predicted a change in length of 10.03 inches. These values were 11.9% lower than the 11.4 inch change measured in the field. Overall, it appears that Procedure A design temperature range is better suited to predict changes in superstructure length with temperature.

There is some shift in the displacements over time; this is seen clearly in Figures 6.2 *a* and *b*. This shift was also seen in the changes in axial force and moment at all instrumented locations; this was expected given its presence in the strain data. Smaller changes in displacement corresponded with higher temperature changes as the temperatures fell through the autumn season. The mechanism responsible for this trend was not investigated; some possible causes of this hysteresis include creep effects, although these were shown in Section 4.4.3 to be very small, or friction between the bearings at the abutments and the superstructure resulting in some amount of longitudinal restraint of the superstructure. No reliable explanation was determined for the hysteresis; it is unknown whether this trend will continue.

6.3 Comparison of Field Superstructure Behavior to Predicted Behavior

The SAP2000 models were used to calculate changes in force and moment to compare with the measured axial force and moment histories. Figures 6.3 and 6.4 show the changes in axial force and moment in the superstructure with respect to temperature. These plots include the five data points calculated using the SAP2000 models, with the results for the DLM_Ref and DLM_Gross models shown separately. The gauges were assumed to be located at the mid-depths of the box-girder elements. These locations were at 658'-4" and 1434'-10" from the west abutment of the bridge for Span 3 and Span 4 respectively.

SAP2000 offers an add-on Bridge Modeler option that was used in the analysis of the finite element models. This add-on provided information about the stresses, axial forces, and moments across the superstructure cross-sections, rather than only the reactions at either end of each frame element. Since the gauges in the superstructure sections were distributed across the cross-sections, this option was necessary in order to be able to compare corresponding values.

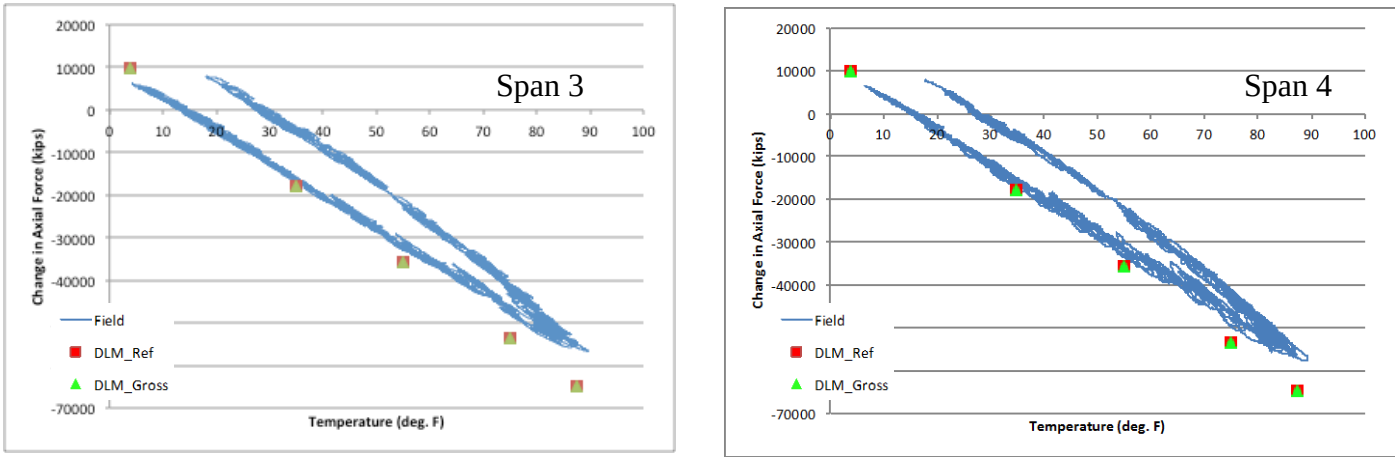

(a) (b)

Figure 6.3: Total change in axial force versus temperature in superstructure, including data points from DLM_Ref and DLM_Gross, for a) Span 3 and b) Span 4.

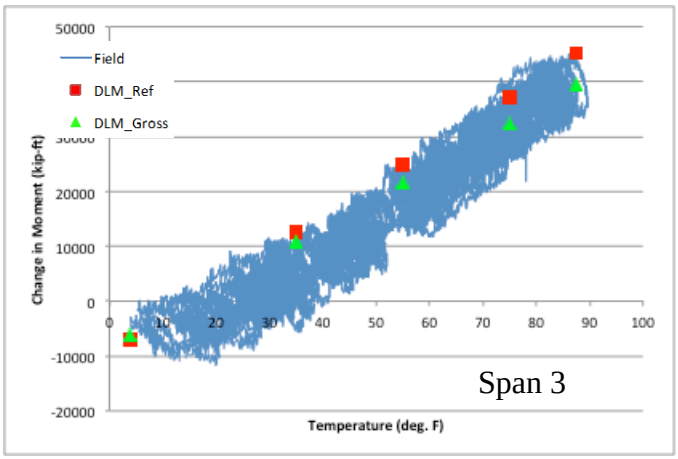

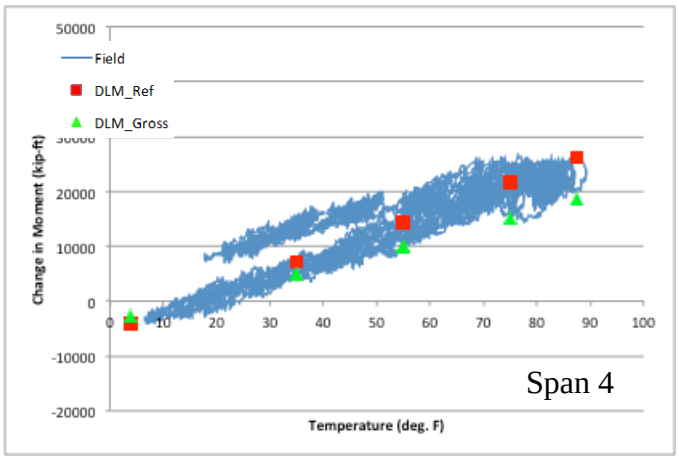

(*a*) (*b*)

Figure 6.4: Total change in moment versus temperature in superstructure, including data points from DLM_Ref and DLM_Gross, for a) Span 3 and b) Span 4.

The maximum compressive forces calculated by the two SAP2000 models were nearly identical. However, both the DLM_Ref and the DLM_Gross models produced axial force values that were more compressive than the measured axial force versus temperature history. This result suggests that the real bridge piers did not provide as much longitudinal restraint as did the modeled bridge piers; i.e. the actual piers were less stiff than they were modeled to be. Table 6.8 provides a summary of the comparison between the models and the collected data.

Table 6.7: Summary of comparison of predicted changes in axial force and field data in superstructure.

	Data	Maximum Axial Force Change (kips)	Minimum Axial Force Change (kips)	% Difference from Field Values
Span 3	Field	-56,733	7,380.	--
	DLM_Ref	-65,059	9,934	14.7
	DLM_Gross	-64,955	9,931	14.5
Span 4	Field	-57,790	7,884	--
	DLM_Ref	-65,080	9,937	12.6
	DLM_Gross	-64,968	9,933	12.4

The SAP2000 models both produced conservatively high changes in compressive force with temperature. However, the magnitude of the change is reasonable given the uncertainty in many of the modeling parameters.

Both models produced accurate values for the change in moment with temperature. In comparing Figures 6.*4a* and 6.4*b* it can be seen that both sets of computer model results fall within the measured moment history corresponding to temperature. At Span 3 the DLM_Gross values were near the lower bound of the actual moment history, while at Span 4 the DLM_Ref values bounded the history on the higher side. Table 6.2 provides a summary of the comparison between the models and the collected data. Note that although both models produced data that

fell within the actual moment history, DLM_Ref more accurately calculated the maximum change in moment due to temperature change for both span sections.

Table 6.8: Summary of comparison of predicted changes in moment and field data in superstructure.

	Data	Maximum Moment Change (kip-ft)	Minimum Moment Change (kip-ft)	% Difference from Field Values
Span 3	Field	45,769	-11,722	--
	DLM_Ref	45,283	-6,914	1.1
	DLM_Gross	39,387	-6,022	13.9
Span 4	Field	26,881	4,248	--
	DLM_Ref	26,322	-3,449	2.1
	DLM_Gross	18,406	-2,814	31.5

The summaries provided in Tables 6.8 and 6.9 verify the previously determined acceptability of both models for use in design. This comparison also confirms that DLM_Gross would be best used as a preliminary model, while the DLM_Ref could be used to provide more accurate information regarding maximum and minimum changes in force or moment along the superstructure.

6.4 Comparison of Field Pier Behavior to Predicted Behavior

After it was determined that both the DLM_Ref and DLM_Gross models were able to calculate acceptable values for the axial force and moment changes in the bridge superstructure, the ability of the models to analyze the behavior of the pier blades was investigated. The gauges in Piers 2 and 4 were located at distances of 519.75 ft, 543.9 ft, 986.0 ft, and 1010.2 ft from the west abutment of the bridge, where the down-station blade of Pier 2 was the gauge line located at 519.75 ft. The values shown here are the moments resulting from the combination of (1) the moments due to the bending of the pier blades and (2) the moment from the compressive axial forces on the pier blades and their eccentricity from the center axis of bending of the pier cross-section. Figures 6.5 and 6.6 show the changes in moment with respect to temperature of the four pier cross-sections.

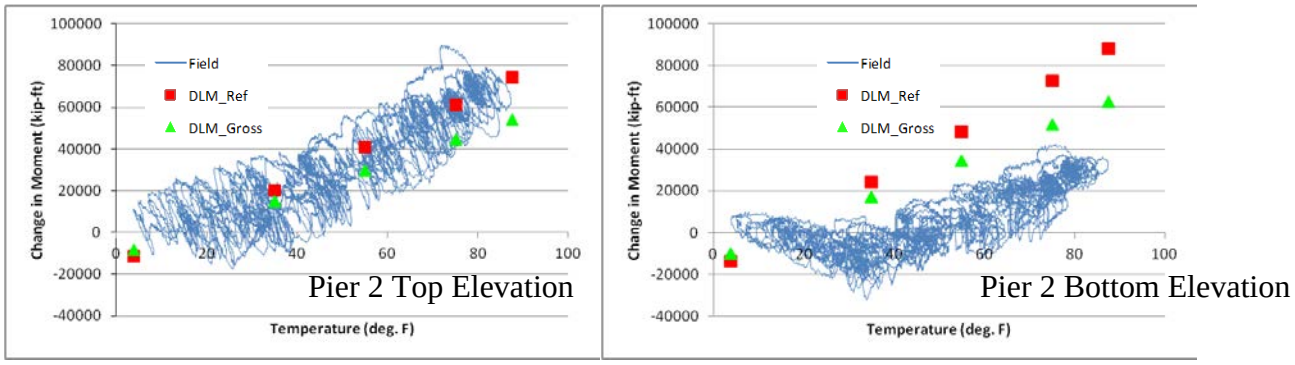

(*a*) (*b*)

Figure 6.5: Change in moment versus temperature for *a*) Top of Pier 2 and *b*) Bottom of Pier 2.

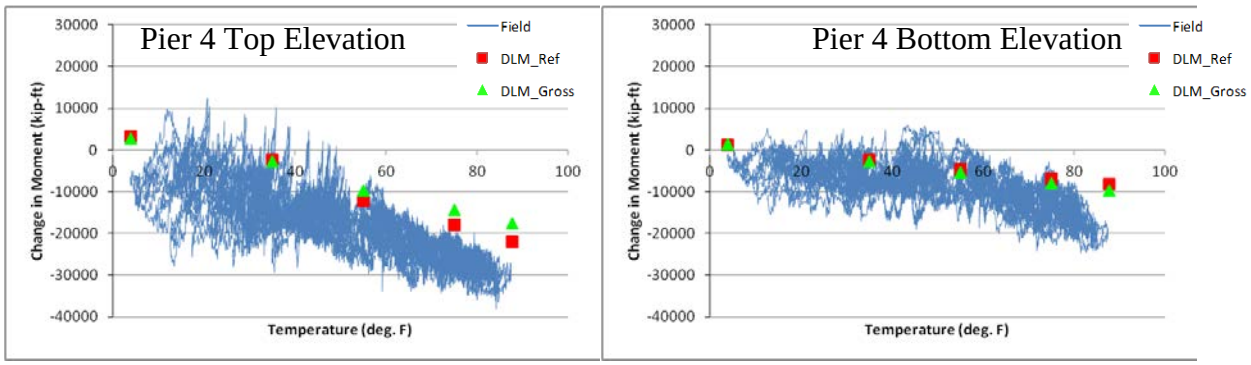

(*a*) (*b*)

Figure 6.6: Change in moment versus temperature for *a*) Top of Pier 4 and *b*) Bottom of Pier 4.

The DLM_Ref predicts the moment changes at the top of Pier 2 very well: The values predicted by this model, shown as red squares, fall within the blue temperature history for this location. The magnitudes of the moments are underestimated by between 30% to 50% in the top and bottom instrumented locations in Pier 4 respectively, while at the bottom of Pier 2, for which the values have the highest uncertainty given the approximations of fixity between pier base and footing in both models, the moment changes are underestimated by approximately 60% for DLM_Ref, and approximately 50% for DLM_Gross.

A summary of the maximum and minimum changes in axial force and moment was presented in Section 5.2; these values are compared here with those resulting from analysis of the DLM_Ref and DLM_Gross finite element models. Note that the values reported in Table 6.10, and the following Tables 6.11-6.14 report the change in moment over the full temperature range of 83.8 °F, from the change in moment due to the smallest negative temperature change to those due to the largest positive temperature change. It may have been appropriate to compare the predicted values to median values from the field data, since the plots of change in moment versus temperature are very "noisy", as seen in Figures 6.5 and 6.6. Considering the median would have reduced this "noise", and would have resulted in a lower range in the change in moment values with temperature. However, a relevant comparison is made between the maximum and minimum values recorded in the field and those predicted by the finite element models.

Table 6.9: Comparison of total changes in moment across pier cross-sections.

	Data	Total Moment Change (kip-ft)	% Difference: Maximum Absolute Values
Pier 2 Top	Actual	107,216	--
	DLM_Ref	85,683	-20%
	DLM_Gross	62,469	-42%
Pier 2 Bottom	Actual	74,735	--
	DLM_Ref	101,735	36%
	DLM_Gross	72,577	-3%
Pier 4 Top	Actual	50,651	--
	DLM_Ref	25,142	-50%
	DLM_Gross	20,129	-60%
Pier 4 Bottom	Actual	30,649	--
	DLM_Ref	9,434	-69%
	DLM_Gross	11,212	-63%

Both DLM_Ref and DLM_Gross predicted similar trends in the changes in moment in the piers. Both predicted larger moment changes in the Pier 2 instrumented sections than in Pier 4, as well as larger moment changes in the top section of Pier 4 than in the bottom section. However, the values predicted by both DLM_Ref and DLM_Gross tended to underestimate the total changes in moment across the field-measured temperature range; there was only one exception to this, DLM_Ref overestimated the change in moment at the bottom of the Pier 2 blades. (Table 6.10).

6.4.1 Calibration of DLM_Ref and DLM_Gross

Some possible reasons for the inconsistencies between the measured changes in moment in the Wakota Bridge piers and those predicted by the two DLM include the fixity between the pier bases and their footings, and inaccurate approximations of the pier section stiffnesses in both DLM_Ref and DLM_Gross. These possibilities were explored in calibration of the models to the field data. Certain of these calibration options were available for implementation in both DLM_Ref and in DLM_Gross, while some were specific to DLM_Ref only due to its more flexible pier stiffness options. Nearly all of the calibration methods investigated resulted in better correlation between the trends of the predicted changes in moment and the field data for Pier 4.

6.4.1.1 DLM_Ref Modifications

The fixity of the bases of Piers 2 and 3 to their footings were varied in order to see the effect that this would have on the overall change in moment in Pier 2. The uncertainties in these support conditions were larger than in any of the other DLM parameters considered. Assumptions had to be made regarding the soil properties and pile behavior in order to define the rotational and vertical stiffness of the springs used to represent the fixity of the pier bases to the footings in the DLM, but these assumptions were not fully verified because there was no information with which to verify them. This was a natural first choice for parameter modification for the purpose of calibrating the models to the field data.

It was not expected that this would have a large effect on the results from Pier 4, since that pier already had a base that was fixed to its footing. With pier bases fully fixed, preventing both translation and rotation of the icebreaker at the footing, the changes in moment in Pier 2 increased. When pinned connections were used, allowing rotation about the horizontal axis perpendicular to the bridge, the changes in moment were significantly decreased in Pier 2. The effect on Pier 4 was expectedly small.

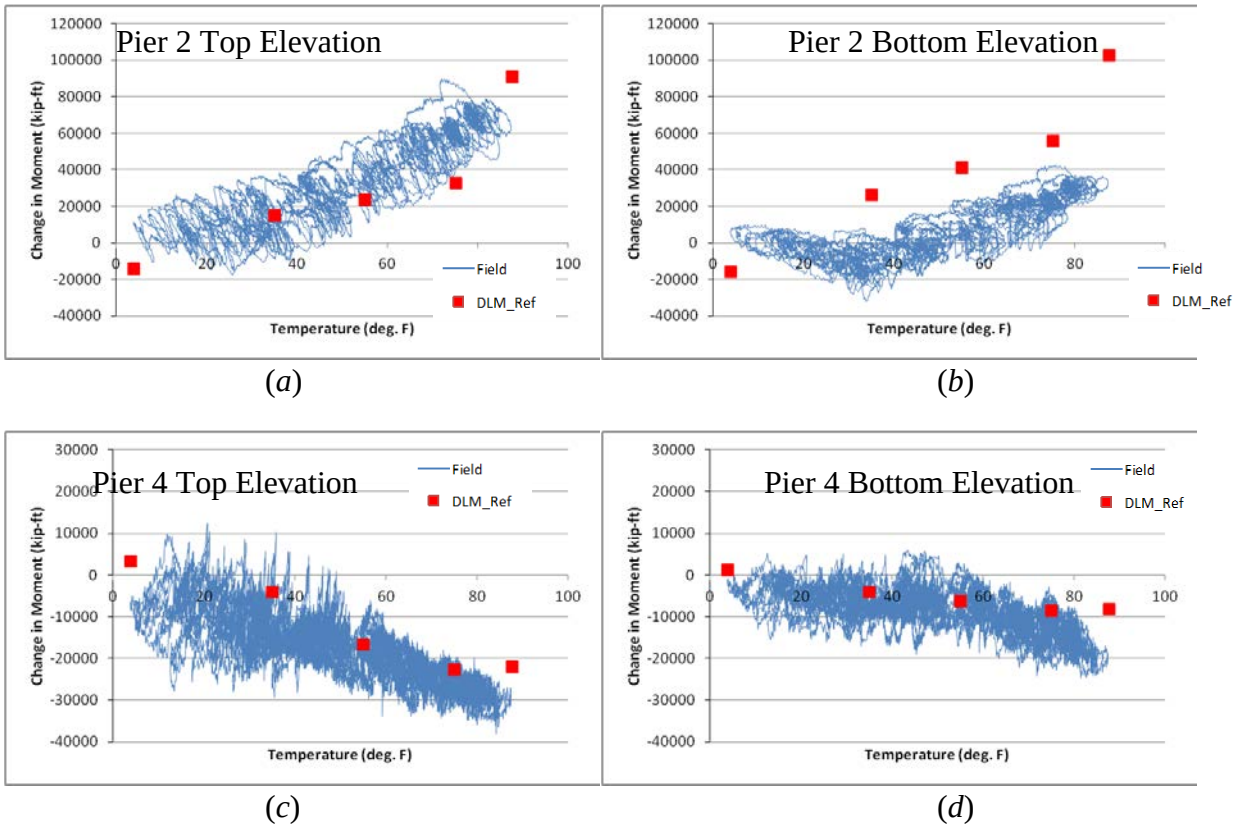

Figure 6.7: Change in moment versus temperature, compared to fixed-connection DLM_Ref for *a*) Top of Pier 2; *b*) Bottom of Pier 2; *c*) Top of Pier 4; and *d*) Bottom of Pier 4.

Table 6.10: Effects of using fixed connections between pier bases and footings in DLM_Ref.

	Data	Total Moment Change (kip-ft)	% Difference from Field: Total Values	% Difference from DLM_Ref Original: Total Values
Pier 2 Top	Field	107,216	--	--
	DLM_Ref (original)	85,683	--	--
	DLM_Ref (modified)	105,151	1.93%	23%
Pier 2 Bottom	Field	74,735	--	--
	DLM_Ref (original)	101,735	--	--
	DLM_Ref (modified)	118,709	-58.84%	17%
Pier 4 Top	Field	50,651	--	--
	DLM_Ref (original)	25,142	--	--
	DLM_Ref (modified)	25,119	50.41%	0%
Pier 4 Bottom	Field	30,649	--	--
	DLM_Ref (original)	9,434	--	--
	DLM_Ref (modified)	9,414	69.28%	0%

Using fully fixed connection between the Piers 2 and 3 bases and footings brought the predicted changes in moment at the bottom of Pier 2 closer to the trend line of the field data, though the maximum predicted change in moment at this location was still a factor of 2 larger than the maximum recorded in the field. The changes in moment in Pier 4 were not affected to a significant degree.

The following plots and Table 6.12 refer to the model DLM_Ref using pinned connections between the pier bases and the footings.

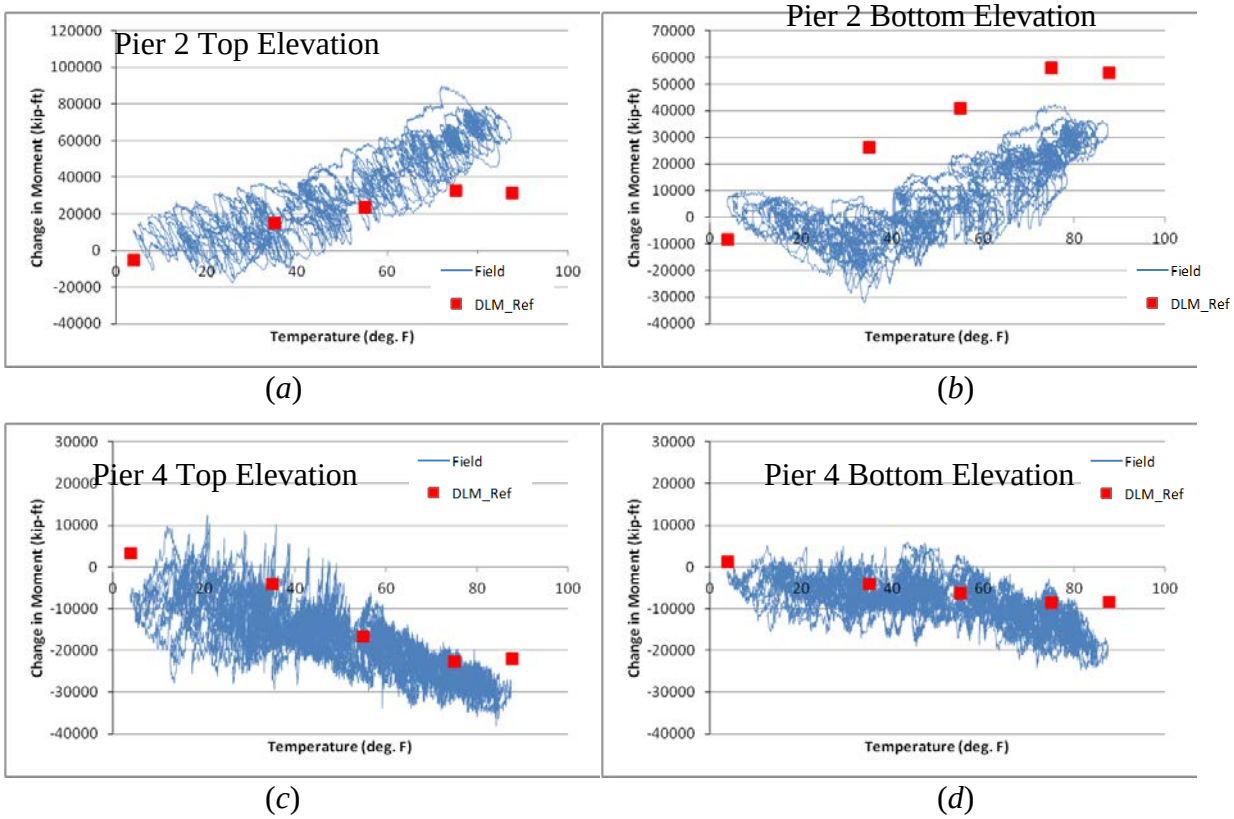

Figure 6.8: Change in moment versus temperature, compared to fixed-connection DLM_Ref for *a*) Top of Pier 2; *b*) Bottom of Pier 2; *c*) Top of Pier 4; and *d*) Bottom of Pier 4.

Table 6.11: Effects of using pinned connections between pier bases and footings in DLM_Ref.

	Data	Total Moment Change (kip-ft)	% Difference from Field: Total Values	% Difference from DLM_Ref Original: Total Values
Pier 2 Top	Field	107,216	--	--
	DLM_Ref (original)	85,683	--	--
	DLM_Ref (modified)	36,558	65.90%	-57%
Pier 2 Bottom	Field	74,735	--	--
	DLM_Ref (original)	101,735	--	--
	DLM_Ref (modified)	62,789	15.98%	-38%
Pier 4 Top	Field	50,651	--	--
	DLM_Ref (original)	25,142	--	--
	DLM_Ref (modified)	25,231	50.19%	0%
Pier 4 Bottom	Field	30,649	--	--
	DLM_Ref (original)	9,434	--	--
	DLM_Ref (modified)	9,503	68.99%	1%

For all cases considered, the changes in moment predicted by both DLM_Gross and DLM_Ref were overestimated at the bottom of Pier 2, and underestimated at all other instrumented pier locations. Another possibility was that the stiffness ratio at these locations was correspondingly over- or under-estimated by the SAP2000 models. Because the refined design method allows for more flexibility in the stiffness distribution along the height of the pier blades than does the gross section method, this calibration investigated increasing the stiffness of only parts of the pier blades. The top-most and bottom-most stiffness-updating sections of Pier 4 were both modified by increasing their stiffness ratios to 0.75*EI*, while in Pier 2, the top-most section was increased to 0.75*EI* and the bottom-most segment was decreased to 0.5*EI* to investigate whether or not the bottom section of Pier 2 would respond to this different variation of blade stiffness.

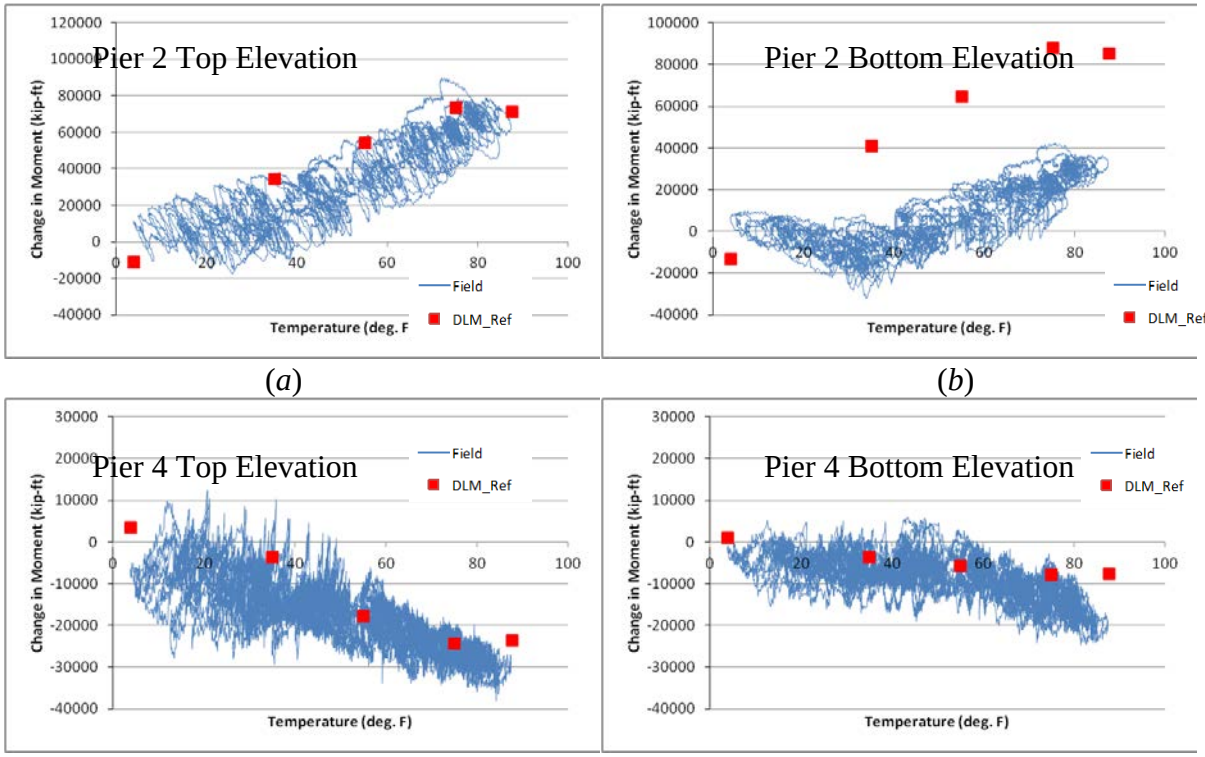

Figure 6.9: Change in moment versus temperature, compared to DLM_Ref with modified blade segment stiffness coefficients for *a*) Top of Pier 2; *b*) Bottom of Pier 2; *c*) Top of Pier 4; and *d*) Bottom of Pier 4.

Table 6.12: Effects of changing stiffness ratios in top and bottom stiffness-updating segments in Pier 2 and 4 in DLM_Ref.

	Data	Total Moment Change (kip-ft)	% Difference from Field: Total Values	% Difference from DLM_Ref Original: Total Values
Pier 2 Top	Field	107,216	--	--
	DLM_Ref (original)	85,683	--	--
	DLM_Ref (modified)	82,473	23.08%	-4%
Pier 2 Bottom	Field	74,735	--	--
	DLM_Ref (original)	101,735	--	--
	DLM_Ref (modified)	98,344	-31.59%	-3%
Pier 4 Top	Field	50,651	--	--
	DLM_Ref (original)	25,142	--	--
	DLM_Ref (modified)	27,162	46.37%	8%
Pier 4 Bottom	Field	30,649	--	--
	DLM_Ref (original)	9,434	--	--
	DLM_Ref (modified)	8,662	71.74%	-8%

Modifying the pier stiffness segments in this way actually decreased the maximum total changes in moment in both Pier 2 and Pier 4. However, the general trend of the predicted values aligned well with the median values of the change in moment versus temperature for all locations except the bottom of Pier 2. Further investigation into the effects of modifying the pier stiffnesses was done in DLM_Gross, as described in Section 6.4.1.2. This calibration method resulted in the best correlation between the moment change versus temperature predictions from the finite element model and the field data. The change due to the maximum temperature range was underpredicted in both instrumented locations in Pier 4, but the general trend of the predicted values matched very well with that seen in the field. The top of Pier 2 had the best correlation between predicted and field values, while the bottom of Pier 2 again had the least correlation.

6.4.1.2 DLM_Gross Modifications

Increasing the overall stiffness of the piers in DLM_Gross had a noticeable impact on the changes in moment predicted. Increasing the stiffness from 0.5*EI* to 0.75*EI* increased the changes in moment in both Pier 2 elevations by approximately 18% from the original predicted values at each elevation, but again decreased the change in moment predicted at the base of Pier 4.

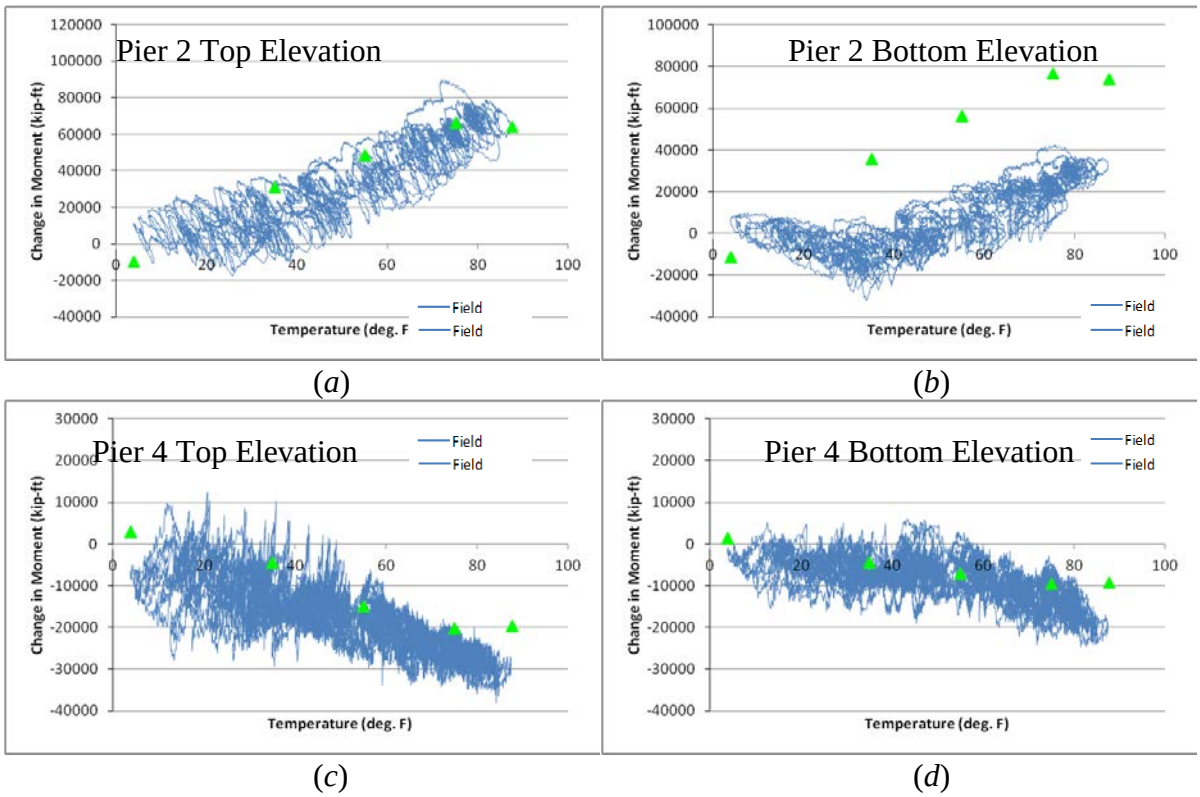

Figure 6.10: Change in moment versus temperature, compared to DLM_Gross with increased overall pier stiffness for *a*) Top of Pier 2; *b*) Bottom of Pier 2; *c*) Top of Pier 4; and *d*) Bottom of Pier 4.

Table 6.13: Effects of increasing overall stiffness of Piers 2 and 4 in DLM_Gross.

	Data	Total Moment Change (kip-ft)	% Difference from Field: Total Values	% Difference from DLM_Gross Original: Total Values
Pier 2 Top	Field	107,216	--	--
	DLM_Gross (original)	62,469	--	--
	DLM_Gross (modified)	74,035	30.95%	19%
Pier 2 Bottom	Field	74,735	--	--
	DLM_Gross (original)	72,577	--	--
	DLM_Gross (modified)	85,617	-14.56%	18%
Pier 4 Top	Field	50,651	--	--
	DLM_Gross (original)	20,129	--	--
	DLM_Gross (modified)	22,592	55.40%	12%
Pier 4 Bottom	Field	30,649	--	--
	DLM_Gross (original)	11,212	--	--
	DLM_Gross (modified)	10,628	65.33%	-5%

As with the pier base modification described in Section 6.4.1.1, modification of the pier stiffness had much greater effect on Pier 2 changes in moment than on the changes in moment at Pier 4.

However, increasing the overall stiffness of Pier 4 in DLM_Gross did increase the change in moment at the top of this pier more than did the changes to pier base to footing connections at Piers 2 and 3.

6.4.2 Model Appropriateness

While further study is necessary to fully calibrate the SAP2000 model to the axial forces and moments measured from the bridge, some conclusions can be made as to the decision of which model is more appropriate for design purposes.

When the temperature range measured at the bridge was applied to the two different models, analysis of DLM_Gross resulted in values that were satisfactory in predicting the bridge superstructure behavior, but it underestimated the total change in moment with temperature at the pier cross-sections. This underestimation was especially large in Pier 4. Analysis of DLM_Ref also produced satisfactory predictions for superstructure behavior, which were even closer to the field data than those from the DLM_Gross analysis, but it also underestimated the total changes in moment in the pier sections. DLM_Ref more closely predicted the total changes in moment at the top of Pier 2, but both models predicted changes in moment at the bottom of the Pier 2 blades that were inconsistent with the field data. One possible reason for this disparity that was investigated was uncertainty in the fixity of the connections of the pier bases to the footings at Piers 2 and 3. Another possibility is that the blades at this elevation have undergone more cracking than predicted, resulting in lower moment changes.

The disparity between the measured changes in moment and those predicted by both of the models at Pier 4 suggest that this pier maintains more of its original stiffness than expected at elevations nearer to points of fixity with the icebreaker and superstructure. Pier 2 was modeled more accurately, though the values at the bottom of Pier 2 were overestimated.

Chapter 7. Summary, Conclusions, and Recommendations

7.1 Summary

This document reported the second part of a monitoring program aimed at investigating the effects of temperature variation on the axial forces and moments in bridges with fixed connections between sub- and super-structure. This report described the collection and analysis of data from instrumentation in place on the MnDOT Bridge 82855 (Wakota Bridge) carrying the eastbound lanes of Interstate 494 across the Mississippi River, the Union Pacific Railroad, and Verderosa Avenue in South St. Paul, Minnesota. This document also presented and discussed a comparison of the collected data to behavior predicted by previously created finite element models.

The Wakota Bridge was chosen for the investigation into the effects of thermal loading on concrete bridges because it employs fixed-flexible twin-blade piers, the behavior of which has not been studied extensively, and also because of the high temperature range, and correspondingly high induced thermal loads, seen in Minnesota. This bridge was also chosen because its recent construction allowed for the placement of data collection instruments within the structure of the bridge.

The field data that was collected consisted of strains, calculated from frequencies measured using vibrating wire gauges, and temperature measurements, obtained from the internal thermistors, from an array of 84 vibrating wire gauges located at various cross-sections of both the superstructure and pier substructure of the bridge, as well as displacement measurements taken from linear string potentiometers located at each abutment of the bridge. Data was collected continuously over a one-year period from January 10, 2010 at 2:00 PM to January 10, 2011 at 2:00 PM, with 15-minute time intervals between gauge measurements. The strain data was analyzed and used to calculate changes in stress, and the stress data was used subsequently to obtain changes in axial force and moment across each instrumented cross-section of the bridge.

The two main topics of interest in the study, within the context of bridges with fixed connections between pier substructure and the superstructure, were the method of approximating the stiffness of the cracked pier sections and the effect of thermal loads on the behavior of the bridge.

Two methods for approximating pier stiffness as allowed by AASHTO LRFD [1] were compared in this study: A common refined design method, which iteratively approximated the stiffness of a variable number of stiffness-updating segments along the height of the piers, and a gross section method, which utilizes a thermal load factor equal to 0.5 to approximate the influence of cracking in the piers. Finite element models that were developed in Phase I were analyzed, and the behavior that they predicted was compared to the actual behavior of the bridge, as determined from field data collected at the bridge site. Various finite element model parameters were investigated to calibrate these models to the field data.

A comparison of the two procedures allowed by AASHTO LRFD Article 3.12.2 was also conducted. Procedure A temperature range is 80 °F in Minnesota. Using a base temperature of 45 °F per MnDOT BDM results in a rise of 35 °F and a fall of 45 °F. Procedure B uses a range of 150 °F as interpreted by the MnDOT BDM from contour maps developed by Roeder [2] in 2002 showing the average maximum and minimum daily temperatures measured throughout the United States. Using a base temperature of 45 °F per the MnDOT BDM results in a rise of 75 °F and a fall of 75 °F.

7.2 Conclusions

Preliminary analysis of the strain data showed the superstructure sections increasing in compression with increasing temperature, and decreasing in compression with decreasing temperature; this was expected given that the concrete of the box-girder superstructure would tend to expand with increasing temperature but restraint provided by the pier stiffness would prevent this expansion, inducing compression within the superstructure. Moreover, since data collection began at the time of the coldest yearly temperature (Jan. 10, 2010), any change in axial force from that time would be compressive. Changes in axial force and moment were calculated from the collected field data. The changes in axial force increased in compression with increasing temperature; the changes in moment were negative with increased temperature, indicating that the bottom flange of the box-girder section tended to have a higher increase in compressive force than did the top flange at the instrumented sections.

Analysis of the strain histories measured in the pier cross-sections indicated that the pier blades underwent double-curvature bending. Changes in axial force and moment were calculated making no assumptions other than satisfying equilibrium, to incorporate both the bending in the individual blades as well as that of each pier cross-section as a whole. The pier cross-sections experienced increased compressive forces as temperature increased, and decreasing compressive force as the temperatures decreased.

Reversed bending was observed in the calculated moment histories for the piers, and Figure 7.1 summarizes the observed behavior of the piers with increasing temperature change. The pier elevation at (*a*) in Figure 7.1 corresponds to zero temperature change (i.e., the beginning of the monitored thermal loading period), while the elevation at (*b*) illustrates exaggerated pier bending due to increased temperature loading.

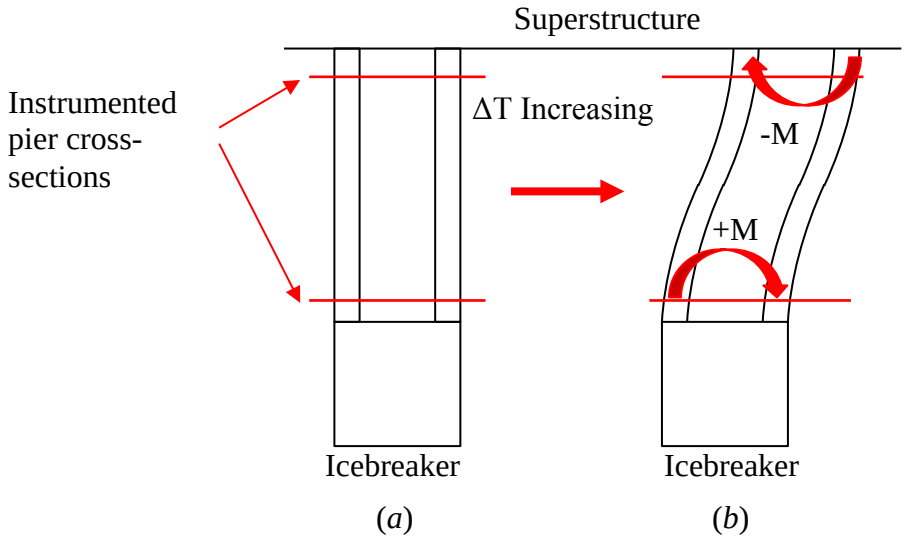

Figure 7.1: Behavior of pier blades with increasing temperature.

In reality the piers would not have been perfectly straight at the time of zero temperature change; jacking produced some initial curvature and creep will have caused curvature in the opposite direction, so the perfectly straight pier shown in Figure 7.1 is a theoretical structure. It was

assumed that the initial deformations did not produce P-Δ effects that were large enough to have a major effect on the temperature analysis.

For the pier sections, negative moment was defined as bending that produced compression on the downstation blades of the piers, and positive moment produced compression on the upstation pier blades. The two instrumented piers had exactly opposite behavior: When the top of Pier 2 was experiencing a negative change in moment, the top of Pier 4 experienced a positive change in moment, and when the bottom of Pier 2 was undergoing positive moment changes, the bottom of Pier 4 underwent negative moment changes. This behavior, which is illustrated in Figure 7.2, is consistent with extension of the superstructure between piers, and the lateral movement of the piers to accommodate it.

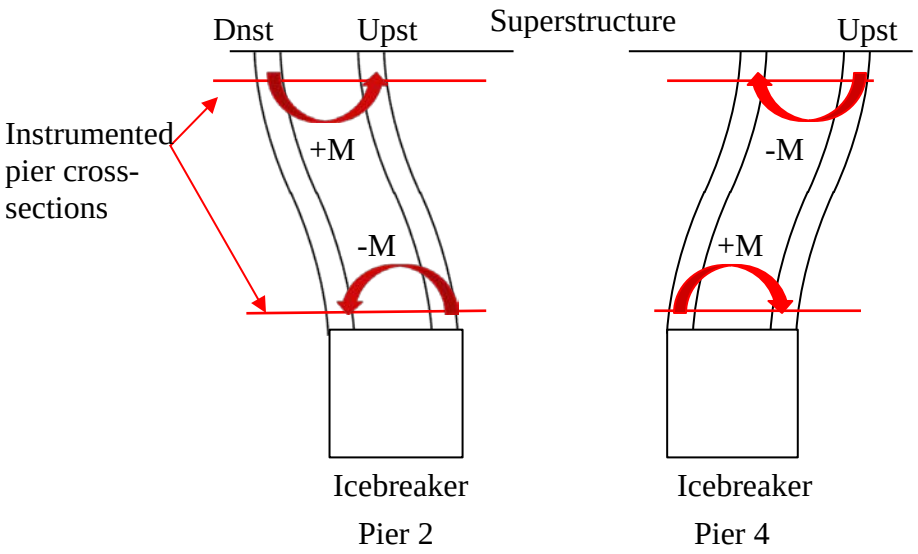

Figure 7.2: Opposing behaviors of Pier 2 and Pier 4 at the same change in temperature.

After initial analysis of the behavior of the bridge, the field data was used to compare the methods of stiffness approximation and the two design temperature ranges allowed by AASHTO LRFD. Finite element models incorporating either the refined design method for pier stiffness approximation or the gross section method were analyzed, and the behaviors predicted from these models were compared to the actual behavior of the bridge.

Changes in axial force and moment across each instrumented superstructure section were compared with values predicted by the two finite element models, DLM_Ref and DLM_Gross, at the same locations. Both DLM_Ref and DLM_Gross showed good correlation to the field data in the superstructure sections. The axial force changes predicted by both finite element models were similar to each other. Both models overestimated the maximum change in compressive force by 14.7% and 14.5% respectively in Span 3, and by 12.6% and 12.4% respectively in Span 4. The changes in moments predicted by DLM_Gross were underestimated by 13.9% in Span 3 and by 31.5% in Span 4, while DLM_Ref predicted values that were underestimated to a smaller degree, 1.1% for Span 3 and 2.1% for Span 4. This suggests that the use of the refined analysis

method of approximating pier stiffness in the finite element model is better suited for predicting the behavior of the bridge superstructure.

The pier behavior was also compared to the behavior predicted by the finite element models. The maximum total changes in moment were underestimated by both DLM_Ref and DLM_Gross in nearly every case; the only location where the change in moment was consistently overestimated was at the bottom instrumented section of Pier 2 in both DLM_Ref and DLM_Gross. The trends of the predicted changes in moment correlated very well with the field data at the top of Pier 2, while at the bottom of Pier 2 the predicted values overestimate the change in moment by 60% and 50% for DLM_Ref and DLM_Gross respectively. This suggests that the AASHTO LRFD and MnDOT BDM Procedure A temperature range of 80 °F, which is very close to the measured average internal concrete temperature range, is appropriate for use in analyzing the median behavior of the bridge, while the more conservative Procedure B 150 °F range would better be able to capture the extreme behavior of the bridge. This would be true both in non-typical bridge designs, as was the case with the Wakota Bridge, and would also be true for typical bridges.

Change in moment was underestimated at the top of Pier 2 by 20% in DLM_ref, and 42% in DLM_Gross; change in moment in the bottom of Pier 2 was overestimated by 36% in DLM_Ref and underestimated by 3% in DLM_Gross. The predicted changes in moment were significantly underestimated in both instrumented elevations of Pier 4, by 50% and 60% respectively for DLM_Ref and DLM_Gross at the top of Pier 4,and by 69% and 63% respectively at the bottom of Pier 4. Much of the disparity between the predicted and measured total changes in moment results from “noise” in the data: The moment across the pier cross-sections fluctuated over brief time periods to a larger extent than the spans, resulting in artificially high total changes in moment. Much of this noise is believed to be error associated with calculating moments on the basis of differences in strains both with small magnitudes. When the trends of the predicted data were compared with those of the field data, much greater correlation was seen in every case except at the bottom of Pier 2.

Two potential sources of error in the finite element predictions of the pier moments were investigated; a) the rotational support at the base of the piers, and b) the stiffness of the piers. These parameters were varied in an attempt to better understand pier behavior and to suggest recommendations for better calibrating the finite element models.

The fixity of the pier bases to the footings at Piers 2 and 3 were modified in DLM_Ref: Use of fixed connections between these pier bases and footings resulted in overestimated changes in moment in Pier 2 by 56% in the bottom instrumented section and an accurate prediction at the top of pier 2, while using pinned connections that allowed more rotation at the pier bases decreased the changes in moment in Pier 2 by between 40% to 60% of the values predicted by the original DLM_Ref. Modifying the fixity of the Piers 2 and 3 bases had little effect on the changes in moment in Pier 4 because the latter was already fixed at the base to simulate a poured mat foundation on bedrock: these values changed by less than 1% from the original DLM_Ref values in both cases.

Increasing the stiffness of the top and bottom stiffness-updating segments in DLM_Ref increased the changes in moment in both Piers 2 and 4, and there was better correlation between the predicted value trend and the field data in Pier 4. Increasing the overall stiffness in DLM_Gross

from 0.5*EI* to 0.75*EI* resulted in similarly good correlation between the predicted changes in moment in Pier 4 and the field data, suggesting that the pier behavior responded most to changes in pier stiffness. This was the best method of calibration.

A plausible way in which the field moments could be obtained by finite element analysis is to use the DLM_Gross model with stiffness coefficients that a) were different for the various piers, or b) were between 0.75 and 1.0. However, this exercise was beyond the scope of the current investigation. The limited parametric study that was conducted indicated that pier moments are highly sensitive to the magnitude and distribution of pier stiffness, and that neither of the two procedures (Common Refined Design Procedure and Gross Section Method) accurately represented the stiffness properties of Piers 2 and 4 in the Wakota Bridge.

It was determined that the use of design temperature range provided in the AASHTO LRFD Procedure B and as interpreted by MnDOT BDM provides an appropriate upper bound on the thermal loads that could be expected to be applied to the bridge. This temperature range is able to capture the peaks in the changes in axial force and moment more accurately than did the lower temperature range in Procedure A. However, the Procedure A temperature range much more closely predicted the median behavior of the bridge. This implies that design considerations that do not depend on maximum values would be better predicted using the Procedure A temperature range, even in non-typical bridges such as the Wakota Bridge.

The use of a common refined design method for approximating the cracked pier stiffness in a non-typical bridge such as the Wakota Bridge was also shown to be appropriate. This approximation much more accurately predicted the behavior of the superstructure than did the gross section method. This was also true, to a lesser extent, for the predicted pier behavior. This suggests that the common refined design method is appropriate for approximating the cracking of the piers in a non-typical bridge. Given that basic principals of engineering were used in the modeling of this bridge, this would be equally true for typical bridges with less complex design considerations than the Wakota Bridge. The gross section method did not predict the behavior of either the superstructure or the piers as well as the refined design method, but it is possible that the inaccuracies resulting from this approximation would be mitigated to some extent in the analysis of a simpler bridge structure.

7.3 Recommendations

Several design recommendations are made here for the method of approximating pier stiffness.

7.3.1 Pier Stiffness Predictions

- Modeling of fixed-flexible pier blades using the refined design method should be used to approximate cracked pier stiffness in order to accurately predict the behavior of the bridge superstructure.
- Modeling of fixed-flexible pier blades using the gross section method can be used to approximate cracked pier stiffness and still predict the behavior of the bridge superstructure satisfactorily, but this method produced less accurate predictions of the changes in moment in the superstructure than did the refined design method. It is recommended that the gross section method should best be used as a preliminary

approximation for stiffness, but that final design should be based on the more accurate refined design method.

- In piers where some rotation of the pier base with respect to the footing is allowed, the refined design method should be used to predict changes in moment.
- In piers with bases fully fixed to the footings and allowing no rotation, a larger assumed ratio of cracked stiffness to gross section stiffness should be applied: Both the refined design method and gross section method for calculating stiffness may underestimate the actual stiffness of the section.

7.3.2 AASHTO LRFD Temperature Design Procedure

Recommendations are made here concerning the AASHTO LRFD temperature design procedures. These recommendations are based on relatively limited data, as only one year of strain and temperature data was analyzed. These recommendations are also limited with regards to the type of bridge. The Wakota Bridge is a non-typical bridge, and is also a massive concrete structure with a large internal air mass; the insulating effects of such large volumes of concrete and trapped air would cause the bridge to behave in a very different way than a bridge with a typical steel girder or prestressed concrete beam superstructure, for example.

- The Procedure B design temperature range should be used as a conservative range for extreme conditions in both typical and non-typical bridge design when considering longitudinal behavior, although this range may overestimate the temperature range as measured within the concrete structure. MnDOT BDM provisions are consistent with this recommendation.
- The Procedure A temperature range reflects the observed longitudinal behavior of the bridge structure with respect to temperature, but should not be used in the design of non-typical bridges, given the possibility of extreme thermal conditions. MnDOT BDM provisions are consistent with this recommendation.
- No recommendations can be made as to which design temperature range should be used to design for transverse behavior due to temperature loading, as the transverse behavior was not investigated in this study.

7.3.3 Recommendations for Future Research

Recommendations for future research based on field study are offered here.

- The effect of temperature at the time of bridge construction on the magnitude of the axial force and moment changes developed in the bridge should be investigated.
- Investigation of the hysteresis noted in the strain, stress, and axial force histories for each of the instrumented sections should be done to determine the reasons why these histories did not return to the initial values after the first year of data collection. This will allow better calibration of the finite element models to predict the bridge behavior.
- Continued data collection from the data acquisition system and analysis of data collected after the year-long contracted data collection period should be performed to identify bridge behavior over multiple yearly cycles of heating and cooling.
- The effect of temperature on typical bridges should be studied to provide comparison for the information presented in this study on a non-typical bridge.

Finally, recommendations based on the finite element study are as follows.

- The fixities of the connections between pier blade and icebreaker and pier blade and box-girder superstructure should also be investigated as these may have an effect on the changes in moments in the pier blades.
- Finally, filtering of the field data should be done in order to reduce short-term, transient deviations (i.e. noise) in the data and more accurately compare finite element predictions with the median trends in the field data.
- The influence of higher deck temperatures on the forces generated by thermal loading should be investigated. This effect is presently treated separately in temperature gradient analysis, but the presence of significantly higher temperatures in the deck have a potential to affect the forces in bridge superstructures and the piers from thermal loading.

References

[1] American Association of State Highway and Transportation Officials, ed. *AASHTO LRFD Bridge Design Specifications*. 4th ed. Washington, DC: AASHTO, 2007.

[2] Roeder, Charles W. "Proposed Design Method for Thermal Bridge Movements." *Journal of Bridge Engineering* January/February (2003): 12-19.

[3] Peng, Yousong. *Analytical Solution to Temperature Variations in Highway Concrete Bridges Due to Solar Radiation.* International Conference on Transportation Engineering 2007, Chengdu, China, ICTE 2007. (2007).

[4] MnDOT Bridge Office, comp. *LRFD Bridge Design Manual*. Oakdale, MN: MnDOT, 2009.

[5] Moorty, Shashi and Charles W. Roeder. "Temperature Dependent Bridge Movements." *Journal of Science and Engineering* 118.4 (1992): 1090-1105.

[6] AASHTO Guide Specifications: Thermal Effects in Concrete Bridge Superstructures. Washington, DC: AASHTO, 1989.

[7] Scheevel, Chris, and Schultz, Arturo E. *An Evaluation of Methods for The Design of R/C Flexible Twin-Walled Bridge Piers*. Oakdale: MnDOT, 2013. Print.

[8] *Response-2000*. Vers. 1.0.5. 2000.

[9] *SAP2000*. Vers. 14. Berkeley, CA: Computers and Structures, Inc, 2009.

[10] Unimeasure, Linear Potentiometer, Position Transducer, Displacement Sensors, String Pot. Accessed 25 May 2010. <http://unimeasure.com/>.

[11] HNTB, *Wakota Bridge Plans and Documents*. Oakdale, MN: MnDOT, 2007.

[12] *Loggernet: Datalogger Support Software*. 2013. Inc. Campell Scientific. 2013 <http://www.campbellsci.com/loggernet>.

[13] Geokon Vibrating Wire Strain Gauge Manual - Model 4200/4202/4204/4210. Lebanon, NH: Geokon, Inc, 2008.

[14] Naik, Tarun R., Kraus, Rudolph N. "Influence of Types of Coarse Aggregates on the Coefficient of Thermal Expansion of Concrete." *Journal of Materials in Civil Engineering*, ASCE 23(4), 467-472.

[15] American Concrete Institute, *Building code requirements for structural concrete and commentary*. ACI Standard ACI 318-08. Farmington Hills, MI; 2008.

[16] American Concrete Institute Committee 209, ACI 209.1R-05 Report on Factors Affecting Shrinkage and Creep of Hardened Concrete. Farmington Hills, MI; 2005.

[17] MnDOT Standard Specifications for Construction. St. Paul, MN: MnDOT, August 2005.

[18] American Concrete Institute Committee 363, *ACI 363R-10 Report on High-Strength Concrete*. Farmington Hills, MI; 2010.

[19] National Oceanic and Atmospheric Association, *NOAA NWS Local Climate Records for St. Paul, MN*. Web. Accessed 20 March 2013. http://www.crh.noaa.gov/mpx/Climate/STPClimate.php.

Appendix A: Strains and Temperatures, Chapter 3

The following are plots showing the collected strain and temperature data after preliminary processing described in Chapter 3.

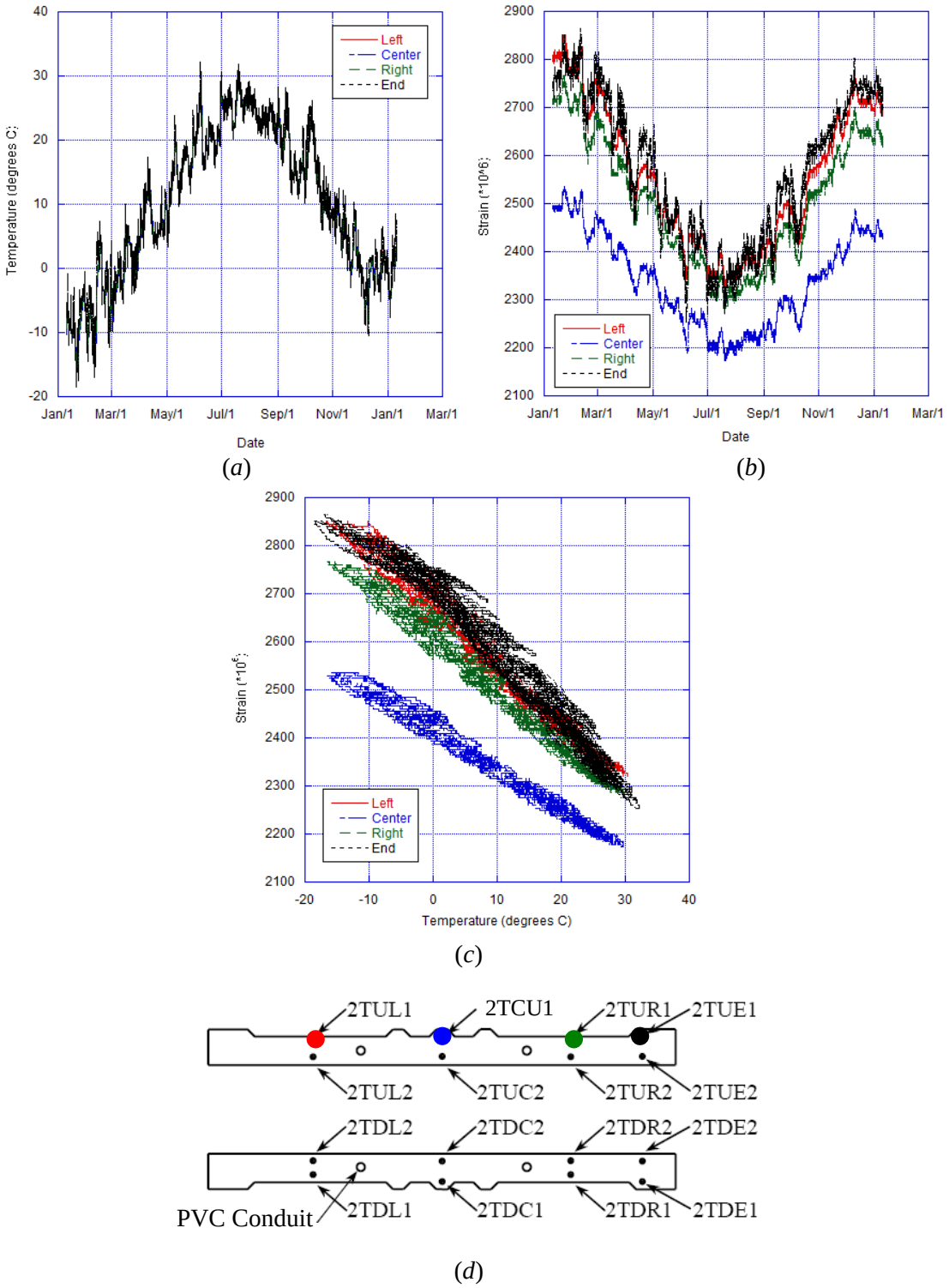

Figure A1: RUTPier2, Rusticated face of the up-station blade of the top instrumented section of Pier 2: a) Temperature versus time; b) Strain (*10^6) versus time; c) Strain (*10^6) versus temperature; d) Instrument locations by color.

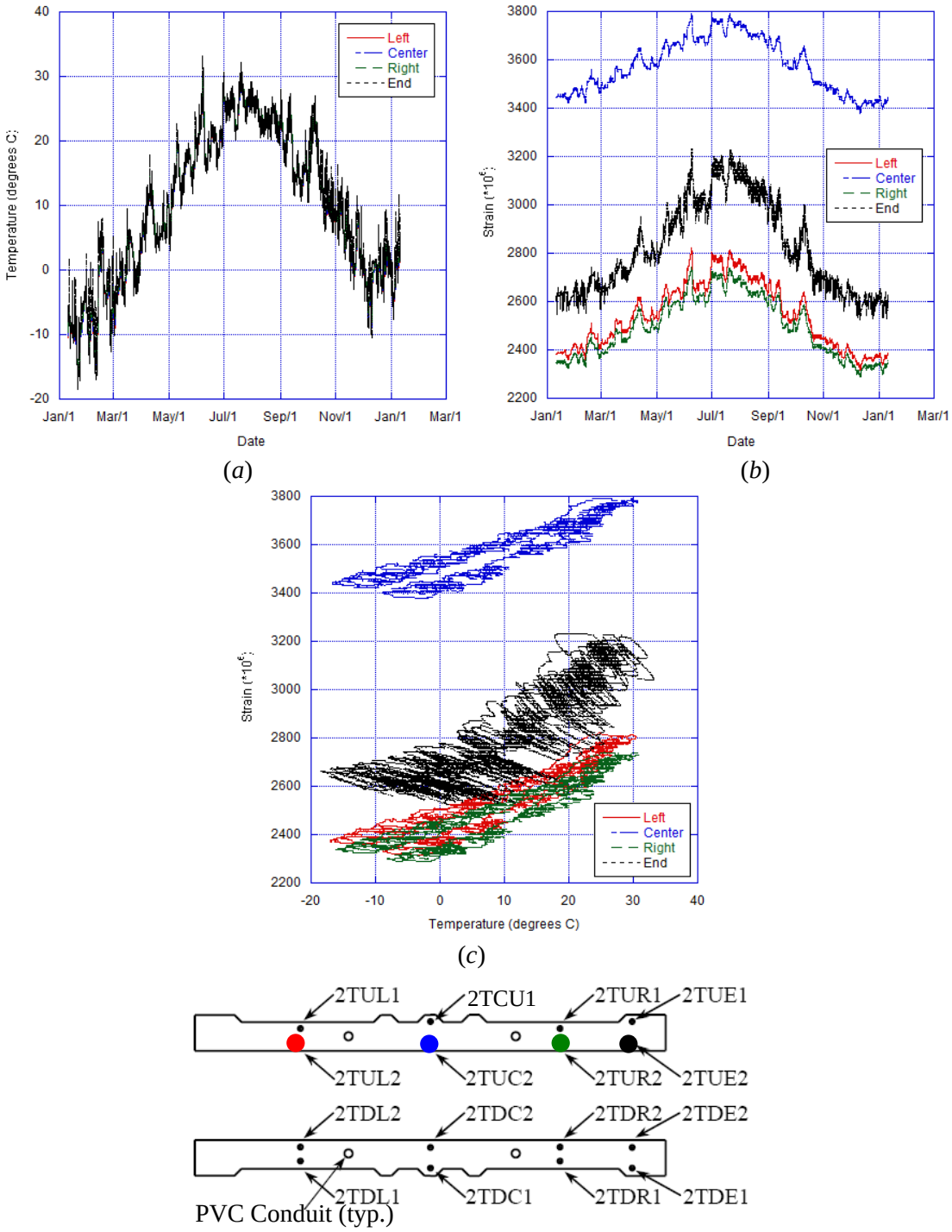

Figure A2: SUTPier2, Smooth face of the up-station blade of the top-instrumented section of Pier 2: a) Temperature versus time; b) Strain (*10^6) versus time; c) Strain (*10^6) versus temperature; d) Instrument locations by color.

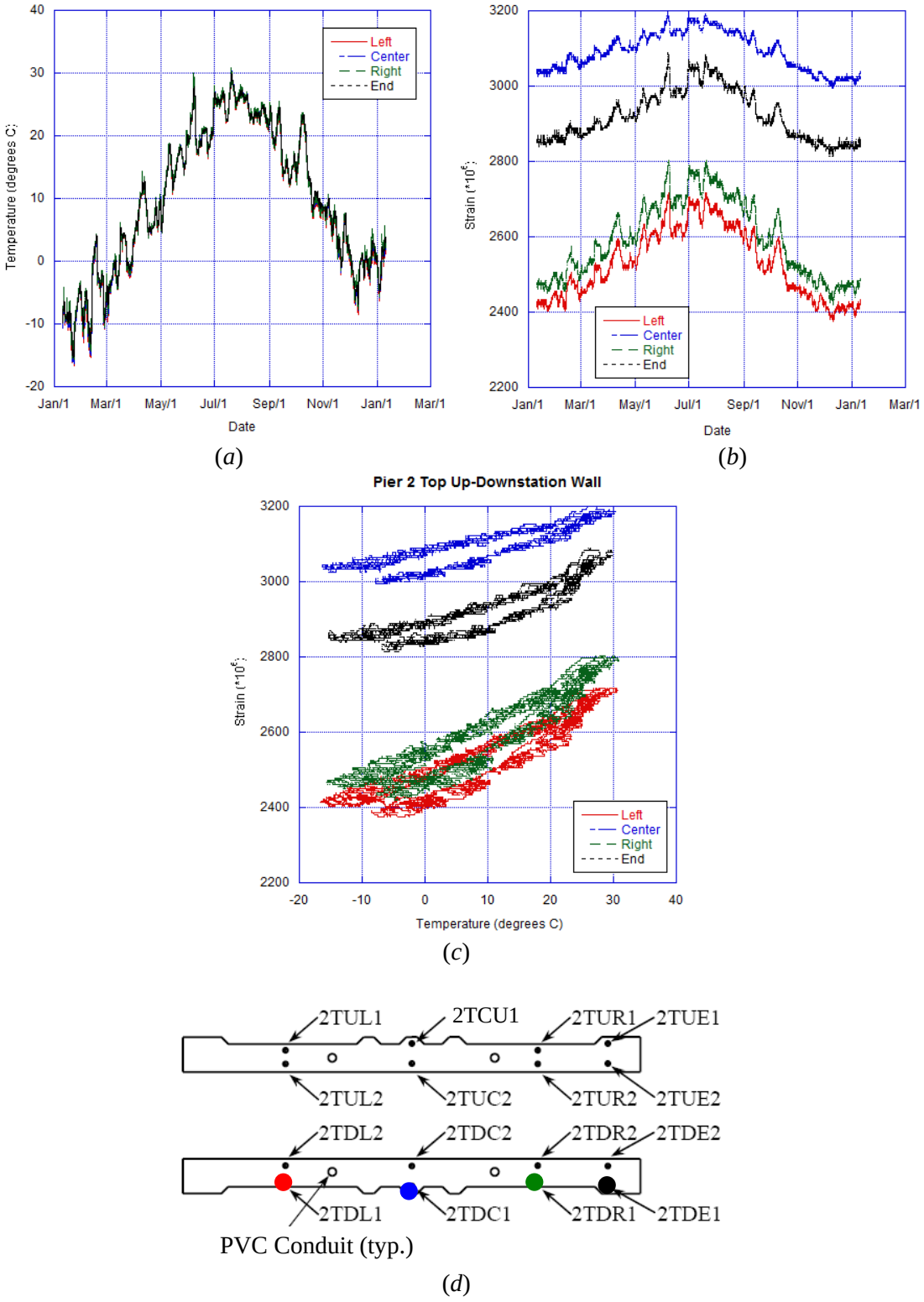

Figure A3: Pier 2, RDTPier2 a) Temperature versus time; b) Strain (*10^6) versus time; c) Strain (*10^6) versus temperature; d) Instrument locations by color.

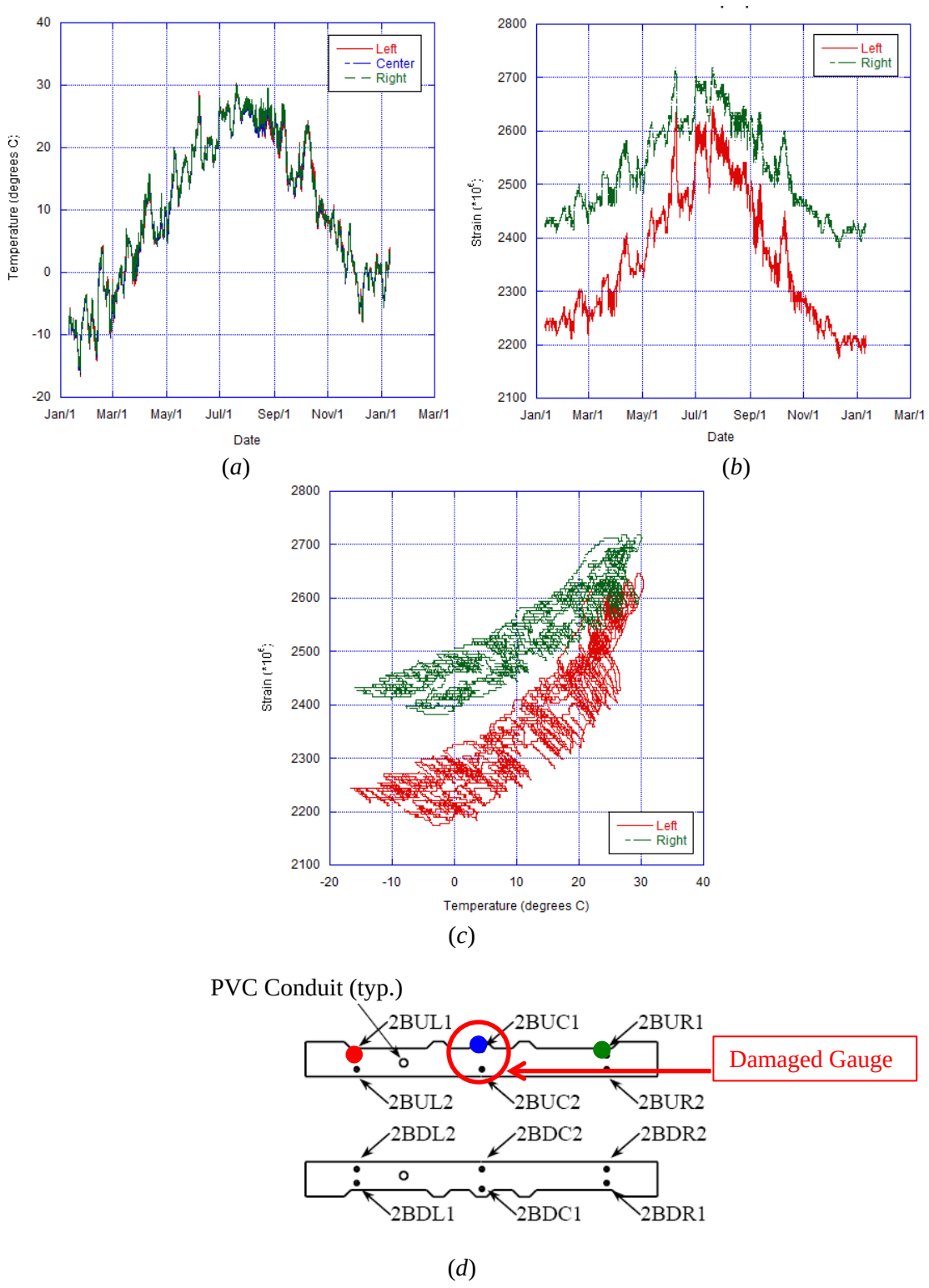

Figure A4: Pier 2, RUBPier2 a) Temperature versus time; b) Strain (*10^6) versus time; c) Strain (*10^6) versus temperature; d) Instrument locations by color.

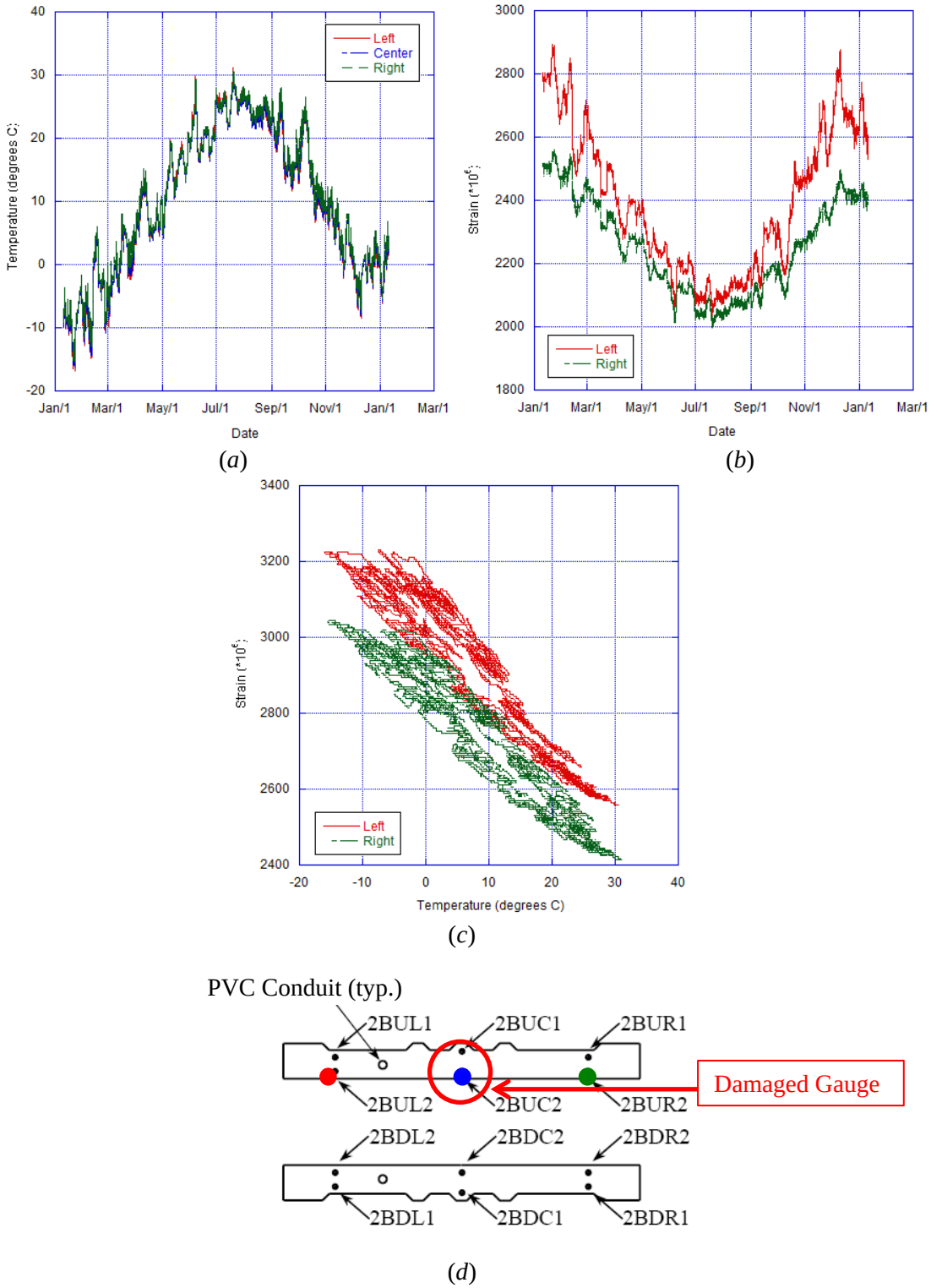

Figure A5: Pier 2, SUBPier2: a) Temperature versus time; b) Strain (*10^6) versus time; c) Strain (*10^6) versus temperature; d) Instrument locations by color.

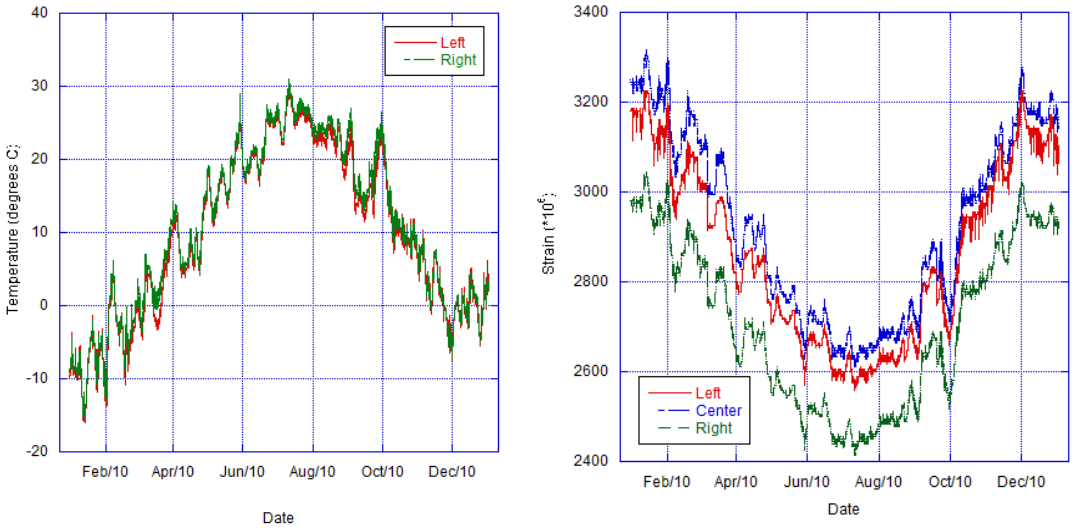

(*a*)

(*b*)

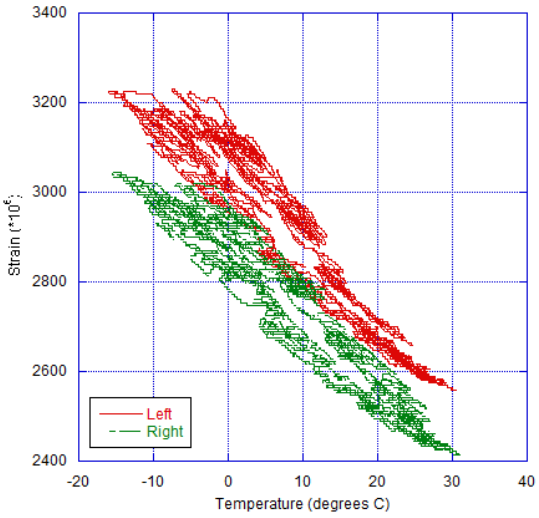

(*c*)

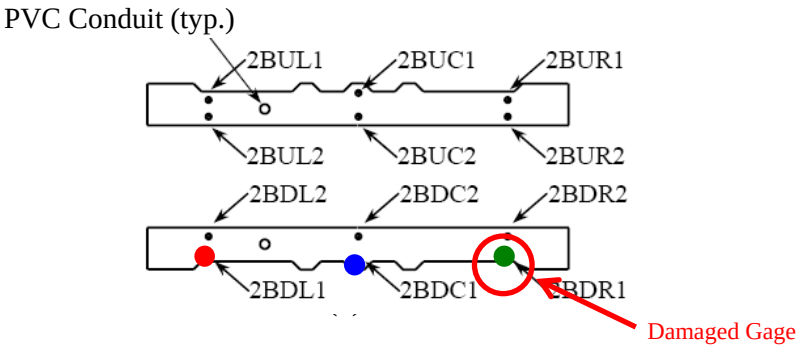

Figure A6: Pier 2, RDBPier2 a) Temperature versus time; b) Strain (*10^6) versus time; c) Strain (*10^6) versus temperature; d) Instrument locations by color.

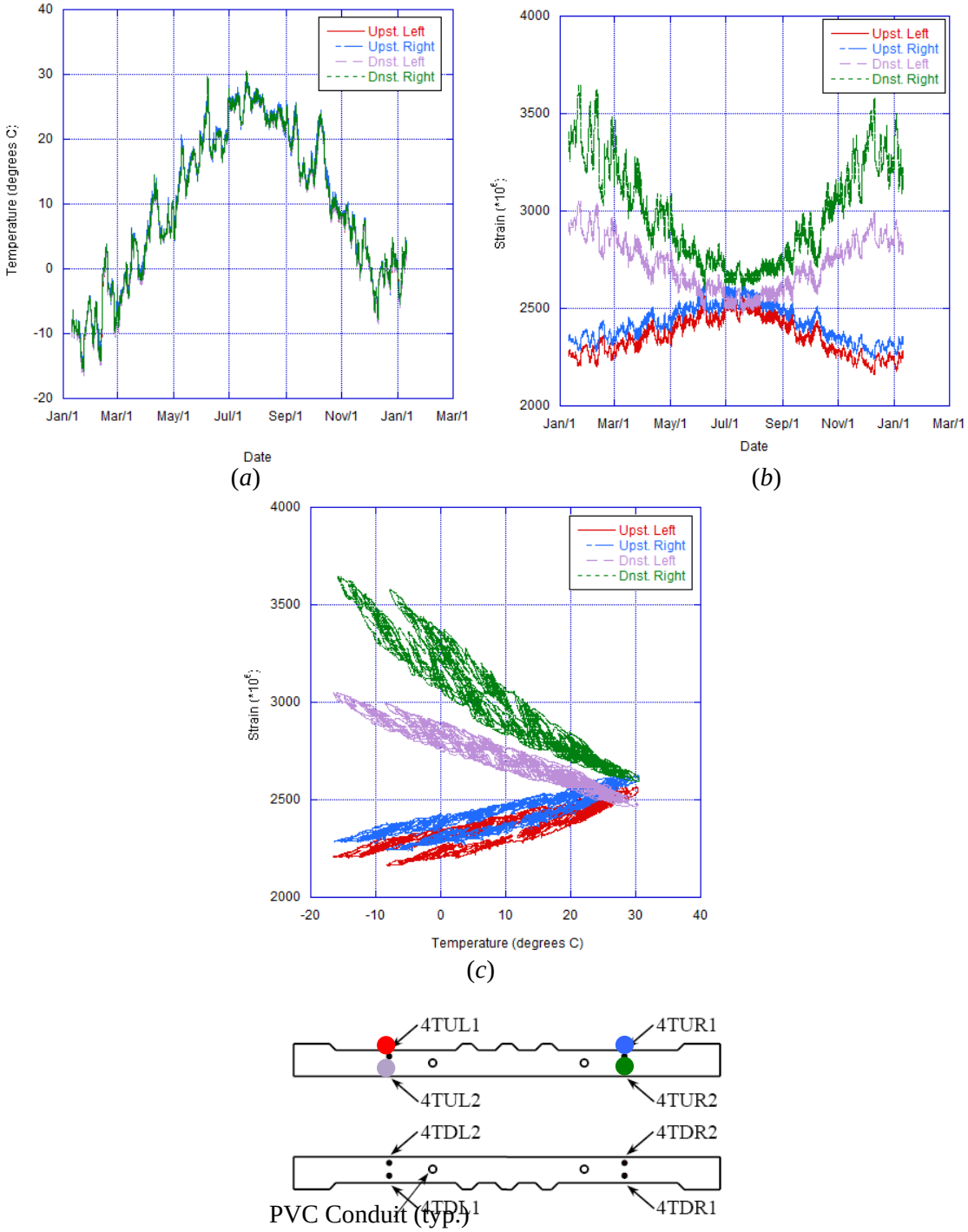

Figure A7: RUTPier4 and SUTPier4: a) Temperature versus time; b) Strain (*10^6) versus time; c) Strain (*10^6) versus temperature; d) Instrument locations by color.

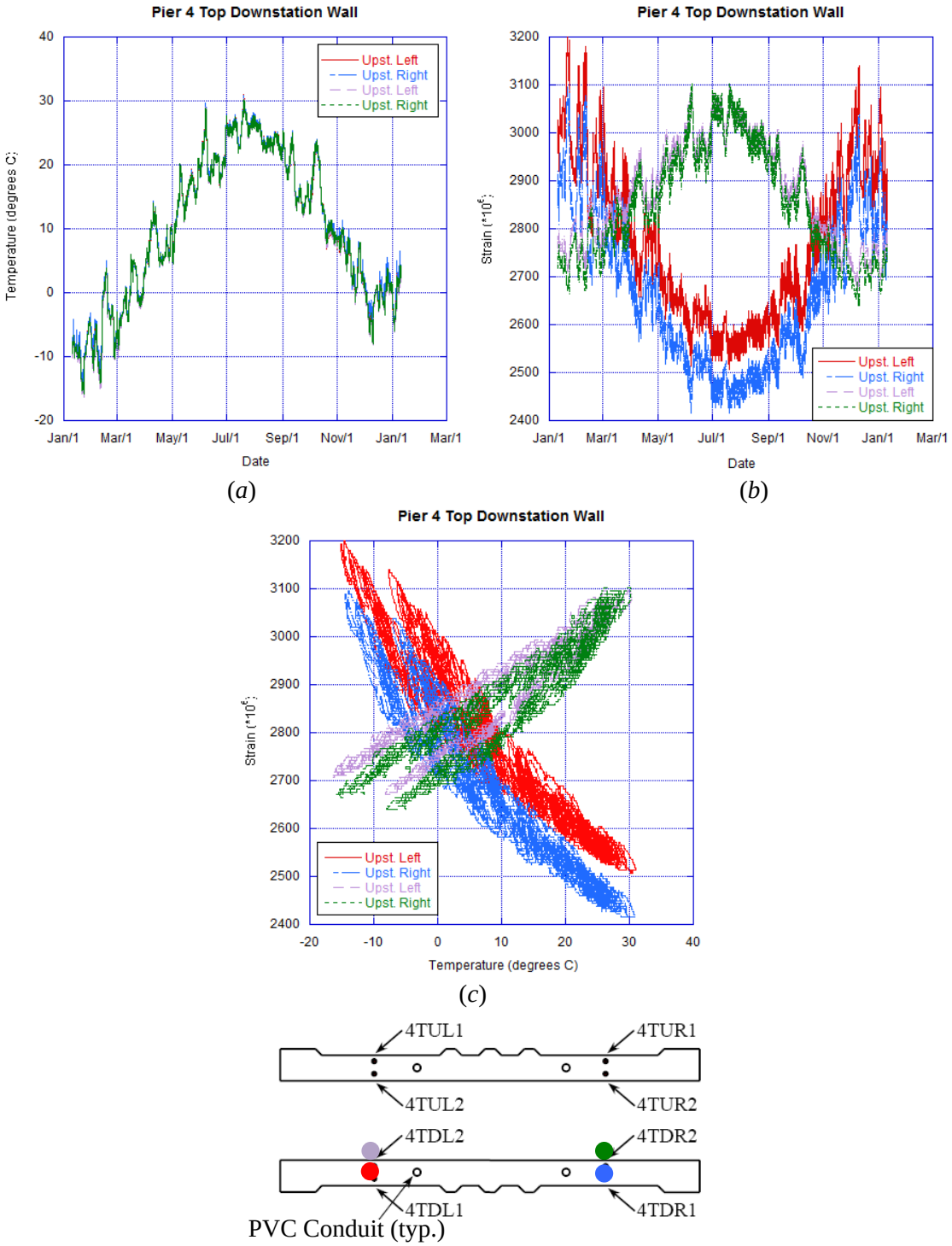

Figure A8: SDTPier4 and RDTPier4: a) Temperature versus time; b) Strain (*10^6) versus time; c) Strain (*10^6) versus temperature; d) Instrument locations by color.

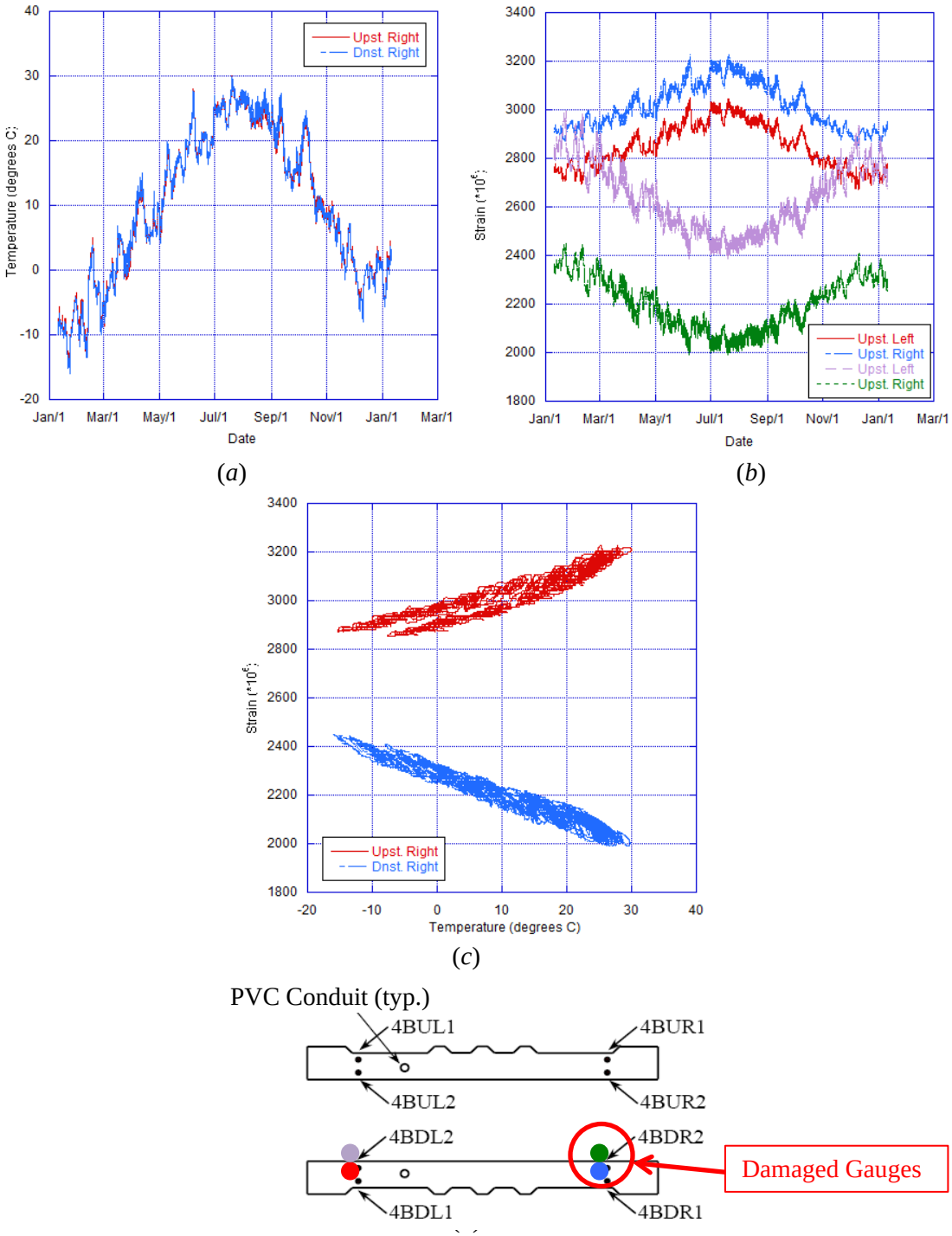

Figure A9: SDBPier4 and RDBPier4: a) Temperature versus time; b) Strain (*10^6) versus time; c) Strain (*10^6) versus temperature; d) Instrument locations by color.

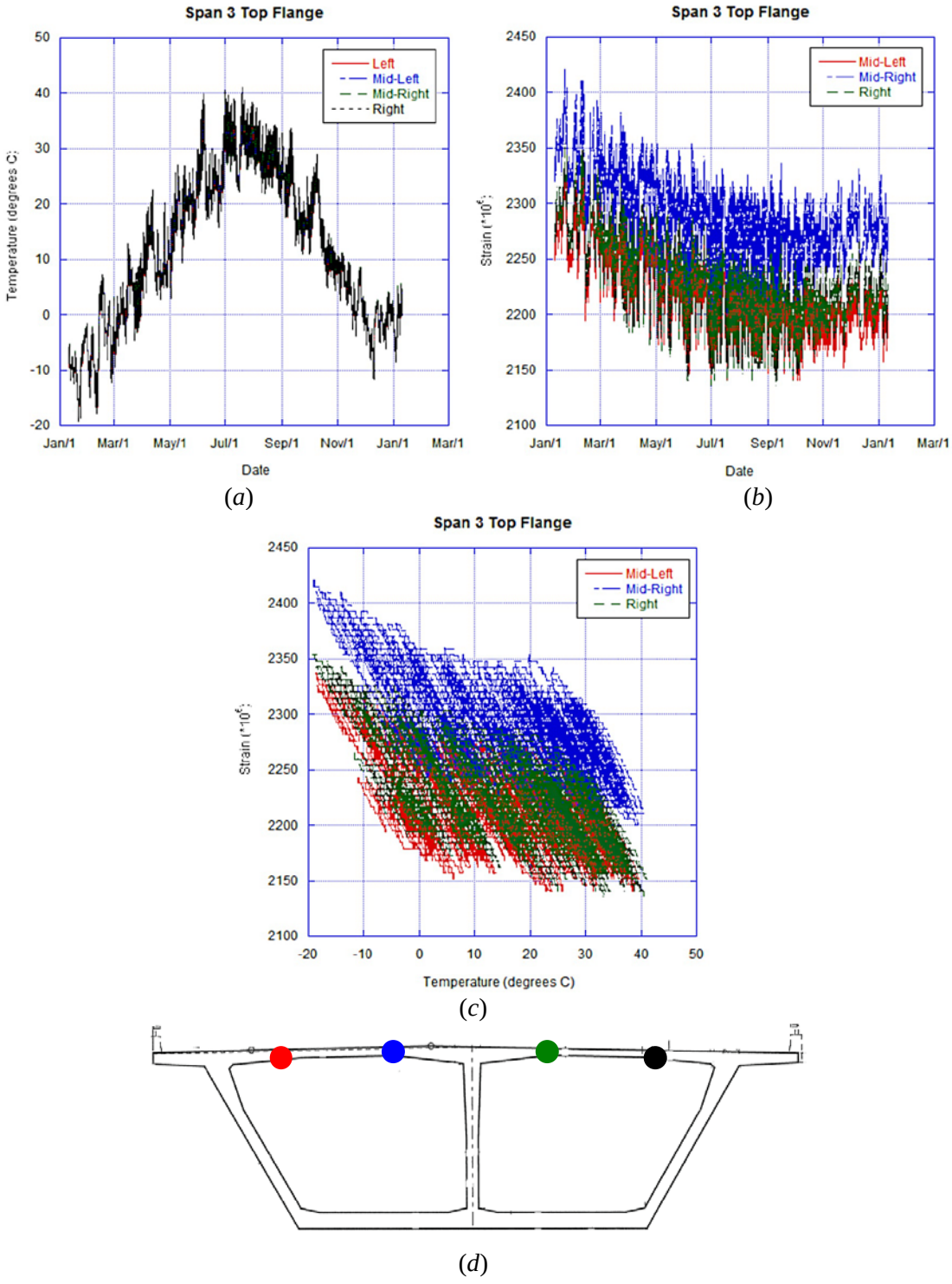

Figure A10: Top flange of Span 3 (TSpan3): a) Temperature versus time; b) Strain (*10^6) versus time; c) Strain (*10^6) versus temperature; d) Instrument locations by color.

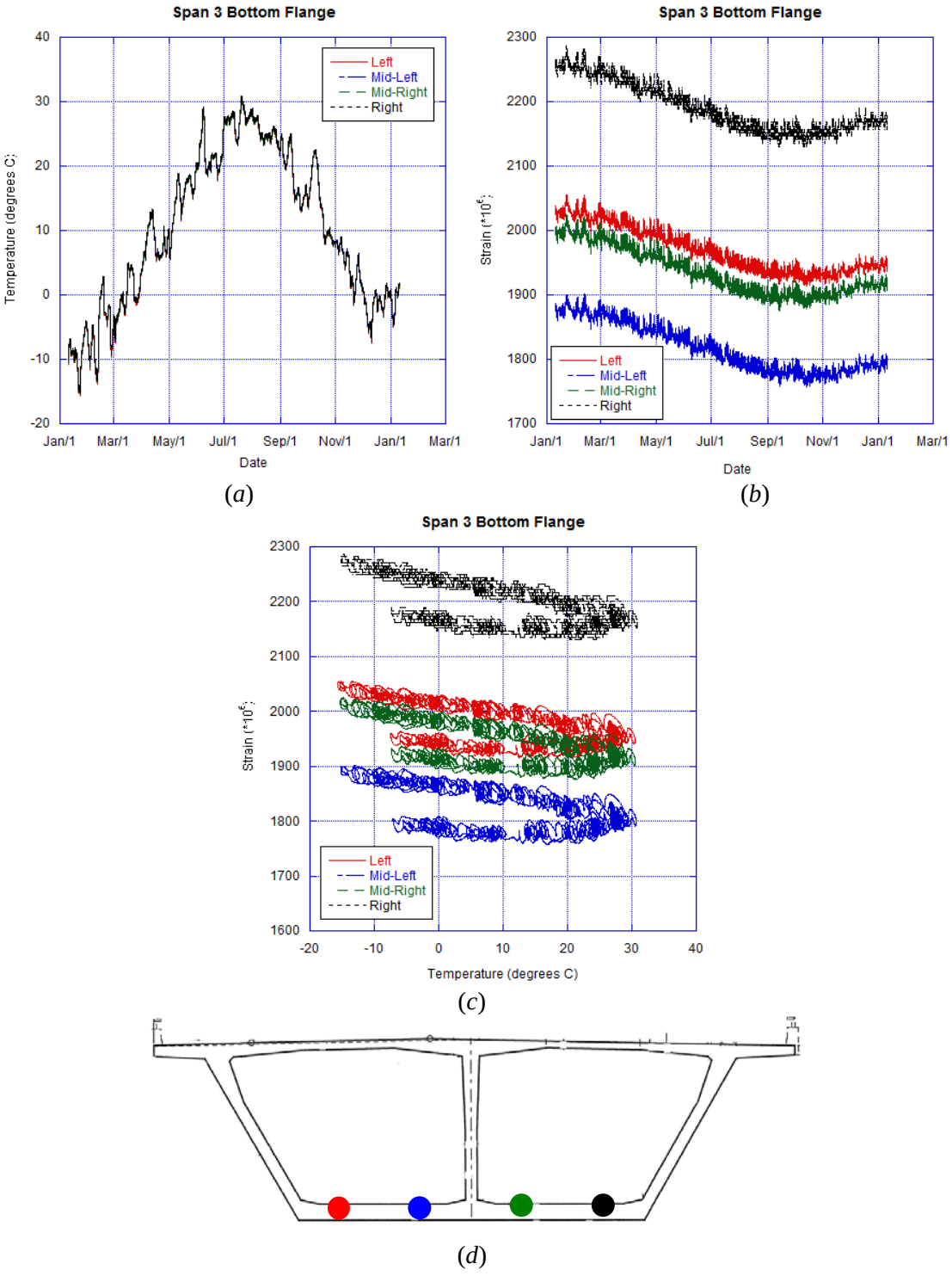

Figure A11: Bottom flange of Span 3 (BSpan3): a) Temperature versus time; b) Strain (*10^6) versus time; c) Strain (*10^6) versus temperature; d) Instrument locations by color.

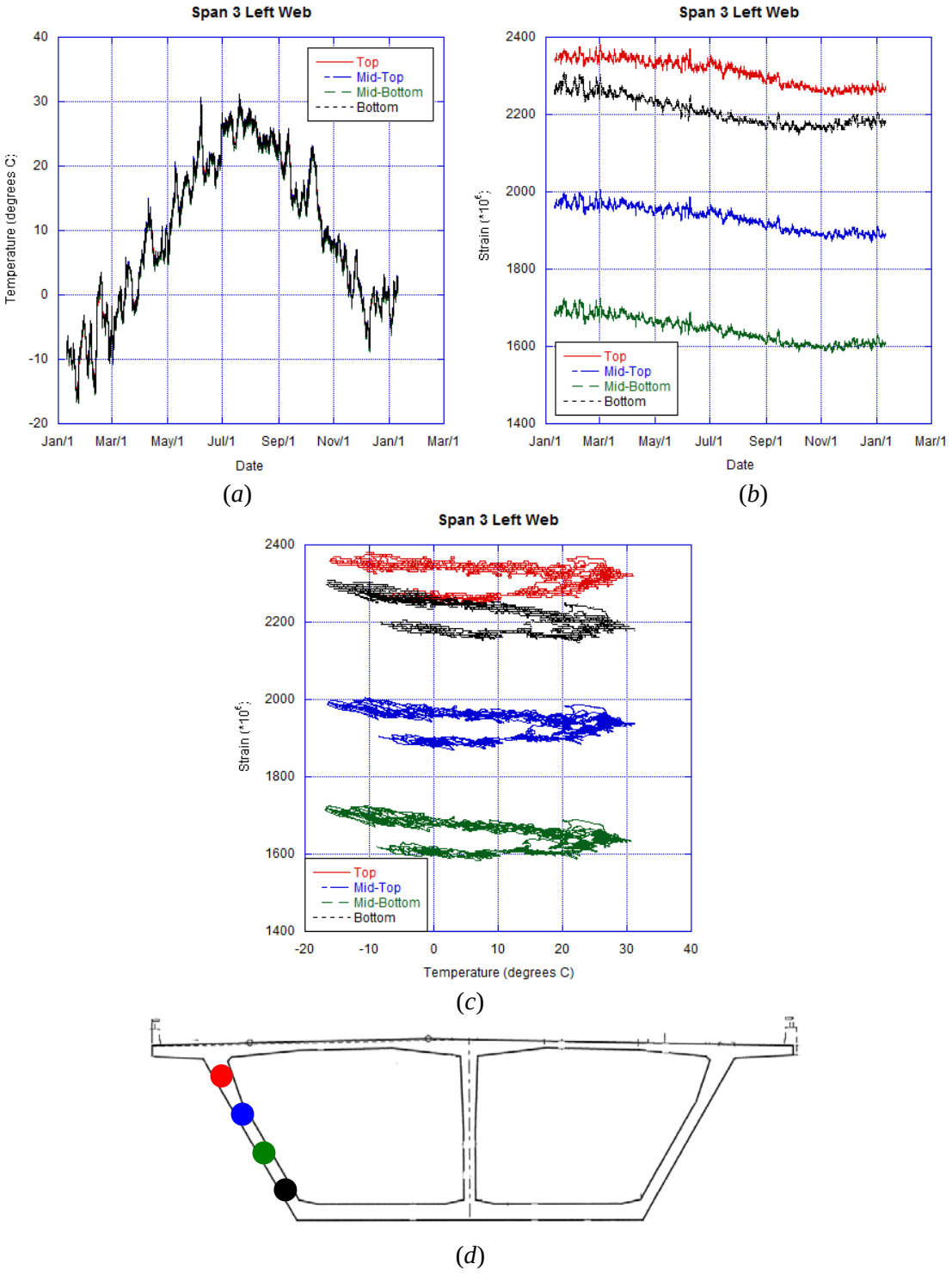

Figure A12: Left web of Span 3, (LSpan3): a) Temperature versus time; b) Strain (*10^6) versus time; c) Strain (*10^6) versus temperature; d) Instrument locations by color.

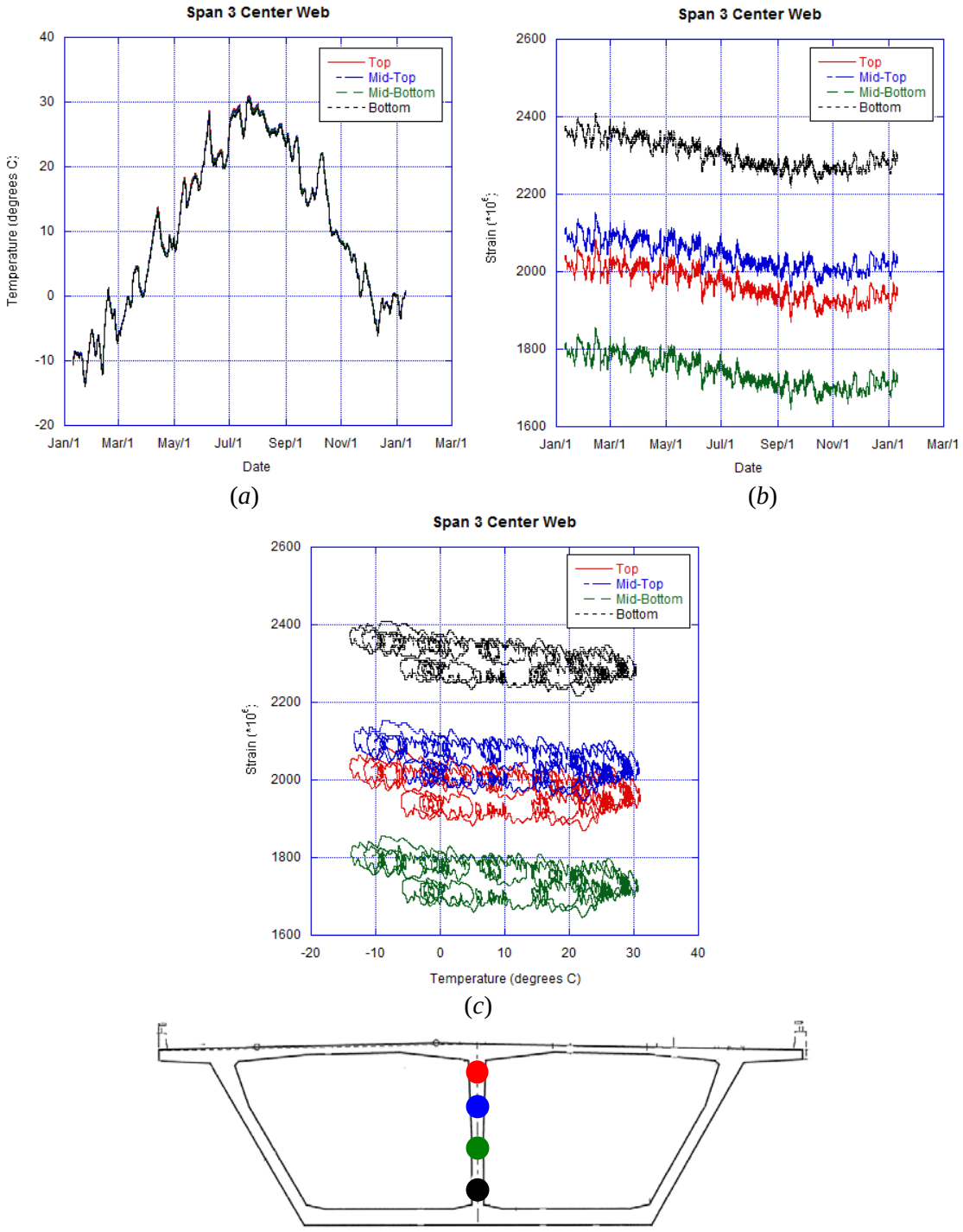

Figure A13: CSpan3: a) Temperature versus time; b) Strain (*10^6) versus time; c) Strain (*10^6) versus temperature; d) Instrument locations by color.

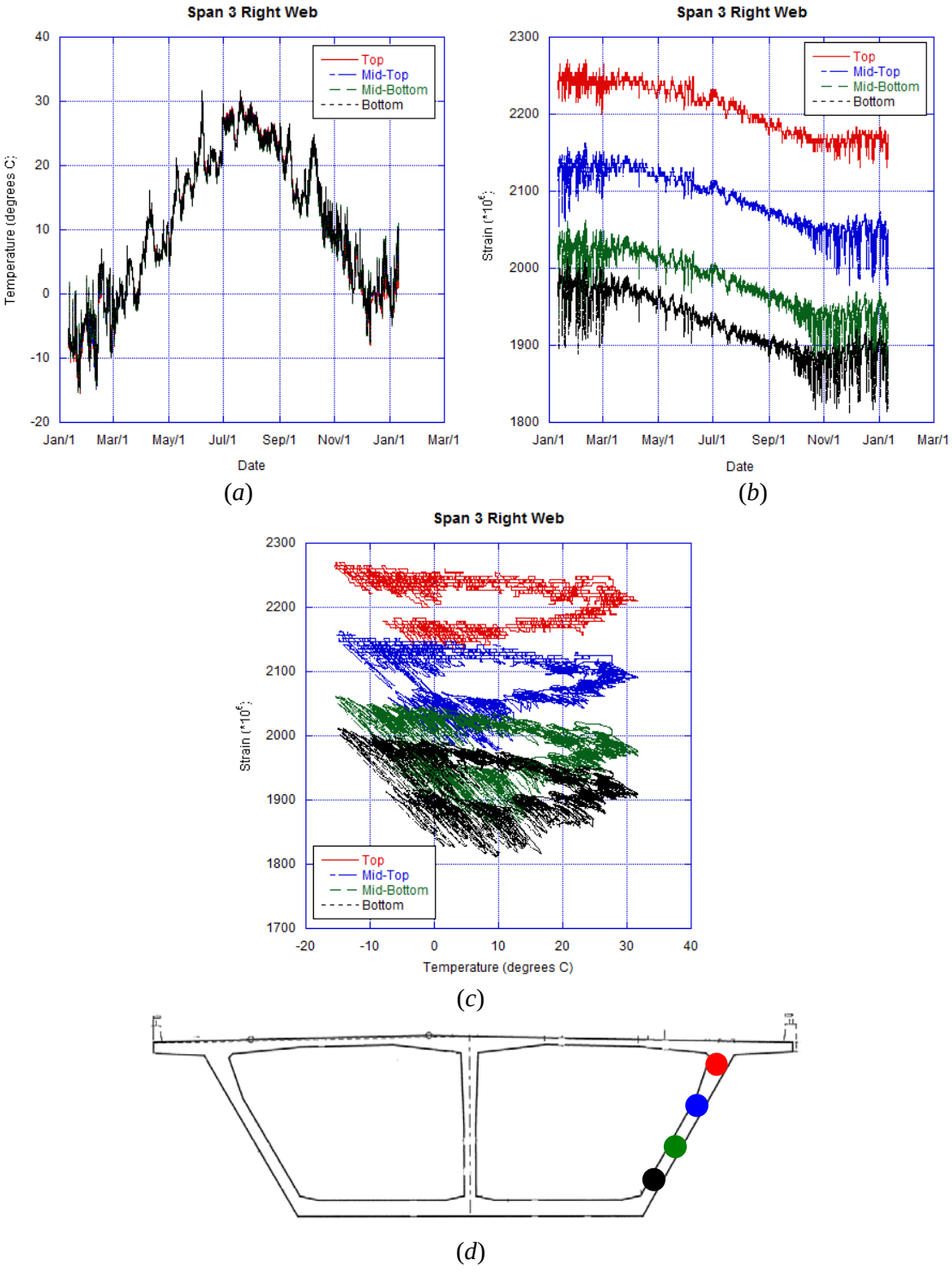

Figure A14: RSpan3: a) Temperature versus time; b) Strain (*10^6) versus time; c) Strain (*10^6) versus temperature; d) Instrument locations by color.

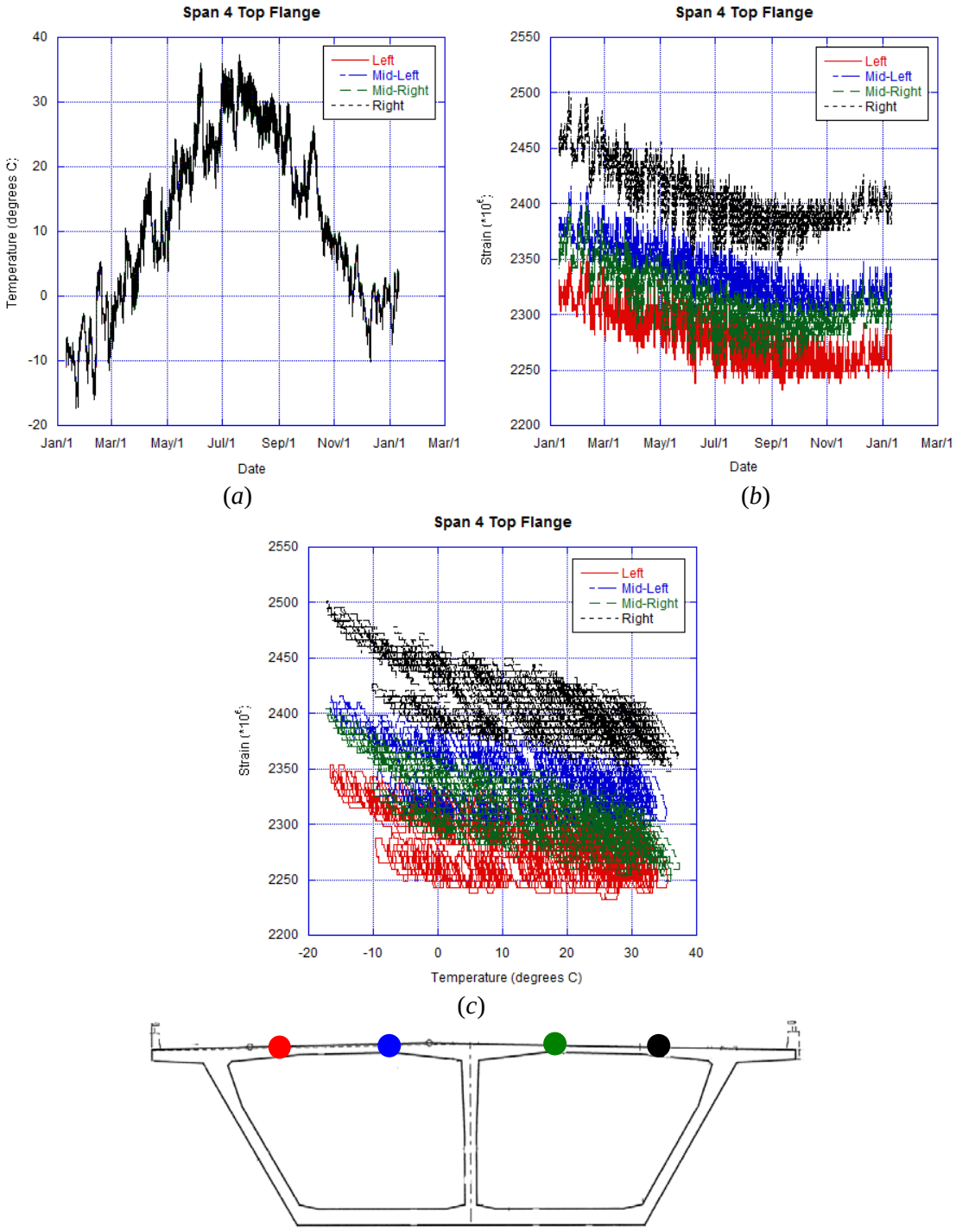

Figure A15: TSpan4: a) Temperature versus time; b) Strain (*10^6) versus time; c) Strain (*10^6) versus temperature; d) Instrument locations by color.

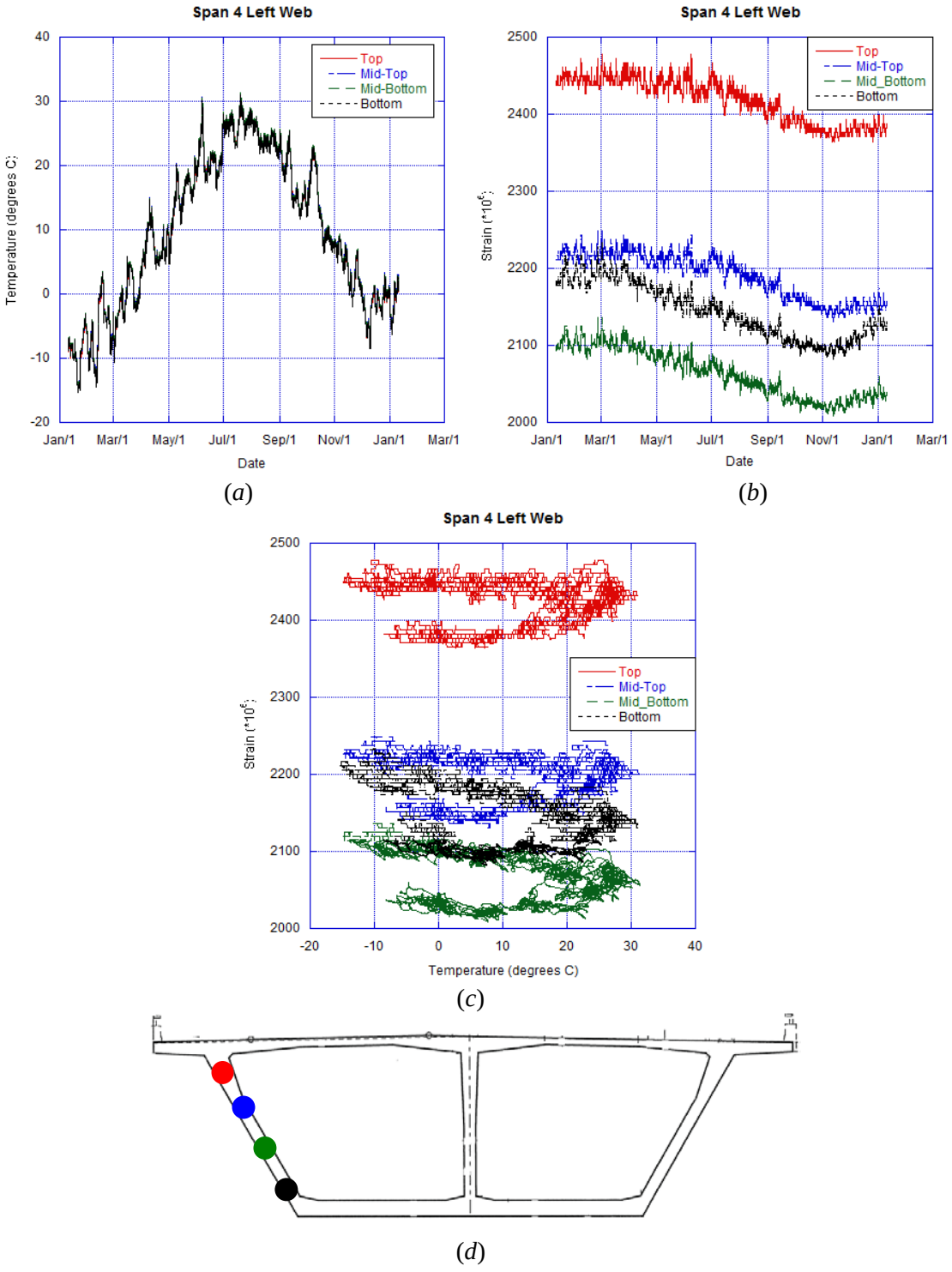

Figure A16: LSpan4: a) Temperature versus time; b) Strain (*10^6) versus time; c) Strain (*10^6) versus temperature; d) Instrument locations by color.

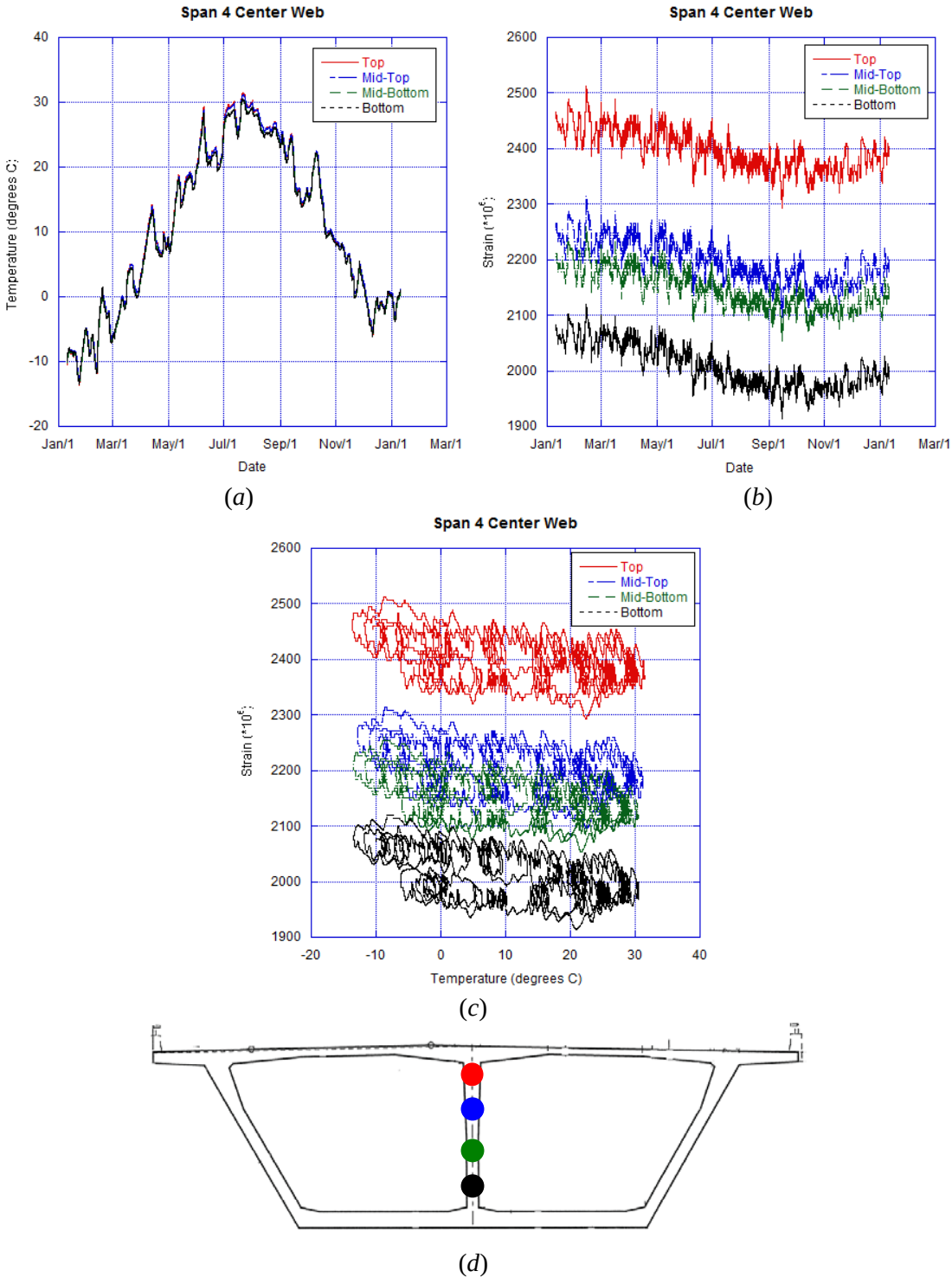

Figure A17: CSpan4: a) Temperature versus time; b) Strain (*10^6) versus time; c) Strain (*10^6) versus temperature; d) Instrument locations by color.

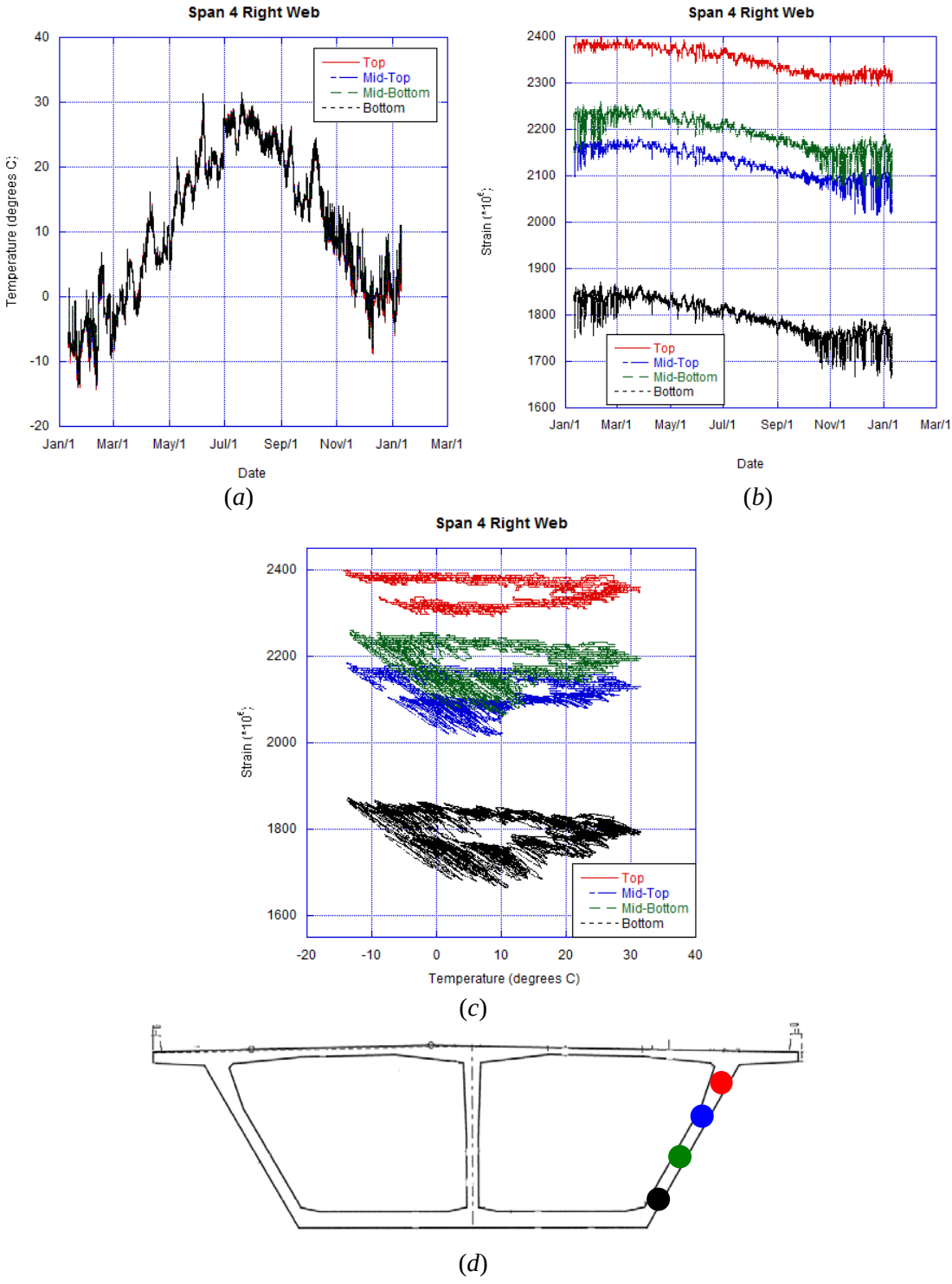

Figure A18: RSpan4: a) Temperature versus time; b) Strain (*10^6) versus time; c) Strain (*10^6) versus temperature; d) Instrument locations by color.

Appendix B: Stresses and Temperatures, Chapter 4

The following are plots showing the calculated stress and temperature data after processing described in Chapter 4.

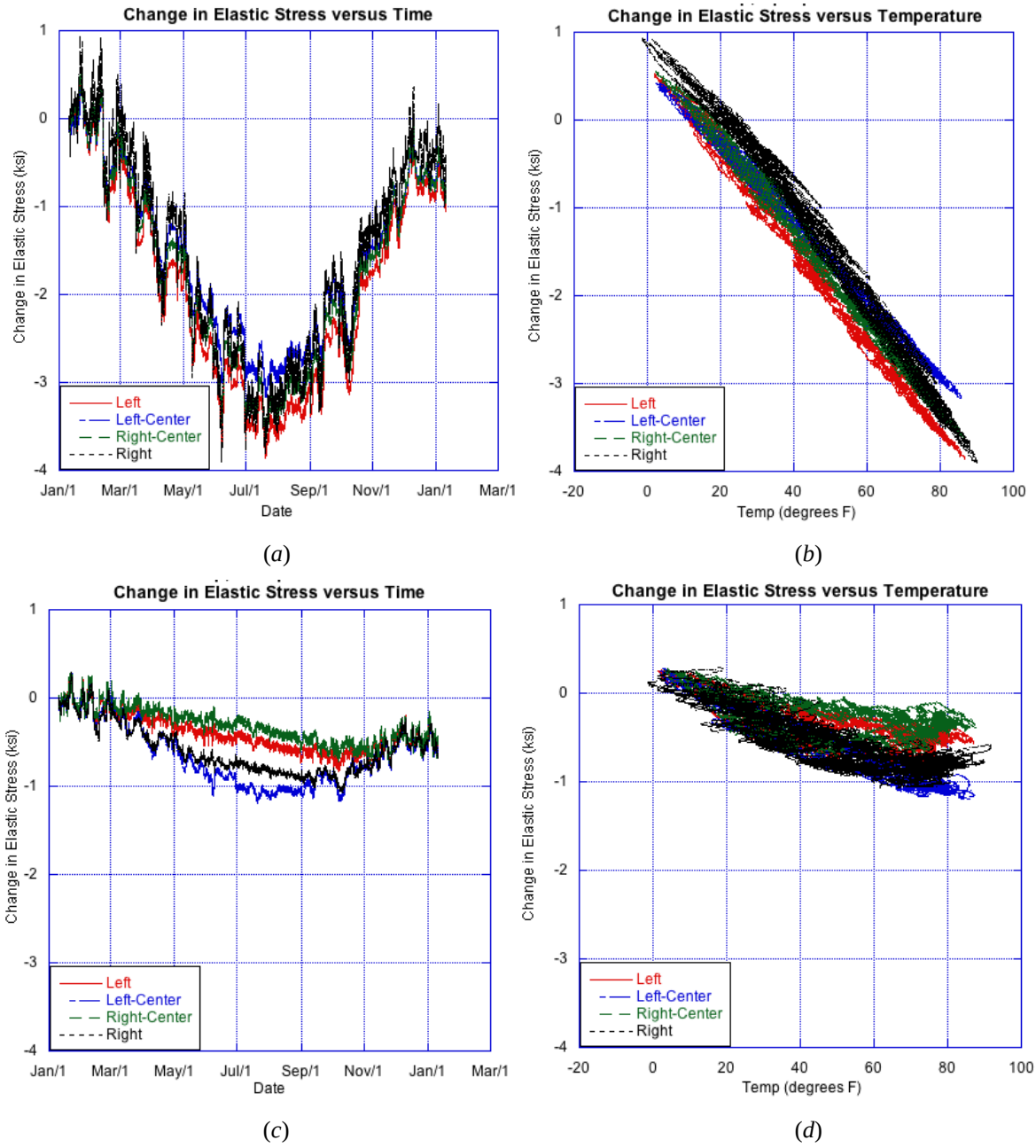

Figure B1: Pier 2, Top Section, Rusticated face of the up-station blade (RUTPier2) (a) Change in stress with time (b) change in stress with temperature; and smooth face of the up-station blade (SUTPier2) (c) Change in stress with time and (d) change in stress with temperature.

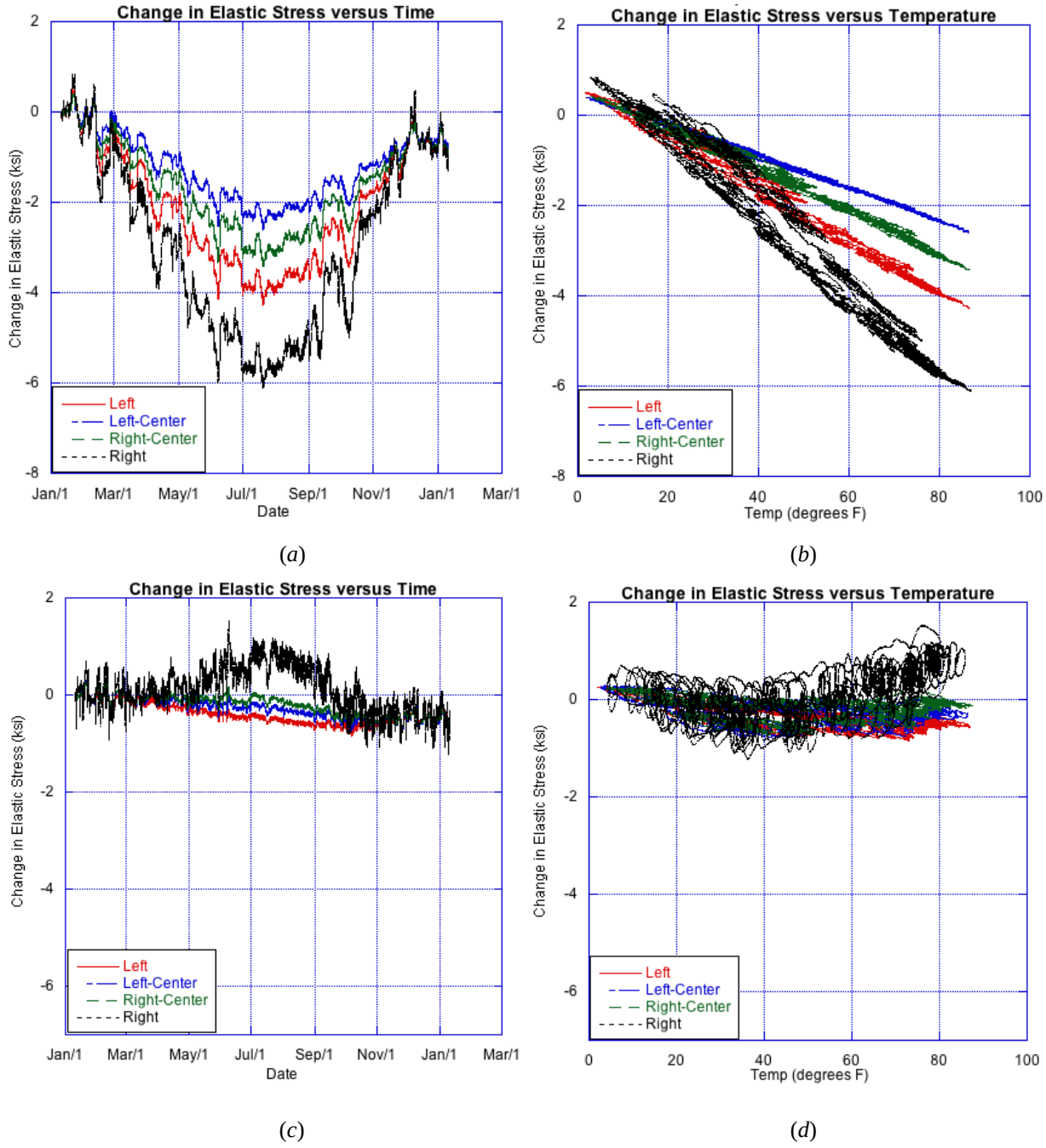

Figure B2: Pier 2, SDTPier2 (a) Change in stress with time (b) change in stress with temperature; and RDTPier2 (c) Change in stress with time and (d) change in stress with temperature.

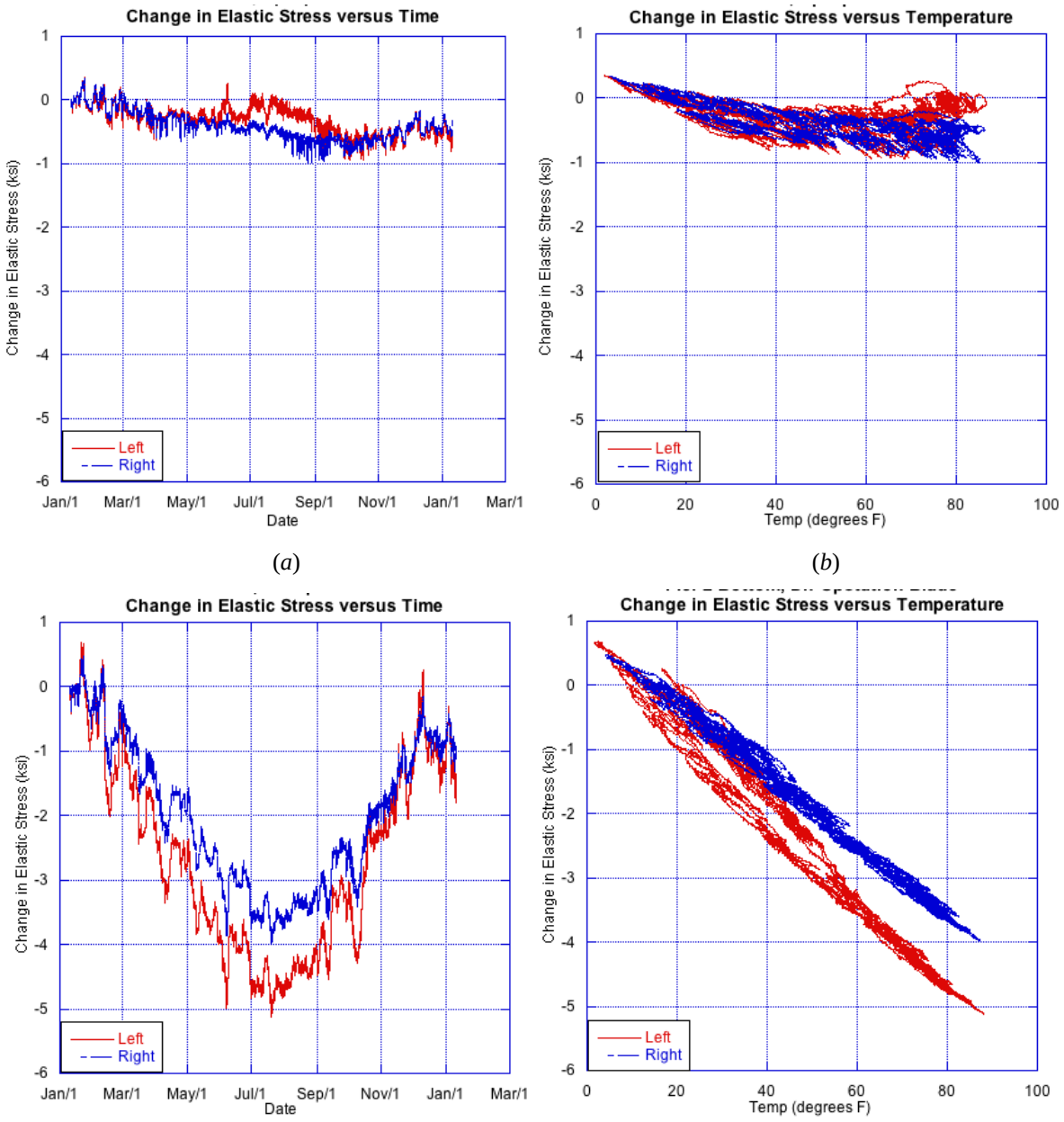

Figure B3: Pier 2, Bottom Section, RUBPier2 (a) Change in stress with time (b) change in stress with temperature; and SUBPier2 (c) Change in stress with time and (d) change in stress with temperature.

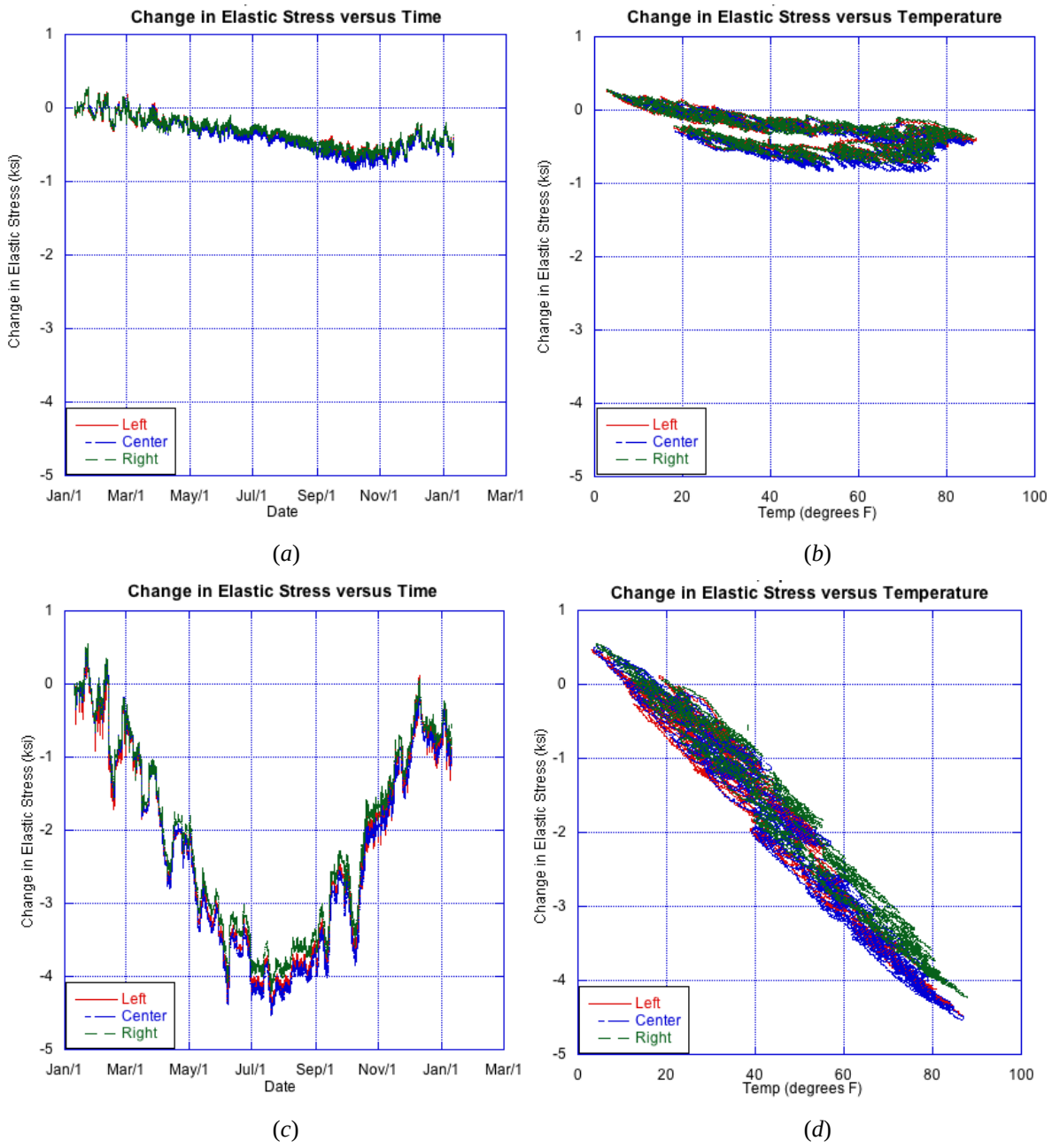

Figure B4: Pier 2, Bottom section, SDBPier2 (a) Change in stress with time (b) change in stress with temperature; and RDBPier2 (c) Change in stress with time and (d) change in stress with temperature.

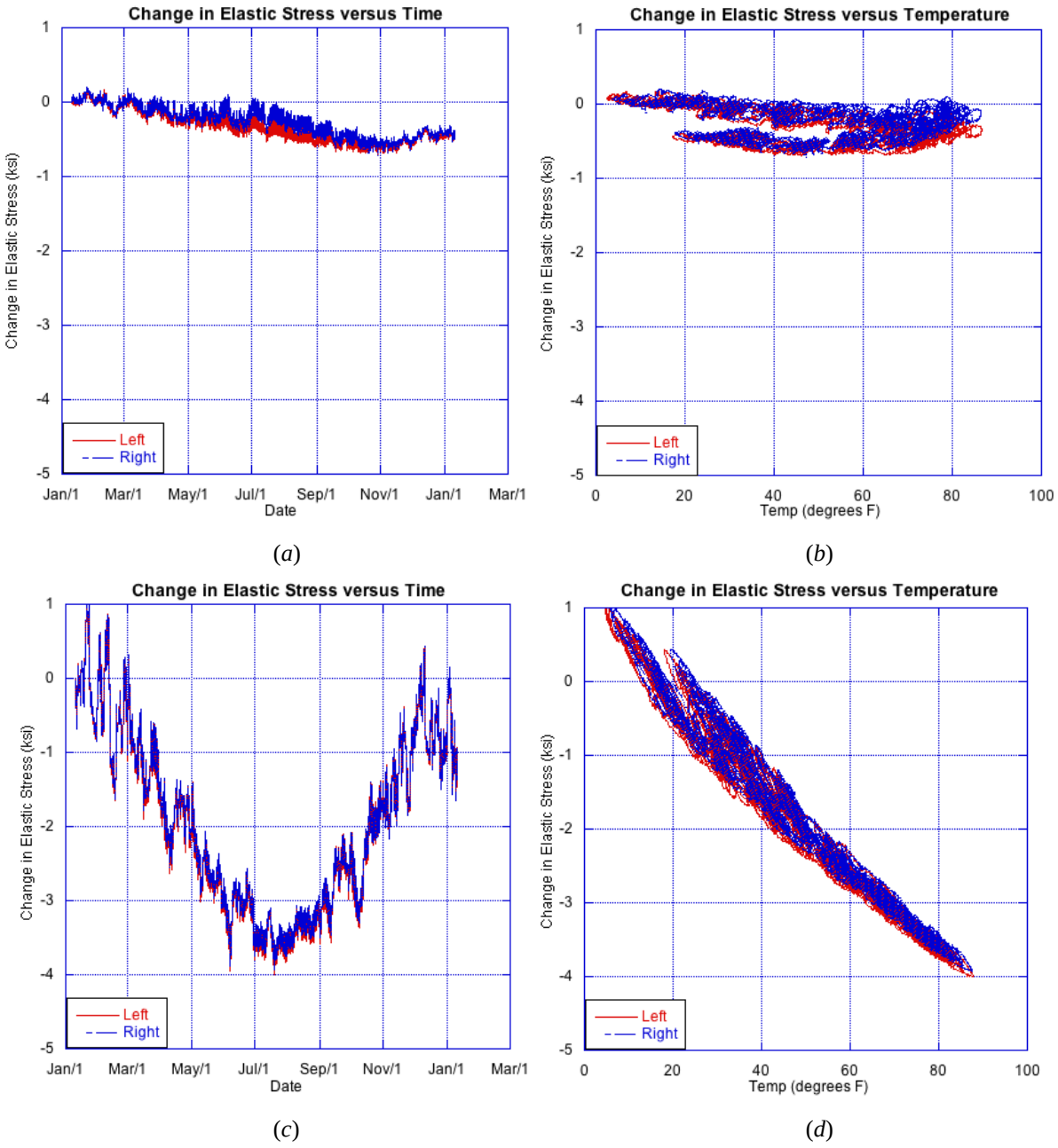

Figure B5: Pier 4, Top Section, SDTPier4 (a) Change in stress with time (b) change in stress with temperature; and RDTPier4 (c) Change in stress with time and (d) change in stress with temperature.

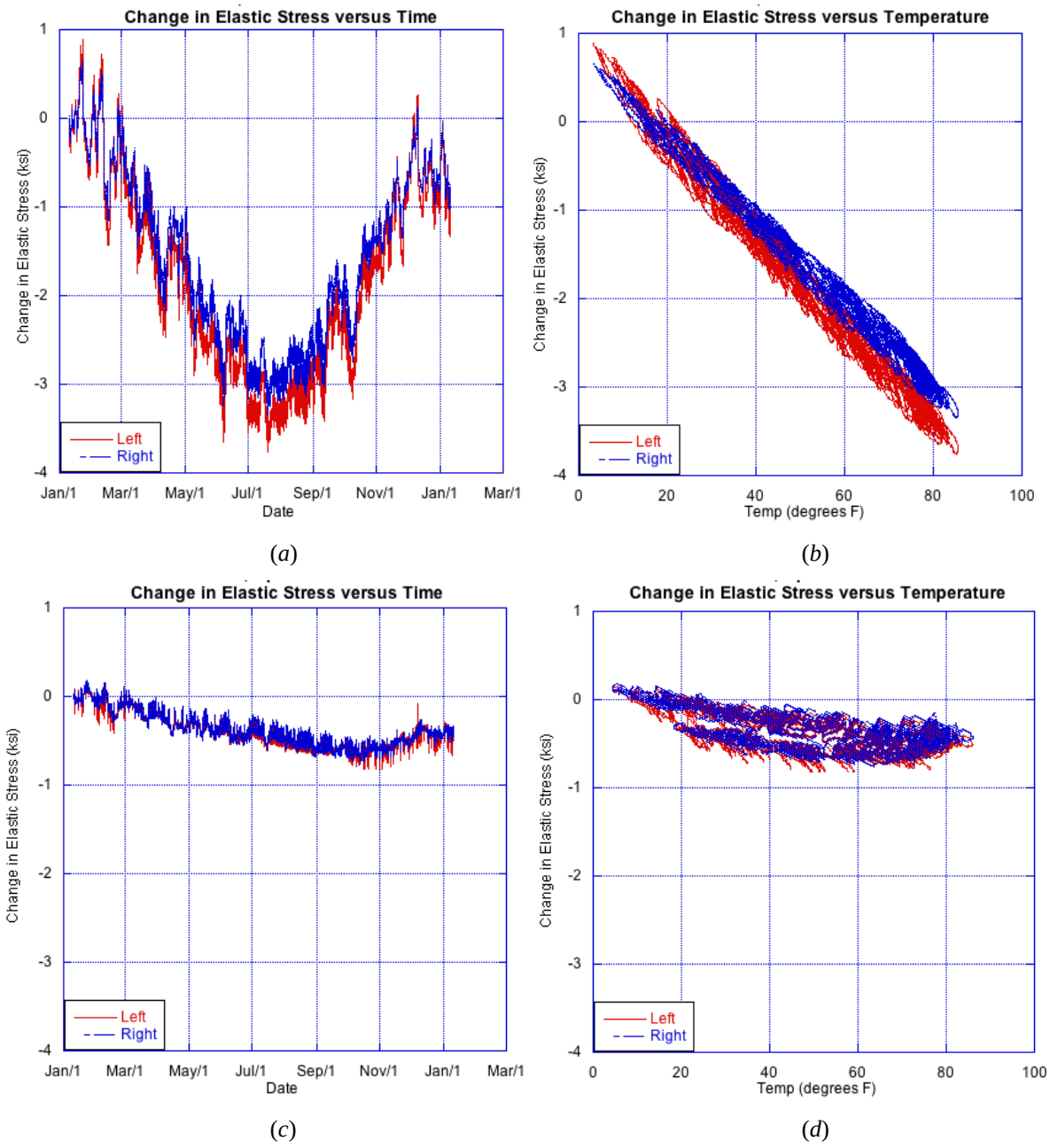

Figure B6: Pier 4, Bottom Section, SDBPier4 (a) Change in stress with time (b) change in stress with temperature; and RDBPier 4 (c) Change in stress with time and (d) change in stress with temperature.

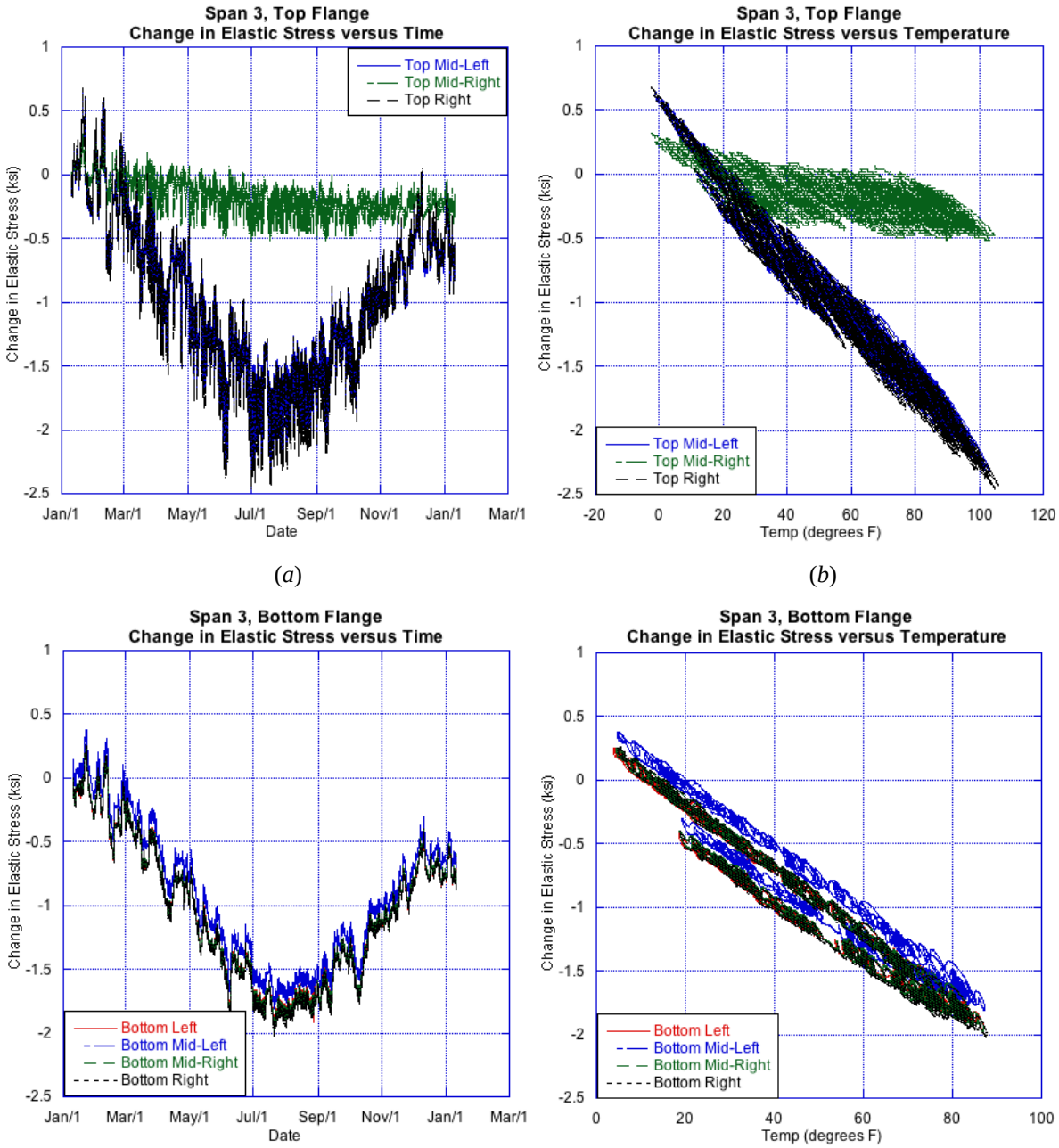

Figure B7: Span 3, Top flange (TSpan 3) (a) Change in stress with time (b) change in stress with temperature; and Bottom flange (BSpan 3) (c) Change in stress with time and (d) change in stress with temperature.

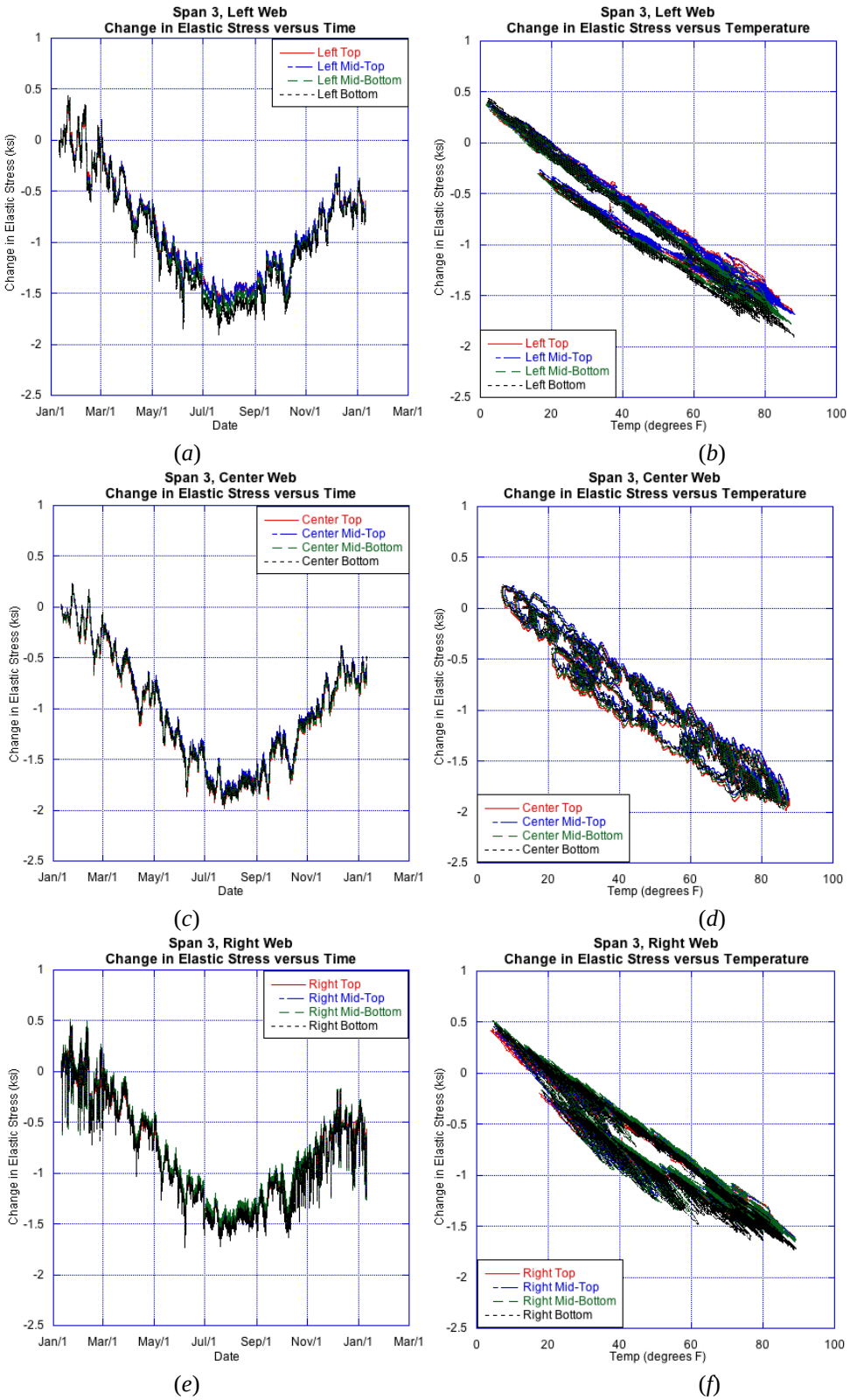

Figure B8: Span 3, Left web (LSpan 3) (a) Change in stress with time (b) change in stress with temperature; CSpan3 (c) Change in moment with time and (d) change in moment with temperature; and RSpan3 (e) Change in stress with time and (f) change in stress with temperature.

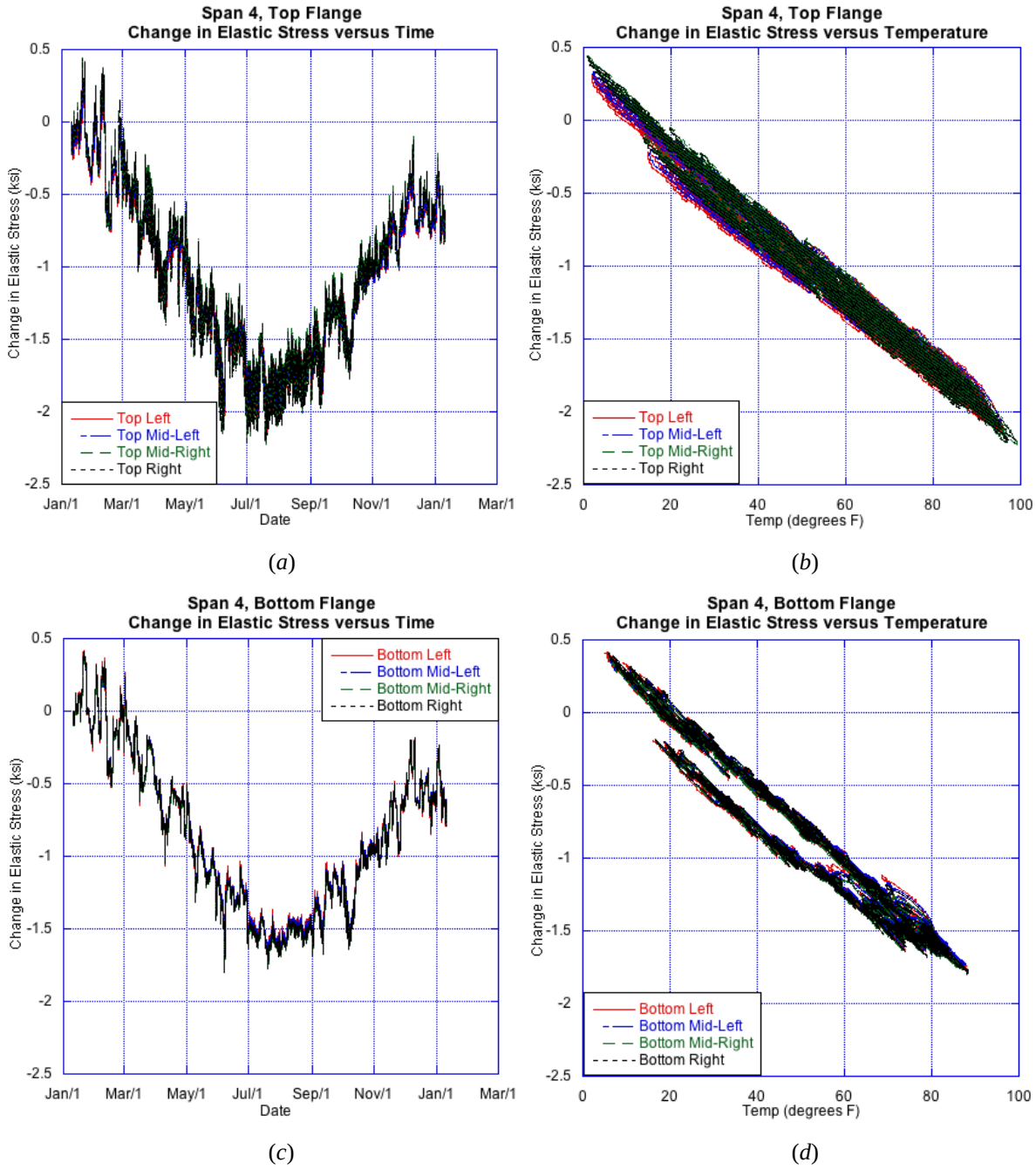

Figure B9: TSpan4 (a) Change in stress with time (b) change in stress with temperature; and BSpan4 (c) Change in stress with time and (d) change in stress with temperature.

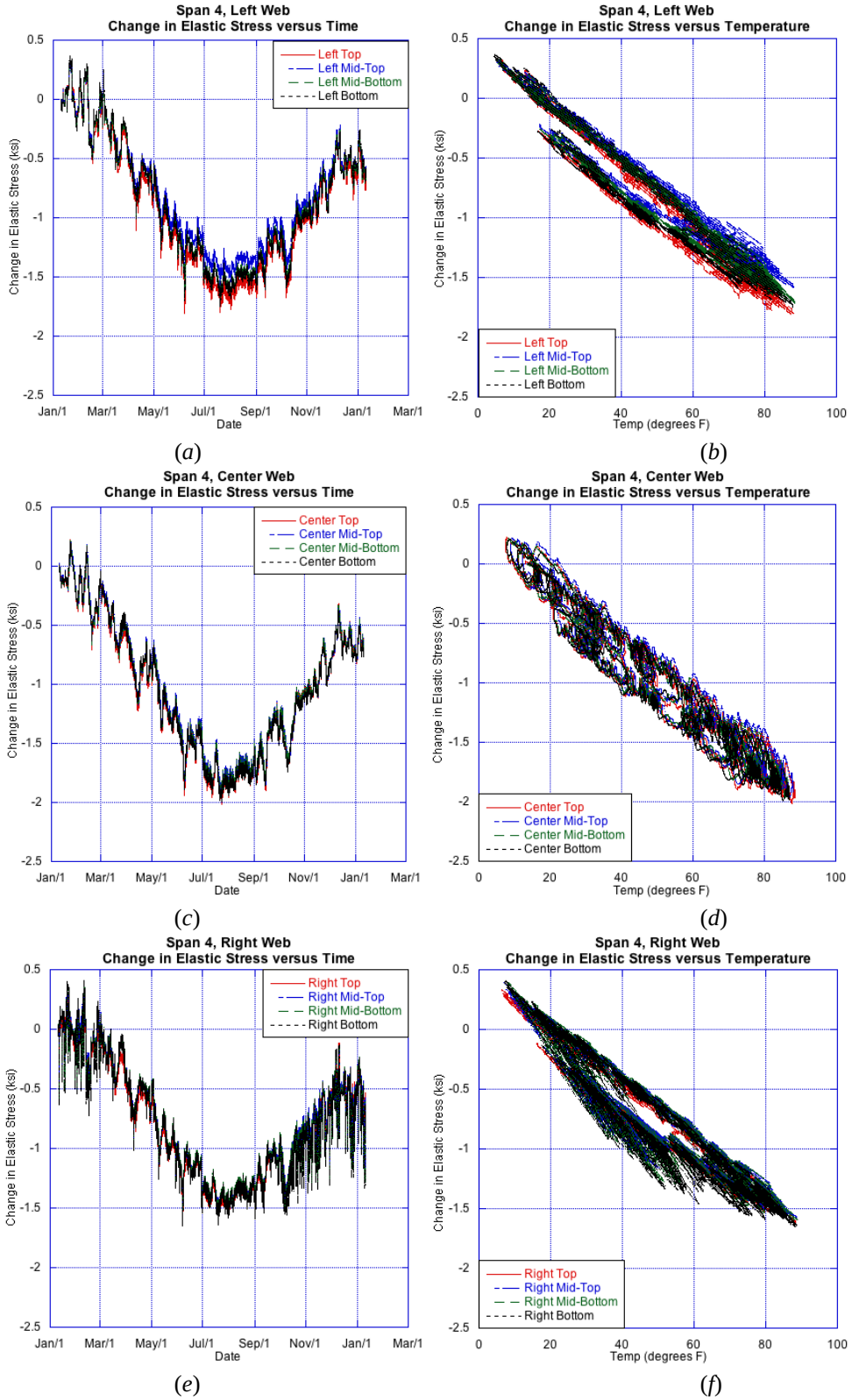

Figure B10: LSpan4 (a) Change in stress with time (b) change in stress with temperature; CSpan4 (c) Change in moment with time and (d) change in moment with temperature; and RSpan4 (e) Change in stress with time and (f) change in stress with temperature.

Appendix C: Manual Procedures for Calculating Pier Forces

1. Procedure A

$$P_U = \frac{\left(\Sigma\sigma_{Ui}\right)}{N} A_{blade} = \frac{A_{blade}}{8}\left(\sigma'_{U1} + 3\sigma_{U1} + 3\sigma_{U2} + \sigma'_{U2}\right); \quad \sigma_{U2} = \sigma'_{U2}$$

$$P_D = \frac{\left(\Sigma\sigma_{Di}\right)}{N} A_{blade} = \frac{A_{blade}}{8}\left(\sigma'_{D1} + 3\sigma_{D1} + 3\sigma_{D2} + \sigma'_{D2}\right); \quad \sigma_{D2} = \sigma'_{D2}$$

$$P_T = P_U + P_D$$

$$\bar{M}_U = \phi_U E_c I_n = \left(\frac{\varepsilon_{U1} - \varepsilon_{U2}}{d''_2}\right) E_c I_n = \left(\frac{\sigma_{U1} - \sigma_{U2}}{d''_2}\right) I_n$$

$$\bar{M}_D = \phi_D E_c I_n = \left(\frac{\varepsilon_{D2} - \varepsilon_{D1}}{d''_2}\right) E_c I_n = \left(\frac{\sigma_{D2} - \sigma_{D1}}{d''_2}\right) I_n$$

$$M_P = \frac{1}{2}\left(P_U - P_D\right) d_s$$

$$M_T = \bar{M}_U + \bar{M}_D + M_P$$

2. Procedure B

$$P_U = \Sigma\left(\sigma_{Ui} A_i\right) \cong \frac{A_{blade}}{8}\left(3\sigma_{U1} + 3\sigma_{U2}\right) + \frac{A_{blade}}{16}\left(2\sigma'_{U1} + 2\sigma'_{U2}\right)$$

$$P_U = \Sigma\left(\sigma_{Ui} A_i\right) \cong \frac{A_{blade}}{8}\left[3\left(\sigma_{U1} + \sigma_{U2}\right) + \left(\sigma'_{U1} + \sigma'_{U2}\right)\right]$$

$$P_D = \Sigma\left(\sigma_{Di} A_i\right) \cong \frac{A_{blade}}{8}\left[3\left(\sigma_{D1} + \sigma_{D2}\right) + \left(\sigma'_{D1} + \sigma'_{D2}\right)\right]$$

$$P_T = P_U + P_D$$

$$\tilde{M}_U \cong -\left(\frac{A_{blade}}{8}\right)\left(3\sigma_{U1} y_1\right) - \left(\frac{A_{blade}}{8}\right)\left(3\sigma_{U2} y_2\right) - \left(\frac{A_{blade}}{16}\right)\left(2\sigma'_{U1}\right) - \left(\frac{A_{blade}}{16}\right)\left(2\sigma'_{U2}\right)$$

$$\tilde{M}_U \cong -\left(\frac{A_{blade}}{8}\right)\left(3\sigma_{U1} y_1 + 3\sigma_{U2} y_2 + \sigma'_{U1} y'_1 + \sigma'_{U2} y'_2\right); \ \sigma_{U2} = \sigma'_{U2} \ \text{ and } \ y_2 = y'_2$$

$$\tilde{M}_D \cong -\left(\frac{A_{blade}}{8}\right)\left(3\sigma_{D1} y_1 + 3\sigma_{D2} y_2 + \sigma'_{D1} y'_1 + \sigma'_{D2} y'_2\right); \ \sigma_{D2} = \sigma'_{D2} \ \text{ and } \ y_2 = y'_2$$

$$M_T = \tilde{M}_U + \tilde{M}_D$$

3. <u>Numerical Constants</u>

$$A_{blade} = 10,841,400 \text{ mm}^2 = 10.8414 \text{ m}^2$$
$$d_s = 6,266 \text{ mm} = 6.266 \text{ m}$$
$$I_n = 7.04622 \times 10^{11} \text{ mm}^4 = 0.704622 \text{ m}^4$$
$$E_c = 25,044 \text{ MPa} = 2.5044 \times 10^{10} \text{ Pa}$$
$$d_2' = 990 - 267.5 - 77.5 \text{ mm} = 645 \text{ mm} = 0.645 \text{ m}$$
$$d_1' = 990 - 77.5 - 77.5 \text{ mm} = 835 \text{ mm} = 0.835 \text{ m}$$

Assuming that the A_i centroids coincide with the gauges, then:

$$y_1' = (7,380/2) - 77.5 \text{ mm} = 3,612.5 \text{ mm} = 3.6125 \text{ m}$$
$$y_1 = (7,380/2) - 267.5 \text{ mm} = 3,422.5 \text{ mm} = 3.4225 \text{ m}$$
$$y_2 = y_2' = (5,400/2) + 77.5 \text{ mm} = 2,777.5 \text{ mm} = 2.7775 \text{ m}$$

Assuming that the A_i centroids coincide with cross-sectional element centerlines, then:

$$y_1' = (7,380/2) - (190 + 400)/2 \text{ mm} = 3,395 \text{ mm} = 3.395 \text{ m}$$
$$y_1 = (7,380/2) - (190) - (400/2) \text{ mm} = 3,300 \text{ mm} = 3.30 \text{ m}$$
$$y_2 = y_2' = (5,400/2) + (400/2) \text{ mm} = 2,900 \text{ mm} = 2.90 \text{ m}$$

4. Notes

- This procedure was developed to check the forces and moments in the blades and section at the top elevation of Pier 2. It can be extended for the other elevations.
- Axial forces and stresses are positive in tension (negative in compression).
- Pier/blade moments are positive if they produce relative compression on the downstation blade/face and relative tension on the upstation blade/face (negative for relative tension on the downstation blade/face and relative compression on the upstation blade/face).
- These formulas are approximations which work best if stresses on a blade are approximately uniform or if they are produced by one-way bending with approximately uniform curvature along the length of the blades (i.e., the width of the pier).
- The moments $\bar{M}$ in Procedure A are about the centroid of each blade.
- The moments $\tilde{M}$ in Procedure B are about the centroid of the pier.
- The moments $\bar{M}$ and $\tilde{M}$ cannot be compared ($\tilde{M}$ includes M_P and $\bar{M}$ does not).
- For the Procedure B, the calculations are based on 10 gauges per blade, with the TUE1/TUE2/TDE1/TDE2 having counterparts at their symmetrically opposite locations that have the same strains as TUE1/TUE2/TDE1/TDE2. Each of these gauges (or virtual counterparts) has an influence area equal to $A_{blade}/16$, while all of the other gauges have an influence area that is twice as large ($A_{blade}/8$).
- Stress and gauge correspondence is as follows:

UPSTATION		**DOWNSTATION**	
Stress	**Gauge(s)**	**Stress**	**Gauge(s)**
σ'_{U1}	TUE1	σ'_{D1}	TDE1
σ_{U1}	TUL1, TUC1, TUR1	σ_{D1}	TDL1, TDC1, TDR1
σ_{U2}	TUL2, TUC2, TUR2	σ_{D2}	TDL2, TDC2, TDR2
σ'_{U2}	TUE2	σ'_{D2}	TDE2

MANUAL CALCULATIONS FOR TEST CASES

1. Case 1

Case 1 is defined as uniform tension stress of 10,000 Pa tension on the upstation blade and uniform compression stress of 10,000 Pa on the downstation blade.

$$\sigma'_{U1} = \sigma_{U1} = \sigma_{U2} = \sigma'_{U2} = +10{,}000 \text{ Pa} = +10 \text{ MPa}$$
$$\sigma'_{D1} = \sigma_{D1} = \sigma_{D2} = \sigma'_{D2} = -10{,}000 \text{ Pa} = -10 \text{ MPa}$$

Procedure A

$$P_U = \frac{A_{blade}}{8}\left(\sigma'_{U1} + 3\sigma_{U1} + 3\sigma_{U2} + \sigma'_{U2}\right) = \frac{\left(10.8414 \text{ m}^2\right)}{8}\left[8\left(10 \text{ MPa}\right)\right] = 108.414 \text{ kN}$$

$$P_D = \frac{A_{blade}}{8}\left(\sigma'_{D1} + 3\sigma_{D1} + 3\sigma_{D2} + \sigma'_{D2}\right) = \frac{\left(10.8414 \text{ m}^2\right)}{8}\left[8\left(-10 \text{ MPa}\right)\right] = -108.414 \text{ kN}$$

$$P_T = P_U + P_D = 108.414 - 108.414 = 0$$

$$\bar{M}_U = \left(\frac{\sigma_{U1} - \sigma_{U2}}{d'_2}\right) I_n = \left[\frac{\left(10 \text{ MPa}\right) - \left(10 \text{ MPa}\right)}{\left(0.645 \text{ m}\right)}\right]\left(0.704622 \text{ m}^4\right) = 0$$

$$\bar{M}_D = \left(\frac{\sigma_{D2} - \sigma_{D1}}{d'_2}\right) I_n = \left[\frac{\left(-10 \text{ MPa}\right) - \left(-10 \text{ MPa}\right)}{\left(0.645 \text{ m}\right)}\right]\left(0.704622 \text{ m}^4\right) = 0$$

$$M_P = \frac{1}{2}\left(P_U - P_D\right) d_s = \frac{1}{2}\left[\left(108.414 \text{ kN}\right) - \left(-108.414 \text{ kN}\right)\right]\left(6.266 \text{ m}\right) = 679.32 \text{ kN-m}$$

$$M_T = \bar{M}_U + \bar{M}_D + M_P = 0 + 0 + 679.32 = 679.32 \text{ kN-m}$$

Procedure B

$$P_U = \frac{A_{blade}}{8}\left[3\left(\sigma_{U1} + \sigma_{U2}\right) + \left(\sigma'_{U1} + \sigma'_{U2}\right)\right]$$

$$P_U = \frac{\left(10.8414 \text{ m}^2\right)}{8}\left[3\left(10 + 10 \text{ MPa}\right) + \left(10 + 10 \text{ MPa}\right)\right] = 108.414 \text{ kN}$$

$$P_D = \frac{A_{blade}}{8}\left[3\left(\sigma_{D1} + \sigma_{D2}\right) + \left(\sigma'_{D1} + \sigma'_{D2}\right)\right]$$

$$P_D = \frac{\left(10.8414 \text{ m}^2\right)}{8}\left[3\left(-10 - 10 \text{ MPa}\right) + \left(-10 - 10 \text{ MPa}\right)\right] = -108.414 \text{ kN}$$

$$P_T = P_U + P_D = 108.414 - 108.414 \text{ kN} = 0$$

$$\tilde{M}_U = -\left(\frac{A_{blade}}{8}\right)\left(3\sigma_{U1}y_1 + 3\sigma_{U2}y_2 + \sigma'_{U1}y'_1 + \sigma'_{U2}y'_2\right)$$

$$\tilde{M}_U = -\left(\frac{10.8414}{8}\right)\left[\left(3\left(-3.6125 - 3.4225\right) + 2\left(-2.7775\right)\right)\left(+10\right)\right] = 361.29 \text{ kN-m}$$

$$\tilde{M}_D = -\left(\frac{A_{blade}}{8}\right)\left(3\sigma_{D1}y_1 + 3\sigma_{D2}y_2 + \sigma'_{D1}y'_1 + \sigma'_{D2}y'_2\right)$$

$$\tilde{M}_D = -\left(\frac{10.8414}{8}\right)\left[\left(3(3.6125+3.4225)+2(2.7775)\right)(-10)\right] = 361.29 \text{ MPa}$$

$$M_T = \tilde{M}_U + \tilde{M}_D = 361.29 + 361.29 = 722.57 \text{ kN-m}$$

If we use the alternate centroidal distances y_i:

$$\tilde{M}_U = \tilde{M}_D = 350.79 \text{ kN-m} \quad \text{and} \quad M_T = 701.57 \text{ kN-m}$$

2. Case 2

Case 2 is a uniform stress of 10,000 Pa compression on upstation and downstation blades.

$$\sigma'_{U1} = \sigma_{U1} = \sigma_{U2} = \sigma'_{U2} = \sigma'_{D1} = \sigma_{D1} = \sigma_{D2} = \sigma'_{D2} = -10{,}000 \text{ Pa} = -10 \text{ MPa}$$

Procedure A

$$P_U = \frac{A_{blade}}{8}\left(\sigma'_{U1} + 3\sigma_{U1} + 3\sigma_{U2} + \sigma'_{U2}\right) = \frac{\left(10.8414 \text{ m}^2\right)}{8}\left[8\left(-10 \text{ MPa}\right)\right] = -108.414 \text{ kN}$$

$$P_D = \frac{A_{blade}}{8}\left(\sigma'_{D1} + 3\sigma_{D1} + 3\sigma_{D2} + \sigma'_{D2}\right) = \frac{\left(10.8414 \text{ m}^2\right)}{8}\left[8\left(-10 \text{ MPa}\right)\right] = -108.414 \text{ kN}$$

$$P_T = P_U + P_D = -108.414 - 108.414 = -216.828 \text{ kN-m}$$

$$\bar{M}_U = \left(\frac{\sigma_{U1} - \sigma_{U2}}{d'_2}\right) I_n = \left[\frac{\left(-10 \text{ MPa}\right) - \left(-10 \text{ MPa}\right)}{\left(0.645 \text{ m}\right)}\right]\left(0.704622 \text{ m}^4\right) = 0$$

$$\bar{M}_D = \left(\frac{\sigma_{D2} - \sigma_{D1}}{d'_2}\right) I_n = \left[\frac{\left(-10 \text{ MPa}\right) - \left(-10 \text{ MPa}\right)}{\left(0.645 \text{ m}\right)}\right]\left(0.704622 \text{ m}^4\right) = 0$$

$$M_P = \frac{1}{2}\left(P_U - P_D\right) d_s = \frac{1}{2}\left[\left(-108.414 \text{ kN}\right) - \left(-108.414 \text{ kN}\right)\right]\left(6.266 \text{ m}\right) = 0$$

$$M_T = \bar{M}_U + \bar{M}_D + M_P = 0$$

Procedure B

$$P_U = \frac{A_{blade}}{8}\left[3\left(\sigma_{U1} + \sigma_{U2}\right) + \left(\sigma'_{U1} + \sigma'_{U2}\right)\right]$$

$$P_U = \frac{\left(10.8414 \text{ m}^2\right)}{8}\left[3\left(-10 - 10 \text{ MPa}\right) + \left(-10 - 10 \text{ MPa}\right)\right] = -108.414 \text{ kN}$$

$$P_D = \frac{A_{blade}}{8}\left[3\left(\sigma_{D1} + \sigma_{D2}\right) + \left(\sigma'_{D1} + \sigma'_{D2}\right)\right]$$

$$P_D = \frac{\left(10.8414 \text{ m}^2\right)}{8}\left[3\left(-10 - 10 \text{ MPa}\right) + \left(-10 - 10 \text{ MPa}\right)\right] = -108.414 \text{ kN}$$

$$P_T = P_U + P_D = -108.414 - 108.414 \text{ kN} = -216.828 \text{ kN}$$

$$\tilde{M}_U = -\left(\frac{A_{blade}}{8}\right)\left(3\sigma_{U1}y_1 + 3\sigma_{U2}y_2 + \sigma'_{U1}y'_1 + \sigma'_{U2}y'_2\right)$$

$$\tilde{M}_U = -\left(\frac{10.8414}{8}\right)\left[\left(3\left(-3.6125 - 3.4225\right) + 2\left(-2.7775\right)\right)\left(-10\right)\right] = -361.29 \text{ kN-m}$$

$$\tilde{M}_D = -\left(\frac{A_{blade}}{8}\right)\left(3\sigma_{D1}y_1 + 3\sigma_{D2}y_2 + \sigma'_{D1}y'_1 + \sigma'_{D2}y'_2\right)$$

$$\tilde{M}_D = -\left(\frac{10.8414}{8}\right)\left[\left(3(3.6125+3.4225)+2(2.7775)\right)(-10)\right] = 361.29 \text{ MPa}$$

$$M_T = \tilde{M}_U + \tilde{M}_D = -361.29 + 361.29 = 0$$

If we use the alternate centroidal distances y_i:

$$\tilde{M}_U = -350.79 \text{ kN-m}; \quad \tilde{M}_D = 350.79 \text{ kN-m} \quad \text{and} \quad M_T = 0$$

3. Case 3

Case 3 is a symmetric stress state for the two blades, with 10,000 Pa tension in the linear array of gauges closest to the outer faces of the blades, and 10,000 Pa compression in the linear array of gauges closest to the inner faces of the blades.

$$\sigma'_{U1} = +15{,}891 \text{ Pa}; \quad \sigma_{U1} = +10{,}000 \text{ Pa}; \quad \sigma_{U2} = \sigma'_{U2} = -10{,}000 \text{ Pa}$$
$$\sigma_{D2} = \sigma'_{D2} = -10{,}000 \text{ Pa}; \quad \sigma'_{D1} = +15{,}891 \text{ Pa}; \quad \sigma_{D1} = +10{,}000 \text{ Pa};$$

Procedure A

$$P_U = \frac{A_{blade}}{8}\left(\sigma'_{U1} + 3\sigma_{U1} + 3\sigma_{U2} + \sigma'_{U2}\right) = \frac{(10.8414)}{8}\left[(15.891) + 3(10) + 4(-10)\right]$$
$$P_U = 7.983 \text{ kN}$$
$$P_D = \frac{A_{blade}}{8}\left(\sigma'_{D1} + 3\sigma_{D1} + 3\sigma_{D2} + \sigma'_{D2}\right) = \frac{(10.8414)}{8}\left[(15.891) + 3(10) + 4(-10)\right]$$
$$P_D = 7.983 \text{ kN}$$
$$P_T = P_U + P_D = 7.983 + 7.983 = 15.967 \text{ kN}$$
$$\bar{M}_U = \left(\frac{\sigma_{U1} - \sigma_{U2}}{d'_2}\right) I_n = \left[\frac{(10) - (-10)}{(0.645)}\right](0.704622 \text{ m}^4) = 21.849 \text{ kN-m}$$
$$\bar{M}_D = \left(\frac{\sigma_{D2} - \sigma_{D1}}{d'_2}\right) I_n = \left[\frac{(-10) - (10)}{(0.645)}\right](0.704622 \text{ m}^4) = -21.849 \text{ kN-m}$$
$$M_P = \frac{1}{2}(P_U - P_D) d_s = \frac{1}{2}\left[(7.983 \text{ kN}) - (7.983 \text{ kN})\right](6.266 \text{ m}) = 0$$
$$M_T = \bar{M}_U + \bar{M}_D + M_P = 21.849 - 21.849 + 0 = 0$$

Procedure B

$$P_U = \frac{A_{blade}}{8}\left[3(\sigma_{U1} + \sigma_{U2}) + (\sigma'_{U1} + \sigma'_{U2})\right]$$
$$P_U = \frac{(10.8414)}{8}\left[3(10 - 10) + (15.891 - 10)\right] = 7.983 \text{ kN}$$
$$P_D = \frac{A_{blade}}{8}\left[3(\sigma_{D1} + \sigma_{D2}) + (\sigma'_{D1} + \sigma'_{D2})\right]$$
$$P_D = \frac{(10.8414)}{8}\left[3(10 - 10) + (15.891 - 10)\right] = 7.983 \text{ kN}$$
$$P_T = P_U + P_D = 7.983 + 7.983 = 15.967 \text{ kN}$$

$$\tilde{M}_U = -\left(\frac{A_{blade}}{8}\right)\left(3\sigma_{U1}y_1 + 3\sigma_{U2}y_2 + \sigma'_{U1}y'_1 + \sigma'_{U2}y'_2\right)$$

$$\tilde{M}_U = -\left(\frac{10.8414}{8}\right)\left[3(10)(-3.4225) + 3(-10)(-2.7775) + (15.891)(-3.6125)\right]$$

$$-\left(\frac{10.8414}{8}\right)\left[+(-10)(-2.7775)\right] = 66.378 \text{ kN-m}$$

$$\tilde{M}_D = -\left(\frac{A_{blade}}{8}\right)\left(3\sigma_{D1}y_1 + 3\sigma_{D2}y_2 + \sigma'_{D1}y'_1 + \sigma'_{D2}y'_2\right)$$

$$\tilde{M}_D = -\left(\frac{10.8414}{8}\right)\left[3(10)(3.4225) + 3(-10)(2.7775) + (15.891)(3.6125)\right]$$

$$-\left(\frac{10.8414}{8}\right)\left[(-10)(2.7775)\right] = -66.378 \text{ kN-m}$$

$$M_T = \tilde{M}_U + \tilde{M}_D = 66.378 - 66.378 = 0$$

If we use the alternate centroidal distances y_i:

$$\tilde{M}_U = -\left(\frac{10.8414}{8}\right)\left[3(10)(-3.30) + 3(-10)(-2.90) + (15.891)(-3.395)\right]$$

$$-\left(\frac{10.8414}{8}\right)\left[+(-10)(-2.90)\right] = 50.074 \text{ kN-m}$$

$$\tilde{M}_D = -\left(\frac{10.8414}{8}\right)\left[3(10)(3.30) + 3(-10)(2.90) + (15.891)(3.395)\right]$$

$$-\left(\frac{10.8414}{8}\right)\left[(-10)(2.90)\right] = -50.074 \text{ kN-m}$$

$$M_T = \tilde{M}_U + \tilde{M}_D = 0$$

4. Case 4

Case 4 is an anti-symmetric stress state with 10,000 Pa tension in the linear array of gauges closest to the upstation faces of the blades, and 10,000 Pa compression in the linear array of gauges closest to the downstation faces of the blades.

$$\sigma'_{U1} = +15{,}891 \text{ Pa}; \quad \sigma_{U1} = +10{,}000 \text{ Pa}; \quad \sigma_{U2} = \sigma'_{U2} = -10{,}000 \text{ Pa}$$
$$\sigma'_{D1} = -15{,}891 \text{ Pa}; \quad \sigma_{D1} = -10{,}000 \text{ Pa}; \quad \sigma_{D2} = \sigma'_{D2} = +10{,}000 \text{ Pa}$$

Procedure A

$$P_U = \frac{A_{blade}}{8}\left(\sigma'_{U1} + 3\sigma_{U1} + 3\sigma_{U2} + \sigma'_{U2}\right) = \frac{(10.8414)}{8}\left[(15.891) + 3(10) + 4(-10)\right]$$
$$P_U = 7.983 \text{ kN}$$
$$P_D = \frac{A_{blade}}{8}\left(\sigma'_{D1} + 3\sigma_{D1} + 3\sigma_{D2} + \sigma'_{D2}\right) = \frac{(10.8414)}{8}\left[(-15.891) + 3(-10) + 4(10)\right]$$
$$P_D = -7.983 \text{ kN}$$
$$P_T = P_U + P_D = 7.983 - 7.983 = 0$$
$$\bar{M}_U = \left(\frac{\sigma_{U1} - \sigma_{U2}}{d'_2}\right) I_n = \left[\frac{(10) - (-10)}{(0.645)}\right](0.704622 \text{ m}^4) = 21.849 \text{ kN-m}$$
$$\bar{M}_D = \left(\frac{\sigma_{D2} - \sigma_{D1}}{d'_2}\right) I_n = \left[\frac{(10) - (-10)}{(0.645)}\right](0.704622 \text{ m}^4) = 21.849 \text{ kN-m}$$
$$M_P = \frac{1}{2}(P_U - P_D) d_s = \frac{1}{2}\left[(7.983 \text{ kN}) - (-7.983 \text{ kN})\right](6.266 \text{ m}) = 50.021 \text{ kN-m}$$
$$M_T = \bar{M}_U + \bar{M}_D + M_P = 21.849 + 21.849 + 50.021 = 93.719 \text{ kN-m}$$

Procedure B

$$P_U = \frac{A_{blade}}{8}\left[3(\sigma_{U1} + \sigma_{U2}) + (\sigma'_{U1} + \sigma'_{U2})\right]$$
$$P_U = \frac{(10.8414)}{8}\left[3(10 - 10) + (15.891 - 10)\right] = 7.983 \text{ kN}$$
$$P_D = \frac{A_{blade}}{8}\left[3(\sigma_{D1} + \sigma_{D2}) + (\sigma'_{D1} + \sigma'_{D2})\right]$$
$$P_D = \frac{(10.8414)}{8}\left[3(-10 + 10) + (-15.891 + 10)\right] = -7.983 \text{ kN}$$
$$P_T = P_U + P_D = 7.983 - 7.983 = 0$$

$$\tilde{M}_U = -\left(\frac{A_{blade}}{8}\right)\left(3\sigma_{U1}y_1 + 3\sigma_{U2}y_2 + \sigma'_{U1}y'_1 + \sigma'_{U2}y'_2\right)$$

$$\tilde{M}_U = -\left(\frac{10.8414}{8}\right)\left[3(10)(-3.4225) + 3(-10)(-2.7775) + (15.891)(-3.6125)\right]$$

$$-\left(\frac{10.8414}{8}\right)\left[(-10)(-2.7775)\right] = 66.378 \text{ kN-m}$$

$$\tilde{M}_D = -\left(\frac{A_{blade}}{8}\right)\left(3\sigma_{D1}y_1 + 3\sigma_{D2}y_2 + \sigma'_{D1}y'_1 + \sigma'_{D2}y'_2\right)$$

$$\tilde{M}_D = -\left(\frac{10.8414}{8}\right)\left[3(-10)(3.4225) + 3(10)(2.7775) + (-15.891)(3.6125)\right]$$

$$-\left(\frac{10.8414}{8}\right)\left[(10)(2.7775)\right] = 66.378 \text{ kN-m}$$

$$M_T = \tilde{M}_U + \tilde{M}_D = 66.378 + 66.378 = 132.756 \text{ kN-m}$$

If we use the alternate centroidal distances y_i:

$$\tilde{M}_U = -\left(\frac{10.8414}{8}\right)\left[3(10)(-3.30) + 3(-10)(-2.90) + (15.891)(-3.395)\right]$$

$$-\left(\frac{10.8414}{8}\right)\left[+(-10)(-2.90)\right] = 50.073 \text{ kN-m}$$

$$\tilde{M}_D = -\left(\frac{10.8414}{8}\right)\left[3(-10)(3.30) + 3(10)(2.90) + (-15.891)(3.395)\right]$$

$$-\left(\frac{10.8414}{8}\right)\left[(10)(2.90)\right] = 50.073 \text{ kN-m}$$

$$M_T = \tilde{M}_U + \tilde{M}_D = 50.073 + 50.073 = 100.147 \text{ kN-m}$$

5. Case 5

Case 5 is a combination of a linear (flexural) variation in stress combined with a constant (axial compression) strain distribution. The upstation face of the upstation blade has the compression stresses of largest magnitude, while the downstation face of the downstation blade has those with the smallest magnitude.

$$\sigma'_{U1} = -34{,}000 \text{ Pa} \; ; \quad \sigma_{U1} = -33{,}132 \text{ Pa} \; ; \quad \sigma_{U2} = \sigma'_{U2} = -30{,}186 \text{ Pa}$$

$$\sigma'_{D1} = -1{,}000 \text{ Pa} \; ; \quad \sigma_{D1} = -1{,}868 \text{ Pa} \; ; \quad \sigma_{D2} = \sigma'_{D2} = -4{,}814 \text{ Pa}$$

Procedure A

$$P_U = \frac{A_{blade}}{8}\left(\sigma'_{U1} + 3\sigma_{U1} + 3\sigma_{U2} + \sigma'_{U2}\right)$$

$$P_U = \frac{(10.8414)}{8}\left[(-34) + 3(-33.132) + 4(-30.186)\right] = -344.675 \text{ kN}$$

$$P_D = \frac{A_{blade}}{8}\left(\sigma'_{D1} + 3\sigma_{D1} + 3\sigma_{D2} + \sigma'_{D2}\right)$$

$$P_U = \frac{(10.8414)}{8}\left[(-1) + 3(-1.868) + 4(-4.814)\right] = -35.045 \text{ kN}$$

$$P_T = P_U + P_D = -344.675 - 35.045 = -379.72 \text{ kN-m}$$

$$\bar{M}_U = \left(\frac{\sigma_{U1} - \sigma_{U2}}{d'_2}\right) I_n = \left[\frac{(-33.132) - (-30.186)}{(0.645)}\right](0.704622 \text{ m}^4) = -3.218 \text{ kN-m}$$

$$\bar{M}_D = \left(\frac{\sigma_{D2} - \sigma_{D1}}{d'_2}\right) I_n = \left[\frac{(-4.814) - (-1.868)}{(0.645)}\right](0.704622 \text{ m}^4) = -3.218 \text{ kN-m}$$

$$M_P = \frac{1}{2}(P_U - P_D) d_s = \frac{1}{2}\left[(-344.675) - (-35.045 \text{ kN})\right](6.266 \text{ m}) = -970.071 \text{ kN-m}$$

$$M_T = \bar{M}_U + \bar{M}_D + M_P = -3.218 - 3.218 - 970.071 = -976.507 \text{ kN-m}$$

Procedure B

$$P_U = \frac{A_{blade}}{8}\left[3(\sigma_{U1} + \sigma_{U2}) + (\sigma'_{U1} + \sigma'_{U2})\right]$$

$$P_U = \frac{(10.8414)}{8}\left[3(-33.132 - 30.186) + (-34 - 30.186)\right] = -344.404 \text{ kN}$$

$$P_D = \frac{A_{blade}}{8}\left[3(\sigma_{D1} + \sigma_{D2}) + (\sigma'_{D1} + \sigma'_{D2})\right]$$

$$P_D = \frac{(10.8414)}{8}\left[3(-1.868 - 4.814) + (-1 - 4.814)\right] = -35.045 \text{ kN}$$

$$P_T = P_U + P_D = -344.404 - 35.045 = -379.449$$

$$\tilde{M}_U = -\left(\frac{A_{blade}}{8}\right)\left(3\sigma_{U1}y_1 + 3\sigma_{U2}y_2 + \sigma'_{U1}y'_1 + \sigma'_{U2}y'_2\right)$$

$$\tilde{M}_U = -\left(\frac{10.8414}{8}\right)\left[3(-33.132)(-3.4225) + 3(-30.186)(-2.7775) + (-34)(-3.6125)\right]$$

$$-\left(\frac{10.8414}{8}\right)\left[(-30.186)(-2.7775)\right] = -1,081.937 \text{ kN-m}$$

$$\tilde{M}_D = -\left(\frac{A_{blade}}{8}\right)\left(3\sigma_{D1}y_1 + 3\sigma_{D2}y_2 + \sigma'_{D1}y'_1 + \sigma'_{D2}y'_2\right)$$

$$\tilde{M}_D = -\left(\frac{10.8414}{8}\right)\left[3(-1.868)(3.4225) + 3(-4.814)(2.7775) + (-1)(3.6125)\right]$$

$$-\left(\frac{10.8414}{8}\right)\left[(-4.814)(2.7775)\right] = 103.367 \text{ kN-m}$$

$$M_T = \tilde{M}_U + \tilde{M}_D = -1,081.937 + 103.367 = -978.57 \text{ kN-m}$$

If we use the alternate centroidal distances y_i:

$$\tilde{M}_U = -\left(\frac{10.8414}{8}\right)\left[3(-33.132)(-3.30) + 3(-30.186)(-2.90) + (-34)(-3.395)\right]$$

$$-\left(\frac{10.8414}{8}\right)\left[+(-30.186)(-2.90)\right] = -1,075.459 \text{ kN-m}$$

$$\tilde{M}_D = -\left(\frac{10.8414}{8}\right)\left[3(-1.868)(3.30) + 3(-4.814)(2.90) + (-1)(3.395)\right]$$

$$-\left(\frac{10.8414}{8}\right)\left[(-4.814)(2.90)\right] = 105.339 \text{ kN-m}$$

$$M_T = \tilde{M}_U + \tilde{M}_D = -1,075.459 + 105.339 = -970.12 \text{ kN-m}$$

6. Case 6

Case 6 is a nonlinear combination of piecewise linear (flexural) variations in stress combined with a constant (axial compression) strain distribution. The upstation blade has larger compression stresses than the downstation blade.

$$\sigma'_{U1} = -24{,}132 \text{ Pa}\,; \quad \sigma_{U1} = -25{,}000 \text{ Pa}\,; \quad \sigma_{U2} = \sigma'_{U2} = -27{,}946 \text{ Pa}$$
$$\sigma'_{D1} = -5{,}868 \text{ Pa}\,; \quad \sigma_{D1} = -5{,}000 \text{ Pa}\,; \quad \sigma_{D2} = \sigma'_{D2} = -2{,}054 \text{ Pa}$$

Procedure A

$$P_U = \frac{A_{blade}}{8}\left(\sigma'_{U1} + 3\sigma_{U1} + 3\sigma_{U2} + \sigma'_{U2}\right)$$
$$P_U = \frac{(10.8414)}{8}\left[(-24.132) + 3(-25) + 4(-27.946)\right] = -285.828 \text{ kN}$$
$$P_D = \frac{A_{blade}}{8}\left(\sigma'_{D1} + 3\sigma_{D1} + 3\sigma_{D2} + \sigma'_{D2}\right)$$
$$P_U = \frac{(10.8414)}{8}\left[(-5.868) + 3(-5) + 4(-2.054)\right] = -39.414 \text{ kN}$$
$$P_T = P_U + P_D = -285.828 - 39.414 = -325.242$$
$$\bar{M}_U = \left(\frac{\sigma_{U1} - \sigma_{U2}}{d'_2}\right) I_n = \left[\frac{(-25) - (-27.946)}{(0.645)}\right](0.704622 \text{ m}^4) = 3.218 \text{ kN-m}$$
$$\bar{M}_D = \left(\frac{\sigma_{D2} - \sigma_{D1}}{d'_2}\right) I_n = \left[\frac{(-2.054) - (-5)}{(0.645)}\right](0.704622 \text{ m}^4) = 3.218 \text{ kN-m}$$
$$M_P = \frac{1}{2}(P_U - P_D)\, d_s = \frac{1}{2}\left[(-285.828) - (-39.414 \text{ kN})\right](6.266 \text{ m}) = -772.015 \text{ kN-m}$$
$$M_T = \bar{M}_U + \bar{M}_D + M_P = 3.218 + 3.218 - 772.015 = -765.579 \text{ kN-m}$$

Procedure B

$$P_U = \frac{A_{blade}}{8}\left[3(\sigma_{U1} + \sigma_{U2}) + (\sigma'_{U1} + \sigma'_{U2})\right]$$
$$P_U = \frac{(10.8414)}{8}\left[3(-25 - 27.946) + (-24.132 - 27.946)\right] = -285.828 \text{ kN}$$
$$P_D = \frac{A_{blade}}{8}\left[3(\sigma_{D1} + \sigma_{D2}) + (\sigma'_{D1} + \sigma'_{D2})\right]$$
$$P_D = \frac{(10.8414)}{8}\left[3(-5 - 2.054) + (-5.868 - 2.054)\right] = -39.414 \text{ kN}$$
$$P_T = P_U + P_D = -287.828 - 39.414 = -325.242$$

$$\tilde{M}_U = -\left(\frac{A_{blade}}{8}\right)\left(3\sigma_{U1}y_1 + 3\sigma_{U2}y_2 + \sigma'_{U1}y'_1 + \sigma'_{U2}y'_2\right)$$

$$\tilde{M}_U = -\left(\frac{10.8414}{8}\right)\left[3(-25)(-3.4225) + 3(-27.946)(-2.7775) + (-24.132)(-3.6125)\right]$$

$$-\left(\frac{10.8414}{8}\right)\left[(-27.946)(-2.7775)\right] = -886.751 \text{ kN-m}$$

$$\tilde{M}_D = -\left(\frac{A_{blade}}{8}\right)\left(3\sigma_{D1}y_1 + 3\sigma_{D2}y_2 + \sigma'_{D1}y'_1 + \sigma'_{D2}y'_2\right)$$

$$\tilde{M}_D = -\left(\frac{10.8414}{8}\right)\left[3(-5)(3.4225) + 3(-2.054)(2.7775) + (-5.868)(3.6125)\right]$$

$$-\left(\frac{10.8414}{8}\right)\left[(-2.054)(2.7775)\right] = 129.224 \text{ kN-m}$$

$$M_T = \tilde{M}_U + \tilde{M}_D = -886.751 + 129.224 = -757.527 \text{ kN-m}$$

If we use the alternate centroidal distances y_i:

$$\tilde{M}_U = -\left(\frac{10.8414}{8}\right)\left[3(-25)(-3.30) + 3(-27.946)(-2.90) + (-24.132)(-3.395)\right]$$

$$-\left(\frac{10.8414}{8}\right)\left[+(-27.946)(-2.90)\right] = -885.745 \text{ kN-m}$$

$$\tilde{M}_D = -\left(\frac{10.8414}{8}\right)\left[3(-5)(3.30) + 3(-2.054)(2.90) + (-5.868)(3.395)\right]$$

$$-\left(\frac{10.8414}{8}\right)\left[(-2.054)(2.90)\right] = 126.368 \text{ kN-m}$$

$$M_T = \tilde{M}_U + \tilde{M}_D = -885.745 + 126.368 = -759.377 \text{ kN-m}$$

COMPARISON OF 'MANUAL' ESTIMATES AND 'SPREADSHEET' CALCULATIONS OF PIER 2 FORCES

Compare the 'manual' values for $P_U, P_D, P_T, \bar{M}_U, \bar{M}_D, \tilde{M}_U, \tilde{M}_D, M_P, M_T$ with the corresponding values obtained from the spreadsheets.

Comparison of Computed Axial Forces and Bending Moments for the Top Section of Pier 2 Using Test Cases

Procedure	Force	Case											
		1		2		3		4		5		6	
		Manual	Sheet	Manual	Sheet	Manual	Sheet	Manual	Sheet	Manual	Sheet	Manual	Sheet
A	P_U	108.41	108.41	-108.41	-108.41	7.98	7.98	7.98	7.98	-344.67	-344.40	-285.83	-285.83
	P_D	-108.41	-108.41	-108.41	-108.41	7.98	7.98	-7.98	-7.98	-35.05	-35.04	-39.41	-39.41
	P_T	0	0	-216.83	-216.83	15.97	15.97	0	0	-379.72	-379.45	-325.24	-325.24
	$\bar{M}_U$	0	0	0	0	21.85	21.85	21.85	21.85	-3.22	-3.22	3.22	3.22
	$\bar{M}_D$	0	0	0	0	-21.85	-21.85	21.85	21.85	-3.22	-3.22	3.22	3.22
	M_P	679.32	679.34	0	0	0	0	50.02	50.02	-970.07	-969.24	-772.02	-772.03
	M_T	679.32	679.34	0	0	0	0	93.72	93.72	-976.51	-975.68	-765.58	-765.60
B	P_U	108.41	108.41	-108.41	-108.41	7.98	9.74	7.98	9.74	-344.40	-344.66	-285.83	-285.57
	P_D	-108.41	-108.41	-108.41	-108.41	7.98	9.74	-7.98	-9.74	-35.05	-34.79	-39.41	-39.67
	P_T	0	0	-216.83	-216.83	15.97	19.47	0	0	-379.45	-379.45	-325.24	-325.24
	$\tilde{M}_U$	361.29 *350.79*	339.69	-361.29 *-350.79*	-339.69	66.38 *50.07*	56.27	66.38 *50.07*	56.27	-1,081.94 *-1,075.46*	-1083.72	-886.75 *-885.75*	-890.97
	$\tilde{M}_D$	361.29 *350.79*	339.69	361.29 *350.79*	339.69	-66.38 *-50.07*	-56.27	66.38 *50.07*	56.27	103.37 *105.34*	105.20	129.22 *126.37*	128.10
	M_T	722.57 *701.57*	679.38	0 *0*	0	0 *0*	0	132.76 *100.15*	112.55	-978.57 *-970.12*	-978.52	-757.53 *-759.38*	-762.87

For moments in Procedure B, the values in parentheses are for the alternate definitions of the centroidal distances.

Verification of Computed Axial Forces and Bending Moments for the Top Section of Pier 2 at Select Times

Time (days)	**Stresses at Gauge Locations** (Pa)							
	Gauge Number							
	1	**2**	**3**	**4**	**5**	**6**	**7**	**8**
	Gauge Code							
	2TUL1	**2TUC1**	**2TUR1**	**2TUE1**	**2TUL2**	**2TUC2**	**2TUR2**	**2TUE2**
194.9583	-17408880	-14903545	-16149831	-14399618	3157181	96937	904211	8529138
237.7500	-20456466	-17077629	-19184533	-18230945	1974424	-1420958	-286477	6488948
308.1250	-14304957	-11714139	-13137590	-12971675	-672894	-2649371	-2168418	-1714211
Time (days)	**Stresses at Gauge Locations** (Pa)							
	Gauge Number							
	9	**10**	**11**	**12**	**13**	**14**	**15**	**16**
	Gauge Code							
	2TDL1	**2TDC1**	**2TDR1**	**2TDE1**	**2TDL2**	**2TDC2**	**2TDR2**	**2TDE2**
194.9583	-2168692	-5489938	-877788	-4552648	-19275205	-10952483	-14957712	-28782349
237.7500	-2624451	-6379697	-1703733	-4668294	-22550186	-13431403	-18005553	-32584765
308.1250	-3439392	-5010491	-2659916	-5048099	-14945226	-8878053	-11703954	-22644697

Time (days)	**Stresses at Various Locations** (Pa)				
	σ'_{U1}	σ_{U1}	σ_{U2}	σ'_{U2}	$\sigma_{U2} = \sigma'_{U2}$
194.9583	-14399618	-16154085	1386110	8529138	3171867
237.7500	-18230945	-18906209	88996	6488948	1688984
308.1250	-12971675	-13052229	-1830228	-1714211	-1801224
Time (days)	**Stresses at Various Locations** (Pa)				
	σ'_{D1}	σ_{D1}	σ_{D2}	σ'_{D2}	$\sigma_{D2} = \sigma'_{D2}$
194.9583	-4552648	-2845473	-15061800	-28782349	-18491937
237.7500	-4668294	-3569294	-17995714	-32584765	-21642977
308.1250	-5048099	-3703266	-11842411	-22644697	-14542983

1. Time t = 194.9583 days

Use separate σ_{U2} and σ'_{U2}, as well as separate σ_{D2} and σ'_{D2}.

$\sigma'_{U1} = -14,400 \text{ MPa};\ \sigma_{U1} = -16,154 \text{ MPa};\ \sigma_{U2} = 1,386 \text{ MPa};\ \sigma'_{U2} = 8,529 \text{ MPa}$

$\sigma'_{D1} = -4,553 \text{ MPa};\ \sigma_{D1} = -2,845 \text{ MPa};\ \sigma_{D2} = -15,062 \text{ MPa};\ \sigma'_{D2} = -28,782 \text{ MPa}$

Procedure A

$$P_U = \frac{A_{blade}}{8}\left(\sigma'_{U1} + 3\sigma_{U1} + 3\sigma_{U2} + \sigma'_{U2}\right)$$

$$P_U = \frac{(10.8414)}{8}\left[(-14,400) + 3(-16,154) + 3(1,386) + (8,529)\right]$$

$$P_U = -67,996 \text{ kN}$$

$$P_D = \frac{A_{blade}}{8}\left(\sigma'_{D1} + 3\sigma_{D1} + 3\sigma_{D2} + \sigma'_{D2}\right)$$

$$P_D = \frac{(10.8414)}{8}\left[(-4,553) + 3(-2,845) + 3(-15,062) + (-28,782)\right]$$

$$P_D = -117,976 \text{ kN}$$

$$P_T = P_U + P_D = -67,996 - 117,976 = -185,792 \text{ kN}$$

$$\bar{M}_U = \left[\frac{3}{4}\left(\frac{\sigma_{U1} - \sigma_{U2}}{d'_2}\right) + \frac{1}{4}\left(\frac{\sigma'_{U1} - \sigma'_{U2}}{d'_1}\right)\right] I_n$$

$$= \left[\frac{3}{4}\frac{(-16,154) - (1,386)}{(0.645)} + \frac{1}{4}\frac{(-14,400) - (8,529)}{(0.835)}\right](0.704622 \text{ m}^4)$$

$$\bar{M}_U = -19,208 \text{ kN-m}$$

$$\bar{M}_D = \left[\frac{3}{4}\left(\frac{\sigma_{D2} - \sigma_{D1}}{d'_2}\right) + \frac{1}{4}\left(\frac{\sigma'_{D2} - \sigma'_{D1}}{d'_1}\right)\right] I_n$$

$$= \left[\frac{3}{4}\frac{(-15,062) - (-2,845)}{(0.645)} + \frac{1}{4}\frac{(-28,782) - (-4,553)}{(0.835)}\right](0.704622 \text{ m}^4)$$

$$\bar{M}_D = -15,121 \text{ kN-m}$$

$$M_P = \frac{1}{2}(P_U - P_D)d_s = \frac{1}{2}\left[(-67,996) - (-117,976 \text{ kN})\right](6.266 \text{ m})$$

$$M_P = 156,587 \text{ kN-m}$$

$$M_T = \bar{M}_U + \bar{M}_D + M_P = -19,208 - 15,121 + 156,587 = 122,258 \text{ kN-m}$$

Procedure B

$$P_U = \frac{A_{blade}}{8}\left[3\left(\sigma_{U1}+\sigma_{U2}\right)+\left(\sigma'_{U1}+\sigma'_{U2}\right)\right]$$

$$P_U = \frac{(10.8414)}{8}\left[3\left(-16,154+1,386\right)+\left(-14,400+8,529\right)\right]=-67,996 \text{ kN}$$

$$P_D = \frac{A_{blade}}{8}\left[3\left(\sigma_{D1}+\sigma_{D2}\right)+\left(\sigma'_{D1}+\sigma'_{D2}\right)\right]$$

$$P_D = \frac{(10.8414)}{8}\left[3\left(-2,845-15,062\right)+\left(-4,553-28,782\right)\right]=-117,976 \text{ kN}$$

$$P_T = P_U + P_D = -67,996-117,976=-185,792$$

$$\tilde{M}_U = -\left(\frac{A_{blade}}{8}\right)\left(3\sigma_{U1}y_1+3\sigma_{U2}y_2+\sigma'_{U1}y'_1+\sigma'_{U2}y'_2\right)$$

$$\tilde{M}_U = -\left(\frac{10.8414}{8}\right)\left[3\left(-16,154\right)\left(-3.4225\right)+3\left(1,386\right)\left(-2.7775\right)+\left(-14,400\right)\left(-3.6125\right)\right]$$

$$-\left(\frac{10.8414}{8}\right)\left[\left(8,529\right)\left(-2.7775\right)\right]=-247,513 \text{ kN-m}$$

$$\tilde{M}_D = -\left(\frac{A_{blade}}{8}\right)\left(3\sigma_{D1}y_1+3\sigma_{D2}y_2+\sigma'_{D1}y'_1+\sigma'_{D2}y'_2\right)$$

$$\tilde{M}_D = -\left(\frac{10.8414}{8}\right)\left[3\left(-2,845\right)\left(3.4225\right)+3\left(-15,062\right)\left(2.7775\right)+\left(-4,553\right)\left(3.6125\right)\right]$$

$$-\left(\frac{10.8414}{8}\right)\left[\left(-28,782\right)\left(2.7775\right)\right]=340,291 \text{ kN-m}$$

$$M_T = \tilde{M}_U + \tilde{M}_D = -247,513+340,291=92,778 \text{ kN-m}$$

If we use the alternate centroidal distances y_i:

$$\tilde{M}_U = -\left(\frac{10.8414}{8}\right)\left(3\sigma_{U1}y_1+3\sigma_{U2}y_2+\sigma'_{U1}y'_1+\sigma'_{U2}y'_2\right)$$

$$\tilde{M}_U = -\left(\frac{10.8414}{8}\right)\left[3\left(-16,154\right)\left(-3.30\right)+3\left(1,386\right)\left(-2.90\right)\right]$$

$$-\left(\frac{10.8414}{8}\right)\left[\left(-14,400\right)\left(-3.395\right)+\left(8,529\right)\left(-2.90\right)\right]$$

$$\tilde{M}_U = -233,118 \text{ kN-m}$$

$$\tilde{M}_D = \left(\frac{A_{blade}}{8}\right)\left(3\sigma_{D1}y_1 + 3\sigma_{D2}y_2 + \sigma'_{D1}y'_1 + \sigma'_{D2}y'_2\right)$$

$$\tilde{M}_D = -\left(\frac{10.8414}{8}\right)\left[3\left(-2,845\right)\left(3.30\right) + 3\left(-15,062\right)\left(2.90\right)\right]$$

$$-\left(\frac{10.8414}{8}\right)\left[\left(-4,533\right)\left(3.395\right) + \left(-28,782\right)\left(2.90\right)\right]$$

$$\tilde{M}_D = 349,719 \text{ kN-m}$$

$$M_T = \tilde{M}_U + \tilde{M}_D = -233,118 + 349,719 = 116,601 \text{ kN-m}$$

2. Time *t* = 237.7500 days

Use separate σ_{U2} and σ'_{U2}, as well as separate σ_{D2} and σ'_{D2}.

$\sigma'_{U1} = -18,231$ MPa; $\sigma_{U1} = -18,906$ MPa; $\sigma_{U2} = 89$ MPa; $\sigma'_{U2} = 6,489$ MPa

$\sigma'_{D1} = -4,668$ MPa; $\sigma_{D1} = -3,569$ MPa; $\sigma_{D2} = -17,996$ MPa; $\sigma'_{D2} = -32,585$ MPa

Procedure A

$$P_U = \frac{A_{blade}}{8}\left(\sigma'_{U1} + 3\sigma_{U1} + 3\sigma_{U2} + \sigma'_{U2}\right)$$

$$P_U = \frac{(10.8414)}{8}\left[(-18,231) + 3(-18,906) + 3(89) + (6,489)\right]$$

$$P_U = -92,413 \text{ kN}$$

$$P_D = \frac{A_{blade}}{8}\left(\sigma'_{D1} + 3\sigma_{D1} + 3\sigma_{D2} + \sigma'_{D2}\right)$$

$$P_D = \frac{(10.8414)}{8}\left[(-4,668) + 3(-3,569) + 3(-17,996) + (-32,585)\right]$$

$$P_D = -138,157 \text{ kN}$$

$$P_T = P_U + P_D = -92,413 - 138,157 = -230,570$$

$$\bar{M}_U = \left[\frac{3}{4}\left(\frac{\sigma_{U1} - \sigma_{U2}}{d'_2}\right) + \frac{1}{4}\left(\frac{\sigma'_{U1} - \sigma'_{U2}}{d'_1}\right)\right] I_n$$

$$= \left[\frac{3}{4}\frac{(-18,906) - (89)}{(0.645)} + \frac{1}{4}\frac{(-18,231) - (6,489)}{(0.835)}\right](0.704622)$$

$$\bar{M}_U = -20,778 \text{ kN-m}$$

$$\bar{M}_D = \left[\frac{3}{4}\left(\frac{\sigma_{D2} - \sigma_{D1}}{d'_2}\right) + \frac{1}{4}\left(\frac{\sigma'_{D2} - \sigma'_{D1}}{d'_1}\right)\right] I_n$$

$$= \left[\frac{3}{4}\frac{(-17,996) - (-3,569)}{(0.645)} + \frac{1}{4}\frac{(-32,585) - (-4,668)}{(0.835)}\right](0.704622 \text{ m}^4)$$

$$\bar{M}_D = -17,710 \text{ kN-m}$$

$$M_P = \frac{1}{2}(P_U - P_D)d_s = \frac{1}{2}\left[(-92,413) - (-138,157 \text{ kN})\right](6.266 \text{ m}) = 143,316 \text{ kN-m}$$

$$M_T = \bar{M}_U + \bar{M}_D + M_P = -20,778 - 17,710 + 143,316 = 104,828 \text{ kN-m}$$

Procedure B

$$P_U = \frac{A_{blade}}{8}\left[3(\sigma_{U1} + \sigma_{U2}) + (\sigma'_{U1} + \sigma'_{U2})\right]$$

$$P_U = \frac{(10.8414)}{8}\left[3(-18,906 + 89) + (-18,231 + 6,489)\right] = -92,413 \text{ kN}$$

$$P_D = \frac{A_{blade}}{8}\left[3(\sigma_{D1}+\sigma_{D2})+(\sigma'_{D1}+\sigma'_{D2})\right]$$

$$P_D = \frac{(10.8414)}{8}\left[3(-3,569-17,996)+(-4,668-32,585)\right] = -138,157 \text{ kN}$$

$$P_T = P_U + P_D = -92,413 - 138,157 = -230,570 \text{ kN}$$

$$\tilde{M}_U = -\left(\frac{A_{blade}}{8}\right)(3\sigma_{U1}y_1 + 3\sigma_{U2}y_2 + \sigma'_{U1}y'_1 + \sigma'_{U2}y'_2)$$

$$\tilde{M}_U = -\left(\frac{10.8414}{8}\right)\left[3(-18,906)(-3.4225)+3(89)(-2.7775)+(-18,231)(-3.6125)\right]$$

$$-\left(\frac{10.8414}{8}\right)\left[(6,489)(-2.7775)\right] = -326,885 \text{ kN-m}$$

$$\tilde{M}_D = -\left(\frac{A_{blade}}{8}\right)(3\sigma_{D1}y_1 + 3\sigma_{D2}y_2 + \sigma'_{D1}y'_1 + \sigma'_{D2}y'_2)$$

$$\tilde{M}_D = -\left(\frac{10.8414}{8}\right)\left[3(-3,569)(3.4225)+3(-17,996)(2.7775)+(-4,668)(3.6125)\right]$$

$$-\left(\frac{10.8414}{8}\right)\left[(-32,585)(2.7775)\right] = 398,373 \text{ kN-m}$$

$$M_T = \tilde{M}_U + \tilde{M}_D = -326,885 + 398,373 = 71,488 \text{ kN-m}$$

If we use the alternate centroidal distances y_i:

$$\tilde{M}_U = -\left(\frac{10.8414}{8}\right)\left[3(-18,906)(-3.30)+3(89)(-2.90)+(-18,231)(-3.395)\right]$$

$$-\left(\frac{10.8414}{8}\right)\left[(6,489)(-2.90)\right] = -310,974 \text{ kN-m}$$

$$\tilde{M}_D = -\left(\frac{10.8414}{8}\right)\left[3(-3,569)(3.30)+3(-17,996)(2.90)+(-4,668)(3.395)\right]$$

$$-\left(\frac{10.8414}{8}\right)\left[(-32,585)(2.90)\right] = 409,592 \text{ kN-m}$$

$$M_T = \tilde{M}_U + \tilde{M}_D = -310,974 + 409,592 = 98,618 \text{ kN-m}$$

3. Time t = 308.1250 days

Use separate σ_{U2} and σ'_{U2}, as well as separate σ_{D2} and σ'_{D2}.

$\sigma'_{U1} = -12,972$ MPa; $\sigma_{U1} = -13,052$ MPa; $\sigma_{U2} = -1,830$ MPa; $\sigma'_{U2} = -1,714$ MPa

$\sigma'_{D1} = -5,048$ MPa; $\sigma_{D1} = -3,703$ MPa; $\sigma_{D2} = -11,842$ MPa; $\sigma'_{D2} = -22,645$ MPa

Procedure A

$$P_U = \frac{A_{blade}}{8}\left(\sigma'_{U1} + 3\sigma_{U1} + 3\sigma_{U2} + \sigma'_{U2}\right)$$

$$P_U = \frac{(10.8414)}{8}\left[(-12,972) + 3(-13,052) + 3(-1,830) + (-1,714)\right]$$

$$P_U = -80,405 \text{ kN}$$

$$P_D = \frac{A_{blade}}{8}\left(\sigma'_{D1} + 3\sigma_{D1} + 3\sigma_{D2} + \sigma'_{D2}\right)$$

$$P_D = \left(\frac{10.8414}{8}\right)\left[(-5,048) + 3(-3,703) + 3(-11,842) + (-22,645)\right]$$

$$P_D = -100,727 \text{ kN}$$

$$P_T = P_U + P_D = -80,405 - 100,727 = -181,132 \text{ kN}$$

$$\bar{M}_U = \left[\frac{3}{4}\left(\frac{\sigma_{U1} - \sigma_{U2}}{d''_2}\right) + \frac{1}{4}\left(\frac{\sigma'_{U1} - \sigma'_{U2}}{d''_1}\right)\right] I_n$$

$$= \left[\frac{3}{4}\frac{(-13,052) - (-1,830)}{(0.645)} + \frac{1}{4}\frac{(-12,972) - (-1,714)}{(0.835)}\right](0.704622)$$

$$\bar{M}_U = -11,570 \text{ kN-m}$$

$$\bar{M}_D = \left[\frac{3}{4}\left(\frac{\sigma_{D2} - \sigma_{D1}}{d''_2}\right) + \frac{1}{4}\left(\frac{\sigma'_{D2} - \sigma'_{D1}}{d''_1}\right)\right] I_n$$

$$= \left[\frac{3}{4}\frac{(-11,842) - (-3,703)}{0.645} + \frac{1}{4}\frac{(-22,645) - (-5,048)}{0.835}\right](0.704622)$$

$$\bar{M}_D = -10,831 \text{ kN-m}$$

$$M_P = \frac{1}{2}(P_U - P_D)\, d_s = \frac{1}{2}\left[(-80,405) - (-100,727)\right](6.266) = 63,669 \text{ kN-m}$$

$$M_T = \bar{M}_U + \bar{M}_D + M_P = -11,570 - 10,381 + 63,669 = 41,718 \text{ kN-m}$$

Procedure B

$$P_U = \frac{A_{blade}}{8}\left[3(\sigma_{U1} + \sigma_{U2}) + (\sigma'_{U1} + \sigma'_{U2})\right]$$

$$P_U = \frac{(10.8414)}{8}\left[3(-13,052 - 1,830) + (-12,972 - 1,714)\right] = -80,405 \text{ kN}$$

$$P_D = \frac{A_{blade}}{8}\left[3\left(\sigma_{D1}+\sigma_{D2}\right)+\left(\sigma'_{D1}+\sigma'_{D2}\right)\right]$$

$$P_D = \left(\frac{10.8414}{8}\right)\left[3\left(-3,703-11,842\right)+\left(-5,048-22,645\right)\right]=-100,727 \text{ kN-m}$$

$$P_T = P_U + P_D = -80,405-100,727=-181,132 \text{ kN}$$

$$\tilde{M}_U = -\left(\frac{A_{blade}}{8}\right)\left(3\sigma_{U1}y_1+3\sigma_{U2}y_2+\sigma'_{U1}y'_1+\sigma'_{U2}y'_2\right)$$

$$\tilde{M}_U = -\left(\frac{10.8414}{8}\right)\left[3(-13,052)(-3.4225)+3(-1,830)(-2.7775)+(-12,972)(-3.6125)\right]$$
$$-\left(\frac{10.8414}{8}\right)\left[(-1,714)(-2.7775)\right]=-272,230 \text{ kN-m}$$

$$\tilde{M}_D = -\left(\frac{A_{blade}}{8}\right)\left(3\sigma_{D1}y_1+3\sigma_{D2}y_2+\sigma'_{D1}y'_1+\sigma'_{D2}y'_2\right)$$

$$\tilde{M}_D = -\left(\frac{10.8414}{8}\right)\left[3(-3,703)(3.4225)+3(-11,842)(2.7775)+(-5,048)(3.6125)\right]$$
$$-\left(\frac{10.8414}{8}\right)\left[(-22,645)(2.7775)\right]=295,193 \text{ kN-m}$$

$$M_T = \tilde{M}_U + \tilde{M}_D = -272,230+295,193=22,963 \text{ kN-m}$$

If we use the alternate centroidal distances y_i:

$$\tilde{M}_U = -\left(\frac{10.8414}{8}\right)\left[3(-13,052)(-3.30)+3(-1,830)(-2.90)\right]$$
$$-\left(\frac{10.8414}{8}\right)\left[(-12,972)(-3.395)+(-1,714)(-2.90)\right]$$

$$\tilde{M}_U = -263,102 \text{ kN-m}$$

$$\tilde{M}_D = -\left(\frac{10.8414}{8}\right)\left[3(-3,703)(3.30)+3(-11,842)(2.90)+(-5,048)(3.395)\right]$$
$$-\left(\frac{10.8414}{8}\right)\left[(-22,645)(2.90)\right]=301,518 \text{ kN-m}$$

$$M_T = \tilde{M}_U + \tilde{M}_D = -263,102+301,518=38,416 \text{ kN-m}$$

4. **Verification Summary**

Compare the values computed at times t = 194.5983, 237.7500 and 308.1250 days for the two manual procedures (i.e., A and B), as well as with the spreadsheet values for these two procedures. Procedure A provides more consistent estimates than Procedure B. That Procedure A is more consistent than Procedure B can be understood in terms of the implicit assumptions of the linear, elastic analysis formula for the moment-curvature relation. This formula implies a linear distribution of flexural stresses, whereas in Procedure B, there is no implicit distribution of strains.

Of the two alternatives for Procedure B, using symmetric stresses for the non-instrumented locations is more consistent than using the extrapolated values. The symmetric images provide more consistent force estimates than the extrapolated stresses because there are relative small strain gradients along the blades, so the extrapolations based on linear least-squares fitting of these strains is subject to larger error.

Verification of Results Summary

Procedure	Force	t = 194.9583 days		t = 237.750 days		t = 308.125 days	
		manual	*Sheet*	*manual*	*sheet*	*manual*	*sheet*
A	P_U	-67,996	-67,995	-92,413	-92,414	-80,405	-80,407
	P_D	-117,976	-117,977	-138,157	-138,158	-100,727	-100,730
	P_T	-185,792	-185,972	-230,570	-230,572	-181,132	-181,137
	$\bar{M}_U$	-19,208	-19,208	-20,778	-20,778	-11,570	-11,569
	$\bar{M}_D$	-15,121	-15,121	-17,710	-17,709	-10,381	-10,381
	M_P	156,187	156,597	143,316	143,316	63,669	63,673
	M_T	122,258	122,268	104,828	104,829	41,718	41,723
B*	P_U	-67,996	-78,035	-92,413	-100,717	-80,405	-81,473
			-70,216		-94,546		-81,419
	P_D	-117,976	-104,289	-138,157	-124,006	-100,727	-89,842
			-116,646		-136,639		-99,680
	P_T	-185,792	-182,235	-230,570	-224,723	-181,132	-171,315
			-186,833		-231,185		-181,099
	$\tilde{M}_U$	-247,513	-265,606	-326,886	-338,400	-272,230	-268,563
		-233,118	-241,591	-310,974	-319,713	-263,102	-268,182
	$\tilde{M}_D$	340,291	311,641	398,373	370,645	295,193	271,243
		349,719	348,518	409,552	408,213	301,518	300,702
	M_T	92,778	46,035	71,488	32,344	22,963	2,680
		116,601	106,927	98,618	88,500	38,415	32,520

*The first of the two values reported for moments (in yellow) is computed using the initial set of centroidal distances (i.e., to the location of the gauge). The second set of values (in blue) is for the alternate definition of centroidal distances (i.e., to the center of the area element). The first of the two spreadsheet values reported for all forces (in pink) is computed using extrapolated stresses for the symmetric (mirror) images of TUE1, TUE2, TDE1 and TDE2. The second of the two spreadsheet values (in green) was computed using the stresses measured at the symmetric locations.